INTEGRATION OF DYNAMIC DATA INTO RESERVOIR DESCRIPTION USING STREAMLINE APPROACHES

A Dissertation

by

ZHONG HE

Submitted to the Office of Graduate Studies of
Texas A&M University
in partial fulfillment of the requirements for the degree of

DOCTOR OF PHILOSOPHY

August 2003

Major Subject: Petroleum Engineering

INTEGRATION OF DYNAMIC DATA INTO RESERVOIR DESCRIPTION USING STREAMLINE APPROACHES

A Dissertation

by

ZHONG HE

Submitted to Texas A&M University
in partial fulfillment of the requirements
for the degree of

DOCTOR OF PHILOSOPHY

Approved as to style and content by:

Akhil Datta-Gupta
(Chair of Committee)

W. John Lee
(Member)

Thomas A. Blasingame
(Member)

Richard L. Gibson
(Member)

Hans C. Juvkam-Wold
(Head of Department)

August 2003

Major Subject: Petroleum Engineering

ABSTRACT

Integration of Dynamic Data into Reservoir Description
Using Streamline Approaches. (August 2003)
Zhong He, B.S., Jianghan Petroleum Institute;
M.S., Research Institute of Petroleum Exploration and Development (RIPED)
Chair of Advisory Committee: Dr. Akhil Datta-Gupta

Integration of dynamic data is critical for reliable reservoir description and has been an outstanding challenge for the petroleum industry. This work develops practical dynamic data integration techniques using streamline approaches to condition static geological models to various kinds of dynamic data, including two-phase production history, interference pressure observations and primary production data. The proposed techniques are computationally efficient and robust, and thus well-suited for large-scale field applications. We can account for realistic field conditions, such as gravity, and changing field conditions, arising from infill drilling, pattern conversion, and recompletion, etc., during the integration of two-phase production data. Our approach is fast and exhibits rapid convergence even when the initial model is far from the solution. The power and practical applicability of the proposed techniques are demonstrated with a variety of field examples.

To integrate two-phase production data, a travel-time inversion analogous to seismic inversion is adopted. We extend the method via a ‘generalized travel-time’ inversion to ensure matching of the entire production response rather than just a single time point while retaining most of the quasi-linear property of travel-time inversion. To integrate the interference pressure data, we propose an alternating procedure of travel-time inversion and peak amplitude inversion or pressure inversion to improve the overall matching of the pressure response.

A key component of the proposed techniques is the efficient computation of the sensitivities of dynamic responses with respect to reservoir parameters. These sensitivities are calculated analytically using a single forward simulation. Thus, our methods can be orders of magnitude faster than finite-difference based numerical approaches that require multiple forward simulations.

Streamline approach has also been extended to identify reservoir compartmentalization and flow barriers using primary production data in conjunction with decline type-curve analysis. The streamline ‘diffusive’ time of flight provides an effective way to calculate the drainage volume in 3D heterogeneous reservoirs. The flow barriers and reservoir compartmentalization are inferred based on the matching of drainage volumes from streamline-based calculation and decline type-curve analysis. The proposed approach is well-suited for application in the early stages of field development with limited well data and has been illustrated using a field example from the Gulf of Mexico.

DEDICATION

To my lovely wife and son, to my beloved mother-in-laws and mother, to all the members of my wife's family and my family, for their love, care, understanding and inspiration.

ACKNOWLEDGMENTS

I would like to express my deep gratitude to my advisor and committee chairman, Dr. Akhil Datta-Gupta for his invaluable advice, financial support, accessibility for discussion and especially for academic guidance.

I would like to thank Dr. W. John Lee, Dr. Thomas A. Blasingame, and Dr. Richard Gibson for serving as committee members and Dr. Doug Hensley for serving as the Graduate Council Representative. I acknowledge their helpful comments and suggestions.

I would like to express my deep appreciation to Dr. Ching Wu for his support, guidance and encouragement during my early years of Ph.D. education.

I wish to take this opportunity to extend my special thanks to Dr. Michael King for sharing his profound knowledge and experience with me and to Pavel Illiassov for his help and hospitality during my summer internship with BP. Thanks are due to many people in El Paso Production Company, especially Tai Pham and Jorge Perez for their help and support when I worked with them last summer.

I want to thank my friends in the reservoir characterization group, Dr. Zhan Wu (now at UT-Austin), Dr. Seongsik Yoon (now with Veritas), Dr. Sang Heon Lee (now with CheveronTexaco), Arun Kharghoria, Ill Nam, Hao Cheng, Harshal Parikh, Ahmed Daoud, Mishal Al-Harbi, Ahmed Al-Huthali, Ichiro Osako, and Hector Perez for helpful discussions, and for making my graduate years enjoyable and memorable.

I would like to acknowledge financial support from the *Joint Industry Project* members and also from the U.S. Department of Energy. The facilities and resources provided by the Petroleum Engineering Department, Texas A&M University, are gratefully acknowledged.

TABLE OF CONTENTS

CHAPTER Page

LIST OF TABLES

LIST OF FIGURES

FIGURE Page

FIGURE Page

FIGURE Page

FIGURE Page

FIGURE Page

CHAPTER I

INTRODUCTION

1.1 Statement of the Problem

Reservoir description is critical to field development and reservoir management. It is well recognized that reservoir heterogeneity, such as the spatial distribution of permeability or porosity significantly affects the flow characteristics of the reservoir. Reservoir compartmentalization and flow barriers such as sealing faults or continuous low permeability trends can also have significant impacts on the field development strategy. To characterize reservoir heterogeneity, fine-scale geological models have been routinely built using geostatistical techniques from static data such as geological descriptions, well logs, seismic attributes, and core data. However, these static geological models often fail to reproduce the dynamic responses of the reservoir. Therefore, it is extremely important to incorporate dynamic data into the geological models for reliable reservoir descriptions. The dynamic responses of reservoir can be time variant measurements and production history, such as water-cut, tracer data, interference pressure and 4D seismic etc. Integration of theses dynamic data involves inferring necessary modifications to the geological model so that the model responses can match the observed dynamic responses.

Integration of dynamic data to estimate reservoir properties is difficult for the following reasons:

1. Dynamic data are sparse and the sampling is often limited at only the well locations.
2. Dynamic data have low resolution and represent integrated responses of the reservoir.
3. The mathematical model is complex, usually requiring numerical simulation of the flow and transport.
4. Integration of dynamic data usually requires the solution of an inverse problem. The inverse problem is usually highly nonlinear and ill-posed. The solution of such inverse

---

This dissertation follows the style and format of the *SPE Journal*.

problems is not only difficult, but also very computationally expensive, and can suffer from instability and non-uniqueness.

Integration of dynamic data has been a challenging task in reservoir description. A critical aspect in dynamic data integration is the computation of sensitivity coefficients as the gradient-based methods are commonly used to solve the inverse problem. The sensitivities provide the information on how the dynamic responses change because of small changes in reservoir properties. Computation of sensitivities often constitutes the most computationally intensive part in inverse modeling. In addition, the high nonlinearity of the inverse problem often leads to inadequate matching of the dynamic data. The past few years have seen significant developments in the area of such dynamic data integration through the use of inverse modeling to estimate reservoir parameters such as permeability or porosity. However, previous works are limited in terms of the number of reservoir parameters to be estimated and also simplified field conditions. One of the main problems is that the computation of sensitivities is still too expensive to be applied to large-scale reservoir models containing several hundred thousand cells. Furthermore, to facilitate the inversion, until now the changing field conditions, such as infill drilling, pattern conversion, were often unaccounted or approximately accounted.

Reservoir compartmentalization and flow barriers are very important in reservoir description. However, very often they cannot be fully described from the static data, especially in the early stages of field development. For example, small-scale faults and flow barriers are often unidentifiable from seismic responses because of the limited resolution of seismic data. Dynamic responses of the reservoir contain important information on these kinds of reservoir properties. However, identification of reservoir compartmentalization and flow barriers from well production responses has remained relatively unexplored.

1.2 Background and Literature Review

The process of inversion is to estimate values of reservoir parameters, such as permeability and porosity from indirect measurements on the reservoir system. It is known as inverse modeling or parameter estimation, since it is the opposite process to the forward modeling that relates known parameters to unknown system state variables. Parameter estimation or inverse modeling usually contains three major components: the forward model; the objective function and the minimization. The forward model predicts the responses of the reservoir system given a set of reservoir parameters. The objective function measures the difference between the observed dynamic data and the predicted responses. The minimization is to derive the unknown parameters by minimizing the objective function. Since the objective function is usually related in a nonlinear fashion to the parameters, consequently the process of minimization must be iterative.

The forward model is constructed based on the physical laws that govern the problem. Those fundamental laws for the dynamics of reservoir system include continuity equation, Darcy's flow equation, an appropriate equation of state and other relevant relationships, such as relative permeability, etc. The forward model usually involves numerical simulation, which can be computationally expensive. Therefore, increasing the computation speed of forward simulation is an important factor in dynamic data integration.

It is very important to properly set up the objective function because the inverse problem in reservoir modeling is usually highly nonlinear and ill-posed. The ill-posed nature of an inverse problem is associated with the non-uniqueness and instability of the solution.[1-4] The non-uniqueness issue typically arises when we have an underdetermined problem, which is unfortunately just the case in dynamic data integration. The amount of dynamic data is often much less than the number of reservoir parameters to be estimated. The instability issue arises if a small change in data results in large fluctuations in the estimation. The ill-posedness can be reduced by including regularization terms in the objective function through reducing the admissible parameter space. The nonlinearity can be also reduced by properly setting up of the objective function.

The minimization algorithms can be classified into two categories: gradient based, such as Gauss-Newton method and conjugate-gradient method, and gradient-free, such as simulated annealing and genetic algorithm. Gradient-based algorithms are commonly used for the minimization.[3] These algorithms require the information on the sensitivity coefficients in order to proceed with the minimization. Because the computation of sensitivities is very computationally intensive, it has constituted the key step in dynamic data integration and most of the research in the area of dynamic data integration has focused on computing sensitivities. In the following review we will discuss the developments of dynamic data integration techniques with special emphasis on sensitivity computation.

There are basically three categories of numerical methods for sensitivity computation: perturbation technique; sensitivity equation method and adjoint state method.[3-4] The perturbation approach is the simplest one. Sensitivities are estimated by simply perturbing each of the reservoir parameters by a small amount and rerunning the forward simulation to see the change in model responses. The required forward simulation runs equal to the number of model parameters plus one.[3] Therefore, it is very time consuming to obtain the sensitivities using this approach.

For sensitivity equation method, the governing equations are differentiated with respect to parameters to obtain the equations for the sensitivity coefficients. These equations are then numerically solved for the sensitivities.[3] This approach is also often called as the gradient simulator method. The computational and storage requirements are also very high for this method because there are as many equations to be solved as the number of parameters. To reduce the computational burden, Anterion *et al.*[5] factored out the common coefficient matrix for all sensitivity equations, and solved the matrix problem with multiple right-hand side vectors associated with each of the model parameters. In the sensitivity equation method, one actually needs to calculate the sensitivities of all grid state variables (pressure or saturation) to each model parameter. By neglecting the sensitivities at grid blocks other than well blocks, Tang *et al.*[6] presented the GPST (Generalized Pulse-Spectrum Technique) for two-phase history matching. Chu *et al.*[7] developed a modified GPST for computing sensitivities. The MGPST is an effective approximation of sensitivity equation method and produces reasonably accurate estimates of sensitivity coefficients to permeability. However, the approximation yields inaccurate estimates of sensitivity coefficients to porosity. In general, the sensitivity equation method is not attractive for high-resolution reservoir models. Even with the MGPST approximation, the computation is still prohibitive if we have a large reservoir model, for example, with hundred thousand to million grid blocks. This is because a matrix problem with N_w right-hand side vectors need to be solved at each time step during the simulation.

The adjoint state method based on the variational approach derives a set of adjoint equations associated with the governing equations to calculate the sensitivities.[8-16] Jacquard and Jain[8] proposed the first automatic history matching procedure using this method for permeability estimation in 2-D reservoirs. Their method used variational analysis to numerically compute sensitivity coefficients based on an analogy of a reservoir to an electric network. Later, followed the basic ideas of Jacquard and Jain, Carter *et al.*[9] derived a method to compute the pressure sensitivities with respect to the discretized permeability and porosity in a numerical reservoir simulator for a two-dimensional single-phase flow problem. The advantage of Carter's method is its computational efficiency over the perturbation-based method regardless of the model size, it requires only *Nw*+1 forward simulations to generate the sensitivity coefficients where *Nw* is the number of wells. Therefore it can save a lot of computational cost. Recently, He *et al.*[11] extended the Carter's method to three-dimensional problems. The major limitation of Carter's method is that it is applicable to single-phase flow, and cannot be directly extended to multi-phase flow. To overcome this problem, Chen *et al.*[12] and Chavent *et al.*[13] applied the optimal control method to efficiently compute the gradient of the objective function with respect to permeability or porosity by solving two differential equations: the diffusivity equation and its adjoint equation. Although they used this method for single-phase history matching, the optimal control formulism can be applied to multi-phase flow problem. For the single-phase flow problem, Carter *et al.*[14] showed the equivalence between Carter's method and the optimal control method. Watson *et al.*[15] extended the optimal control method to two-phase flow problems for estimating absolute and relative permeability and porosity using two-phase production as well as pressure data. It is believed that sensitivity information can be more valuable than gradient information from the optimization point of view, because more efficient minimization algorithms, such as a Gauss-Newton method with quadratic convergence rate can be used to minimize least square type objective function. Therefore, Wu *et al.*[16] applied the optimal control to develop a procedure to compute sensitivities of pressure and water-cut with respect to reservoir parameters for a two-phase problem and utilized Gauss-Newton approach to generate estimates of reservoir parameters. The optimal control method is computationally efficient if the gradient of the objective function with respect to permeability or porosity is computed because it requires the solutions of only two differential equations per iteration. However, same level of computational efforts as Carter's method is required if the optimal control method is formulated to compute the sensitivity coefficients. That means, if there are *Nw* wells with *Nd* data points, to obtain the sensitivities, *Nw*Nd* additional equations need to be adjointed with the diffusivity equation.[14,16] Therefore, adjoint method is still computationally expensive for large-scale problems.

The above approaches are usually limited to applications with relatively small number of parameters (several thousand parameters). In the past few years, streamline-based production data integration technique has undergone rapid development to meet the needs of integrating production data into high-resolution large-scale reservoir models.[17-19] Vasco *et al.*[17] presented a streamline-based production data integration approach for the inversion of water-cut and tracer data with 50,000 parameters. One advantage of streamline model is its computational efficiency as a forward model. The streamline model is usually orders of magnitude faster than conventional finite difference simulators.[20-21] More importantly, the sensitivities are computed analytically using a single forward simulation under the simplified field conditions.[17-18] Yoon *et al.*[19] extended this method to the estimation of residual oil phase saturation by integrating interwell partitioning tracer tests. The streamline-based production data integration technique needs to be further developed to account for the actual field conditions, such as gravity, infill drilling, pattern conversion etc.

Gradient-free minimization algorithms, such as simulated annealing and genetic algorithm, have also been used for dynamic data integration.[22-26] These algorithms have the advantage of the ability of converging to global minimum and the convenience of incorporating different kinds of data. However, they are computationally inefficient and have a slow rate of convergence. Several thousands of iterations are usually required to converge even for problems with a few hundred parameters. They are impractical for large-scale problems.

As discussed before, the inverse problem is ill-posed. To deal with this undesired problem, the objective function is often regularized by including certain prior knowledge of model parameters.[1-4] The regularization can be deterministic or stochastic. In deterministic regularization, additional terms are imposed onto the objective function to ensure that the solution does not deviate too much from the prior model and reproduces the dominant features of parameter structure.[1-4,17-18,27] In the stochastic approach, Bayesian theorem is applied to define a posteriori pdf, which represents the probability density of model parameters based on both the dynamic data and the prior information.[1,4,28-30] The flatness of the posteriori density function is reduced by the prior information so that the inverse problem becomes less ill-posed.[28-30] In fact, the deterministic and Bayesian's approaches are equivalent, as shown by Tarantola.[1]

Instead of matching the dynamic data directly, Datta-Guptta *et al.*[18] and Vasco *et al.*[17] developed a travel time inversion technique to integrate multiphase production data following the seismic wave inversion.[31-34] The arrival time of water front is derived from the original observed data. Then, the objective function is defined in terms of the difference between the observed and calculated arrival times. Kulkarni *et al.*[35] and Vasco *et al.*[36] also extended the travel time inversion approach to interference transient pressure data. Unlike the conventional ‘amplitude’ matching (direct match of the data), which is highly nonlinear, the travel time inversion has quasi-linear properties.[34,37] Therefore, the minimization proceeds rapidly and is relatively insensitive to the initial model.[37]

1.3 Objectives of Research

The primary objective of this research is to develop highly efficient dynamic data integration techniques that are suitable for fine-scale reservoir descriptions and practical field applications. The specific objectives are:

- Development of a ‘generalized’ travel time inversion technique to integrate two-phase production data into high-resolution reservoir models. The technique is particularly well-suited to large-scale field applications with gravity and changing field conditions.

- Development of analytical approaches to compute the sensitivities of two-phase production data with respect to reservoir parameters such as permeability, and porosity. The approaches are able to account for changing field conditions, such as infill drilling, pattern conversion and rate changes etc. The approaches require only a single streamline simulation, offering extremely efficient ways of computing the sensitivities.

- Development of an alternating travel time/peak amplitude or pressure amplitude inversion technique to integrate interference pressure data into reservoir models. The technique significantly improves the overall matching of transient pressure data over the previous inversion method that uses travel time match only. The technique facilitates a stable and robust solution of highly undetermined inverse problems.

- Development of approximate analytical approaches to compute the sensitivities of transient pressure data with respect to reservoir parameters such as permeability, and porosity. The approaches analytically compute the sensitivities for travel time, and pressure amplitude using a single forward simulation.

- Development of a novel approach to identify reservoir compartmentalization and flow barriers using primary production data. The approach is based on streamline-based drainage volume calculation and decline-type curve analysis. It is well-suited for application in the early stages of field development with limited well data.

- Application of the techniques to field examples: integration of two-phase production history for the Goldsmith San Andres Unit (GSAU) in West Texas, and a giant middle eastern oil field with water injection and aquifer support; integration of multi-well interference tests at the Conoco Borehole Test Facility; and the identification of flow barriers from primary production data for an offshore oil reservoir in the Gulf of Mexico.

1.4 Dissertation Outline

Chapter II discusses the general methodology of parameter estimation adopted in this work. Dynamic data integration involves the solution of an inverse problem, which requires an effective methodology in terms of both computational efficiency and robustness. The primary components of our methodology consist of fast streamline simulation as a forward model for two-phase flow; efficient inversion procedures, such as travel-time inversion and 'generalized travel-time' inversion for integration of two-phase production data, an alternating inversion of travel-time and peak amplitude or pressure for integration of interference pressure data; analytical computation of sensitivities and regularization of objective function in the minimization.

Chapter III presents a streamline-based production data integration technique via travel-time and 'generalized travel-time' inversion to condition large-scale geological models to two-phase production data. The fundamentals of streamline simulation are first discussed. Then, the concept of 'generalized travel-time' is illustrated as an extension of conventional travel-time. A streamline model not only serves as an efficient forward model for inversion but also provides unique ways to compute sensitivities from a single streamline simulation. Based on streamline time-of-flight formulation, an analytical approach for sensitivity computations is developed. The approach can account for gravity effects and changing field conditions. Finally, the power and computational efficiency of the proposed approach are demonstrated by synthetic and field examples. One of the field examples is a giant Middle Eastern oil field. The production data integration was efficiently carried out on an upscaled model (93,600 cells) in less than 6 CPU hours and on a fine-scale model (921,600 cells) in 28 CPU hours in a PC for this field, and resulted significant improvement in the production history match.

Chapter IV presents an efficient approach to integrate interference transient pressure data into reservoir models. The proposed method extends travel time inversion into an alternating inversion of travel time match followed by peak amplitude match or pressure match. Utilizing the concept of streamline ‘diffusive’ time of flight and zero-order expansion developed from the asymptotic solution for compressible flow, we developed analytical approaches to estimate the sensitivities for travel time, peak amplitude and pressure amplitude using a single forward simulation. A synthetic example is used to illustrate and validate the proposed inversion technique. The approach has been applied to a field example to characterize a naturally fractured reservoir. The inversion on one interference test produced an estimation of permeability distribution consisting of an orthogonal fracture pattern, which is consistent with field experimental observations and interpretations. Using the estimated permeability model, another interference test has been successfully predicted, with satisfactory match of the observed pressure responses.

Chapter V discusses a novel approach that utilizes the streamline-based drainage volume computations for identification of reservoir compartmentalization and flow barriers using primary production data. Based on matching of the streamline-based drainage volumes with those from the decline curve analysis, reservoir compartmentalization and flow barriers are inferred. The approach is validated via synthetic and field examples. The practical feasibility of the approach is demonstrated with a field example from the Gulf of Mexico. Starting with a reservoir model based on well log and seismic data, reservoir compartmentalization and flow barriers are identified from three years of primary production data.

In Chapter VI, the new developments from this work and their practical applicabilities are summarized. Potential future research works are also suggested.

CHAPTER II

METHODOLOGY OF PARAMETER ESTIMATION

As discussed in the previous chapter, integration of dynamic data involves the solution of an inverse problem and constitutes a challenging task in reservoir description. An inverse problem is often difficult to solve because of its properties of high non-linearity and ill-posedness. Moreover, the solution of an inverse problem usually involves an iterative process that requires extensive computations. With existing approaches, integration of dynamic data is not applicable to large-scale problems. In order to make dynamic data integration technique practically feasible to large-scale field applications, the methodology for parameter estimation should be effective in terms of both computational efficiency and robustness. This chapter explains the general methodology of parameter estimation used in this research.

2.1 Fast Streamline Simulation as a Forward Model

We use a 3D streamline simulator to model two-phase flow in a reservoir. The streamline simulation is an IMPES type simulation: we solve pressure first and then saturation. Based on pressure solution, streamlines are generated. Unlike conventional finite-difference type simulation, the streamline method decouples the transport calculation from the underlying grid on which pressure field is obtained. Saturation is moved along streamlines characterized by time of flight coordinate. The decoupling allows large time steps with fewer pressure solutions without suffering from numerical instability or dispersion. Consequently, the streamline simulation has a superior simulation speed, often orders of magnitude faster that conventional finite-difference simulator.

Compressibility and gravity are included in the streamline simulation. The effects of gravity on simulation are two fold. Its effect on pressure solution is considered by including the gravity terms into the pressure equation. Its effect on saturation is considered with an operator splitting. Changing field conditions arising from rate changes or infill drilling are accounted via pressure updating followed by regeneration of streamlines and re-initialization of saturation along the streamlines. Saturation advancement along the streamlines is carried out through a numerical solution of the transport equation. Capillary pressure is not included into the simulation, although it is possible to do so. More detailed discussion on streamline simulation is presented in the next chapter.

Because of its superior computational efficiency, streamline simulation can effectively model large-scale problems, for example, multimillion cell detailed geologic models. Therefore, streamline simulation has received increasing applications in various aspects, such as ranking of multiple geostatistical reservoir models,[38] upscaling[21] of geological models and dynamic data integration etc.[17]

Besides its computational efficiency as a forward model, streamline simulation offers another advantage for inverse modeling - sensitivities to reservoir parameters can be formulated along streamlines and obtained analytically from a single streamline simulation. This results in significant savings in computation time and makes high-resolution reservoir description possible.

2.2 Travel-time Inversion for Efficient Integration of Dynamic Data

Traditionally, dynamic data integration is performed by directly matching the data, for example, water-cut, tracer concentration and pressure data. This is denoted as 'amplitude matching' (**Fig. 2.1**). Recently, the approach of 'travel-time matching' has shown great promise for practical field applications.[17-18,35-36] In this approach, the observed data and model predictions are lined up at some reference time such as the breakthrough or arrival time (**Fig. 2.1**). The travel-time matching offers several advantages for dynamic data integration. First, unlike amplitude matching, which can be highly nonlinear, the travel-time inversion has quasi-linear properties.[37] As a result, travel-time inversion is robust and converge rapidly even if the initial model is not close to the solution. It has been shown that the amplitude inversion can be orders of magnitude more non-linear compared to the travel-time inversion.[37] The highly non-linearity of amplitude inversion results in difficulties for convergence, often leading to an inadequate history match. Because of its quasi-linear property, the travel-time inversion can reduce the chances for the solution to converge to secondary peaks, resulting in a better matching to the dynamic data. Second, the travel-time inversion is more computationally efficient because the number of travel-time is equal to the number of wells, regardless of the number of dynamic data points. This leads to considerable savings in computational time for the minimization. Finally, the travel-time inversion is very efficient to resolve the large-scale features of heterogeneity.[17]

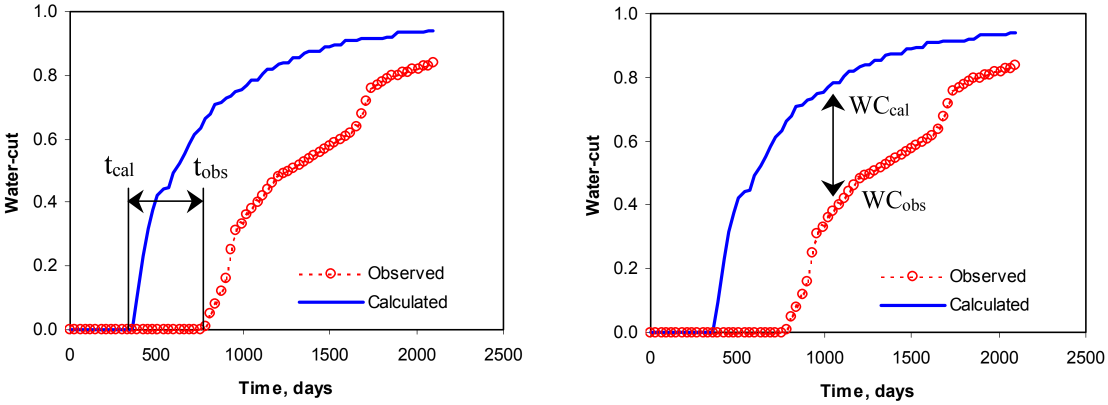

(a)

(b)

Figure 2.1—Illustration of (a) travel-time inversion, (b) amplitude inversion for water-cut response at a well.

In this research, we adopt travel-time inversion as the driving force for efficient integration of dynamic data. For two-phase production data, the travel-time is usually defined as the time that water-cut at a producer reaches at certain value, for example, 10%. By generalizing the concept of travel-time as an overall discrepancy between the whole observed and calculated water-cut curves, a 'generalized travel-time' inversion technique is developed. The 'generalized travel-time' inversion ensures matching of entire production responses rather than just a single time point while retaining most of the desirable properties of travel-time inversion. The concept of 'generalized travel-time' will be discussed in more details in the next chapter.

For interference pressure data, the travel-time is derived by differentiating pressure responses with respect to time for each observing wells.[35-36] The time corresponding to the maximum of pressure temporal derivative is defined as the travel-time or arrival time of the transient pressure front and the maximum magnitude of the derivative is defined as the peak amplitude. The travel-time is first performed to infer the large-scale features of reservoir models. Then peak amplitude inversion or pressure inversion follows by taking the estimates from travel-time inversion as the initial models. The travel-time inversion and the peak amplitude or pressure inversion are further alternated to improve the overall matching. Although the peak amplitude or pressure inversion is helpful to improve the overall matching, the travel-time inversion plays a vital role in the process of integration of interference pressure data.

2.3 Streamline-based Analytical Computation of Sensitivities

The sensitivities quantify the change in dynamic responses because of a small perturbation in reservoir properties. As discussed before, sensitivity computation is a vital part in dynamic data integration. Without efficient approaches for computing the sensitivities required by the inverse modeling, it is not possible to integrate the dynamic data into large-scale models. In this research, we develop analytic formulations for sensitivity computation using streamline approaches. Our analytic approaches for sensitivity computation are extremely efficient since the sensitivities of all kinds of dynamic data with respect to reservoir properties can be obtained using a single forward simulation. Here, we give a brief discussion on the general ideas of analytical computation of sensitivities. The details will be presented in the following chapters.

For two-phase production data, the sensitivity calculations are based on streamline time-of-flight formulation and can account for gravity and changing field conditions arising from rate changes, infill drilling and pattern conversions etc. Analytical formulations for the sensitivities of travel-time and 'generalized travel-time' are developed. For interference transient test data, Analytic approaches are developed to compute the sensitivities of travel time, peak amplitude and pressure response based on the concept of streamline 'diffusive' time of flight and zero-order approximation derived from the asymptotic solution of pressure equation.

2.4 Regularization of Objective Function in Minimization

Our goal is to reconcile high-resolution geologic models to dynamic field responses. In our approach, we start with a static model that already incorporates geologic, well log and seismic data. Such a model can be constructed using geostatistical algorithms or by other means. We then minimize a locally linearized data misfit function, which is the sum of the squares of the residuals.

$$J = \left\| \delta\mathbf{d} - \mathbf{S}\delta\mathbf{R} \right\| = \sum_{i=1}^{n} \left(\delta d_i - \sum_{j=1}^{m} S_{ij}\delta R_j \right)^2 \tag{2.1}$$

where || || denotes the Euclidean norm of a vector; $\delta\mathbf{d}$ is the data residual vector, that is the difference between the observed and calculated dynamic responses; the particular data depends on the types of inversion, for example, for the travel-time inversion, the data will be travel-time, or for the ‘generalized travel-time’ inversion, the data will be the ‘generalized’ travel time. Also **S** is the sensitivity matrix that quantifies the change in predicted responses because of a small change in reservoir properties, such as permeability or porosity; and $\delta\mathbf{R}$ is the reservoir property change vector that we are looking for in the inversion.

Our inverse problem is typically underdetermined and ill-posed. To regularize or stabilize the inverse problem, two additional penalty terms are included into the objective misfit function.[1-2,17-18]

$$J = \|\delta\mathbf{d} - \mathbf{S}\delta\mathbf{R}\| + \beta_1\|\delta\mathbf{R}\| + \beta_2\|\mathbf{L}\delta\mathbf{R}\| \tag{2.2}$$

where $\beta_1\|\delta\mathbf{R}\|$ is the “norm” constraint and $\beta_2\|\mathbf{L}\delta\mathbf{R}\|$ is the “roughness” constraint, **L** is a second-order spatial difference operator, β_1 and β_2 are two weights which determine the relative strengths of the norm term and the roughness term.

$$\|\delta\mathbf{R}\| = \sum_{j=1}^{M}(\delta\mathbf{R}_j)^2 \tag{2.3}$$

$$\|\mathbf{L}\delta\mathbf{R}\| = \sum_{j=1}^{M}(\Delta\delta\mathbf{R}_j)^2 \tag{2.4}$$

The norm constraint penalizes the large deviation of reservoir property from the initial model because our initial or prior model already contains the available geological and static information of the reservoir. This helps preserve geologic realism because our initial or prior model already incorporates available geologic and static information related to the reservoir. The roughness constraint penalizes the model that has rapid spatial property variations. This is motivated by the fact that our data represent an integrated response of the reservoir, and thus, are suited to resolve the large-scale features instead of small-scale property variations.

The minimum in Eq.2.2 can be obtained by an iterative least-squares solution to the following augmented linear system

$$\begin{pmatrix} \mathbf{S} \\ \beta_1\mathbf{I} \\ \beta_2\mathbf{L} \end{pmatrix}\delta\mathbf{R} = \begin{pmatrix} \delta\mathbf{d} \\ \mathbf{0} \\ \mathbf{0} \end{pmatrix} \tag{2.5}$$

The weights β_1 and β_2 determine the relative strengths of the prior model and the roughness term. The selection of these weights can be somewhat subjective although there are guidelines in the literature.[39] In general, the inversion results will be sensitive to the choice of these weights. An iterative sparse matrix solver, LSQR, is used for solving this augmented linear system efficiently.[40] Details of LSQR algorithm is discussed in Appendix A. The LSQR algorithm is well suited for highly ill-conditioned systems and has been widely used for large-scale tomographic problems in seismology.[41]

CHAPTER III

INTEGRATION OF TWO-PHASE PRODUCTION DATA*

This chapter presents a streamline-based approach via travel-time or ‘generalized travel-time’ inversion to integrate two-phase production data into high-resolution reservoir model. Since a 3D streamline simulator is used as our forward model, the fundamental of streamline simulation is first discussed. Then, we illustrate the concept of ‘generalized travel-time’. We also show the relationship between our proposed ‘generalized travel time’ inversion and the more traditional ‘amplitude’ inversion. Next, we develop the analytical sensitivity computations for travel-time and generalized travel time that can account for changing field conditions based on streamline time-of-flight formulation.

Finally, the power and computational efficiency of our approach are demonstrated by applications to synthetic and field examples. The synthetic examples include a large-scale 3D example with quarter-million grid cells involving infill drilling and pattern conversions. One of the field examples is from the Goldsmith San Andres Unit (GSAU) in West Texas and includes multiple patterns with 11 injectors and 31 producers. Starting with a reservoir model based on well log and seismic data, we integrate water-cut history for 20 years in less than 2 hours on a PC. Another field example is from a giant middle eastern oil field. The field has been under peripheral water injection with 16 injectors and 70 producers, and aquifer support. A total of 30 years of water-cut history was integrated into the geological model. The production data integration was efficiently carried out on an upscaled model (93,600 cells) in less than 6 CPU hours and on a fine-scale model (921,600 cells) in 34 CPU hours in a PC. The realistic field conditions, such as rate variation, infill drilling and reperforation, were incorporated. Gravity and compressibility effects were also considered. The production data integration resulted in significant improvement in the production history match.

---

* Part of this chapter is reprinted with permission from “Streamline-Based Production Data Integrating With Gravity and Changing Field Conditions” by Zhong He, Seongsik Yoon and Akhil Datta-Gupta, 2002. *SPE Journal*, **4**(4), 423-436, Copyright 2002 by the Society of Petroleum Engineers.

3.1 Introduction

It is well known that geological models derived from static data only such as well log, core and seismic data, often fail to reproduce the production history. Reconciling geologic models to the dynamic response of the reservoir is critical to building reliable reservoir models. The past few years have seen significant developments in the area of such dynamic data integration through the use of inverse modeling.[17-19,42-49] Streamline models have shown great promise in this regard.[17-19,47-49] The key advantages of streamline-based production data integration are its computational efficiency as a "forward" model and analytic computations of sensitivities of the production response with respect to reservoir parameters.[17-19] Sensitivities describe the change in production response because of a small perturbation in reservoir properties such as porosity and permeability and are a vital part of the dynamic data integration process.

Previous works on streamline-based production data integration followed directly from seismic waveform inversion and utilized a two-step procedure:[17-19] (i) a travel time match that involves matching of the 'first arrival' or breakthrough times and (ii) an amplitude match involving matching of the actual production response. The two-step approach has been shown to substantially speed-up the computation and also prevents the solutions from being trapped by secondary peaks in the production response. However, a majority of the production data misfit reduction occurs during the travel time inversion and most of the large-scale features of heterogeneity are resolved at this stage.[17,18]

There are several advantages associated with a travel time inversion of production data.[34,37] First, it is robust and computationally efficient. Unlike conventional 'amplitude' matching which can be highly non-linear, it has been shown that the travel time inversion has quasi-linear properties.[17-19, 34,37] As a result, the minimization proceeds rapidly even if the initial model is not close to the solution. Second, the travel time sensitivities are typically more uniform between wells compared to 'amplitude' sensitivities that tend to be localized near the wells. This prevents over-correction in the near-well regions. Finally, for practical field applications, the production data are often characterized by multiple peaks (for example, tracer response). Under such conditions, the travel time inversion can prevent the solution from converging to secondary peaks in the production response.[17-19,37]

In this chapter, we utilize concepts from wave-equation travel time tomography to propose a 'generalized travel time' inversion method for production data integration into high-resolution reservoir models. Our approach is motivated by the work of Lou and Schuster[34] in the context of seismic waveform inversion and is particularly well-suited for large-scale field applications with gravity and changing field conditions arising from infill drilling, pattern conversions and other operating constraints such as rate changes, well shut-in etc. The approach is very general, robust and computationally efficient and actually reduces the previously proposed two-step inversion (travel time and amplitude) into a single step procedure while retaining most of the desirable features of the travel time inversion. Most importantly, we developed analytical formulations to compute the sensitivities of the travel time and 'generalized travel time' with respect to reservoir properties, which can account for the general field conditions, such as infill drilling and pattern conversion. The analytical computation of sensitivities uses only a single forward streamline simulation, therefore, resulting in extremely efficient inversion of the production data.

3.2 Streamline Simulation Fundamentals

The fundamental laws that govern the dynamics of the reservoir include: Continuity Equation (Conservation of Mass), 2) Darcy Equation: empirical solution of Equation of Motion (Conservation of Momentum), and 3) Equation of State. Conventional reservoir simulators are constructed with a system of differential equations that is based on the above basic equations. Streamline simulators share the same basis. Streamline simulation involves four major steps: (**Fig. 3.1**)

- **Step 1: Numerical pressure solution**
  Given reservoir properties, boundary conditions, and production/injection conditions, pressure field is computed numerically on the physical grids discretizing the reservoir using finite difference method or finite-element methods.
- **Step 2: Streamline tracing and time of flight computation**
  Based on the pressure field, velocity field is generated and streamline is traced. Then particle travel time along streamline is computed.
- **Step 3: Saturation advancing along streamlines**
  From coordinate transformation, 3D spatial coordinate is transformed into 1D time-of-flight coordinate along streamline. Then fluid saturation is advanced along the streamlines by

solving the 1D saturation equation numerically. Finally the saturations along streamlines are mapped onto the underlying grid.

- **Step 4: Pressure and streamline updating**

  To account for rate variations and changing field conditions, pressure distribution is updated. Based the updated pressure field, the streamlines are retraced and saturation is computed along the retraced streamlines.

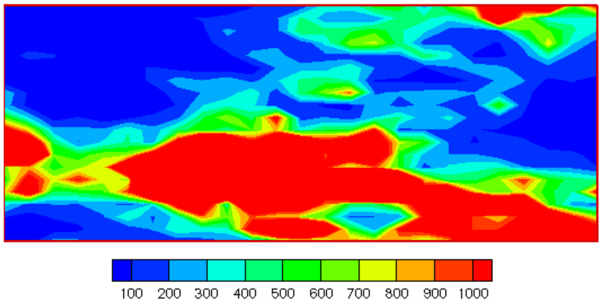

Permeability Field (md)

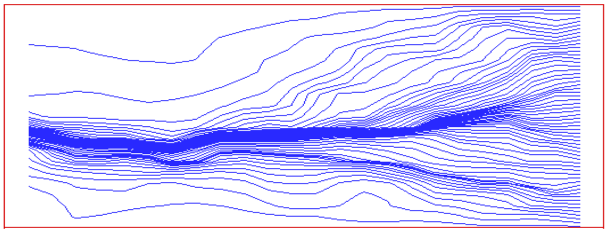

Streamlines

Figure 3.1—A stepwise illustration of streamline simulation, an injector is placed on the left side and a producer is on the opposite side.

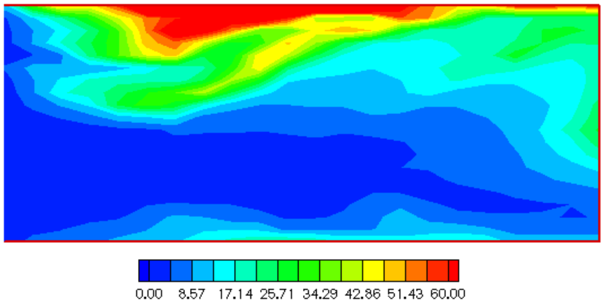

Time of Flight (Days)

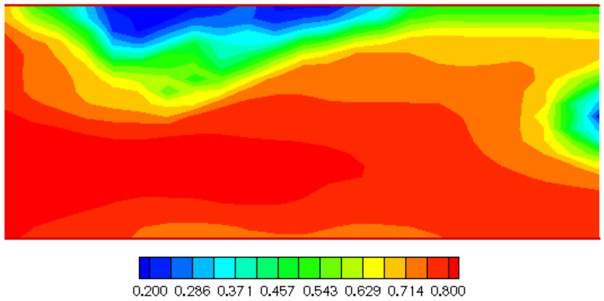

Water Saturation Distribution

Figure 3.1—(Continued).

3.2.1 Pressure Solving

The pressure equation from the continuity equations is given by

$$\phi c_t \frac{\partial P}{\partial t} + \nabla \cdot \mathbf{u}_\mathbf{t} = q \tag{3.1}$$

Compressibility and gravitational effects are considered in the above equation, but capillary force is ignored. Where $\mathbf{u}_t$ is the total Darcy velocity defined by

$$\mathbf{u}_\mathbf{t} = -\mathbf{k}\left(\lambda_t \nabla P + \lambda_g \nabla D\right) \tag{3.2}$$

where $\mathbf{k}$ is permeability tensor, P is pressure, D is the depth, and q is the source/sink term at well locations. λ_t is total relative mobility, λ_g is total gravity mobility, which are defined as

$$\lambda_t = \sum_{j=o,w} \frac{k_{rj}}{\mu_j} \qquad \lambda_g = \sum_{j=o,w} \frac{k_{rj}\rho_j g}{\mu_j} \tag{3.3}$$

where ρ is the density of fluid, and g is the gravitational constant. Pressure field over the entire grids can be obtained by solving the above equation with finite difference scheme. Implementation of gravity on pressure solution is discussed in Appendix B in more details. Upon this pressure field, the velocity field can be derived by applying Darcy's law on every grid basis.

3.2.2 Streamline Tracing and Time of Flight Computation

By definition, streamlines are tangential to velocity field at a moment and can be represented by

$$\frac{dx_1}{u_1} = \frac{dx_2}{u_2} = \frac{dx_3}{u_3} = \frac{d\tau}{\phi} \tag{3.4}$$

where u_i is i^{th} component of the Darcy velocity, ϕ is porosity, and τ is the time of flight, or actual transit time of particle. Assuming linear velocity variation within a grid block,[50] a particle transit time within a grid block, $\Delta\tau$ can be computed by direct integration of the above equation and multiplying porosity.

$$\begin{aligned} \Delta T_{i2} &= \int_{inlet}^{outlet} \frac{dx_i}{u_i} = \frac{1}{a_i} \ln\left[\frac{u_{i2}}{u_{i1}}\right] \\ \Delta\tau_{i2} &= \phi \Delta T_{i2} \end{aligned} \tag{3.5}$$

where a_i is i^{th} component linear velocity gradient across the grid block, u_{i1} is the inlet i^{th} component velocity, and u_{i2} is outlet i^{th} component velocity. Since the particle must exit through one of the faces, the actual transit time of the particle is given by the minimum time. Then the outlet (or exit) location of the streamline within the grid block can be given

$$x_i = \frac{1}{a_i}[u_{i1} \exp(a_i \Delta T) - u_{i0}] \tag{3.6}$$

where u_{i0} is the i^{th} component velocity at grid origin (or center of the grid block), and ΔT is the minimum time in the grid block. Thus streamline locus can be obtained by backtracking the particle movement from the point of interest to an injector. The time of flight τ can be obtained by integrating individual transit time $\Delta\tau$ along a streamline ψ.

3.2.3 Saturation Advancing along Streamlines

For 3D potential (irrotational) flow, curl **u** = 0, we have

$$\mathbf{u} = \nabla\psi \times \nabla\chi \tag{3.7}$$

where ψ and χ are stream functions of three-dimensional flow and the streamlines are defined by the intersection of the stream-surfaces defined by τ, ψ, χ . Now we are to consider saturation movement along the streamlines. This can be achieved by the coordinate transformation of actual grid dimension (x,y,z) to streamline dimension (τ, ψ, χ).

From the elementary calculus, transformation of gradient operator to (τ, ψ, χ) coordinate can be given by

$$\nabla = \nabla\tau\frac{\partial}{\partial\tau} + \nabla\psi\frac{\partial}{\partial\psi} + \nabla\chi\frac{\partial}{\partial\chi} \tag{3.8}$$

where ∇ is evaluated in (x,y,z) coordinate system. Integral form of time of flight definition

$$\tau(x,y,z) = \int_0^{(x,y,z)} \frac{\phi}{\|\mathbf{u}\|}dr \tag{3.9}$$

can be written in differential form

$$\frac{d\tau}{dr} = \frac{\phi}{\|\mathbf{u}\|} \tag{3.10}$$

where r is measured along streamlines. If we expand the LHS using chain rule,

$$\begin{gathered}\frac{\partial\tau}{\partial x}\frac{\partial x}{\partial r} + \frac{\partial\tau}{\partial y}\frac{\partial y}{\partial r} + \frac{\partial\tau}{\partial z}\frac{\partial z}{\partial r} = \frac{\phi}{\|\mathbf{u}\|} \\ \left(\frac{\partial x}{\partial r}\hat{i} + \frac{\partial y}{\partial r}\hat{j} + \frac{\partial z}{\partial r}\hat{k}\right)\cdot\left(\frac{\partial\tau}{\partial x}\hat{i} + \frac{\partial\tau}{\partial y}\hat{j} + \frac{\partial\tau}{\partial z}\hat{k}\right) = \frac{\phi}{\|\mathbf{u}\|}\end{gathered} \tag{3.11}$$

where $\hat{i}$, $\hat{j}$, and $\hat{k}$ are base vectors of (*x,y,z*) coordinate. Since the first vector on the LHS is unit vector in velocity direction, this can be simplified as

$$\mathbf{u} \cdot \nabla \tau = \phi \,. \tag{3.12}$$

Combining Eq. 3.8 and 3.12 and the orthogonality condition between gradient of stream function and velocity, we can simplify the coordinate transformation as

$$\begin{aligned} \mathbf{u} \cdot \nabla &= \mathbf{u} \cdot \nabla \tau \frac{\partial}{\partial \tau} + \mathbf{u} \cdot \nabla \psi \frac{\partial}{\partial \psi} + \mathbf{u} \cdot \nabla \chi \frac{\partial}{\partial \chi} \\ &= \phi \frac{\partial}{\partial \tau} \end{aligned} \tag{3.13}$$

From the material balance, the flow of water phase away from source can be expressed by

$$\phi \frac{\partial S_w}{\partial t} + \mathbf{u} \cdot \nabla f_w + \nabla \cdot \mathbf{G}_w = q_w \tag{3.14}$$

where the water phase velocity resulting from gravity effects is given as

$$\mathbf{G}_w = \mathbf{k} g \nabla D \frac{\lambda_{rw} \lambda_{ro}}{\lambda_{rt}} \left(\rho_o - \rho_w \right) \tag{3.15}$$

Using operator splitting, Eq. 3.14 can be separated into two parts: a convective term and a gravity term:

$$\phi \frac{\partial S_w}{\partial t} + \mathbf{u} \cdot \nabla f_w = q_w \tag{3.16}$$

$$\phi \frac{\partial S_w}{\partial t} + \nabla \cdot \mathbf{G}_w = 0 \tag{3.17}$$

Apply the coordinate transformation to Eq. 3.16, the 3D convective differential equation is reduced to series of one-dimensional ones along the streamlines in the time of flight coordinate.

$$\frac{\partial S_w}{\partial t} + \frac{\partial f_w}{\partial \tau} = 0 \tag{3.18}$$

This 1D equation can be solved analytically or numerically. If the initial water saturation is uniform, Buckley-Leverett type analytical solution can be used. If the initial water saturation is not uniform, it has to be solved numerically.

After the convective term is solved, water saturation is further updated along the gravity lines using Eq. 3.17. Implementation of gravity on saturation solution is discussed in Appendix B in more details.

3.2.4 Pressure and Streamline Updating

In the cases of changing well conditions or more drastically, infill drilling cases, streamline trajectories are significantly changed. Thus, streamlines need to be regenerated by updating pressure in order to account for such new conditions. Even if constant well conditions are assumed, occasional pressure updates might be necessary to take into account changes in the total mobility due to the saturation variation over the flooding period. Saturation can then be advanced along the new streamlines.

3.3 Generalized Travel Time Inversion

Instead of just looking at a single time point for travel time, a 'generalized travel time' or 'travel time shift' is computed by systematically shifting the computed production response towards the observed data until the cross-correlation between the two is maximized. The approach accounts for the whole behavior of production data, but represents the production data misfit at a well in terms of a single 'travel time shift'. As discussed later, it can be shown to reduce to the more traditional least-squared misfit function as we approach near the solution.

As illustrated in **Fig. 3.2,** the calculated water-cut response is systematically shifted in small time increments towards the observed response, and the data misfit is computed for each time increment. Taking well j as an example, the optimal shift will be given by the Δt_j that minimizes the misfit function,

$$J = \sum_{i=1}^{Ndj} \left[y_j^{obs}\left(t_i + \Delta t_j\right) - y_j^{cal}\left(t_i\right) \right]^2 = f(\Delta t_j) \tag{3.19}$$

Or, alternatively maximizes the coefficient of determination given by the following

$$R^2(\Delta t_j) = 1 - \frac{\sum\left[y_j^{obs}(t_i+\Delta t_j) - y_j^{cal}(t_i)\right]^2}{\sum\left[y_j^{obs}(t_i) - \overline{y_j^{obs}}\right]^2} \tag{3.20}$$

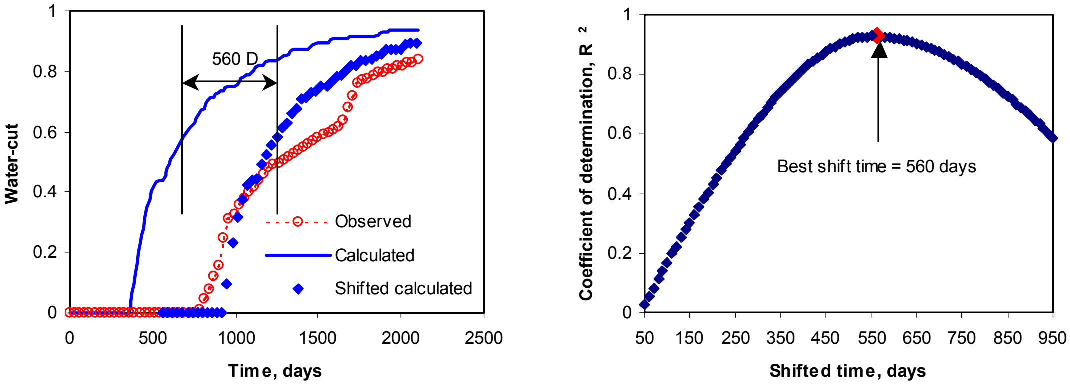

Figure 3.2—Generalized travel time calculation by shifting the calculated response to maximize R^2.

Thus, we define the generalized travel time as the 'optimal' time-shift $\Delta\tilde{t}_j$ that maximizes the $R^2(\Delta t_j)$ as shown in **Fig. 3.2**. It is important to point out that the computation of the optimal shift does not require any additional flow simulations. It is carried out as a post-processing at each well after the calculated production response is derived using a flow simulation. The overall production data misfit can now be expressed in terms of a generalized travel time misfit at all wells as follows

$$J = \sum_{j=1}^{Nw} (\Delta\tilde{t}_j)^2 \tag{3.21}$$

It is worth-mentioning here an important practical aspect of the data integration procedure. Our experience indicates that the minimization in Eq.3.21 is more robust and less sensitive to the choice of the weighting terms if the sensitivities are made to be dimensionless. A simple procedure would be to minimize the logarithm of the generalized travel time misfit to derive logarithmic changes to the estimated parameters.[23] The relevant sensitivities in this case would be

$$\frac{\partial(\log(|\Delta\tilde{t}|))}{\partial(\log(m))} = \frac{\partial\Delta\tilde{t}/\Delta\tilde{t}}{\partial m/m} = \frac{m}{\Delta\tilde{t}}\frac{\partial\Delta\tilde{t}}{\partial m} \tag{3.22}$$

3.3.1 Generalized Travel Time Inversion vs. Amplitude Inversion

It can be shown that the generalized travel time inversion actually reduces to a form of the traditional least-squared amplitude inversion as we approach the solution to the inverse problem. Thus, we are able to get a satisfactory match to the overall production history just by minimizing the travel time shift. In the vicinity of the solution, we can make the following approximation

$$\left.\frac{\partial y_j^{obs}(t_i+\Delta\tilde{t}_j)}{\partial T}\right|_{T=t_i+\Delta\tilde{t}_j} \approx \frac{y_j^{obs}(t_i+\Delta\tilde{t}_j)-y_j^{obs}(t_i)}{\Delta\tilde{t}_j} \approx \frac{y_j^{cal}(t_i)-y_j^{obs}(t_i)}{\Delta\tilde{t}_j} \tag{3.23}$$

We can rearrange Eq. 3.23 to obtain the following

$$\Delta\tilde{t}_j \approx \frac{y_j^{cal}(t_i)-y_j^{obs}(t_i)}{\overset{\bullet}{y}_j^{obs}} \tag{3.24}$$

where we have used the notation

$$\overset{\bullet}{y}_j^{obs} = \left.\frac{\partial y_j^{obs}(t_i+\Delta\tilde{t}_j)}{\partial T}\right|_{T=t_i+\Delta\tilde{t}_j} \tag{3.25}$$

Now, the generalized travel time misfit can be obtained by summing Eq.3.24 over all the data points and for all the wells,

$$\sum_j (\Delta\tilde{t}_j)^2 = \sum_j\sum_i \frac{\left[y_j^{cal}(t_i)-y_j^{obs}(t_i)\right]^2}{\left(N_{dj}\,\dot{y}_j^{obs}\right)^2} \tag{3.26}$$

In the above expression, N_{dj} refers to the number of data points for well j with nonzero derivatives of the observed response with respect to time. Clearly, Eq. 3.26 is a weighted form of amplitude misfit.

3.3.2 An Illustrative Example

Here we illustrate the 'generalized travel-time' inversion using an example that involves integration of water-cut data in the presence of infill drilling. The reference permeability field for this case is shown in **Fig. 3.3a**. It has a mesh size of 21x21 and the major features are a low permeability region towards the north and an east-west high permeability trend. The example involves conversion from an inverted 5-spot pattern to an inverted 9-spot pattern (**Fig. 3.3b**). Four infill wells are brought into production at 300 days and a total of 600 days of water-cut data is integrated. The water-cut history at the producing wells for the reference model is shown by the solid curves in **Fig. 3.4**. A total of six pressure updates were used to account for mobility effects and changing field conditions. Our prior model for this case was a uniform permeability field that is conditioned at the wells. **Fig. 3.4** also compares the water-cut responses from the initial and the reference model for the eight producers.

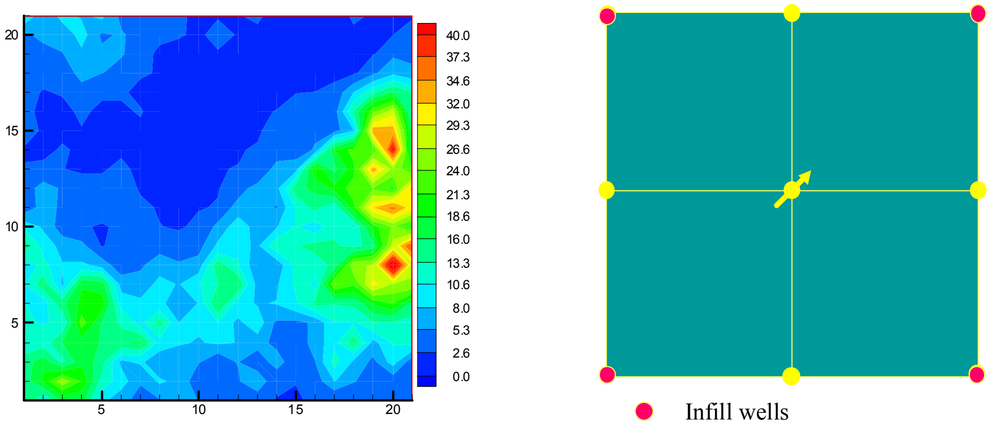

3a. The reference permeability field

3b. Well pattern with infill drilling

Figure 3.3—The reference permeability field and well patterns for the synthetic 2-D example.

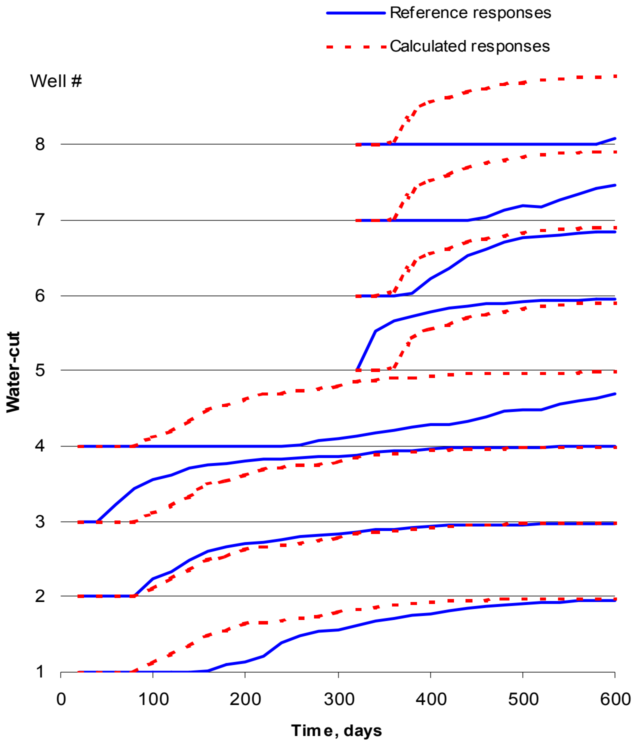

Figure 3.4—Initial match from an uniform permeability field.

A generalized travel time inversion was performed to match the production response from the reference field. As mentioned before, we first determine the 'travel time shift' at each producing well and iteratively minimize the shift. **Fig. 3.5** shows the water-cut match after the 'generalized travel time' inversion. The matches are clearly satisfactory both in terms of reproducing the breakthrough time and the 'amplitude' of the production response. **Fig. 3.6** shows the permeability field derived from the inversion. On comparison with the reference permeability field **(Fig. 3.3a)**, we can see that we are able to capture most of its large-scale features. This is consistent with the low resolution of the production data which can be used to infer large-scale trends rather than small-scale variations. **Fig. 3.7** shows plots of data misfit versus number of iterations during the inversion. The correspondence between the reduction in the generalized travel time misfit and the overall production data misfit is quite apparent here.

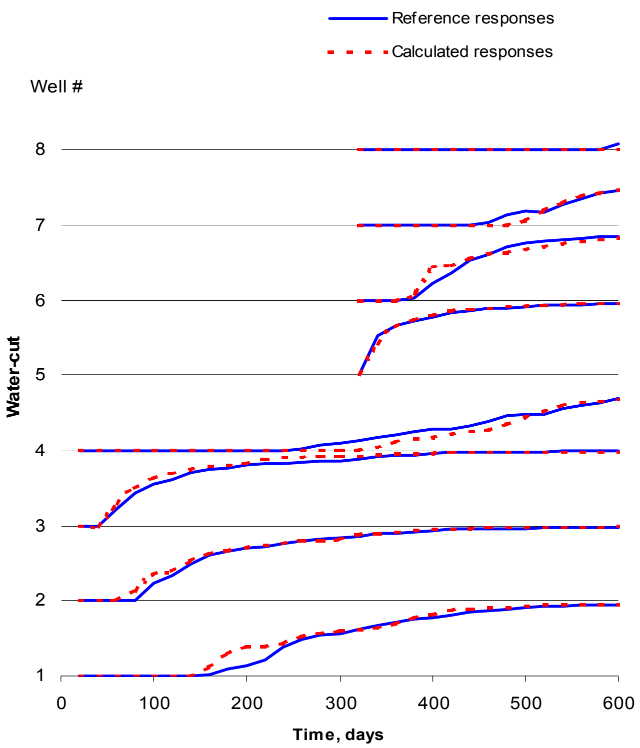

Figure 3.5—Final match after ‘generalized travel time’ inversion.

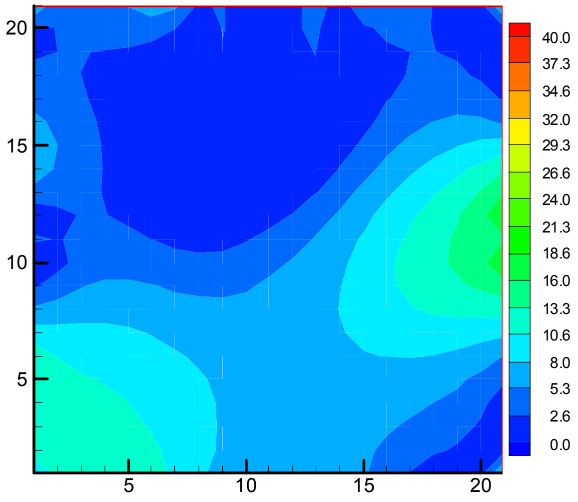

Figure 3.6—Permeability field derived by generalized travel time inversion.

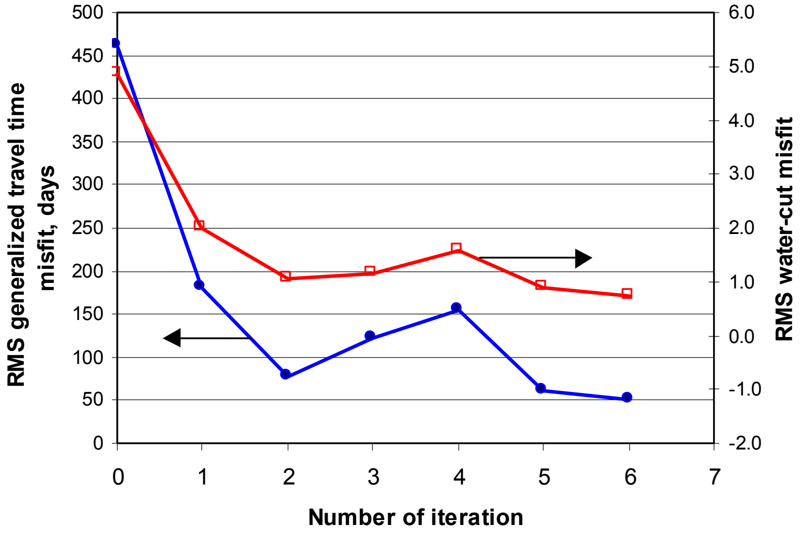

Figure 3.7—Generalized travel time and amplitude misfit vs. iterations.

3.4 Streamline-based Analytical Computation of Sensitivities

This section derives the analytical formulations for sensitivity calculations using streamline approach. The formulations can account for gravity and changing field conditions arising from rate changes or infill drilling.

3.4.1 Sensitivity of the Generalized Travel Time

Consider a small perturbation in reservoir properties, $\delta\mathbf{m}$ such that it results in a time-shift δt_j for the entire computed production response at well j, that is, every data point of well j has a common time-shift. We then have the following relationship for the observed times $((t_{1,j},.........,t_{N_{dj},j})$

$$\begin{aligned}
\delta t_j &= \delta t_{1,j} = \left[\frac{\partial t_{1,j}}{\partial \mathbf{m}}\right]^T \delta\mathbf{m} \\
&\cdots\cdots \\
\delta t_j &= \delta t_{N_{dj},j} = \left[\frac{\partial t_{N_{dj},j}}{\partial \mathbf{m}}\right]^T \delta\mathbf{m}
\end{aligned} \tag{3.27}$$

where **m** represents the reservoir parameter vector. Summing Eq. 3.27 over all the data points, we can arrive at the following simple expression for the sensitivity of the travel time shift with respect to the reservoir parameter, m, which represents a component of the vector **m.**

$$\frac{\partial t_j}{\partial m} = \frac{\sum_{i=1}^{N_{dj}} \left(\partial t_{i,j} / \partial m \right)}{N_{dj}} \tag{3.28}$$

Also, based on the definition of the generalized travel time, we have the following

$$\frac{\partial \Delta \tilde{t}_j}{\partial m} = -\frac{\partial t_j}{\partial m} \tag{3.29}$$

The negative sign in Eq. 3.29 reflects the sign convention adopted for defining the generalized travel time shift which is considered positive if the computed response is to the left of the observed data as shown in **Fig. 3.2**. For example, the travel time will decrease if permeability increases; however, the 'travel time shift' will increase.

Combining Eqs. 3.27-3.29, we obtain a rather simple expression for the sensitivity of the generalized travel time with respect to reservoir parameters as follows

$$\frac{\partial \Delta \tilde{t}_j}{\partial m} = -\frac{\sum_{i=1}^{N_{dj}} \left(\partial t_{i,j} / \partial m \right)}{N_{dj}} \tag{3.30}$$

It now remains to calculate the sensitivity of the arrival times at the producing well, $\partial t_{i,j} / \partial m$. These sensitivities can be easily obtained in terms of the sensitivities of the streamline time of flight as discussed below.

3.4.2 Sensitivity of the Travel Time

Consider two-phase incompressible flow of oil and water in a non-deformable permeable medium. The transport equation can be written in the streamline time of flight coordinates as follows

$$\frac{\partial S_w}{\partial t} + \frac{\partial F_w}{\partial \tau} = 0 \tag{3.31}$$

Rearranging Eq. 3.31,

$$\frac{\partial S_w}{\partial t} = -\frac{\partial F_w}{\partial S_w}\frac{\partial S_w}{\partial \tau} \tag{3.32}$$

In the above expression, τ represents the streamline time of flight which is the travel time of a neutral tracer along a streamline[18],

$$\tau = \int_{\Sigma} s(\mathbf{x})\,dx \tag{3.33}$$

where the integral is along the streamline trajectory, Σ and $s(\mathbf{x})$ is the 'slowness' defined as the reciprocal of the total interstitial velocity [9,10]

$$s(\mathbf{x}) = \frac{1}{|v(\mathbf{x})|} = \frac{\mu\phi(\mathbf{x})}{k(\mathbf{x})|\nabla P|} \tag{3.34}$$

If we assume that the streamlines do not shift because of small perturbations in reservoir properties, then the changes in the water saturation at the outlet node of a streamline is given by

$$\delta S_w = \frac{\partial S_w}{\partial t}\delta t + \frac{\partial S_w}{\partial \tau}\left[\frac{\partial \tau}{\partial \mathbf{m}}\right]^T \delta\mathbf{m} \tag{3.35}$$

The propagation of a fixed saturation can be expressed by simply setting $\delta S_w = 0$ as follows

$$0 = \frac{\partial S_w}{\partial t}\delta t + \frac{\partial S_w}{\partial \tau}\left[\frac{\partial \tau}{\partial \mathbf{m}}\right]^T \delta\mathbf{m} \tag{3.36}$$

We can now combine Eq. 3.36 with Eq. 3.32 in order to obtain the following expression for travel time sensitivity in terms of the streamline time of flight,

$$\frac{\partial t}{\partial m} = \frac{\dfrac{\partial \tau}{\partial m}}{\dfrac{\partial F_W}{\partial S_W}} \tag{3.37}$$

In the above expression, the fractional flow derivatives are computed at the saturation of the outlet node of the streamline. The time of flight sensitivities can be obtained analytically in terms of simple integrals along streamline. For example, the time of flight sensitivity with respect to permeability will be given by[9,10]

$$\frac{\partial \tau}{\partial k(\mathbf{x})} = \int_{\Sigma} \frac{\partial s(\mathbf{x})}{\partial k(\mathbf{x})} dx = -\int_{\Sigma} \frac{s(\mathbf{x})}{k(\mathbf{x})} dx \tag{3.38}$$

where the integrals are evaluated along the streamline trajectory. Note that the sensitivity computations require a single streamline simulation regardless of the number of parameters or the number of data points.

3.4.3 Accounting for Pressure Updates and Gravity

The travel time sensitivities derived so far do not explicitly account for the saturation distribution along streamlines. For changing field conditions requiring pressure updates and mapping of saturation between streamlines, permeability changes will have an impact on the saturation distribution. Also, including gravity via operator splitting will change saturation distribution along streamlines.[17] Such saturation variations can be rigorously accounted for by using numerical approaches to sensitivity computation such as the sensitivity equation method described in the Appendix.[19] However, major drawbacks of the sensitivity equation method are the computational cost arising from the time-stepping requirements and also the huge storage cost (proportional to the square of the number of grid blocks) required for mapping sensitivities between pressure updates. This makes the method infeasible for large-scale field applications.

The analytic sensitivity computations discussed before can be extended to account for pressure updates, gravity and changing field conditions. The change in water saturation at the outlet node of a streamline will now be a function of time, reservoir parameters and also the initial saturation distribution along the streamline at the beginning of the pressure update,

$$\delta S_w^{n+1} = \frac{\partial S_w^{n+1}}{\partial t} \delta t + \frac{\partial S_w^{n+1}}{\partial \tau} \left[\frac{\partial \tau}{\partial \mathbf{m}} \right]^T \delta \mathbf{m} + \left[\frac{\partial S_w^{n+1}}{\partial \mathbf{S}_w^n} \right]^T \delta \mathbf{S}_w^n \tag{3.39}$$

Here, n represents the previous pressure updating and n+1 represents the current pressure updating, so $\mathbf{S}_w^n$ is representing the initial water distribution for the current pressure updating.

We assume that the changes in water saturation at the outlet node will primarily be a function of its own initial saturation and re-write Eq. 3.39 as follows,

$$\delta S_w^{n+1} = \frac{\partial S_w^{n+1}}{\partial t} \delta t + \frac{\partial S_w^{n+1}}{\partial \tau} \left[\frac{\partial \tau}{\partial \mathbf{m}} \right]^T \delta \mathbf{m} + \frac{\partial S_w^{n+1}}{\partial S_w^n} \delta S_w^n \tag{3.40}$$

The above approximation has, indeed, minimal impact on the sensitivity calculations. We will demonstrate this by comparing the analytic sensitivity calculations with the results from the sensitivity equation method and also from the direct perturbation method. Because the initial water saturation is a function of the reservoir parameters, we further have,

$$\delta S_w^{n+1} = \frac{\partial S_w^{n+1}}{\partial t}\delta t + \frac{\partial S_w^{n+1}}{\partial \tau}\left[\frac{\partial \tau}{\partial \mathbf{m}}\right]^T \delta\mathbf{m} + \frac{\partial S_w^{n+1}}{\partial S_w^n}\left[\frac{\partial S_w^n}{\partial \mathbf{m}}\right]^T \delta\mathbf{m} \tag{3.41}$$

Again we consider the propagation of a constant saturation by setting $\delta S_w = 0$,

$$0 = \frac{\partial S_w^{n+1}}{\partial t}\delta t + \frac{\partial S_w^{n+1}}{\partial \tau}\left[\frac{\partial \tau}{\partial \mathbf{m}}\right]^T \delta\mathbf{m} + \frac{\partial S_w^{n+1}}{\partial S_w^n}\left[\frac{\partial S_w^n}{\partial \mathbf{m}}\right]^T \delta\mathbf{m} \tag{3.42}$$

Differentiating Eq. 3.42 with respect to m, any component in the parameter vector **m**, we obtain the following expression for travel time sensitivity in the presence of pressure updates

$$\frac{\partial t}{\partial m} = -\frac{\dfrac{\partial S_w^{n+1}}{\partial \tau}\dfrac{\partial \tau}{\partial m} + \dfrac{\partial S_w^{n+1}}{\partial S_w^n}\dfrac{\partial S_w^n}{\partial m}}{\dfrac{\partial S_w^{n+1}}{\partial t}} \tag{3.42}$$

or, using Eq. 3.32

$$\frac{\partial t}{\partial m} = \frac{\dfrac{\partial \tau}{\partial m}}{\dfrac{\partial F_w}{\partial S_w}} + \frac{\partial t^n}{\partial m} \tag{3.43}$$

In the above equation, $\partial t^n / \partial m$ is the travel time sensitivity at the beginning of the pressure update. For multiple pressure updates, $\partial t^n / \partial m$ will correspond to that of the last update. Note that all the quantities in Eq. 3.43 can be obtained analytically from a single forward simulation. Thus the sensitivity computations are extremely efficient and do not require any additional simulations regardless of the number of data points or the number of parameters.

3.4.4 Comparison of Sensitivity Computations

Based on travel time sensitivity, water-cut sensitivity can be calculated as

$$\frac{\partial F_w}{\partial m} = \frac{\partial F_w}{\partial t} \frac{\partial t}{\partial m} \tag{3.44}$$

Where $\partial F_w / \partial t$ can be evaluated numerically during the streamline simulation. **Fig. 3.8** compares water-cut sensitivities to permeability obtained using the streamline-based analytic method, direct perturbation method and the sensitivity equation method. This is a quarter five-spot example with an infill well introduced at the upper left corner. This can be seen from the streamline patterns in **Figs. 3.8a** and **3.8b**. The water-cut sensitivities in **Figs. 3.8c** through **3.8e** correspond to the original producer at 80 days after the infill drilling. All three sensitivities have the same general shape. However, the sensitivity calculation using the direct perturbation method is highly sensitive to the magnitude of the perturbation and this leads to the apparent instability in **Fig. 3.8c**. The results from the sensitivity equation appear to be smeared (**Fig. 3.8e**) and this is clearly because of mapping of sensitivities from the streamlines to grid blocks at the time of infill drilling and pressure updating.

The sensitivity equation method is discussed in detail in the Appendix C. Briefly, in this method the sensitivity equations are obtained by taking partial derivatives of the governing equation with respect to the reservoir parameters. The sensitivities are then constructed numerically by solving these equations. Although this approach is able to rigorously account for changing field conditions, its applicability is highly limited, particularly for large-scale field applications. The method requires numerical evaluation of sensitivities along all streamlines at every time step, making it very computationally demanding. It also requires very large storage for mapping sensitivities from streamlines to grid blocks and vice versa.

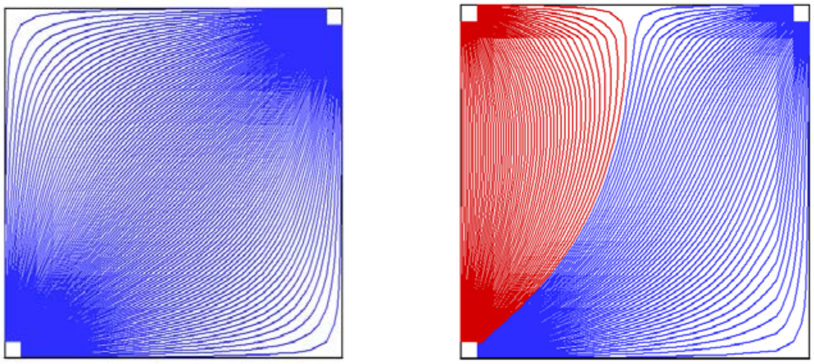

a. Stremlines before infill

b. Streamlines after infill

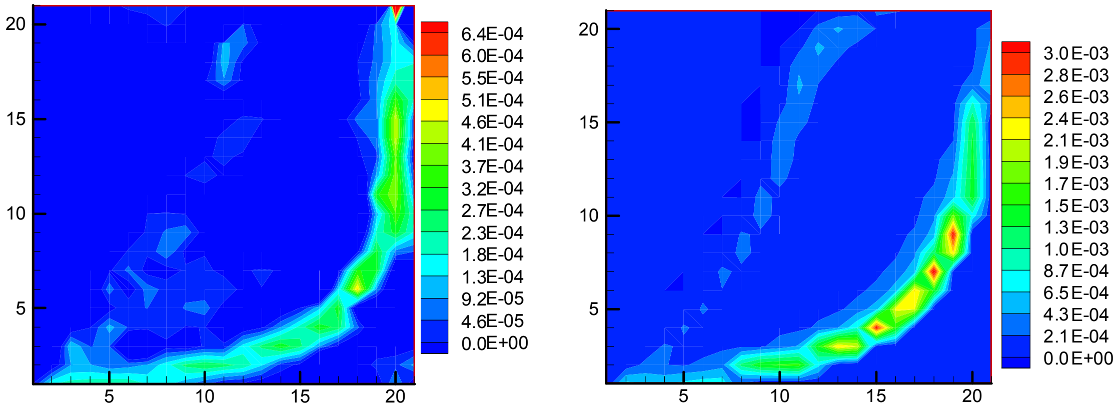

c. Perturbation Method

d. Proposed Analytic Method

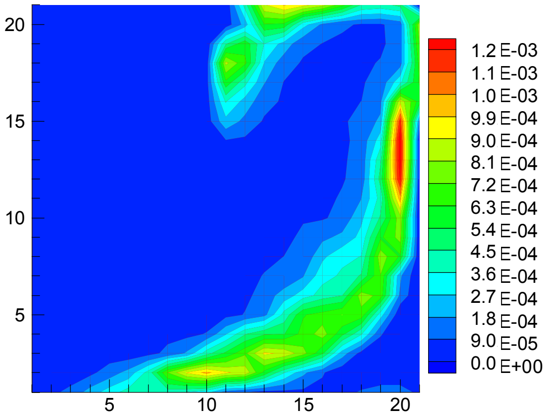

e. Sensitivity equation method

Figure 3.8—Comparison of water-cut sensitivity computations for an infill case.

3.5 Applications

3.5.1 A Synthetic Large-Scale 3D Waterflooding

This example consists of a mesh size of 150x75x25 with a total of 281,250 grid cells. Six infill wells join production at 1200 days and a total of 3000 days of water-cut data from 7 initial and 6 infill producers is integrated (**Fig. 3.9a**). The reference permeability field is shown in **Fig. 3.9b**. We generated the initial permeability model in **Fig. 3.9c** using a Sequential Gaussian Simulation with the well data as conditioning points.[51] **Fig. 3.10** shows the water-cut responses from the initial and the reference model. There are large discrepancies between the reference and calculated water-cut responses, particularly for the infill wells. **Fig. 3.11** shows the results of water-cut matching after our 'generalized travel time' inversion. The matches show significant improvement for all the wells, especially the infill wells.

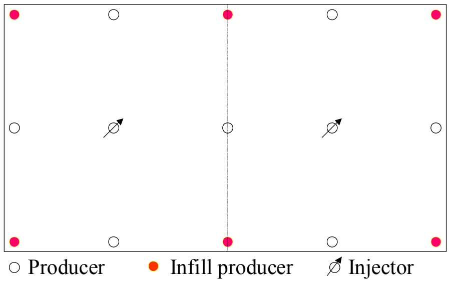

a. Well pattern

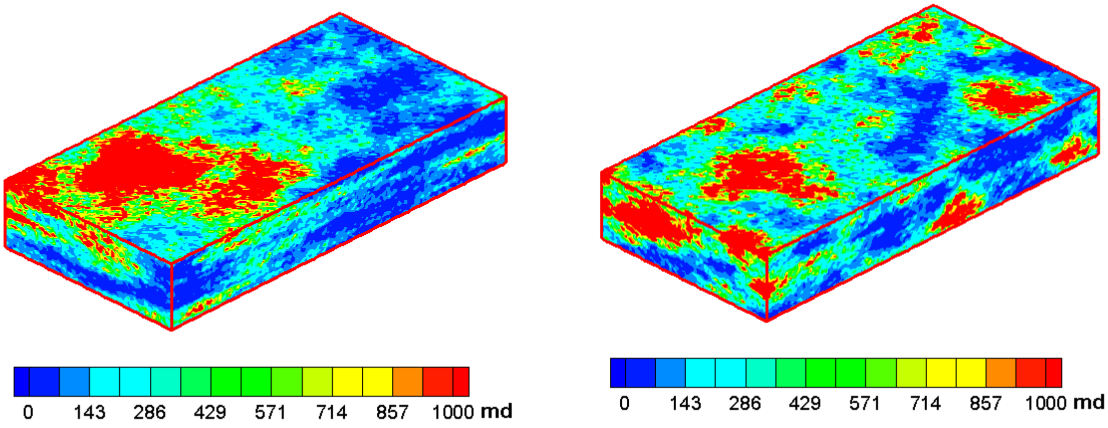

b. Reference permeability field

c. Initial permeability field

Figure 3.9—Well pattern, reference and initial permeability fields for the synthetic 3D example.

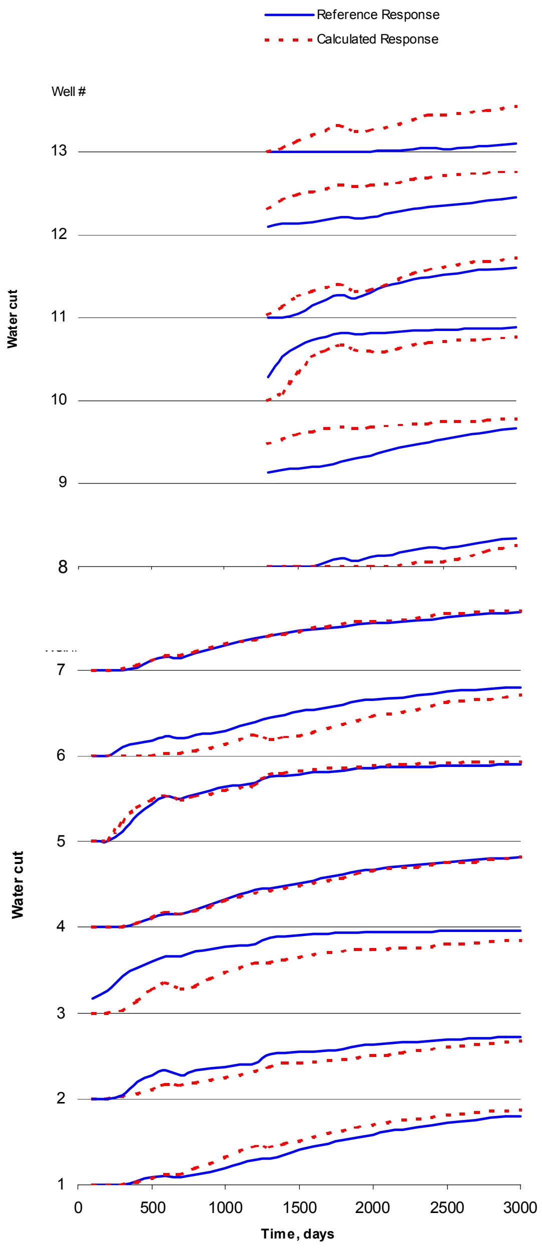

Figure 3.10—Water-cut match from the initial permeability model.

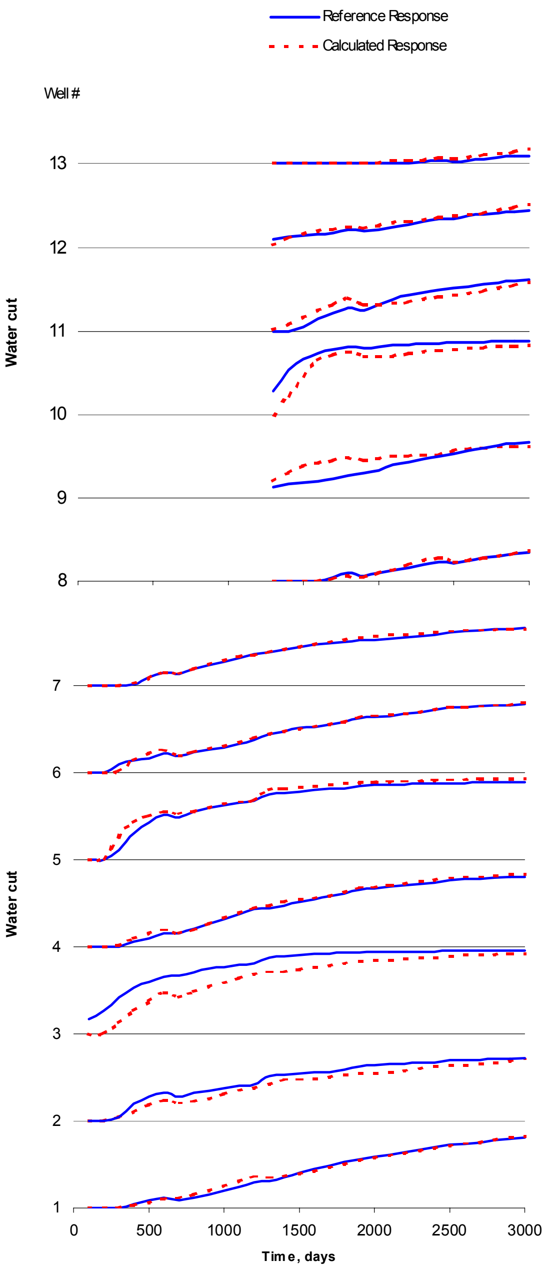

Figure 3.11—Water-cut match after the ‘generalized travel time’ inversion.

The final permeability field and the changes from the initial permeability model are shown in **Fig. 3.12**. These changes can be visualized in more details by the layered views in **Fig. 3.13**. **Fig. 3.14** plots the 'generalized travel time' misfit and also the conventional least-squared amplitude misfit as a function of number of iterations. Clearly, the reduction in amplitude misfit is fairly consistent with the reduction in the generalized travel time misfit. The computation time for this example with more than a quarter-million grid cells and six pressure updates was about 12 hours in a PC.

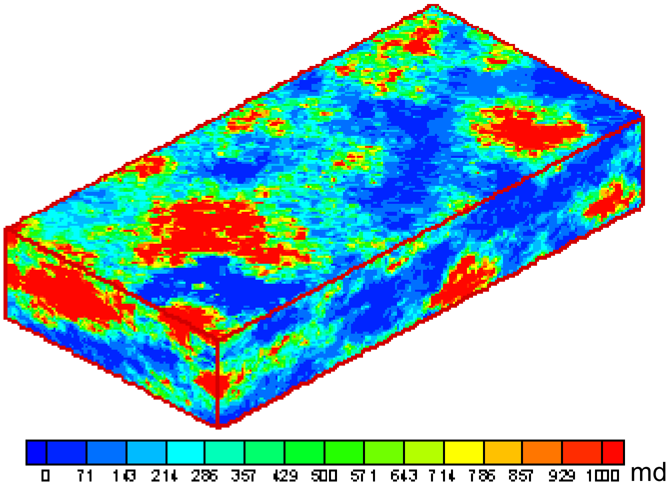

a. Final permeability field

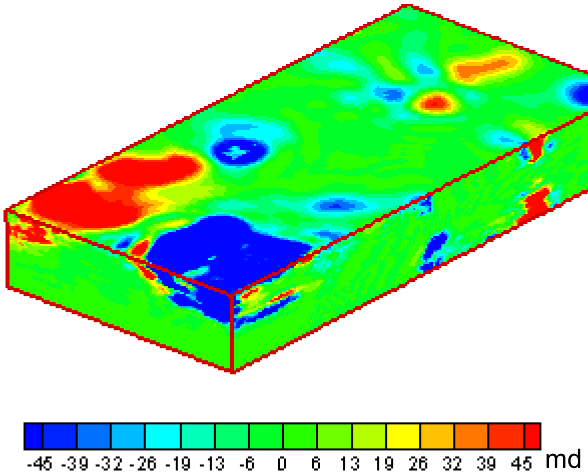

b. Permeability changes from the initial model

Figure 3.12—The final permeability field and permeability changes from the initial permeability model.

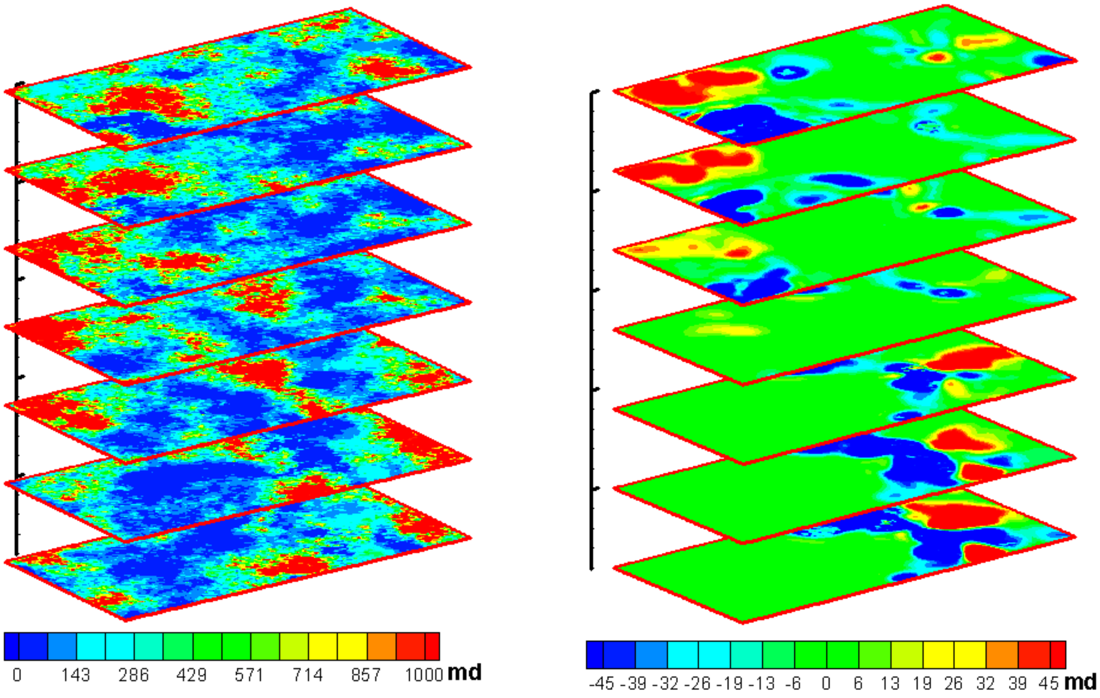

a. Final permeability field

b. Permeability changes from initial model

Figure 3.13—Layered views of the final permeability field and permeability changes.

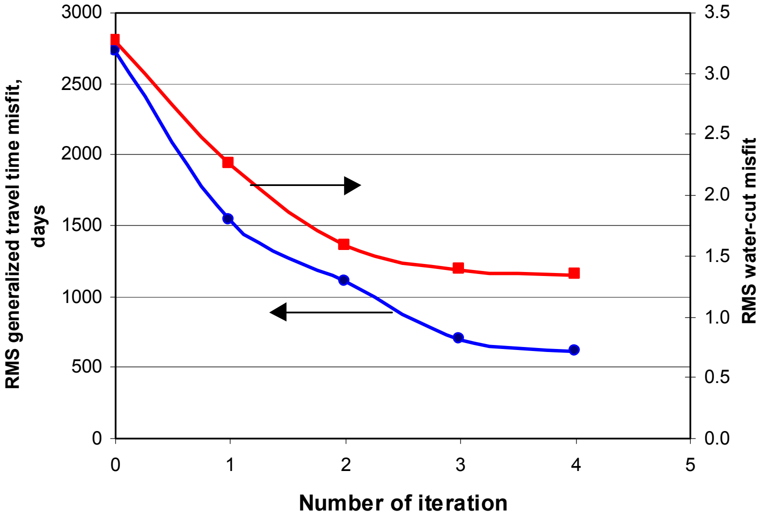

Figure 3.14—Misfit reduction for the synthetic 3D example.

3.5.2 Field Example 1 - Goldsmith San Andres Unit

We have applied our approach to a CO_2 pilot project area in the Goldsmith San Andres Unit (GSAU), a dolomite formation located in west Texas. The pilot area consists of nine inverted 5-spot patterns covering around 320 acres with average thickness of 100ft and has over 50 years of production history prior to CO_2 project initiation in Dec. 1996. **Fig. 3.15** shows the CO_2 pilot project site in the GSAU. We performed a history matching for 20 years of waterflood prior to the initiation of CO_2 injection. Gravity effects were not considered in this example.

Because of the practical difficulties in obtaining correct boundary conditions for the pilot area, extra wells located outside the pilot area were included in this study. The extended study area is shown in **Fig. 3.16** with 11 water injectors and 31 producers. Among the producers within the study area, 9 wells showed significant water-cut response before the initiation of the CO_2 injection and are used for data integration. These 9 producers are specified with well name in **Fig. 3.17**. **Fig. 3.17** summarizes the well schedule indicating infill drilling, well conversions and also well shut-in. To account for the changing production rates and different starting times of the injection and production wells, 11 pressure updates were used in the simulation. The actual well rates and the averaged production rates for these 11 time periods are shown in **Fig. 3.18**.

The study area is discretized into 58x53x10 mesh or a total of 30,740 grid cells. The porosity field, shown in **Fig. 19a**, is obtained by a Sequential Gaussian Simulation using the well log data and is not altered during the inversion. The initial permeability field is generated via a cloud transform based on the porosity-permeability relationship (**Fig. 3.19b**). Water cut histories for the 9 producers for the period May 1968 to Dec. 1989 are shown in **Fig. 3.20** as solid lines. Note that most of these wells are located in the northeast region of the pilot area. Thus, production data is expected to primarily resolve permeability variations in this region.

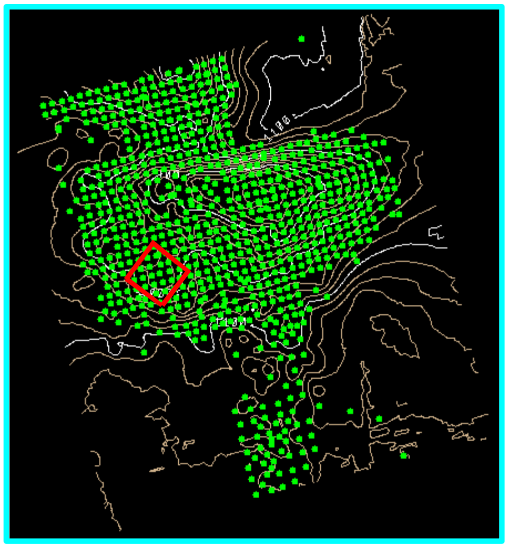

Figure 3.15—Goldsmith field CO_2 project area.

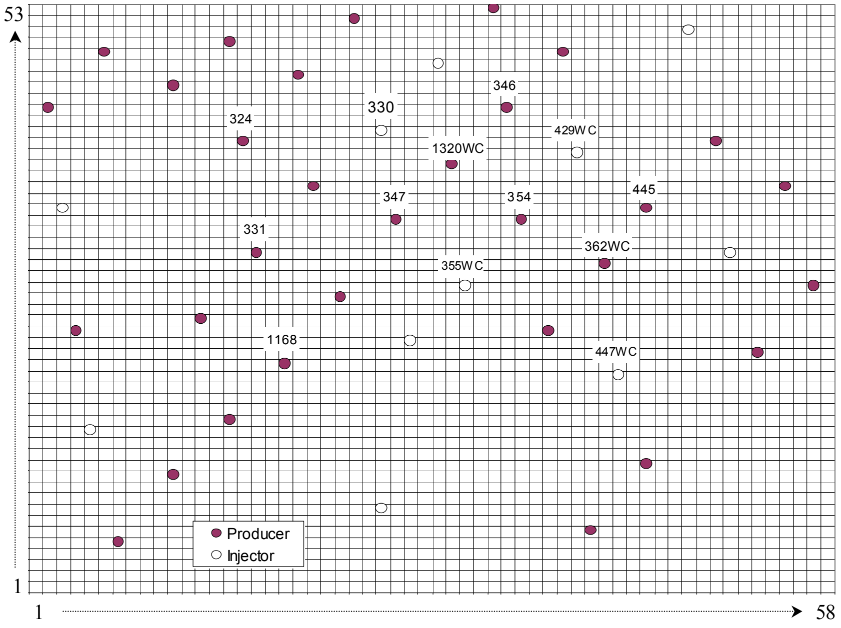

Figure 3.16—Well configurations of the study area.

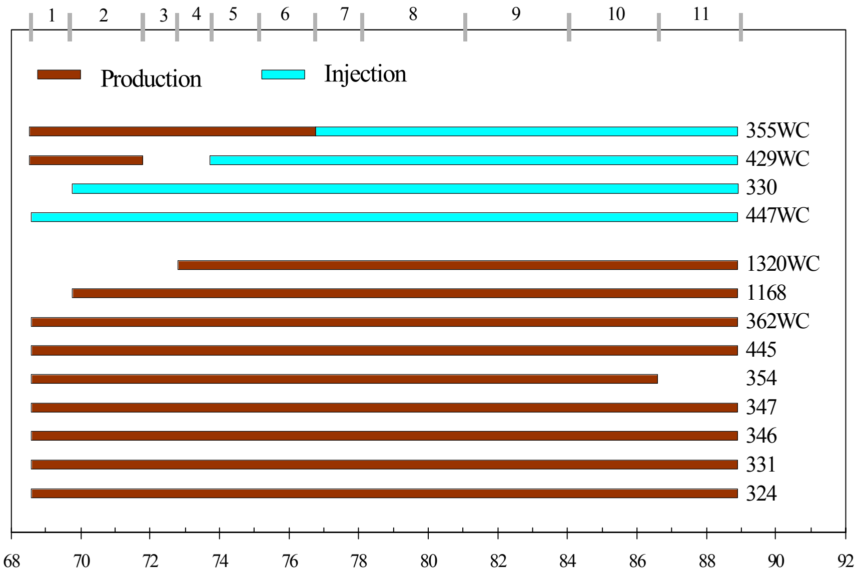

Figure 3.17—Well schedule: infill wells, well shut-in and conversions.

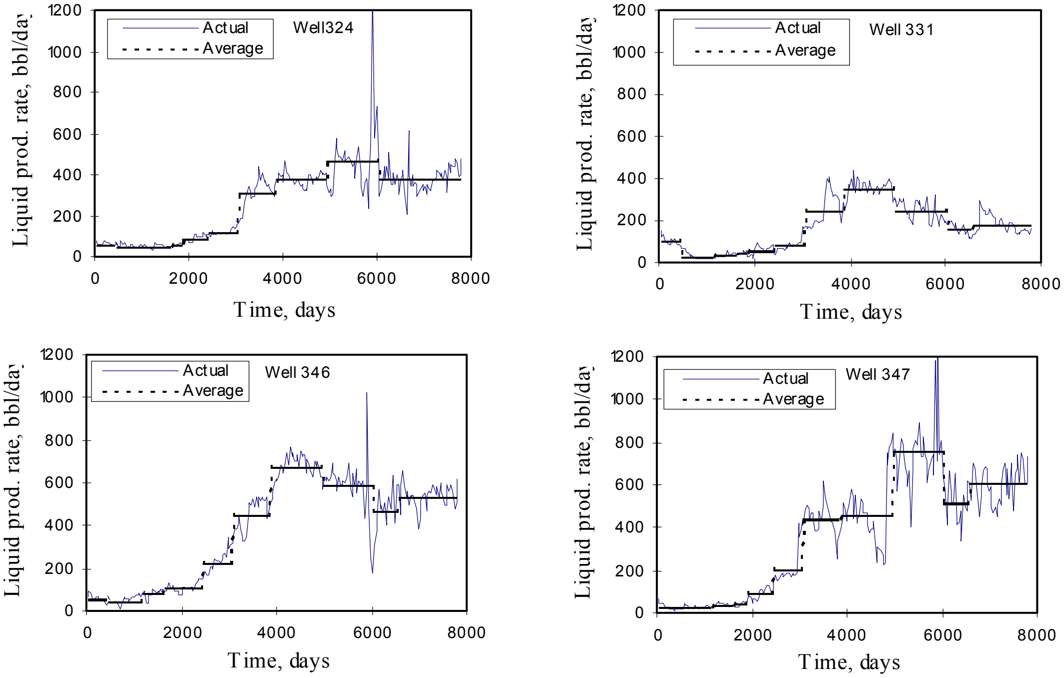

Figure 3.18—Actual well production rates vs. the averaged rates used for streamline simulation.

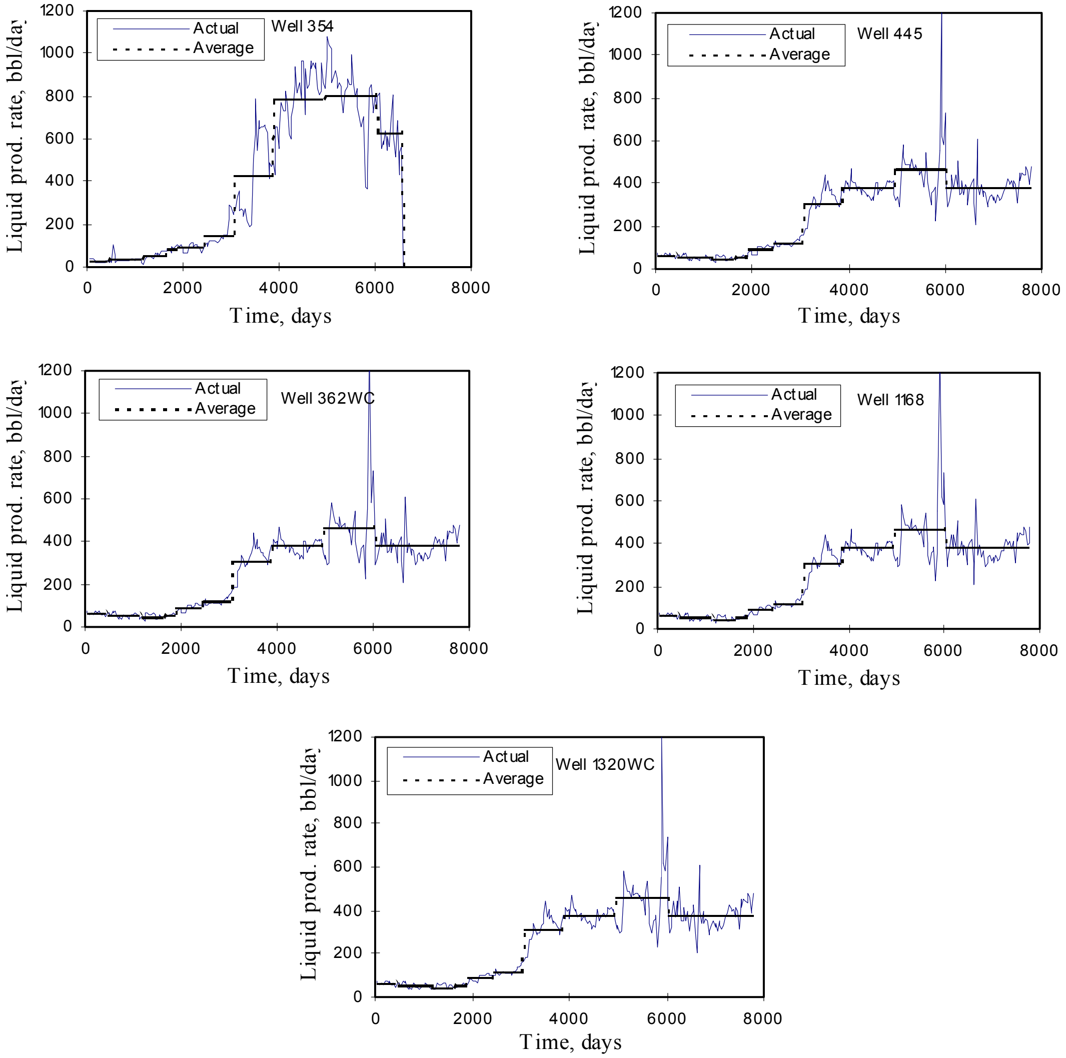

Figure 3.18— (continued).

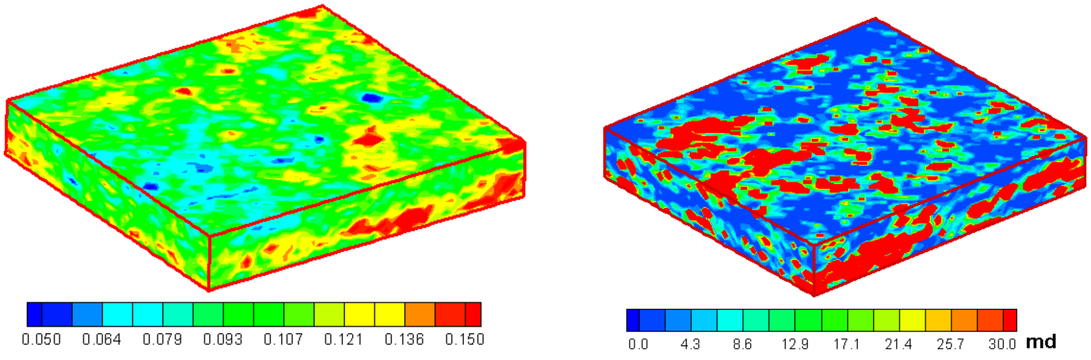

a. Porosity distribution

b. Permeability model from cloud transform

Figure 3.19—Porosity distribution and the initial permeability model for the Goldsmith case.

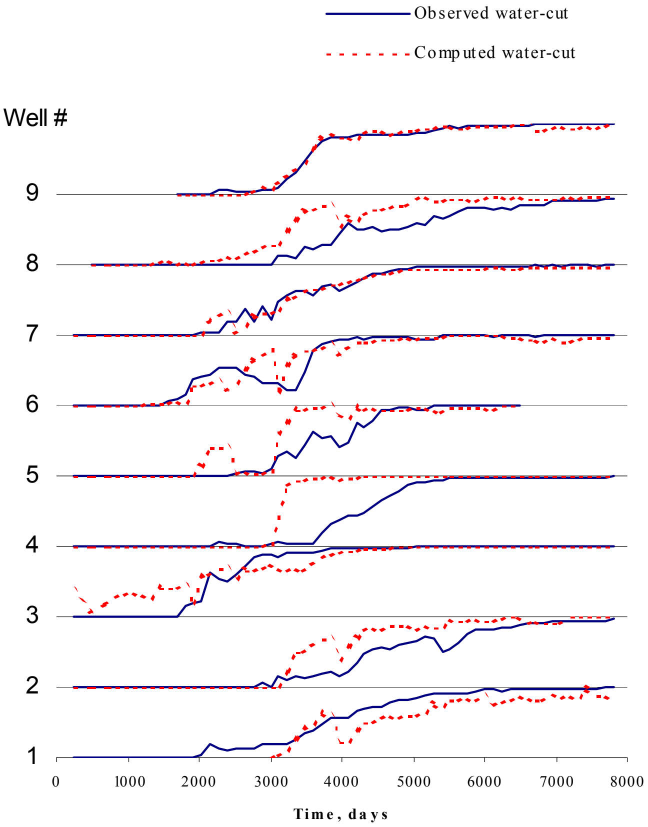

Figure 3.20—History match from initial permeability model.

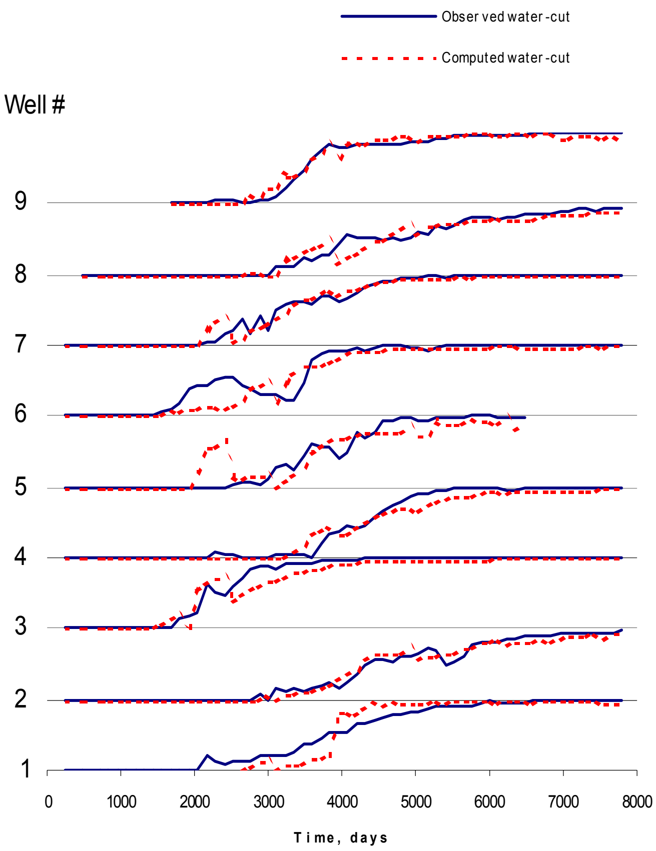

Figure 3.21—History match after the generalized travel time inversion.

In **Fig. 3.20**, we have superimposed the water-cut responses from the initial model and the actual production history. The water-cut matches after the generalized travel time inversion is shown in **Fig. 3.21**. We want to emphasize here that for large-scale problems the convergence is more robust and rapid when the minimization is carried out in the logarithmic space as indicated earlier. Overall, we see a significant improvement in the production history match. In particular, wells 2,3,4,5 and 8 show a much better match after the inversion (**Fig. 3.21**). The final permeability field and the changes from the initial model are shown in **Fig. 3.22**. Notice that because of the 'norm' constraint, the changes to the initial permeability model are kept to a minimum while matching the production history. This allows us to preserve the geologic realism during history matching. For comparison purposes, **Fig. 3.23** shows the histograms of permeability before and after the inversion and no significant differences can be seen. **Fig. 3.24** shows the misfit versus the number of iterations during the inversion. For this field example with 31 producers, 11 injectors and 11 pressure updates, the computation time requirement was less than 2 hours in a PC.

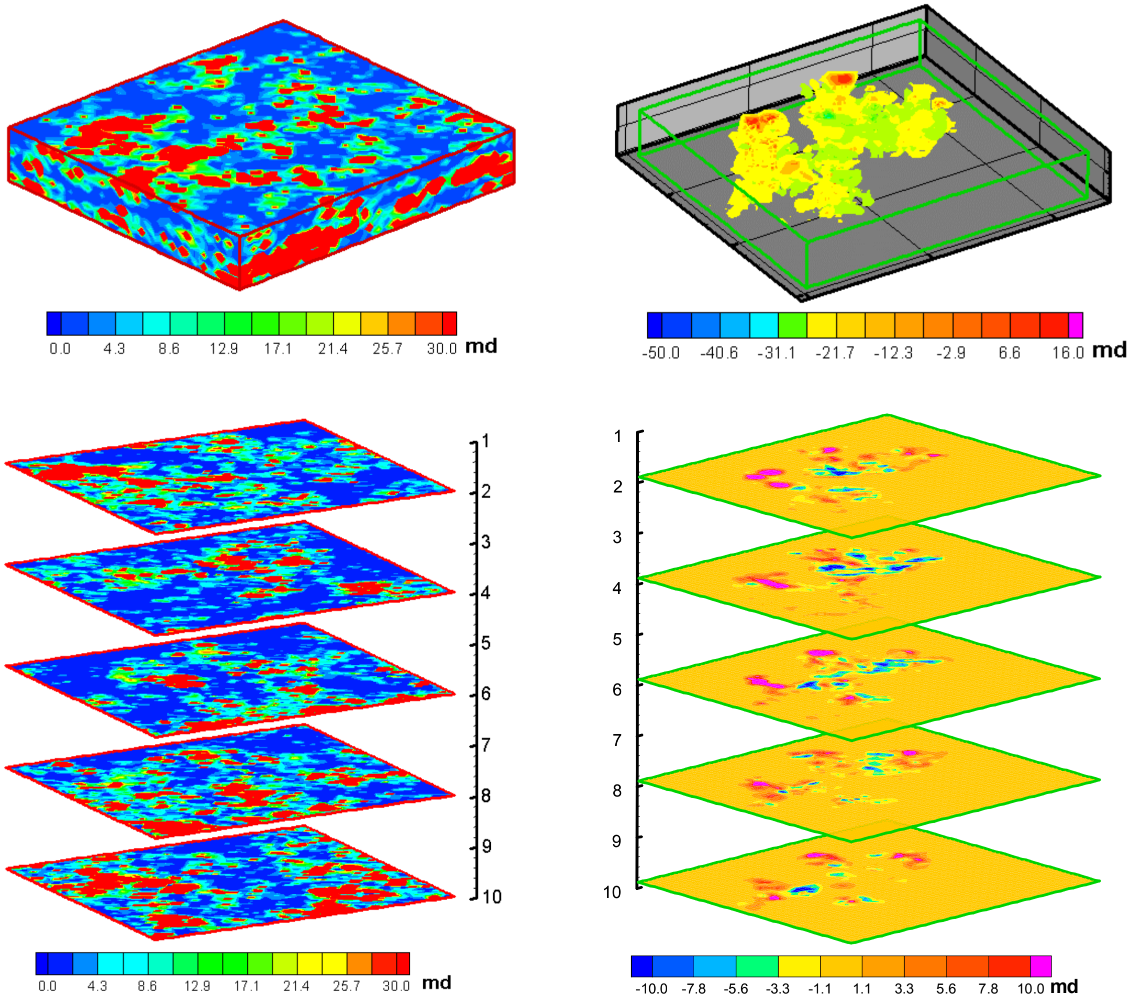

a. Final permeability model

b. Permeability changes from initial model

Figure 3.22—The final permeability model and permeability changes from the initial model.

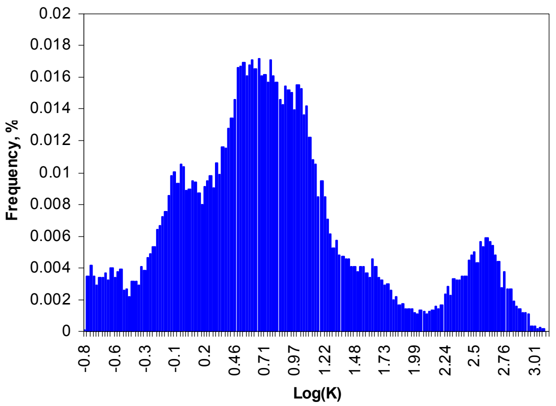

Histogram of log(k) before production data integration

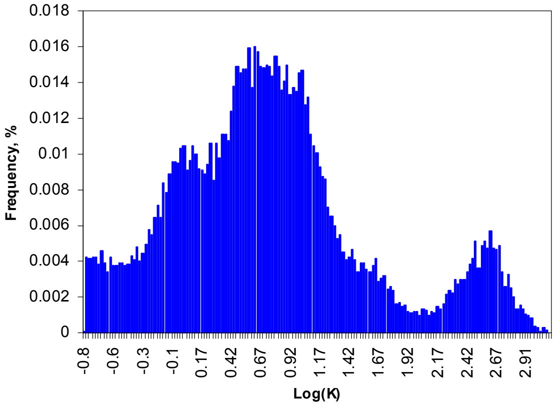

Histogram of log(k) after production data integration

Figure 3.23—Permeability histograms before and after production data integration for the Goldsmith case.

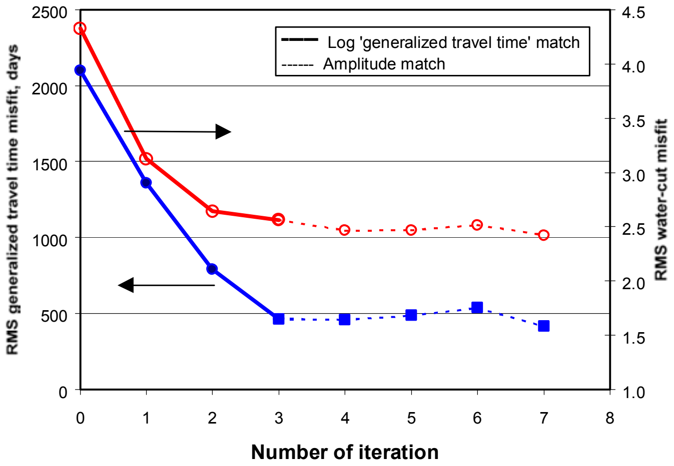

Figure 3.24—The generalized travel time and amplitude misfit vs. iterations – Goldsmith case.

3.5.3 Field Example 2 – A Giant Middle Eastern Oil Field.

This field ranks the 22nd largest in the world. It is a large north-south carbonate anticline measuring 25 km by 15 km and contains extra light crude at an average depth of 8000ft.[52.53] The reservoir comprises of a large-scale coarsening and shallowing upward carbonate reservoir platform sequence of about 500 ft thick. The field has been under peripheral water injection with 16 injectors and 70 producers, and a strong aquifer influx into the field, with a total of 30 years of production history.

Geologic and Simulation Model. The initial geologic model was created based on well log derived porosity, facies information and 3-D seismic data.[54] Geologic facies have been developed based on the depositional features with 9 reservoir facies and 2 non-reservoir facies. The best reservoir facies are skeletal conglomerates and grainstones with high permeability and porosity. The mudstones have very low permeability and porosity and are treated as the non-reservoir facies. The 11 different facies types were combined into 6 facies groups in the order of decreasing quality and having distinct porosity-permeability relationship. Then a 3-D facies model was generated using indicator kriging (**Fig. 3.25**). A scatter plot of porosity and seismic acoustic impedance indicated a fairly strong correlation with a correlation coefficient of -0.75. Multiple realizations of porosity distribution in the reservoir were generated using facies-based sequential Gaussian cosimulation with well data guided by the seismic acoustic impedance as a secondary variable.[54] The particular porosity distribution used in this study is shown in **Fig. 3.26**.

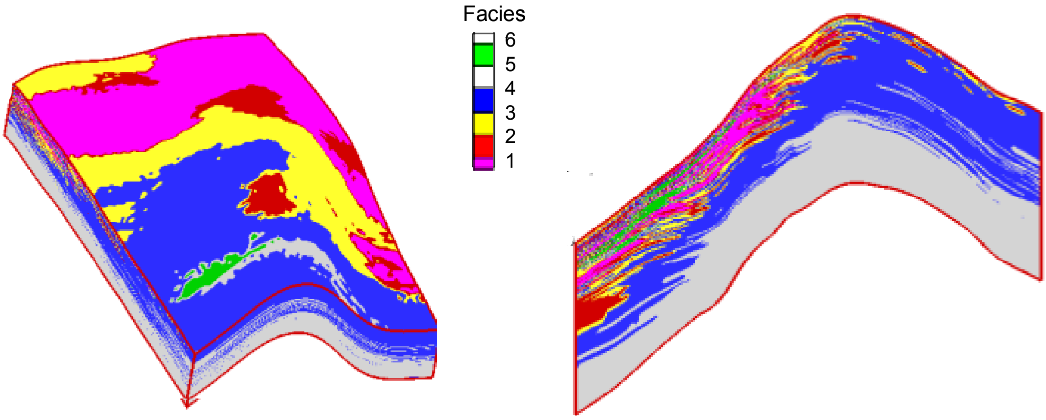

Figure 3.25—Fieldwide facies model and N-S cross section of the facies model.

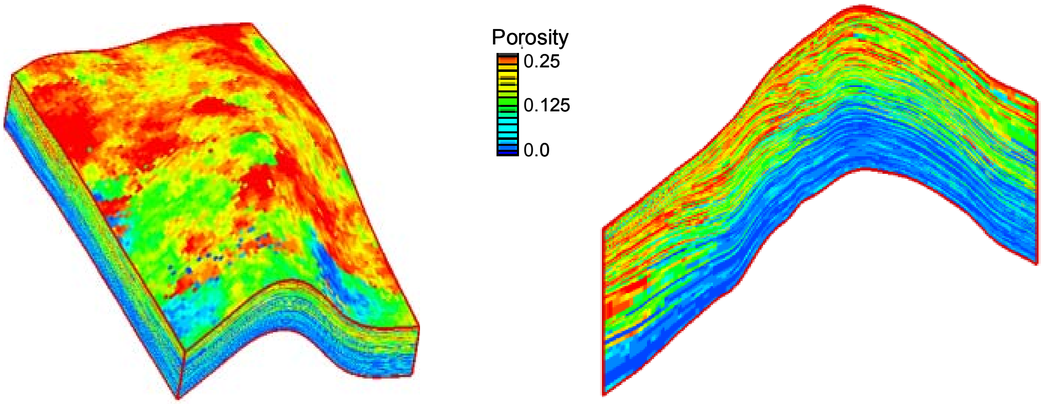

Figure 3.26—Fieldwide porosity model and the N-S cross sectional view.

From the facies based porosity model, 3-D permeability distributions were generated using appropriate core based porosity permeability transforms. The permeability model used in this study is shown in **Fig. 3.27**.

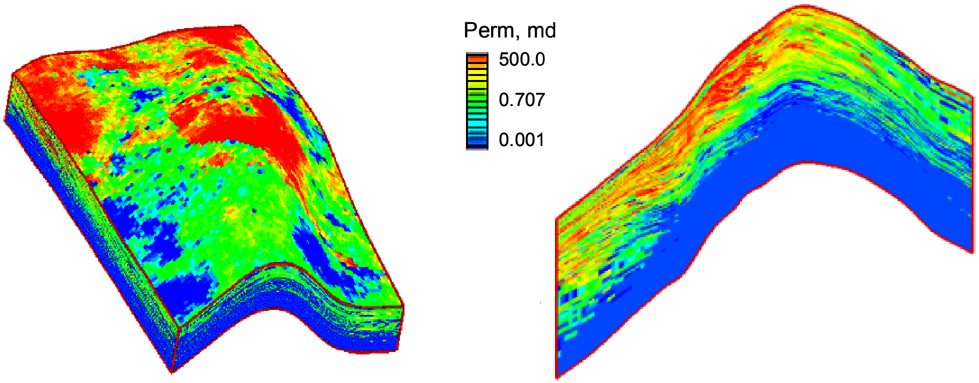

Figure 3.27—Fieldwide permeability model and the N-S cross sectional view.

The initial water saturation in the flow simulation model was obtained using facies-based J-curves and capillary-gravity equilibrium conditions (**Fig. 3.28)** To minimize the computation costs, we removed some of the aquifer grid blocks from the simulation model as indicated in **Fig.**

3.29 This resulted in a fine-scale simulation model with a mesh size of 72x100x128 or a total of 921,600 grid blocks.

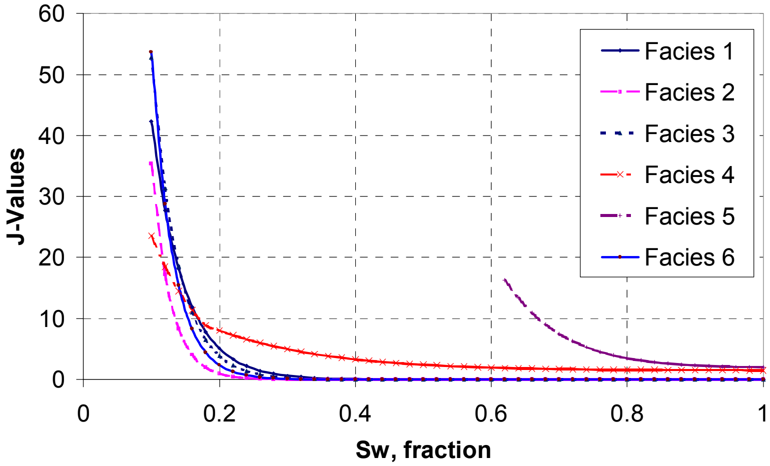

Figure 3.28—Facies J-curves and initial water saturation.

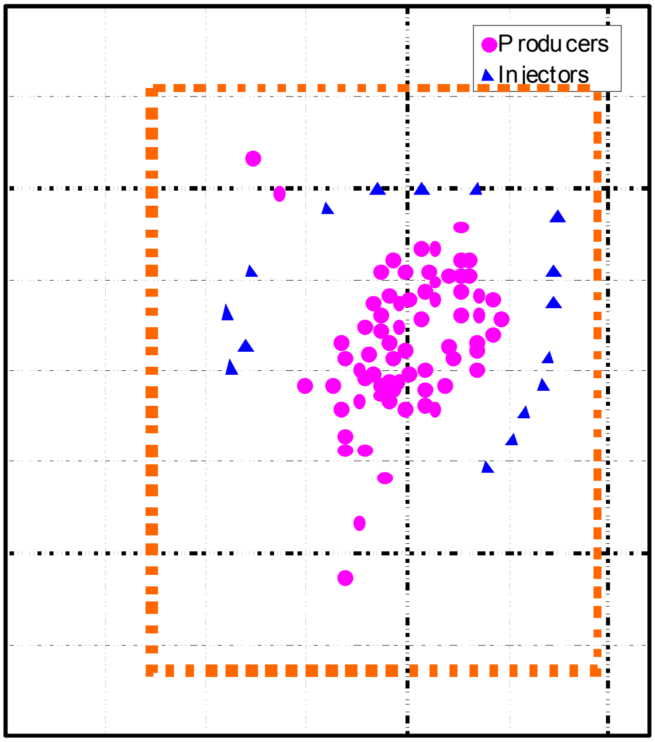

Figure 3.29—Well location map, dotted lines denote simulation area.

Gravity effects were included in the simulation model via operator splitting and had a significant impact on the results, especially on the water-cut responses because of water-slumping. In addition, it was important to include fluid compressibility and aquifer influx to obtain a pressure history consistent with the field observations. Note that the streamline tracing is valid for compressible flow, although it generally requires more frequent updating of the pressure field.[18,35] However, for the slightly compressible water-oil system considered here, it was not a major issue. For modeling aquifer influx, we used pore volume multipliers for the aquifer blocks and the multipliers were chosen so as to obtain a reasonable match to the overall observed field pressure history and fluid flow rates.

We defined 34 pressure updates to consider the detailed rate schedule to account for infill drilling, reperforations/recompletions and any significant rate changes. This required averaging of well rates for all injection and production wells. Some examples of such averaging are shown in **Fig. 3.31**. We also performed a sensitivity study for the number of pressure updates required. A simulation with 45 pressure updates did not show any significant change in the pressure history and water-cut response.

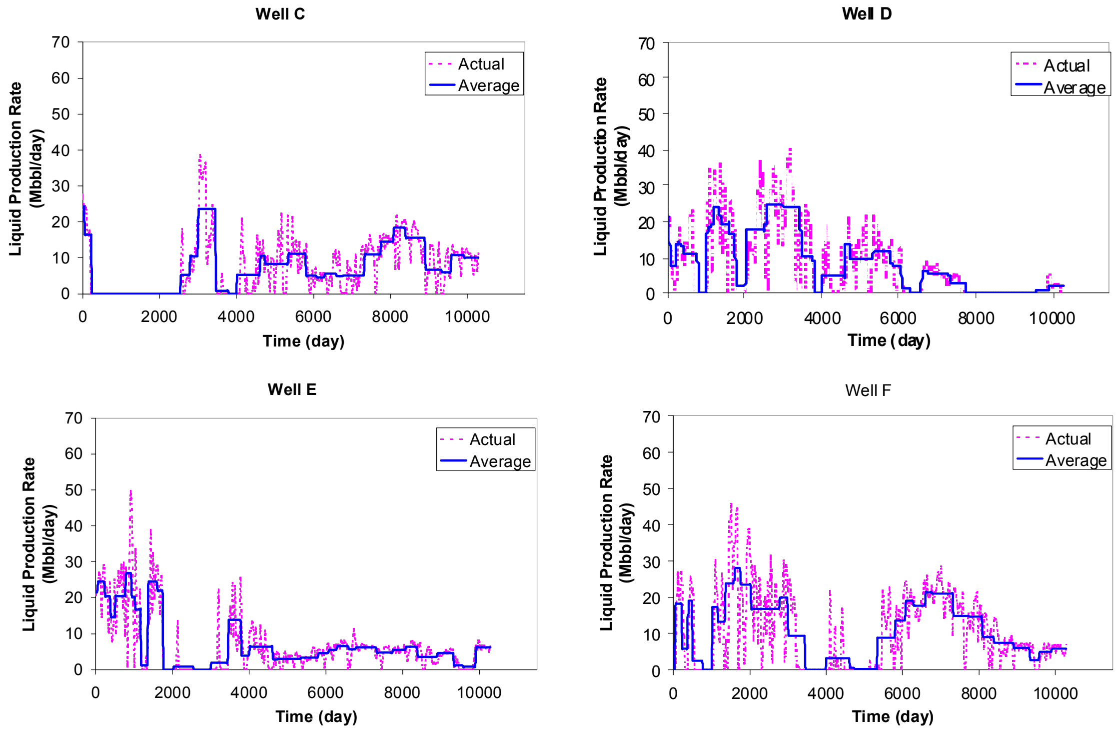

Figure 3.30—Examples of averaging of well rates for pressure updates in streamline simulation.

For illustration purposes, streamlines at the beginning (60 days) and end (10290 days) of a simulation run are shown in **Fig. 3.31** The compressibility effects are clearly apparent in the streamlines at 60 days for the single producer that has no aquifer or injection support.

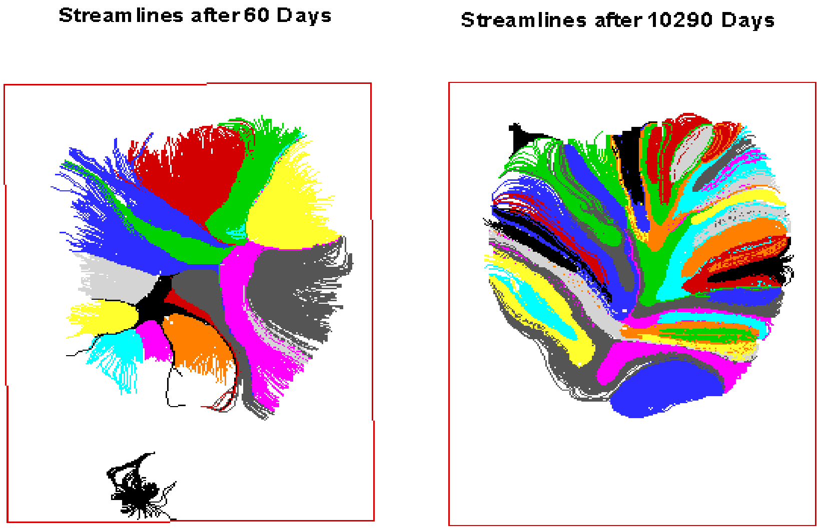

Figure 3.31—Streamlines after 60 days and 10290 days.

Production Data Integration. We attempted two different methods to integrate water-cut response into the fine-scale geologic model. The first method is a two-tep approach that utilizes an upscaled model for production data integration and then propagates the changes in permeability to the fine-scale model via a downscaling procedure. It is computationally efficient because the production data integration is performed using the upscaled model and thus, requires estimation of fewer parameters during inverse modeling. This method took about 6 hours in a PC. The second method is a single step approach that performs direct integration of production data into the fine-scale model. Although both the methods result in the same general trend in permeability changes, the two-step approach was found to be more stable and resulted in faster convergence.

We performed a vertical upscaling of the geologic model to 13 layers based on the geologic markers. The areal dimensions of the upscaled model were kept the same as the geologic model dimensions (250 meters by 250 meters) to avoid relocation of wells. The vertically upscaled model combines several geologic layers into one simulation layer. Because the lower part of the reservoir consists of tight and non-reservoir formation, a relatively large part of the formation was grouped into an upscaled block whereas the details of permeability variations in the upper part of the reservoir were preserved. **Fig. 3.32** show cross-sections of the detailed geologic model and the corresponding upscaled model for both porosity and permeability distributions in the reservoir.

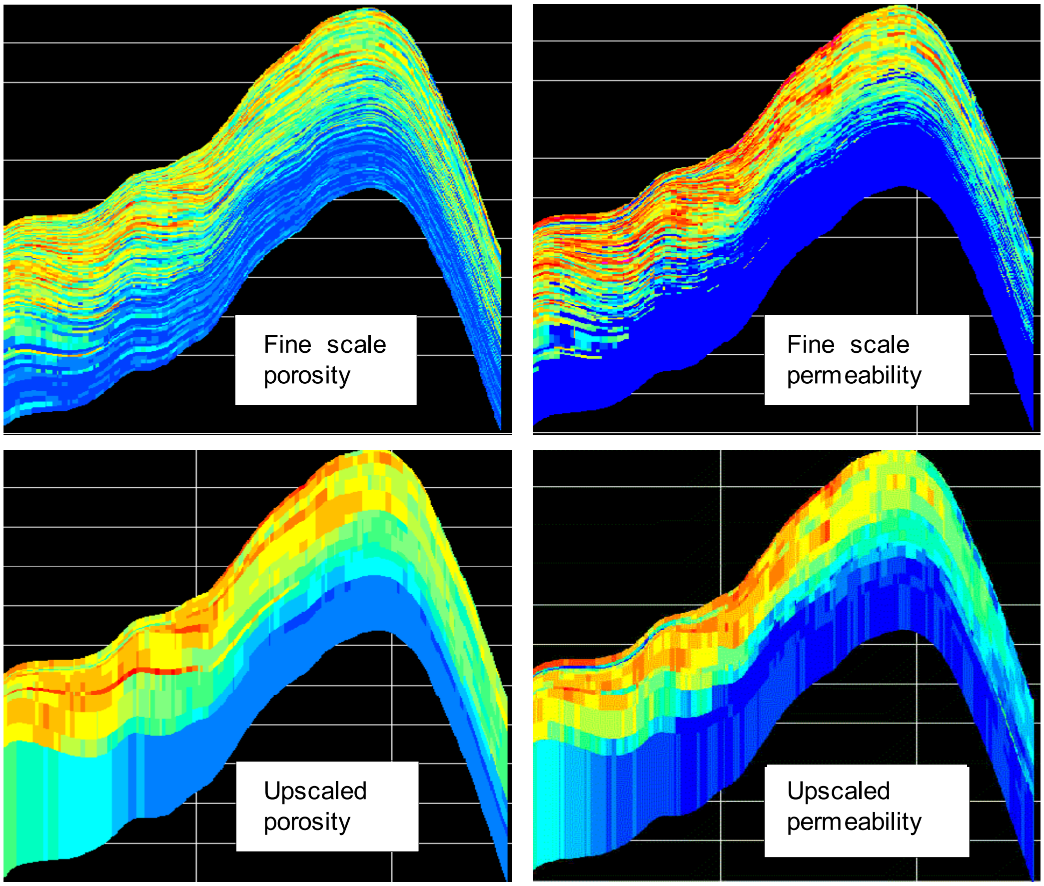

Figure 3.32—Comparison of fine-scale and upscale models.

The upscaled porosity was calculated using bulk-volume-weighted arithmetic averaging to preserve the pore volume of the original fine scale model. The upscaled permeabilities were computed using a combination of arithmetic and harmonic averaging. To consider the effect of flow direction, arithmetic averaging is used for x-directional upscaled permeability, k_x and harmonic averaging for z-directional upscaled permeability, k_z. To preserve the OOIP, water saturation is calculated using pore-volume weighted arithmetic averaging from initial water saturation based on the fine scale geologic model.

Out of the 70 producers in the field, 48 wells had water-cut response. Starting with the upscaled model, the grid block permeabilities were changed via the travel time inversion to match the water breakthrough times at the 48 producers. **Fig. 3.33a** compares the observed and calculated water breakthrough times using the initial (upscaled) static model. After 6 iterations of travel time inversion, the corresponding breakthrough times are shown in **Fig. 3.33b**. There is a significant reduction in the scatter indicating a close match between the observed and calculated water breakthrough times. The matching of the breakthrough times also resulted in a significant improvement of the overall production history match as observed in our previous experience.[17,18]

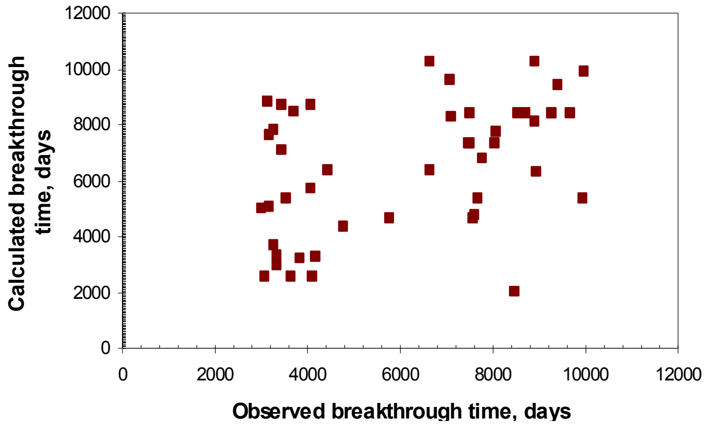

(a)

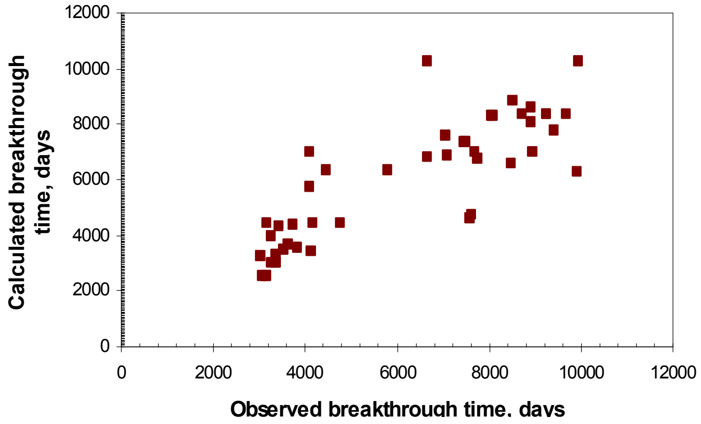

(b)

Figure 3.33—Traveltime match from (a) initial model and (b) after 6 iterations of travel-time inversion on upscaled model.

Fig. 3.34 demonstrates the water-cut match for several example wells after the travel time inversion. Most of the wells (about 70%) exhibited good to moderate matches in the overall production history. The wells that did not show improvements in matching appeared to be the ones with incomplete or inconsistent completion data.

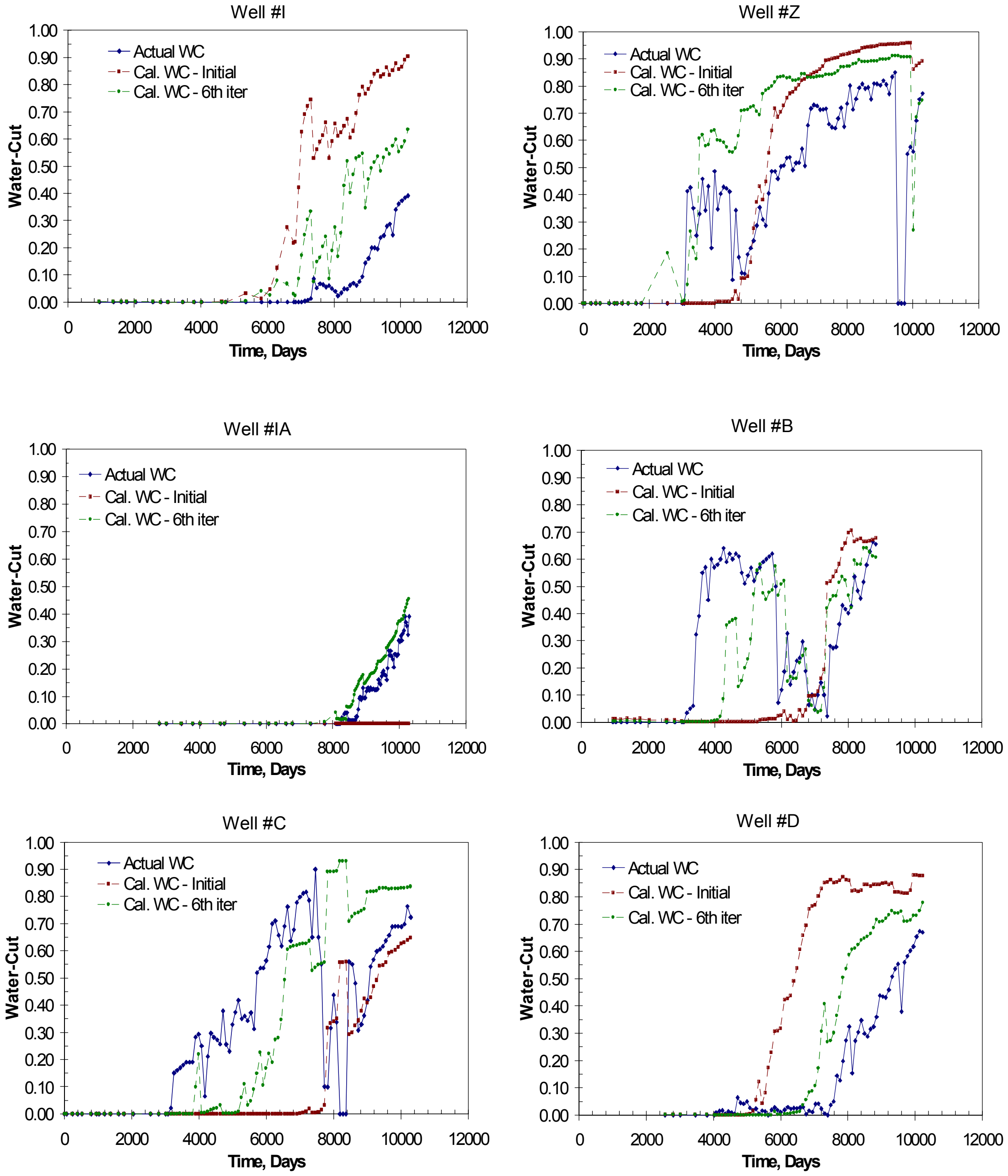

Figure 3.34—Water-cut match after traveltime inversion on the upscaled model.

Fig. 3.35 compares the initial permeability field with the final permeability field derived after inversion. From a visual examination, it is difficult to discern any differences. This is a direct consequence of the 'norm' constraint during the inversion that attempts to preserve the initial geologic model. Also, the final permeability distribution does not show any artificial discontinuities or geologically unrealistic features that generally arise when permeability multipliers are used during manual history matching. **Fig. 3.36** shows the difference between the initial and the final model indicating regions where permeabilities have been altered during inversion. We examine these changes in more detail in the next section.

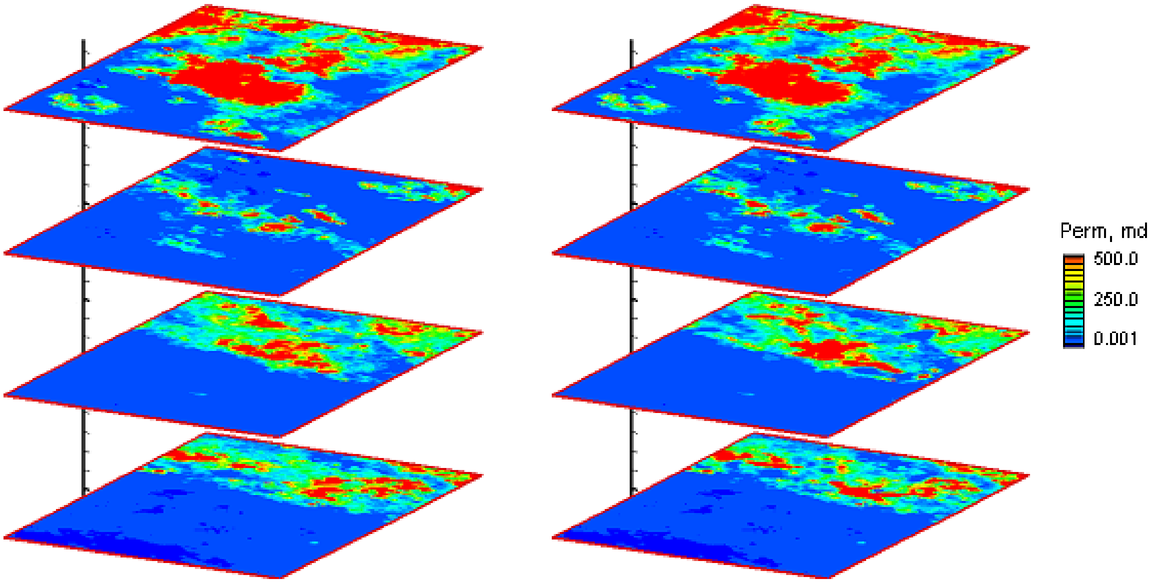

Figure 3.35—Initial upscaled permeability field (left) and final upscaled permeability field (right) after production data integration.

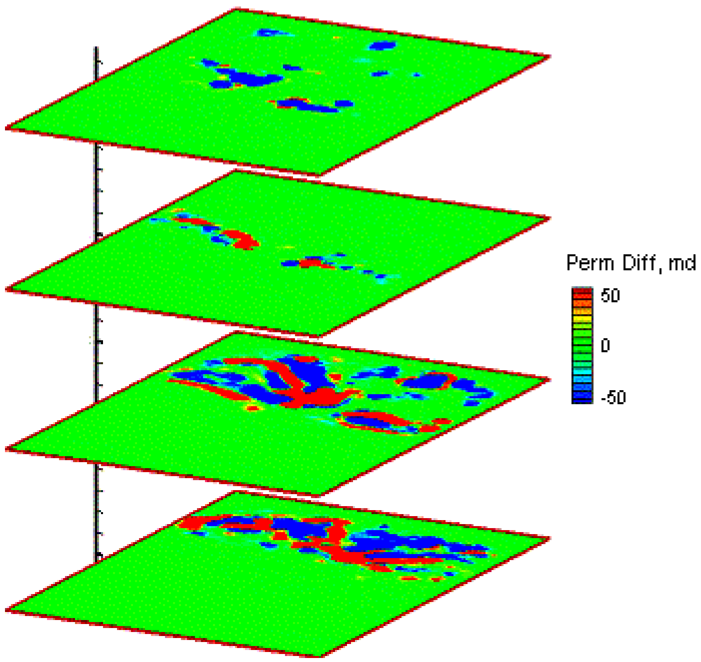

Figure 3.36—Difference in permeability for the upscaled model after production data integration.

Permeability changes in the upscaled model were transferred to the fine-scale model via downscaling. A simple procedure based on scale factors computed from the ratio of the grid block permeabilities of the initial and the final upscaled models were used to adjust permeabilities in the fine-scale model. A more comprehensive geostatistical downscaling procedure did not result in any significant improvement and was not pursued further.[55,56] The permeability changes in the fine-scale model were then compared with the facies model to examine any underlying trends.

Fig. 3.37 shows the permeability changes in the fine-scale model for a few selected layers. Alongside, we have also shown the facies map for the corresponding layer. It is clear that the permeability changes are mostly aligned with the facies, in particular ‘good facies’. Permeabilities increased at the northern higher elevation. No permeability enhancements were observed in the lower interval that represents low quality reservoir. All of the changes resulting from the production data integration were found to be geologically realistic.

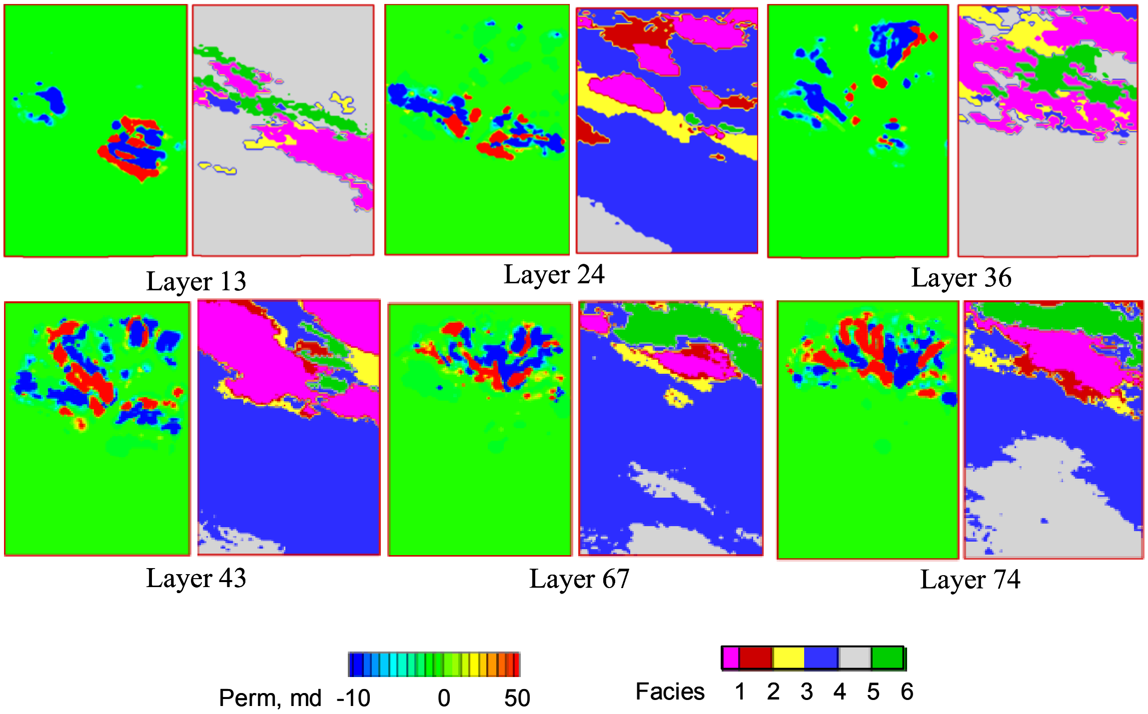

Figure 3.37—Comparison of permeability difference (left) with facies maps (right).

To further validate the model, a fine-scale flow simulation was performed using the updated permeability model. This allows us to check if the history match was still preserved after the downscaling. Also, the model results were compared with field surveillance data. About 70% of the wells exhibited good to moderate match to the overall production history. Some examples of these matches are shown in **Fig. 3.38**.

The saturation distribution in the field at the end of the simulation is shown in **Fig. 3.39**. The water encroachment patterns and the unswept areas indicated by the simulation were found to be consistent with the field surveillance data. The simulation model also shows evidence of water override. Such water override has also been confirmed by the field surveillance data.

As mentioned before, we also attempted production data integration directly into the fine scale geologic model without any upscaling. **Fig. 3.40** shows the changes from the initial permeability model. The computation time for this example with 0.95 million grid cells and 34 pressure updates was about 28 hours in a PC as compared to 6 hours for the two-step approach.

Although the permeability changes from the direct integration were generally consistent with the two-step approach, the overall history matches were less satisfactory for this case.

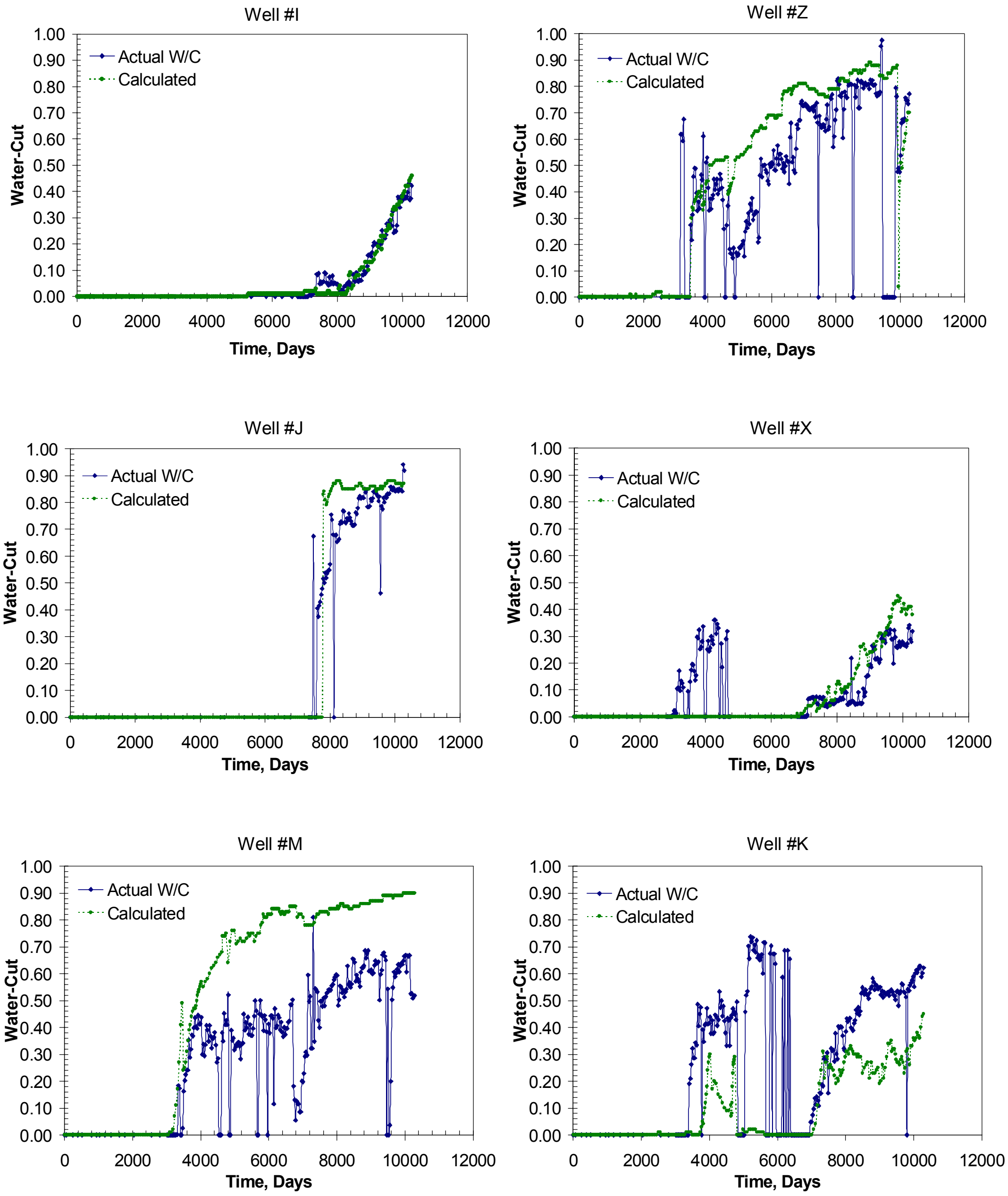

Figure 3.38—Examples of water cut match after finescale simulation with the updated model.

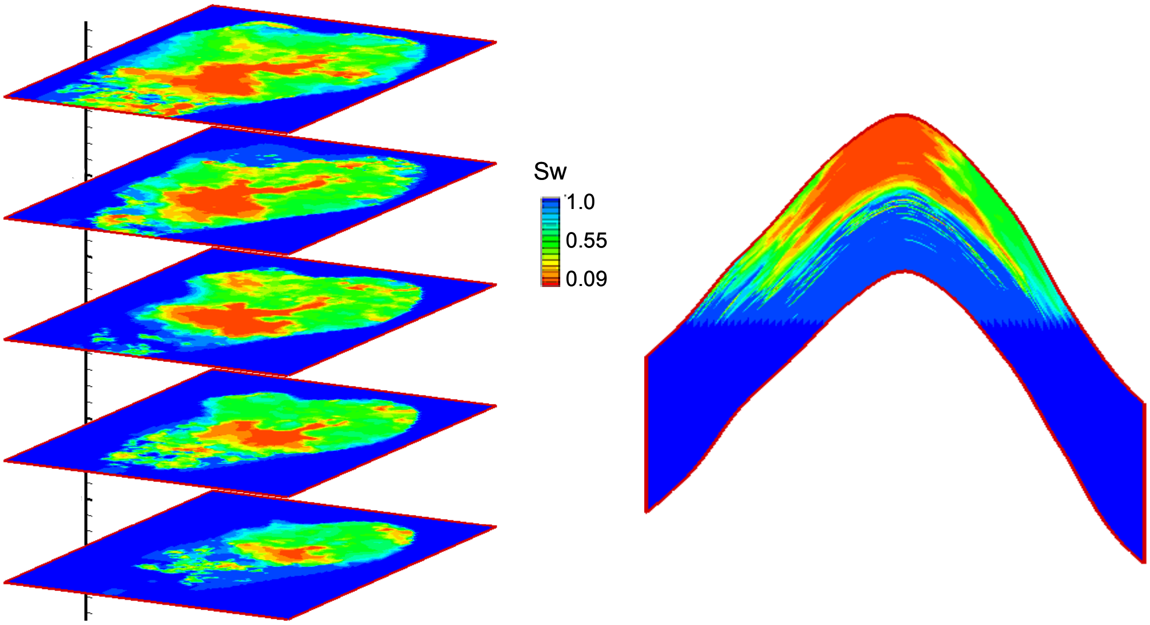

Figure 3.39—Saturation profile at 10290 days after finescale simulation (left), water override is evident in the East-West cross sectional view (right).

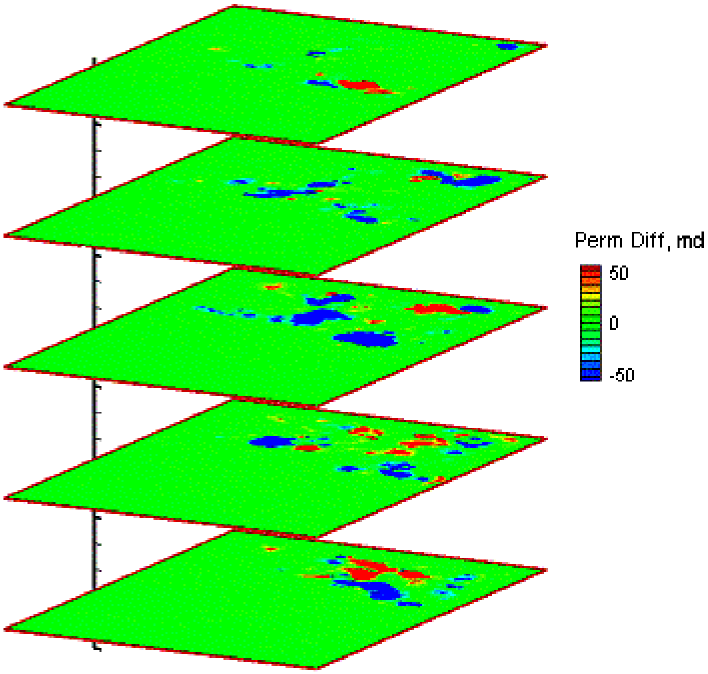

Figure 3.40—Examples of change in permeability after direct fine-scale integration.

3.6 Chapter Summary

A streamline-based production data integration technique was developed to integrate two-phase production data into high-resolution reservoir models. The technique is very general, robust and computationally efficient and is particularly well-suited for large-scale field applications with gravity and changing field conditions. A unique feature of our method has been the concept of a 'travel time' match that is analogous to seismic tomography and has allowed the use of efficient and proven techniques from geophysics. As an extension of travel-time inversion, we proposed a 'generalized travel time' inversion method for production data integration, which minimizes a 'travel time shift' derived by maximizing a cross-correlation between the observed and computed production response at each well. We developed analytical formulations to compute the sensitivities required by inverse modeling. This constitutes a critical component of our method and makes integration of production data into the large-scale models practically feasible. We demonstrate the power and utility of our proposed method using synthetic and field examples. Successful applications of our approach to large-scale field examples (from hundred thousand cells to million cells) clearly indicate the technical feasibility of the approach for routine application in reservoir characterization and management.

CHAPTER IV

INTEGRATION OF INTERFERENCE PRESSURE DATA

Interference transient pressure observation is an important source of dynamic data for reservoir characterization. The observed transient pressure data can be used to estimate the spatial distribution of reservoir properties, such as permeability or porosity. However, this typically requires the solution of an inverse problem. The difficulties of integrating transient pressure data into reservoir models include intensive computational efforts of inverse modeling and the non-linear relationship between transient pressure data misfit function and reservoir properties.

This chapter presents a robust and computationally efficient approach to integrate the interference transient pressure data into reservoir models. The proposed method extends our previous travel time inversion into an alternating inversion of travel time match followed by peak amplitude match or pressure match. Utilizing the concept of streamline ‘diffusive’ time of flight developed from the asymptotic solution for compressible flow, we developed analytical approaches to estimate the sensitivities for travel time, peak amplitude and pressure response.

The proposed inversion approach has been applied to synthetic and field examples. The synthetic example represents an interference test from a nine-spot pattern with a center injection well and eight surrounding observation wells. The spatial distribution of permeability is estimated by matching the pressure responses in the observation wells. In the field example, two interference tests were conducted in a skewed five-spot pattern. The transient pressure measurement from one test is first used to image the fracture patterns. Then, the estimated permeability model is used to predict the transient pressure responses of another test for the purpose of verification. The predominant fracture patterns emerging from the inversion are found to be consistent with the field geophysical and borehole data.

4.1 Introduction

Interference tests have been commonly conducted in the field to estimate reservoir properties because of its larger area of investigation and rapid responses. In this test, production or injection is carried out in one well while pressure changes from one or more surrounding wells are observed. Compared to single well tests, the interference test doubles the area of investigation.[57]

The investigation area of interference test consists of a rectangular area with a width of $2r_{in}$ and a length of $(r_{ws}+2r_{in})$,[57] where r_{in} is the radius of investigation of a single well and r_{ws} is the distance between the active well and observing well. Unlike other dynamic data, such as fluid or tracer production, which may take months or years to obtain sufficient responses, interference pressure responses in observation wells can be obtained in hours or days after starting the test. The pressure observations are directly related to flow properties of the reservoir, such as permeability and porosity. Thus by analyzing the pressure responses, one can estimate such reservoir properties. It is well recognized that reservoir models derived from static data such as geological descriptions, well logs, seismic attributes, and core data, often fail to reproduce the dynamic responses of reservoir because of large uncertainties within the models. Therefore, integration of interference pressure data into reservoir models is significant since the reservoir models can be conditioned to dynamic data at very early stages of field development.

Traditional well test analysis usually assumes homogeneous reservoir properties, thus only providing estimates of the average reservoir parameters.[58-60] Efforts have been made to use the transient pressure observations to estimate the spatial distribution of reservoir permeability and/or porosity.[11,23-26,45-46] Inverse modeling techniques are employed in conjunction with finite-difference or finite-element flow simulators. For example, Datta-Gupta *et al.,* employed two inverse approaches to integrate transient pressure information to construct fracture flow models.[23] A finite-element simulator was used as the forward model and simulated annealing was used as the optimization algorithm. Sagar *et al.* also used a simulated annealing approach to determine reservoir heterogeneity based on pressure data.[26] He *et al.* used a finite-difference simulator as the forward model and a Gauss-Newton method as the optimization algorithm to condition the transient pressure data into reservoir models. [11]

One of the difficulties in interpreting the pressure observations is the intensive computation requirement for solving the inverse problem. It is not unusual for such inverse modeling to require orders of magnitude more computational efforts compared to forward modeling or forward simulation. The major computation burdens come either from repeated forward simulations required by the specific inversion algorithms, such as simulated annealing,[23-26] or from the numerical computation of sensitivities of pressure responses with respect to reservoir parameters, such as permeability and porosity.[11,45-46] Numerical computation of sensitivities is usually expensive since either multiple forward simulations are required or multiple right-hands matrix problem needs to be solved at each iteration.

Current approaches to numerically compute sensitivities generally fall into three categories: perturbation technique; sensitivity equation method and adjoint state method.[3-4] The perturbation approach is the simplest one. Sensitivities are estimated by simply perturbing each of the reservoir parameters by a small amount and rerunning the forward simulation to see the change in model responses. The required number of forward simulation runs is equal to the number of model parameters plus one.[3] Thus, it is very time consuming if there is a large number of model parameters. In the sensitivity equation method, sensitivities are computed by solving a linear system obtained from differentiating the governing equations with respect to a model parameter.[3-7] Although the coefficient matrix of the linear system doesn't change with model parameters, the right-hand vector does depend on the model parameter. Each model parameter has one right-hand vector. Therefore, a multiple right-hand side (equals to the number of model parameters) matrix problem must be solved to obtain the sensitivities, requiring similar order of computations as the perturbation technique. The adjoint state method derives a set of adjoint equations associated with the governing equations to calculate the sensitivities.[3, 8-16] It also needs to solve additional systems of linear equations depending on the number of data points or number of wells.[16] Therefore, for large scale problems, the required computations are still very expensive.

Another difficulty in interpreting the pressure observations is the highly non-linear relationship between transient pressure responses and reservoir properties. Non-linearity is often characterized by the presence of multiple local minima in the data misfit function.[61] Since most of the inversion approaches use a linearized technique to iteratively estimate the model parameters, the high non-linearity can result in slow convergence or make the minimization to be easily stuck at a local minimum. This hampers our ability to find the minimum of a data misfit function to obtain a representative set of reservoir parameters conditioned to the dynamic data.[61] Furthermore, pressure variations are more strongly influenced by the flow properties near the active and observing wells.[36] This localized nature of pressure sensitivities also introduces difficulties into the inversion process.[36]

Recently, Datta-Guptta *et al.*,[18] Kulkarni *et al.*,[35] and Vasco *et al.*[36] utilized an inversion of travel times of pressure changes to integrate interference pressure data into reservoir models. The travel time is derived from differentiating the transient pressure curve with respect to time and defining the arrival time of the peak of transient pressure temporal derivative. The approach is based on an asymptotic solution[18,35-36] to the diffusivity equation and follows the procedures of seismic ray tomography.[62] The streamline time of flight equation was derived for compressible flow using concepts from geometric optics and seismology.[62-63] Because of the quasi-linear property of travel time inversion[37] and more uniform sensitivities of travel time to reservoir properties either in the vicinity of wells or between the active and observing wells,[36] the travel time inverse problem is more robust compared to the conventional direct pressure inversion. Using the concept of streamline 'diffusive' time of flight, the sensitivities of travel times were computed analytically from a single forward simulation.[18,35] Thus the computational efficiency of inversion was significantly increased. However, the travel time inversion also has limitations. Even though the travel time can be perfectly matched, it cannot guarantee a good matching of the pressure.

In this chapter, the previous travel time inversion has been extended into an alternating two-step inversion of travel time match followed by peak amplitude match or pressure match. The peak amplitude is defined as the peak of the transient pressure derivative curve. The inversion first lines up the arrival times of transient pressures for all the observing wells. Then taking the estimates from travel time inversion as a starting model, peak amplitude match or pressure match is followed to further improve the matching of pressure. The alternating inversion switches the objective function between travel time misfit and peak amplitude misfit or pressure misfit, providing the chances of bypassing the local minima. More importantly, analytic approaches for sensitivity computation were developed by utilizing the asymptotic solution of diffusivity equation and the concept of streamline 'diffusive' time of flight. The sensitivities of travel time, peak amplitude and pressure can all be computed analytically using a single forward simulation. Therefore, the proposed inversion approach is highly computationally efficient.

4.2 Alternating Inversion of Travel-time and Peak Amplitude or Pressure

As discussed before, integration of dynamic data to estimate reservoir properties typically involves the solution of an inverse problem. The major difficulties of solving the inversion problem result from the intensive computational requirements and the highly nonlinear and ill-posed properties associated with the inverse problem. The general methodology of handling these difficulties for efficient parameter estimation has been discussed in chapter 2, and will also be applied to integrate transient pressure data. The travel-time inversion will be used throughout as the driving force to integrate transient pressure data. Because of its quasi-linear property, the travel time inversion is more robust with respect to the initial model. However, we note that the travel time inversion cannot guarantee a good matching of pressure even though the travel time can be perfectly matched. In order to improve the overall matching of the pressure data themselves, we use an alternating two-step inversion of travel time and peak amplitude or pressure, that is we first match the travel time, followed by peak amplitude matching or pressure matching, then alter between the travel time matching and peak amplitude matching or pressure matching for multiple cycles if necessary. In this section, we discuss the ideas behind this inversion method, and other related issues, for example sensitivity calculations. A synthetic example will be given for illustration.

As mentioned before, for interference transient pressure data, we define the travel time as the arrival time of the peak slope of transient pressure curve, while the peak amplitude is defined as the peak slope of transient pressure curve. **Fig.4.1** and **Fig.4.2** illustrate these concepts. The calculated as well as the observed transient pressures at observing wells are differentiated with respect to time. The transient pressure response will show a peak for an impulse source or sink. The travel time is determined as the arrival time of the peak. The injection or production with a constant rate can be considered as a step function (Heaviside function) source; since a time derivative of Heaviside function is a delta (impulse) function, the behavior of the time derivative of pressure will be analogous to the pressure responses corresponding to an impulsive source, and the travel time and peak amplitude determined from the pressure derivatives simply represent the arrival time and magnitude of the maximum pressure buildup or drawdown introduced by an impulse source/sink, respectively.

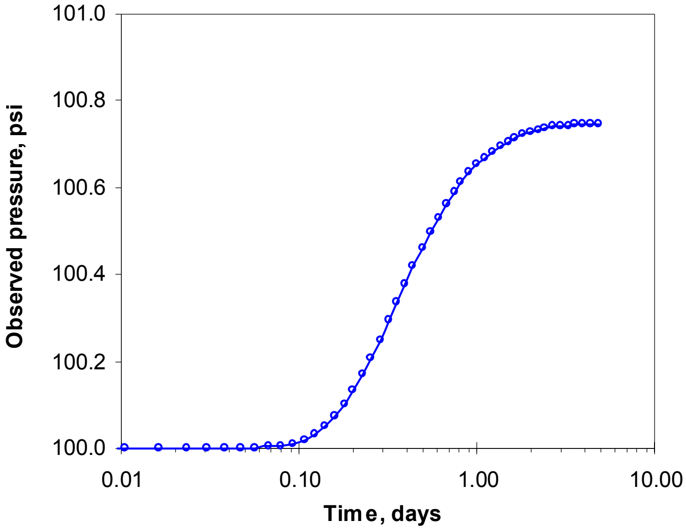

Figure 4.1—Transient pressure responses at an obersering well.

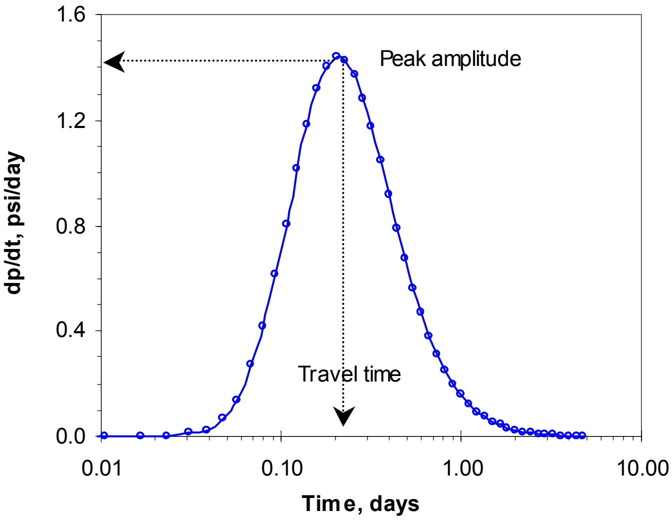

Figure 4.2—Temporal derivative of transient pressure responses at an observing well.

Because of the ill-posed nature of the inverse problem, the minimization is often stuck in local minimum. The idea is to alternatively switch the objective misfit functions in the process of inversion so as to provide the chances of bypassing the local minimum. The peak amplitude match or pressure match takes the estimates from travel time inversion as a starting model to further improve the matching of pressure. The travel time match and peak amplitude match or pressure match are alternated for multiple cycles until no further improvement on pressure matching can be obtained. Therefore, the alternating inversion is very helpful to achieve the overall best matching.

In the integration of interference pressure data, we adopt a finite-difference simulator as the forward model. The forward model predicts calculated pressure responses at observing wells and pressure distribution at all grid cells.

Since we adopt a gradient-based minimization algorithm, the sensitivity is the essential information in order to proceed with the inversion. Based on the concept of streamline 'diffusive' time of flight derived from the asymptotic solution of pressure,[35-36] analytic approaches for computing the sensitivities of travel time and peak amplitude are developed. Streamline trajectories are first constructed based on the pressure distribution at the final timestep from the finite-difference simulation. Then, the sensitivities of travel time and peak amplitude are calculated as one-dimensional integrals of analytic functions along streamlines. Note that streamline trajectories may vary with time for a compressible system. However, previous experience indicates that the stabilization of streamlines is a quick process and the time required for the stabilization is usually shorter than the time of our interest (the arrival time of the transient pressure).[35] Therefore, tracing the streamlines at the last time step is reasonable. For the pressure sensitivities, we also developed an analytic approach. The approach transfers the grid block permeability perturbation into multiple source and sink, and uses the zero-order approximation of the asymptotic solution as the Green's function for the general heterogeneous media. Since the source and sink introduced by a grid permeability perturbation are generally time variant, the pressure sensitivities are obtained by convolving the Green's function solution with the time variant source and sink. To increase the computational efficiency, the propagation of the pressure perturbation introduced by a source or sink is approximated as a straight line. Therefore, the calculated sensitivities of pressure are approximate. However, since the approximation captures the dominant behavior of sensitivity distribution, as we will illustrate later, they are sufficient for their use in the inversion.

4.2.1 A Synthetic Illustrative Example

In this example, we have a single layer heterogeneous permeability field, as shown in **Fig. 4.3**. It consists of a large area of low permeability in the northwestern part and a high permeability extending in the northeastern direction. The model has a grid of 21×21 with the grid size of $62.86 ft \times 62.86 ft$ and a nine-spot well pattern (**Fig. 4.4**). An interference test, which is injecting at center well and observing pressure responses at eight surrounding wells, is simulated based on the reference permeability field. **Fig. 4.5** shows the reference transient pressure responses of the eight observing wells, which will be used as the observed data.

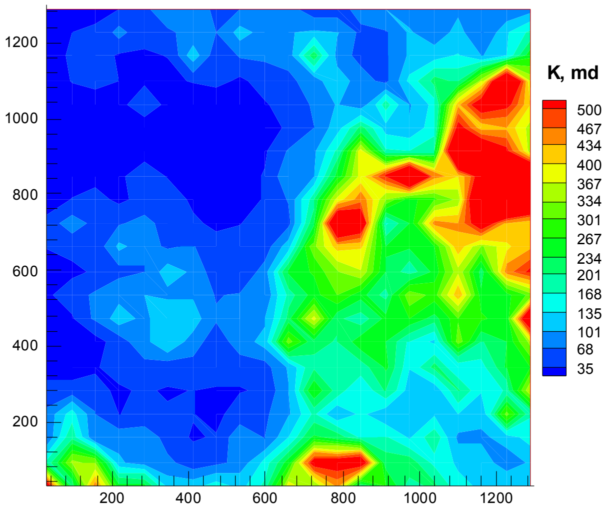

Figure 4.3—The reference heterogeneous permeability field.

We start from an uniform initial permeability distribution of 100 md. Three sets of inversion were performed and are demonstrated in the following sections. One is the travel time matching; another one is the alternating travel time/peak amplitude matching; and the third one is the alternating travel time/pressure matching.

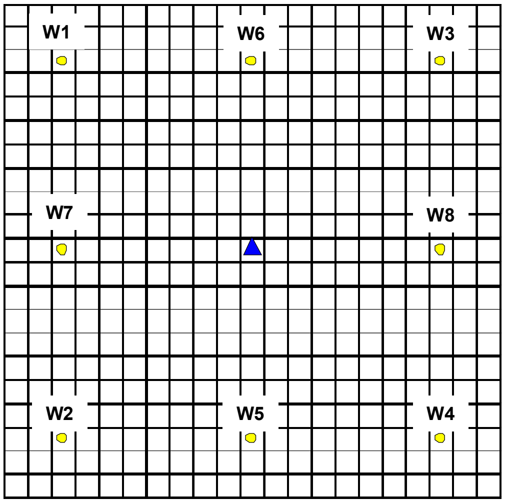

Figure 4.4—Mesh grid and well pattern of the synthetic example.

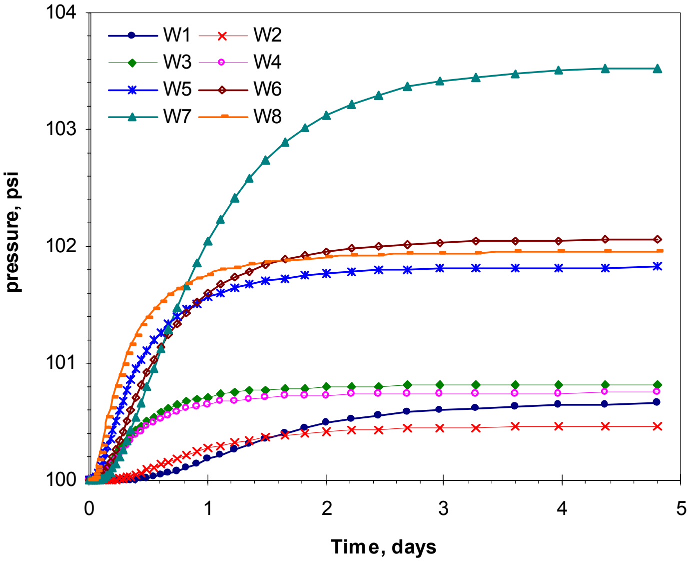

Figure 4.5—Reference pressure responses at observing wells.

Travel time matching. Based on given initial reservoir model, a forward simulation is run to predict the transient pressure responses to this model. As discussed before, the pressure responses are differentiated with respect to time. The travel time of pressure is then identified as the time when the pressure temporal derivative reaches a maximum. This is illustrated in **Fig. 4.6**, which shows both the observed (reference) responses and the responses from our initial model. Taking the square root of the determined arrival time as our data, travel time inversion is conducted to minimize the misfit between the observed arrival time and calculated arrival time for all observation wells. **Fig. 4.7** shows the temporal derivative of pressure response at the end of travel time match. We can see that the peaks are lined up by travel time matching. The initial arrival time match, as well as the final arrival time match at eight observing wells, are shown in **Fig. 4.8**. The final arrival time match is perfect; the calculated and observed data points align along the 45^o line. The estimated permeability model by travel time match is shown in **Fig. 4.9**. Comparing this figure with **Fig. 4.3**, we can see that the large-scale features of permeability distribution are produced from the travel time inversion. The magnitude of permeability is recovered well in the low permeable region, but somewhat underestimated in the high permeable region. **Fig. 4.10** shows the matching of pressure responses themselves from travel time inversion. We can see that the matching of pressure responses is not satisfactory after travel time inversion. In general, matching the arrival time of pressure front helps to improve the pressure matching, but cannot guarantee a good matching of pressure responses themselves.

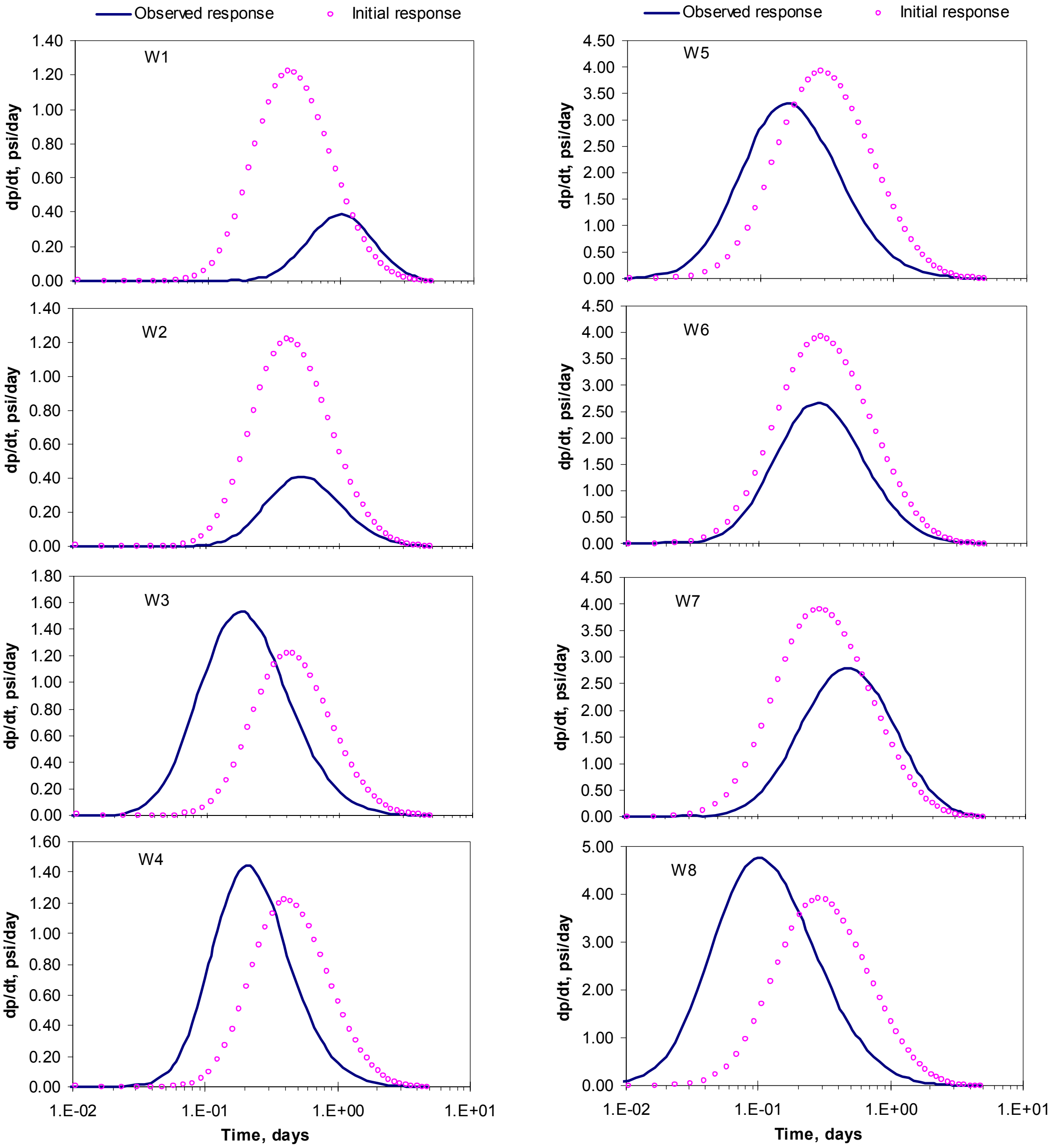

Figure 4.6—Pressure temporal derivative from the initial and reference models.

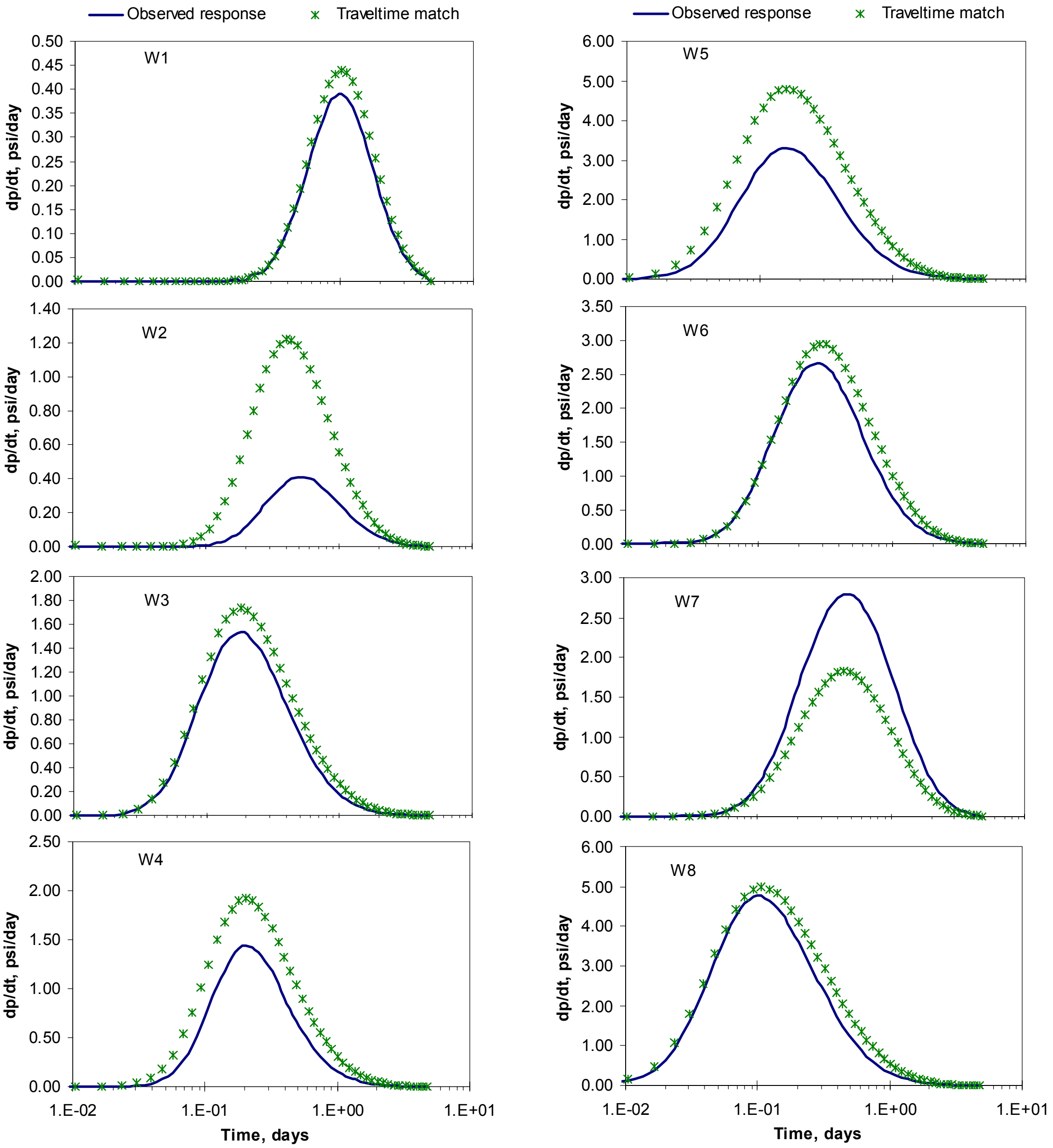

Figure 4.7—Observed vs. calculated pressure temporal derivative after travel time match.

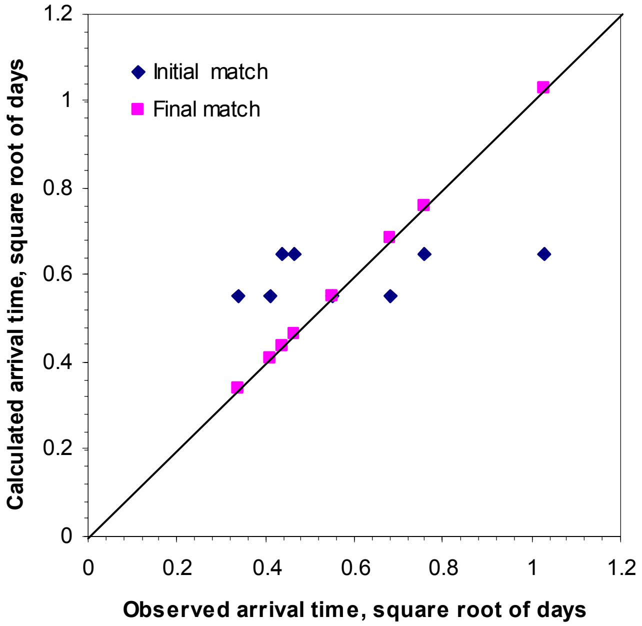

Figure 4.8—Travel time (pressure–front arrival time) match for a synthetic example.

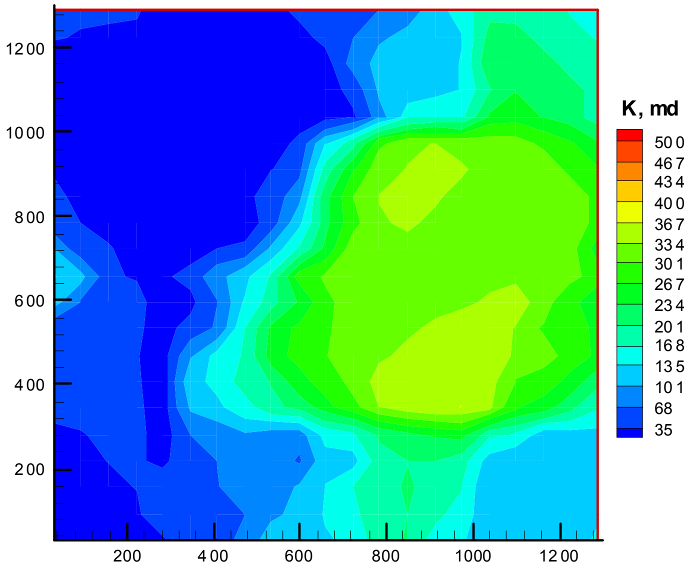

Figure 4.9—Estimated permeability distribution from travel time inversion.

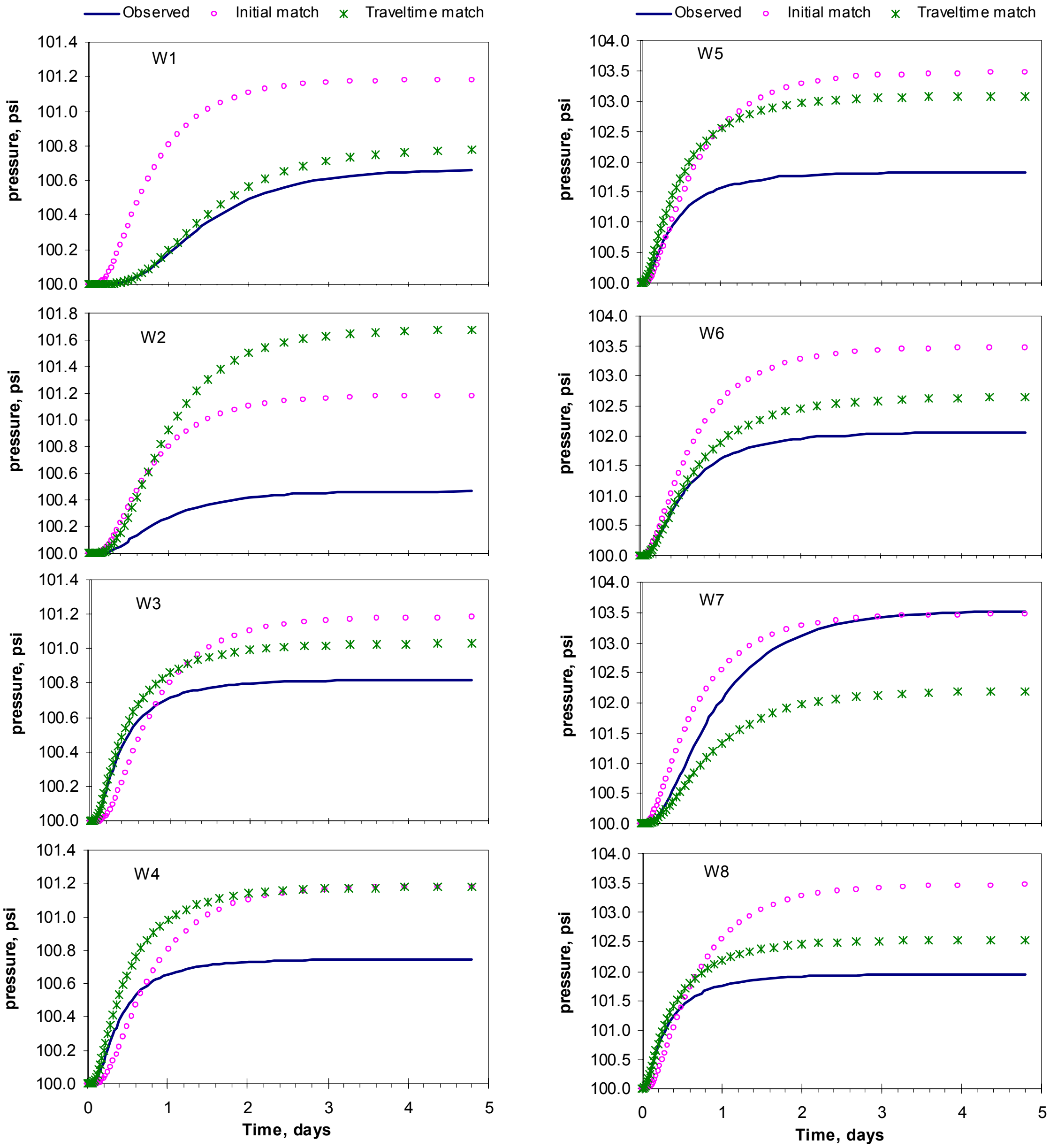

Figure 4.10—Matching of pressure responses after travel time match.

Alternating Travel Time/Peak Amplitude Matching. It is observed that if we can match the peak amplitude of the pressure temporal derivative after lining up the arrival time of the peak (see **Fig. 4.7**), the pressure matching will be significantly improved. This motivates us to further perform peak amplitude matching after travel time inversion. In peak amplitude inversion, we minimize the misfit between the observed and calculated peak pressure temporal derivatives. The estimated permeability model from travel time match will be used as a starting model for the next peak amplitude inversion. The travel time match and peak amplitude match are alternated for two cycles until no further improvement on pressure matching can be obtained. **Fig. 4.11** shows the match of pressure temporal derivative after our alternating travel time/peak amplitude inversion, while **Fig. 4.12** shows the corresponding match of pressure responses. It is clear that the pressure match has been significantly improved and now the pressure responses themselves are reasonably well matched. The resulting inversion permeability model, shown in Fig. **4.13**, contains some more details of permeability distribution compared with the estimation from travel time inversion (**Fig. 4.9**). In particular, a narrow trough of high permeability emerges at the northeastern portion of the model.

In **Fig. 4.14**, we show the root mean squared errors of travel time and peak amplitude during the iterations of the inversion, while **Fig. 4.15** shows the corresponding misfit of the pressure responses. It can been seen that the initial travel time inversion produces a perfect match of pressure arrival times after 8 iterations (**Fig. 4.14**), however, the pressure misfit is still at a high level (**Fig. 4.15**); the following peak amplitude match gets quick misfit reductions for both peak amplitude and pressure at the first several iterations after the switching, and stalls in the late iterations; although the second cycle travel time match does not significantly improve the pressure matching **(Fig. 4.15**), it helps the following second cycle peak amplitude match to produce a sharp misfit reduction for both peak amplitude and pressure (**Fig. 4.14** and **4.15**). This indicates that alternation of misfit functions in the process of inversion helps the minimization get rid of being trapped at local minima and approach to the global minima.

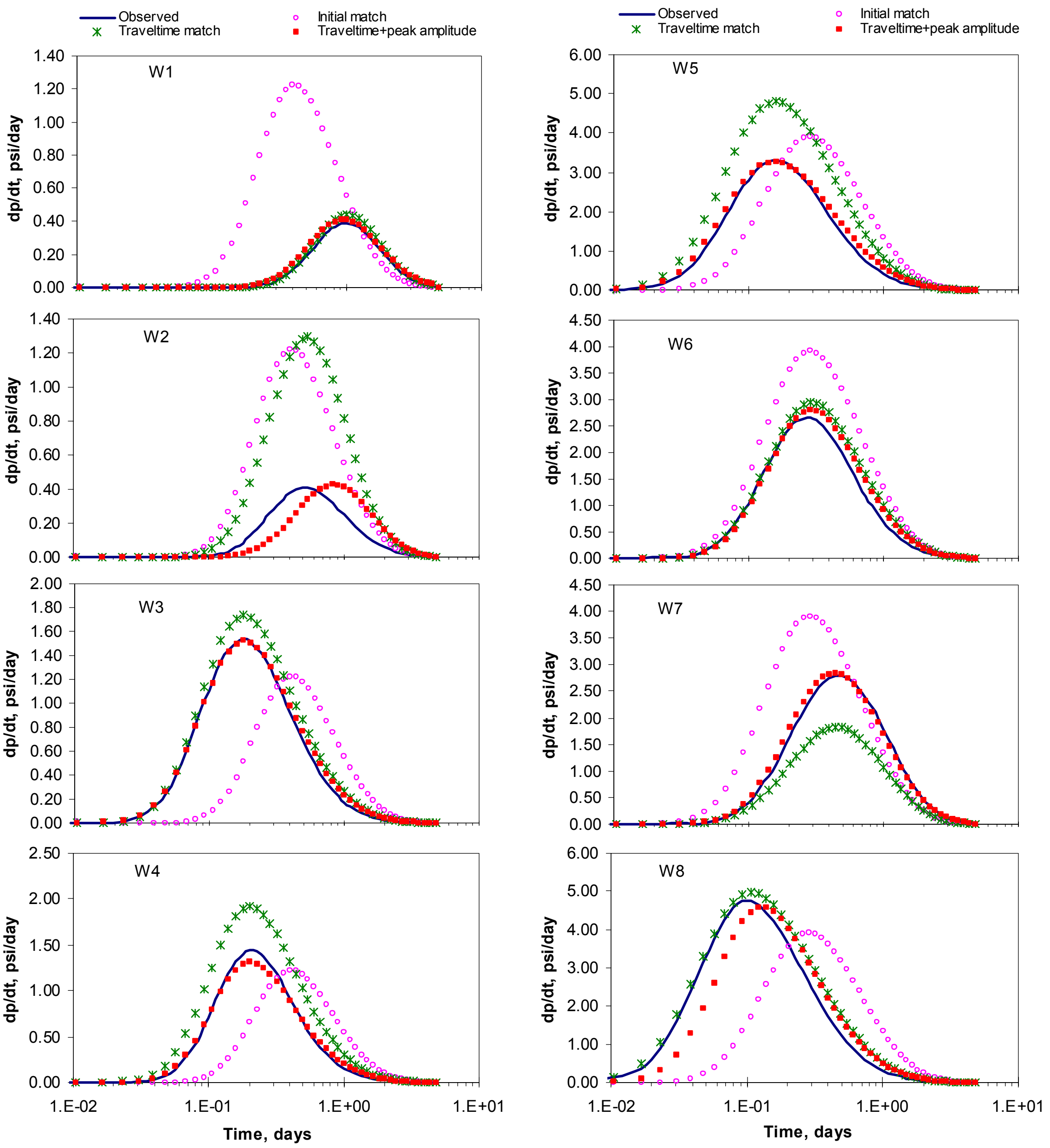

Figure 4.11—Pressure derivative matching from alternating travel time/peak amplitude inversion.

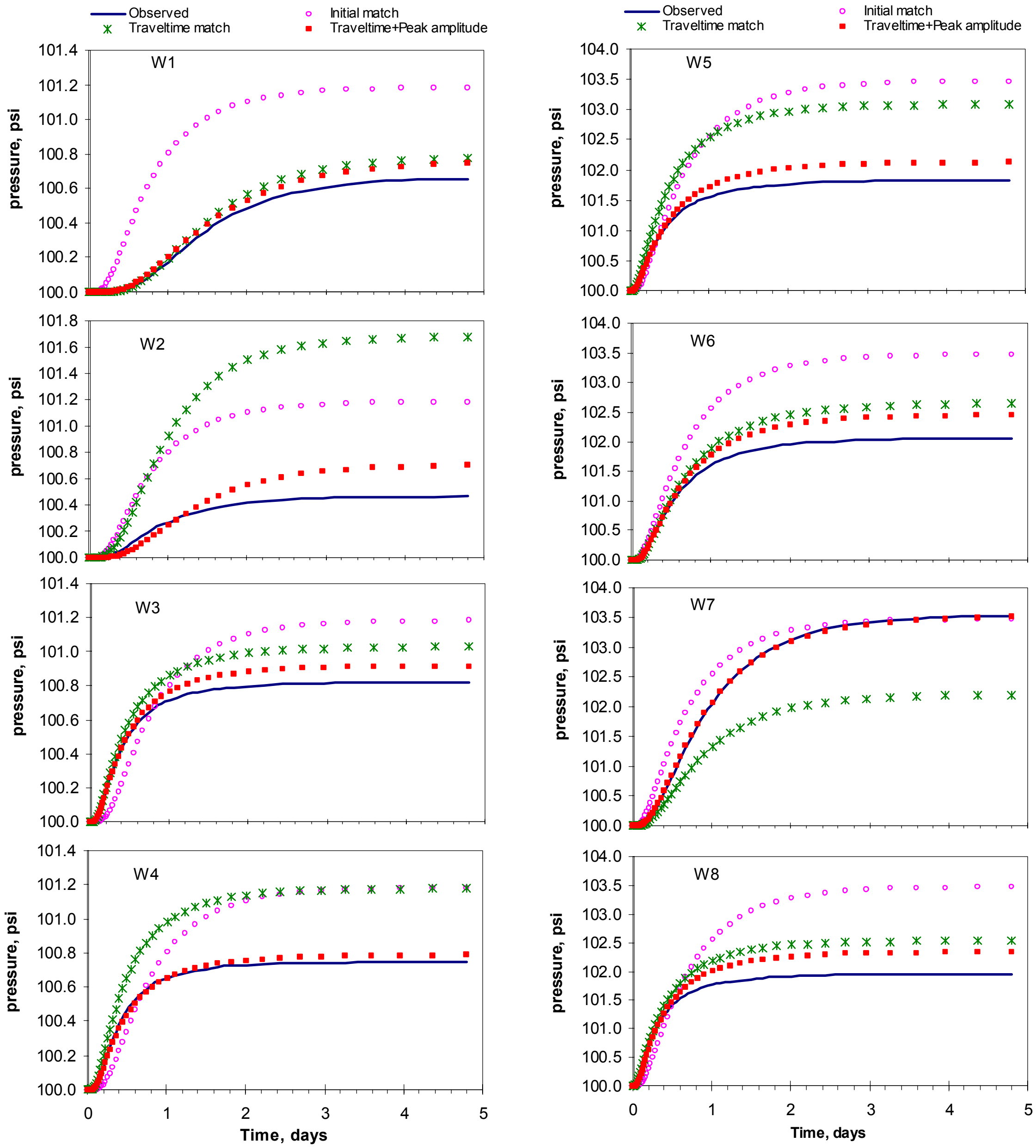

Figure 4.12—Pressure matching from alternating travel time/peak amplitude inversion.

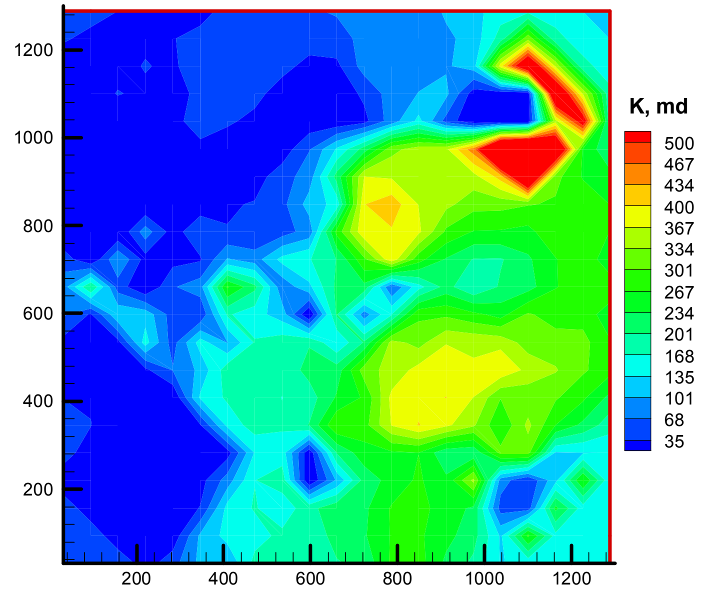

Figure 4.13—Estimated permeability distribution from alternating travel time/peak amplitude inversion.

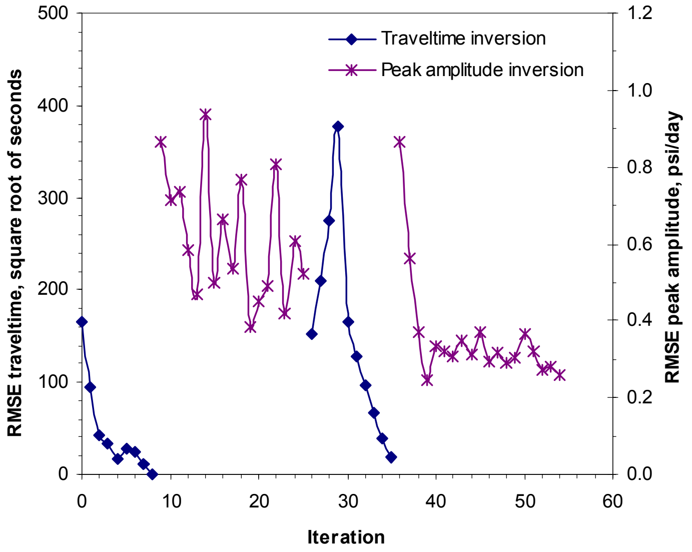

Figure 4.14—Root mean squared errors vs. number of iteration for the alternating travel time/peak amplitude inversion.

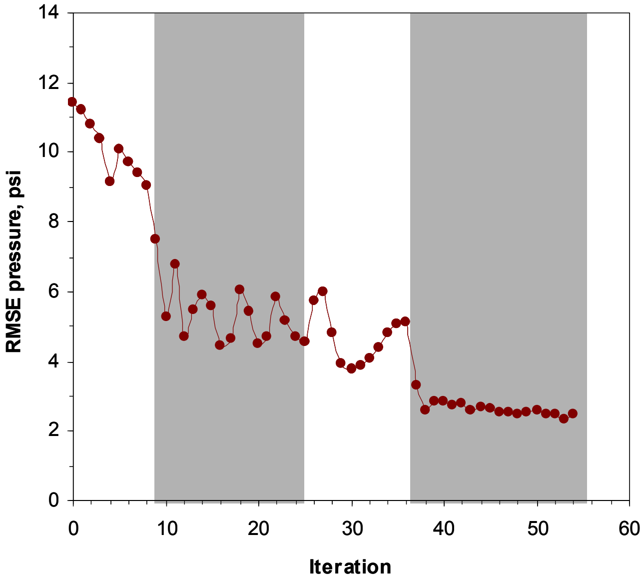

Figure 4.15—Root mean squared error of pressure in the alternating inversion of travel time and peak amplitude (shadow indicates peak amplitude match).

Alternating Travel Time/Pressure Matching. We also conduct another inversion - alternating travel time/pressure matching. Again, we used the estimated permeability model from travel time inversion as the starting model for the following pressure match. In pressure match, we minimize the misfit between the observed and calculated pressure responses themselves. The travel time match and pressure match are alternated for four cycles. Each cycle consists of 8 iterations of travel time match and 8 iterations of pressure match. **Fig. 4.16** shows the final match of pressure responses, as well as the match from the initial travel time inversion. The matches are very satisfactory for all eight observation wells. The final inverted permeability model is shown in **Fig. 4.17**. Compared with the estimation from travel time inversion (**Fig. 4.9**) and the reference permeability model (**Fig. 4.3**), we can see that more details of permeability distribution have been recovered. In particular, the image of the high permeability region at the northeastern portion of the model is improved, although the magnitude of estimated permeability in this region is still lower than that of the reference model.

Fig. 4.18 shows the root mean squared errors of travel time and pressure during the iterations of the inversion. Again, we can see that the alternation of travel time match and pressure match helps the minimization to reach the global minimum.

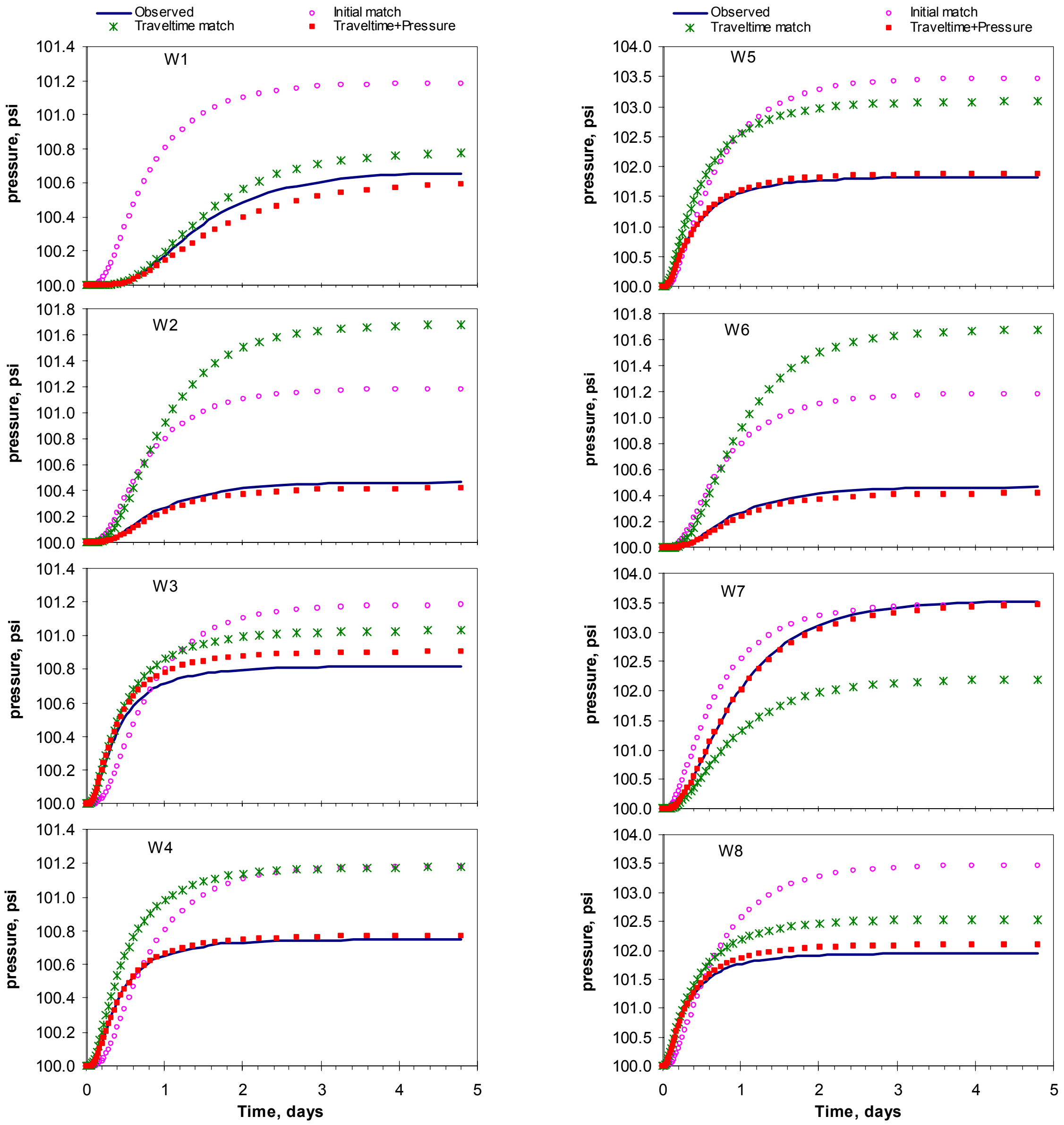

Figure 4.16—Pressure matching from alternating travel time/pressure inversion.

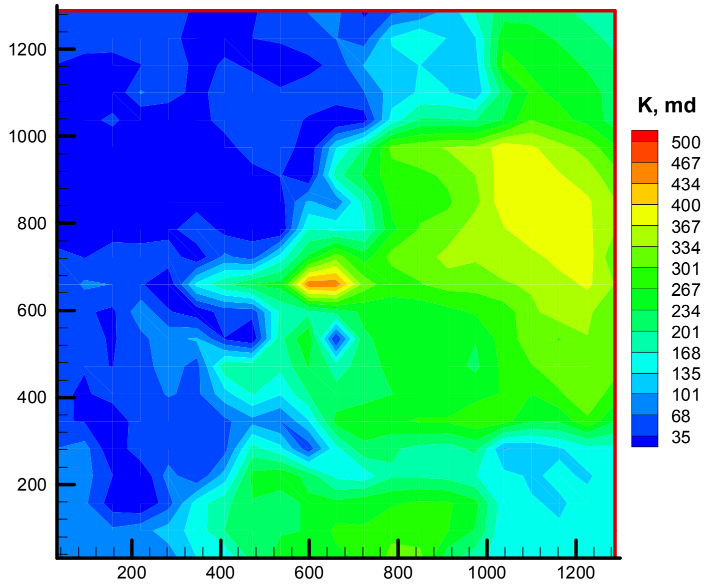

Figure 4.17—Estimated permeability distribution from alternating travel time/pressure inversion.

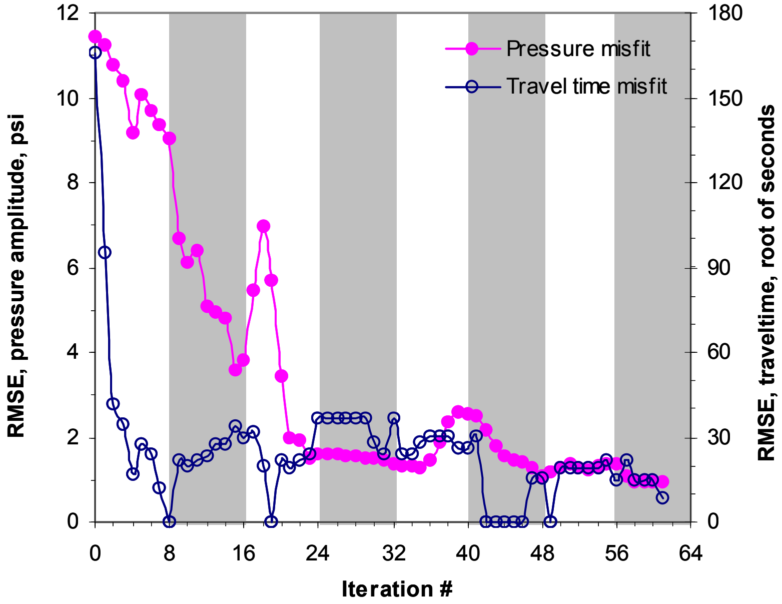

Figure 4.18—Root mean squared errors of travel time and pressure in the alternating inversion of travel time and pressure (shadow indicates pressure match).

4.3 Asymptotic Solution for Compressible Flow

Asymptotic approach has been extensively used in the study of electromagnetic and seismic wave propagation.[64,65] The asymptotic solution involves properties of the wave front and ray paths of the wave propagation.[64] Many of the concepts such as rays and propagating interfaces or discontinuities have direct counterparts in hydrology and petroleum engineering.[66,67] The approach has also been extended to the propagation problems with diffusive components,[36,62] and proved valuable in the analysis of front propagation in general. Recently, the asymptotic approach has been generalized to solve the transient pressure problem.[18,35-36] Based on the asymptotic solution, the streamline approach has been extended to compressible flows by deriving the concept of a 'diffusive' time of flight.[18, 35] A key advantage of the asymptotic solutions is that by utilizing these solutions the sensitivities required for inverse modeling can often be formulated analytically.[35-36] In this section, we briefly discuss the asymptotic solution of the pressure diffusivity equation, and the associated concepts of streamline 'diffusive' time of flight and zero-order approximation of the asymptotic solution. In the next section, we will use these concepts to derive analytical methods for computing the sensitivities of travel time, peak amplitude and pressure.

The diffusivity equation, governing the transient pressure behavior in a heterogeneous permeable media, is given as

$$\phi(\mathbf{x})\mu c_t \frac{\partial P(\mathbf{x},t)}{\partial t} - \nabla \cdot \left(k(\mathbf{x})\nabla P(\mathbf{x},t)\right) = 0 \qquad (4.1)$$

where $P(x,t)$ represents pressure, $\phi(x)$ denotes porosity, $k(x)$ denotes permeability, μ and c_t represent fluid viscosity and total compressibility, respectively.

We can consider the diffusivity equation in the frequency domain by applying the Fourier transform

$$\widetilde{P}(\mathbf{x},\omega) = \int_{-\infty}^{\infty} P(\mathbf{x},t)\, e^{-i\omega t} dt \qquad (4.2)$$

The transformed diffusivity equation now becomes

$$\frac{\phi(\mathbf{x})\mu c_t}{k(\mathbf{x})}(-i\omega)\widetilde{P}(\mathbf{x},\omega) - \nabla^2 \widetilde{P}(\mathbf{x},\omega) - \frac{\nabla k(\mathbf{x})}{k(\mathbf{x})}\nabla \widetilde{P}(\mathbf{x},\omega) = 0 \qquad (4.3)$$

Following the asymptotic approach for diffusive phenomenon, if we consider a solution in terms of inverse powers of $\sqrt{-i\omega}$, then asymptotic solution to the above equation can be expressed as the following infinite sum[62]

$$\tilde{P}(\mathbf{x},\omega) = e^{-\sqrt{-i\omega}\,\tau(\mathbf{x})} \sum_{k=0}^{\infty} \frac{A_k(\mathbf{x})}{\left(\sqrt{-i\omega}\right)^k} \tag{4.4}$$

The initial terms of the series are significant since they represent the rapidly varying (high frequency) components of the solution. Thus, we are interested in the zero-order term, which will correspond the propagation of a 'sharp' front (pressure front).

$$\tilde{P}(\mathbf{x},\omega) = e^{-\sqrt{i\omega}\,\tau(\mathbf{x})} A_0(\mathbf{x}) \tag{4.5}$$

Substituting Eq. 4.5 into Eq. 4.4 and equating the coefficients of different powers of $\sqrt{-i\omega}$, we will obtain a series of differential equations for $\tau(\mathbf{x})$ and $A_k(\mathbf{x})$.[36, 62-63] For the high frequency approximation (Eq. 4.5), the highest order, $\left(\sqrt{-i\omega}\right)^2$ corresponds to the equation associated with $\tau(\mathbf{x})$ and the order $\sqrt{-i\omega}$ corresponds to the equation associated with $A_o(\mathbf{x})$ as shown below:

$$\left(\sqrt{-i\omega}\right)^2: \quad \alpha(\mathbf{x})\left(\nabla\tau(\mathbf{x})\right)^2 = 1\,. \tag{4.6}$$

$$\left(\sqrt{-i\omega}\right): \quad A_o(\mathbf{x})\nabla^2\tau(\mathbf{x}) + 2\nabla A_o(\mathbf{x}) \bullet \nabla\tau(\mathbf{x}) + A_o(\mathbf{x})\frac{\nabla k(\mathbf{x})}{k(\mathbf{x})} \bullet \nabla\tau(\mathbf{x}) = 0 \tag{4.7}$$

where α is the diffusivity,

$$\alpha(\mathbf{x}) = \frac{k(\mathbf{x})}{\phi(\mathbf{x})\mu c_t}\,. \tag{4.8}$$

4.3.1 Streamline 'Diffusive' Time of Flight

Eq. 4.6 has the form of the eikonal equation, which governs many types of propagation processes.[64] It relates the pseudophase function which describe the propagation of the wave front to reservoir properties contained in the diffusivity. It can also be written as

$$\sqrt{\alpha(\mathbf{x})}\ \left\| \nabla \tau(\mathbf{x}) \right\| = 1 \tag{4.9}$$

Comparing with the streamline time of flight equation for a propagating tracer front,

$$\mathbf{v}(\mathbf{x}) \bullet \nabla \tilde{\tau}(\mathbf{x}) = 1 \tag{4.10}$$

where $\mathbf{v}(\mathbf{x})$ is the interstitial velocity and is the tracer time of flight for incompressible flow,[20,50] we can see that they have the same form. Thus the pressure front propagates with a velocity of $\sqrt{\alpha(\mathbf{x})}$. We can now define a time of flight for diffusive or compressible flow along streamlines as follows[18, 35]

$$\tau(\mathbf{x}) = \int_{\Sigma} \frac{ds}{\sqrt{\alpha(\mathbf{x})}} \tag{4.11}$$

where $\sum$ refers to a streamline and s is distance along the streamline. Note that the 'diffusive' time of flight will have units of square root of time, which is consistent with the scaling behavior of diffusive flow.

The physical significance of the 'diffusive' time of flight can be realized by examining the time domain solution to the zero-order asymptotic expansion for an impulse source, which is the inverse Fourier transform of Eq. 4.7. [62]

$$P(t) = A_0(\mathbf{x}) \frac{\tau(\mathbf{x})}{2\sqrt{\pi t^3}} \exp\left(-\frac{\tau^2(\mathbf{x})}{4t} \right) \tag{4.12}$$

At a fix position x, the pressure response will be maximized when its temporal derivative is zero

$$\frac{\partial P(t)}{\partial t} = 0 = A_0(\mathbf{x}) \frac{\tau(\mathbf{x})}{2\sqrt{\pi}} \exp\left(-\frac{\tau^2(\mathbf{x})}{4t} \right) \left[-\frac{3}{2\sqrt{t^5}} + \frac{\tau^2(\mathbf{x})}{4\sqrt{t^7}} \right] \tag{4.13}$$

This results the following relationship between the observed time and the diffusive time of flight

$$t_{\max} = \frac{\tau^2(\mathbf{x})}{6} \tag{4.14}$$

This indicates that for an impulse source, the peak of pressure response (pressure drawdown or buildup) appears at the time $\tau^2(\mathbf{x})/6$ at the position $\mathbf{x}$. The surface of constant $\tau(\mathbf{x})$ represents the spatial positions of the peak pressure response at time $\tau^2(\mathbf{x})/6$. Therefore, $\tau(\mathbf{x})$ is associated with the propagating front of the maximum pressure drawdown or buildup for an impulse source or sink.[18, 35]

As an illustration, we consider a well producing in a heterogeneous permeability media, shown in **Fig. 4.19**. The well is located at the center of the model. Based on Eq. 4.11, we compute the diffusive time of flight along the streamlines. **Fig. 4.20** shows the streamlines associated with the heterogeneous media. **Fig. 4.21** shows the calculated diffusive time of flight distribution. For comparison purpose, we also show the tracer time-of-flight (**Fig. 4.22**); it is clear that the pressure front propagates much faster than tracer front, as might be expected for diffusive transport.

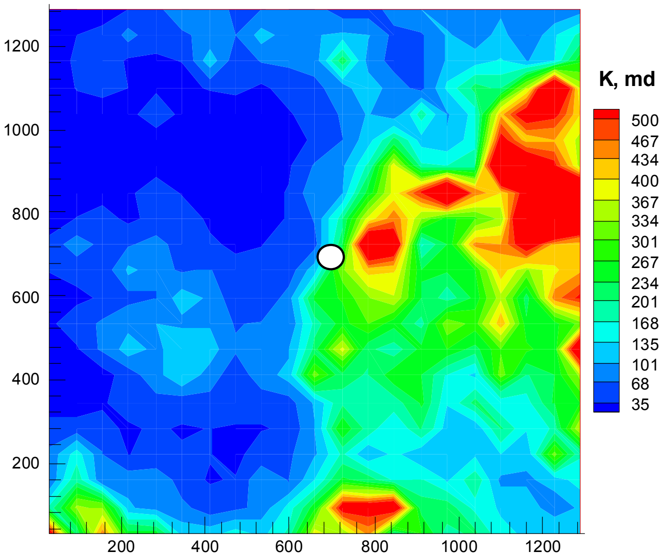

Figure 4.19—The heterogeneous permeability field used in an illustration.

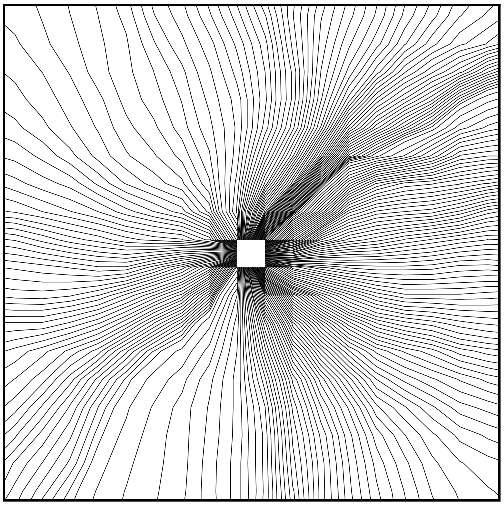

Figure 4.20—Streamlines corresponding to the heterogeneous media in Fig. 4.19.

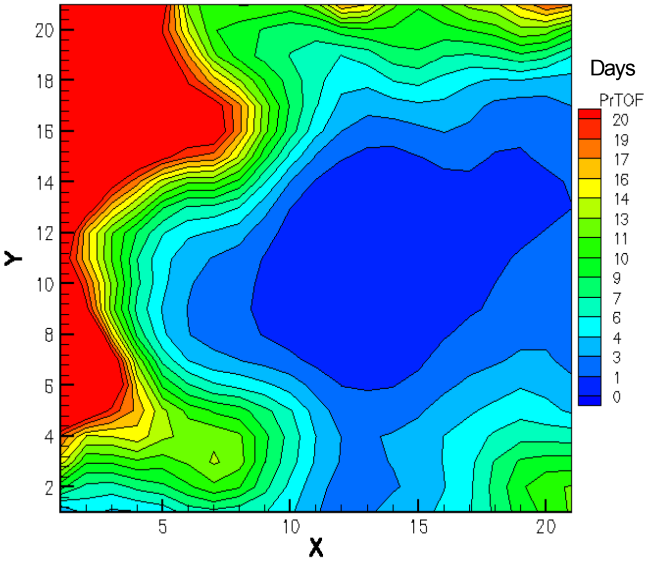

Figure 4.21—Pressure front in the heterogeneous media in Fig. 4.19.

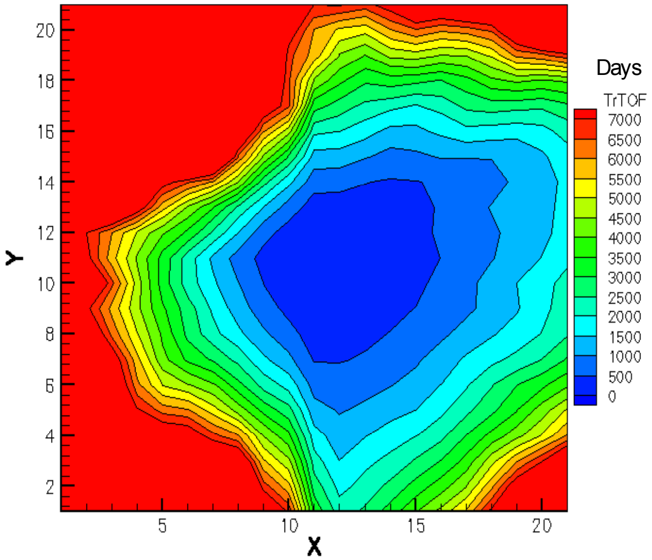

Figure 4.22—Tracer front in the heterogeneous media in Fig. 4.19.

The concept of diffusive time of flight is closely related to the drainage radius or drainage area during primary recovery or compressible flow.[18,35] It has been shown that for a homogeneous media, the contour of diffusive time of flight is identical to the location of radius of investigation or radius of drainage. Since the concept of diffusive time of flight is derived from the most general conditions (3D and heterogeneous media), we can easily define the radius of drainage or drainage volume for any arbitrary heterogeneous media by calculating the diffusive time of flight. In the next chapter, we will use it to compute the drainage volume from reservoir models for identification of reservoir compartmentalization using primary production data.

4.3.2 Zero-order Asymptotic Solution

To obtain the zero-order solution, we need to further determine $A_o(x)$ by solving Eq. 4.7, which is again given below:

$$A_o(\mathbf{x})\nabla^2\tau(\mathbf{x}) + 2\nabla A_o(\mathbf{x}) \bullet \nabla\tau(\mathbf{x}) + A_o(\mathbf{x})\frac{\nabla k(\mathbf{x})}{k(\mathbf{x})} \bullet \nabla\tau(\mathbf{x}) = 0 \qquad (4.7)$$

For an impulse source, the solution of this equation was developed[36,62] as follows

$$A_o(s) = A_o(s_o)\sqrt{\frac{k(s_o)}{k(s)}}\sqrt{\sqrt{\frac{\alpha(s)}{\alpha(s_o)}}}\sqrt{\frac{J(s_o)}{J(s)}} \tag{4.15}$$

where $A_o(s_o)$ is the initial pressure amplitude at the source, and $J(s)$ is the Jacobian which defines the pressure front surface perpendicular to the streamline with two coordinates ξ and η associated with the curvilinear coordinate s,[36,62,68] e.g.

$$J(s) = \frac{\partial(x,y,z)}{\partial(\xi,\eta,s)} = \begin{vmatrix} \frac{\partial x}{\partial \xi} & \frac{\partial x}{\partial \eta} & \frac{\partial x}{\partial s} \\ \frac{\partial y}{\partial \xi} & \frac{\partial y}{\partial \eta} & \frac{\partial y}{\partial s} \\ \frac{\partial z}{\partial \xi} & \frac{\partial z}{\partial \eta} & \frac{\partial z}{\partial s} \end{vmatrix} \tag{4.16}$$

It measures the expansion of the pressure front along the streamlines.[36] Eq. 4.15 gives the evolution of the amplitude along the streamline.[36]

Substituting Eq. 4.15 into Eq. 4.12, we can write the zero-order asymptotic solution in time domain as

$$P(s,t) = A_o(s_o)\sqrt{\frac{k(s_o)}{k(s)}}\sqrt{\sqrt{\frac{\alpha(s)}{\alpha(s_o)}}}\sqrt{\frac{J(s_o)}{J(s)}}\frac{\tau(s)}{2\sqrt{\pi t^3}}\exp\left(-\frac{\tau^2(s)}{4t}\right) \tag{4.17}$$

This asymptotic solution provides an approximate solution of pressure response for an impulse source in a 3D heterogeneous medium. For a 3D homogeneous medium, it turns out to be the exact solution.[62] The exact solution of pressure response for an impulse source with a strength of $4\pi\delta(\mathbf{x}-\mathbf{x}_o)$ in a 3D homogeneous media is given as[69-70]

$$P(\mathbf{x},t) = \frac{1}{2\sqrt{\pi\alpha t^3}}\exp\left(-\frac{R^2(\mathbf{x},\mathbf{x}_o)}{4\alpha t}\right) \tag{4.18}$$

where $R(\mathbf{x})$ is the distance between the source and the point $\mathbf{x}$. In a homogeneous media, $\alpha(\mathbf{x})$ becomes a constant α. Since the path of the pressure front propagation is a straight line in a homogeneous media, $\tau(\mathbf{x},\mathbf{x}_o) = R(\mathbf{x},\mathbf{x}_o)/\sqrt{\alpha}$, therefore, Eq. 4.18 can be rewritten as

$$P(\mathbf{x},t)=\frac{1}{R(\mathbf{x},\mathbf{x}_o)}\frac{\tau(\mathbf{x},\mathbf{x}_o)}{2\sqrt{\pi t^3}}\exp\left(-\frac{\tau^2(\mathbf{x},\mathbf{x}_o)}{4t}\right) \tag{4.19}$$

On the other hand, $k(s)=k(s_o)$, $\alpha(s)=\alpha(s_o)$ and the Jacobian is equal to $R^2(s)$ in a 3D homogeneous media,[68] so Eq. 4.17 can be reduced to

$$P(s,t)=\frac{A_o(s_o)}{R(s)}\frac{\tau(s)}{2\sqrt{\pi t^3}}\exp\left(-\frac{\tau^2(s)}{4t}\right) \tag{4.20}$$

We can see that Eq. 4.19 and Eq. 4.20 have the exact same form, except Eq. 4.20 has a source with the strength to be $4\pi A_o(s_o)\delta(s-s_o)$.

The above analysis naturally leads to the Green's function for a 3D heterogeneous media

$$G(s,t)=\sqrt{\frac{k(s_o)}{k(s)}}\sqrt{\sqrt{\frac{\alpha(s)}{\alpha(s_o)}}}\sqrt{\frac{J(s_o)}{J(s)}}\frac{\tau(s)}{2\sqrt{\pi t^3}}\exp\left(-\frac{\tau^2(s)}{4t}\right) \tag{4.21}$$

which is the solution of the following equation

$$\frac{\phi(\mathbf{x})\mu c_t}{k(\mathbf{x})}(-i\omega)\widetilde{P}(\mathbf{x},\omega)-\nabla^2\widetilde{P}(\mathbf{x},\omega)-\frac{\nabla k(\mathbf{x})}{k(\mathbf{x})}\nabla\widetilde{P}(\mathbf{x},\omega)=4\pi\delta(\mathbf{x}-\mathbf{x_o}) \tag{4.22}$$

In general, the streamlines associated with the paths of pressure front propagation are curves in a 3D heterogeneous media, but if we assume the paths are straight lines, Eq. 4.21 can be greatly simplified to produce an approximate Green's function

$$G(\mathbf{x},t)=\sqrt{\frac{k(\mathbf{x}_o)}{k(\mathbf{x})}}\sqrt{\sqrt{\frac{\alpha(\mathbf{x})}{\alpha(\mathbf{x}_o)}}}\frac{1}{2\sqrt{\pi\overline{\alpha}(\mathbf{x},\mathbf{x}_o)t^3}}\exp\left(-\frac{R^2(\mathbf{x},\mathbf{x}_o)}{4\overline{\alpha}(\mathbf{x},\mathbf{x}_o)t}\right) \tag{4.23}$$

where $\overline{\alpha}(\mathbf{x},\mathbf{x}_o)$ is the harmonic average of diffusivity along the straight line between **x** and source point **x₀**. Similarly, for a 2D heterogeneous case, the Green's function can be approximated as

$$G(\mathbf{x},t)=\sqrt{\frac{k(\mathbf{x}_o)}{k(\mathbf{x})}}\sqrt{\sqrt{\frac{\alpha(\mathbf{x})}{\alpha(\mathbf{x}_o)}}}\frac{1}{\sqrt{\overline{\alpha}(\mathbf{x},\mathbf{x}_o)t}}\exp\left(-\frac{R^2(\mathbf{x},\mathbf{x}_o)}{4\overline{\alpha}(\mathbf{x},\mathbf{x}_o)t}\right) \tag{4.24}$$

Eqs. 4.23 and 4.24 are very useful since for a general source, such as a time variant source, the pressure solution can be obtained by convolving the Green's function solution with this time variant source. In the next section, we will use this approximate Green's function to derive analytical formalism for the sensitivity of transient pressure response.

4.4 Sensitivity Computation

Using the 'diffusive' time of flight and the zero-order asymptotic solution, we will develop analytical formalism to compute the sensitivities for pressure front travel time, peak amplitude and pressure in this section. Although we give out the sensitivities to both permeability and porosity, we only use the sensitivities to permeability in our inversion since we assume that the porosity field is known and focus on estimating the permeability distribution.

4.4.1 Sensitivity of Travel-time of Pressure Front

In the previous section, we have shown that the diffusive time of flight is related to the arrival time of the maximum pressure drawdown or buildup for an impulse source or sink. This time of flight was found to be a function of reservoir properties along the streamline. Combining Eq. 4.8, Eq. 4.11 and Eq. 4.14, we get an equation relating the observed time to reservoir properties,[35,36]

$$\sqrt{t_{\max}} = \frac{1}{\sqrt{6}} \int \sqrt{\frac{\phi(\mathbf{x})\mu c_t}{k(\mathbf{x})}}\, ds \tag{4.25}$$

where s is the distance along the streamline. The integrand in Eq. 4.25 is a function of permeability and porosity,

$$\sqrt{\frac{\phi(\mathbf{x})\mu c_t}{k(\mathbf{x})}} = f(k, \phi) \tag{4.26}$$

If we assume that small perturbations of reservoir properties do not shift the streamlines, we can formulate the change in arrival time because of small perturbations of reservoir properties as follows

$$\delta\sqrt{t_{\max}} = \frac{1}{\sqrt{6}} \int \left(\frac{\partial f}{\partial k} dk + \frac{\partial f}{\partial \phi} d\phi \right) ds \tag{4.27}$$

where

$$\frac{\partial f}{\partial k(x)} = -\frac{1}{2}\frac{\sqrt{\phi(\mathbf{x})\mu c_t}}{k(\mathbf{x})\sqrt{k(\mathbf{x})}} = -\frac{1}{2}\frac{f(k,\phi)}{k(\mathbf{x})} \tag{4.28}$$

and

$$\frac{\partial f}{\phi(x)} = \frac{1}{2}\frac{\sqrt{\mu c_t}}{\sqrt{\phi(\mathbf{x})k(\mathbf{x})}} = \frac{1}{2}\frac{f(k,\phi)}{\phi(\mathbf{x})} \tag{4.29}$$

Therefore, the travel time sensitivities can be formulated as

$$\frac{\partial\sqrt{t_{\max}}}{\partial k_j(x)} = -\frac{1}{2\sqrt{6}}\frac{f(k_j,\phi_j)}{k_j(\mathbf{x})}\delta s_j \tag{4.30}$$

$$\frac{\partial\sqrt{t_{\max}}}{\partial \phi_j(x)} = -\frac{1}{2\sqrt{6}}\frac{f(k_j,\phi_j)}{\phi_j(\mathbf{x})}\delta s_j \tag{4.31}$$

where j represents the cell that streamline passes through and δs_j is the length of streamline trajectory in cell j. The above sensitivities are evaluated analytically after a single streamline simulation. This can lead to substantial savings in computation time during the inversion process.

4.4.2 Peak Amplitude Sensitivity

As discussed previously, the pressure solution for an impulse source can be approximated with the zero-order term of the asymptotic solution.

$$P(t) = A_0(\mathbf{x})\frac{\tau(\mathbf{x})}{2\sqrt{\pi t^3}}\exp\left(-\frac{\tau^2(\mathbf{x})}{4t}\right) \tag{4.12}$$

Since the peak pressure response occurs at time, $t = \tau^2(\mathbf{x})/6$, the peak amplitude can be easily found as

$$P_{\max}(t) = A_0(x)\frac{6\sqrt{6}}{2\sqrt{\pi}}\frac{e^{-6/4}}{\tau^2(x)} = A_0(x)\frac{\sqrt{6}}{2\sqrt{\pi}}\frac{e^{-6/4}}{t_{\max}} \tag{4.32}$$

Again, assuming that small perturbations of reservoir properties do not shift the streamline, and do not affect A_o, we can get

$$\frac{\partial P_{\max}}{\partial k_j} = A_0(x)\frac{6\sqrt{6}}{\sqrt{\pi}}\frac{e^{-6/4}}{\tau^3(x)}\frac{\partial \tau}{\partial k_j} = A_0(x)\frac{\sqrt{6}}{\sqrt{\pi}}\frac{e^{-6/4}}{t_{\max}^{3/2}}\frac{\partial\sqrt{t_{\max}}}{\partial k_j} \tag{4.33}$$

$$\frac{\partial P_{\max}}{\partial \phi_j} = A_0(x)\frac{6\sqrt{6}}{\sqrt{\pi}}\frac{e^{-6/4}}{\tau^3(x)}\frac{\partial \tau}{\partial \phi_j} = A_0(x)\frac{\sqrt{6}}{\sqrt{\pi}}\frac{e^{-6/4}}{t_{\max}^{3/2}}\frac{\partial\sqrt{t_{\max}}}{\partial \phi_j} \tag{4.34}$$

The travel time sensitivities can be obtained from the previous section, and A_o and $t_{\max}$ are readily available from the simulated pressure responses. Thus, the above sensitivities can also be evaluated analytically after a single forward simulation.

For a step function source that we usually have in practice, we simply differentiate the simulated pressure responses with respect to time to obtain the impulse response. Then the pressure temporal derivatives can be used in the above equations. The arrival time, $t_{\max}$, is determined as the time corresponding to the peak derivative, and the amplitude term A_o is determined with Eq. 4.32 using the peak amplitude. For example, in **Fig. 4.23**, we show a simulated pressure time derivative of an observing well. By fitting the simulated derivative responses with Eq. 4.12, we determine the values of $t_{\max}$ and A_o, as shown in the figure.

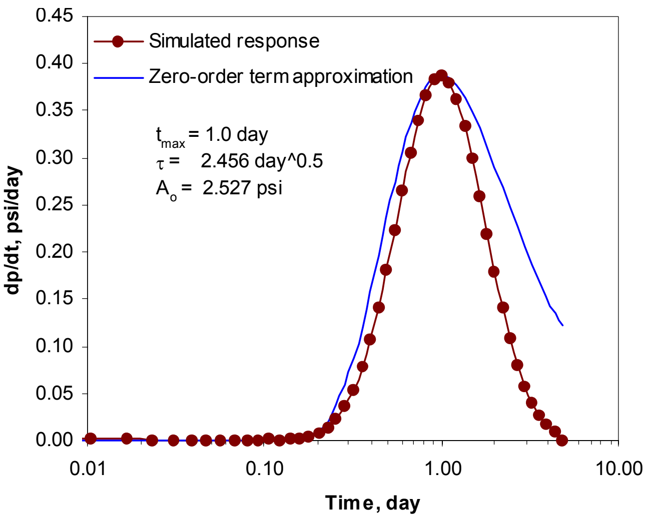

Figure 4.23—Zero-order approximation of the simulated pressure derivative responses.

4.4.3 Pressure Sensitivity

As shown before, the diffusivity equation, governing the transient pressure behavior in a heterogeneous permeable media, is given as

$$\phi(\mathbf{x})\mu c_t \frac{\partial P(\mathbf{x},t)}{\partial t} - \nabla\cdot\left(k(\mathbf{x})\nabla P(\mathbf{x},t)\right) = 0 \tag{4.35}$$

If the permeability is perturbed by $\delta k(\mathbf{x})$, the diffusivity equation becomes

$$\phi(\mathbf{x})\mu c_t \frac{\partial\left(P(\mathbf{x},t)+\delta P(\mathbf{x},t)\right)}{\partial t} - \nabla\cdot\left(\left(k(\mathbf{x})+\delta k(\mathbf{x})\right)\nabla\left(P(\mathbf{x},t)+\delta P(\mathbf{x},t)\right)\right) = 0 \tag{4.36}$$

Subtracting Eq. 4.35 from Eq. 4.36, we come up with the diffusivity equation for pressure perturbation

$$\phi(\mathbf{x})\mu c_t \frac{\partial \delta P(\mathbf{x},t)}{\partial t} - \nabla\cdot\left(k(\mathbf{x})\nabla\delta P(\mathbf{x},t)\right) - \nabla\cdot\left(\delta k(\mathbf{x})\nabla\left(P(\mathbf{x},t)+\delta P(\mathbf{x},t)\right)\right) = 0 \tag{4.37}$$

Neglecting the second order term, we have an approximation as follows,

$$\phi(\mathbf{x})\mu c_t \frac{\partial \delta P(\mathbf{x},t)}{\partial t} - \nabla\cdot\left(k(\mathbf{x})\nabla\delta P(\mathbf{x},t)\right) - \nabla\cdot\left(\delta k(\mathbf{x})\nabla P(\mathbf{x},t)\right) = 0 \tag{4.38}$$

Note that the first two terms have the same form as the original diffusivity equation for pressure (Eq. 4.35). If we just perturb the permeability at a specific point $\boldsymbol{x}_i$, e.g., a single cell in finite-difference simulation, Eq. 4.38 can be rewritten as

$$\phi(\mathbf{x})\mu c_t \frac{\partial \delta P(\mathbf{x},t)}{\partial t} - \nabla\cdot\left(k(\mathbf{x})\nabla\delta P(\mathbf{x},t)\right) = \nabla\cdot\left(\delta k(\mathbf{x})\nabla P(\mathbf{x},t)\right)\delta(\mathbf{x}-\mathbf{x}_i) \tag{4.39}$$

This equation indicates that perturbing the permeability at a point is equivalent to introducing a source at this point, with the source strength related to the divergence of pressure solution of the original problem. Similarly, if we perturb the porosity at a specific point $\boldsymbol{x}_i$, we can come up with the following equation

$$\phi(\mathbf{x})\mu c_t \frac{\partial \delta P(\mathbf{x},t)}{\partial t} - \nabla\cdot\left(k(\mathbf{x})\nabla\delta P(\mathbf{x},t)\right) = -\delta\phi(\mathbf{x})\mu c_t \frac{\partial P(\mathbf{x},t)}{\partial t}\delta(\mathbf{x}-\mathbf{x}_i) \tag{4.40}$$

The solution of Eq. 4.39 or Eq. 4.40 can be analytically formulated by convolving the source with the Green's function[69,70]

$$\delta P(\mathbf{x},t) = \int_0^t q_i(t) G(x - x_i, t - \tau) d\tau + \sum_{\partial\Omega_j} \int_0^t \left(G \frac{\partial \delta P}{\partial n_j} - \delta P \frac{\partial G}{\partial n_j} \right) d\tau \tag{4.41}$$

where $\partial\Omega_j$ denotes the boundary sections of the reservoir domain, n represent the outer normal direction of the boundary section, and the Green's function is the solution of the following equation

$$\phi(\mathbf{x}) \mu c_t \frac{\partial \delta P(\mathbf{x},t)}{\partial t} - \nabla \cdot \left(k(\mathbf{x}) \nabla \delta P(\mathbf{x},t) \right) = 4\pi \delta(\mathbf{x} - \mathbf{x}_i, t - 0) \tag{4.42}$$

and

$$q_i(t) = \frac{1}{4\pi} \nabla \cdot \left(\delta k(\mathbf{x}_i) \nabla P(\mathbf{x},t) \right) \qquad \textit{for} \quad \textit{Eq}.4.39 \tag{4.43}$$

$$q_i(t) = -\frac{1}{4\pi} \delta\phi(\mathbf{x}_i) \mu c_t \frac{\partial P(\mathbf{x},t)}{\partial t} \qquad \textit{for} \quad \textit{Eq}.4.40 \tag{4.44}$$

The summation terms in Eq. 4.41 account for the boundary conditions. If the reservoir is infinite, these terms vanish. Neglecting the boundary effects, Eq. 4.41 is simplified as

$$\delta P(\mathbf{x},t) = \int_0^t q_i(t) G(x - x_i, t - \tau) d\tau \tag{4.45}$$

Note that the source terms in Eq. 4.43 and Eq. 4.44 are associated with the pressure solutions of the original problem. They can be easily obtained using the simulated grid pressures from the forward simulation. Thus, the pressure sensitivities can be evaluated analytically using a single forward simulation if we know the Green's function. However here G is the Green's function in a heterogeneous media. In general, the Green's function is problem-specified (the flow media, boundary conditions etc.). Although many Green's functions for homogeneous medium are available in the literature, they are usually not applicable to heterogeneous media. Fortunately, in the previous section, we have developed an approximate Green's function solution for a heterogeneous media using the zero-order asymptotic solution.

$$G(\mathbf{x},t)=\sqrt{\frac{K(\mathbf{x}_o)}{K(\mathbf{x})}}\sqrt{\sqrt{\frac{\alpha(\mathbf{x})}{\alpha(\mathbf{x}_o)}}}\frac{1}{2\sqrt{\pi\bar{\alpha}(\mathbf{x},\mathbf{x}_o)t^3}}\exp\left(-\frac{R^2(\mathbf{x},\mathbf{x}_o)}{4\bar{\alpha}(\mathbf{x},\mathbf{x}_o)t}\right) \tag{4.23}$$

As discussed in previous section, we derived this approximation by assuming that the pressure fronts propagate along straight lines. It is applicable to a 3D infinite media. For a 2D heterogeneous case, the approximate Green's function is

$$G(\mathbf{x},t)=\sqrt{\frac{K(\mathbf{x}_o)}{K(\mathbf{x})}}\sqrt{\sqrt{\frac{\alpha(\mathbf{x})}{\alpha(\mathbf{x}_o)}}}\frac{1}{\sqrt{\bar{\alpha}(\mathbf{x},\mathbf{x}_o)t}}\exp\left(-\frac{R^2(\mathbf{x},\mathbf{x}_o)}{4\bar{\alpha}(\mathbf{x},\mathbf{x}_o)t}\right) \tag{4.24}$$

In order to use Eq. 4.45 to compute the sensitivities, we store the pressure at all grids at each time step in the forward simulation. After the forward simulation is done, we scan each grid to obtain its source terms using Eq. 4.43 and Eq. 4.44 from the simulated grid pressures. We then convolve them with their corresponding Green's function associated with the pair of the perturbing grid and the point of interest (an observation well), so that approximate pressure sensitivities can be obtained from a single forward simulation. As a result, the computation of pressure sensitivities is extremely efficient.

This approach works for porosity sensitivity using the source term defined by Eq. 4.44, but does not produce correct sensitivities for permeability using the source term defined by Eq. 4.43. Since the Green's function is always positive for all the time, and the source term associated with a positive permeability perturbing at the grid is also positive, based on Eq. 4.43, the pressure sensitivity will be always positive. This is just the case shown in **Fig. 4.25**. This source term is for the marked grid (**Fig. 4.24**). It is calculated from the forward simulation of pressure (on a 100 md homogeneous permeability model). Since it has all positive values (**Fig. 4.25**), we should expect positive sensitivities based on Eq.4.43 and Eq. 4.45. However, the numerical perturbation sensitivities demonstrate a distribution with both positive and negative sensitivities (**Fig. 4.26**). We found the reason behind this inconsistency is that the source term associated with permeability perturbations is not a conventional source, but a doublet source.

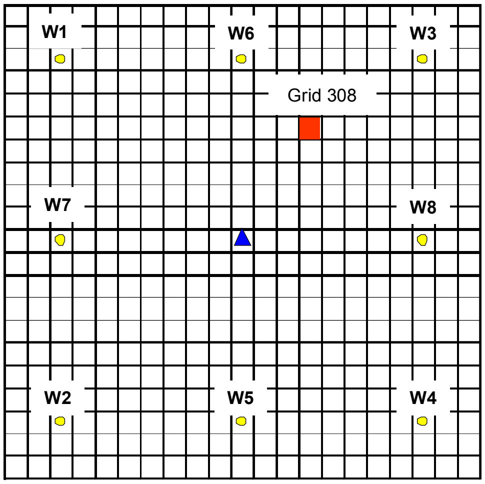

Figure 4.24—The location of source grid (grid 308).

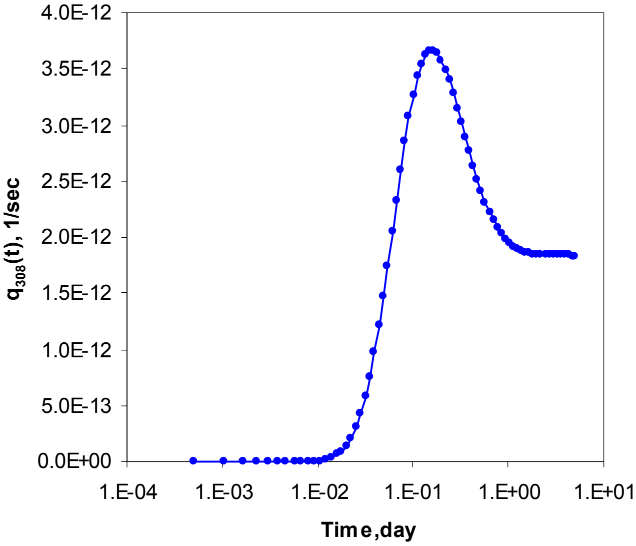

Figure 4.25—Source term associated with the permeability perturbation at the marked grid shown in Fig. 4.24.

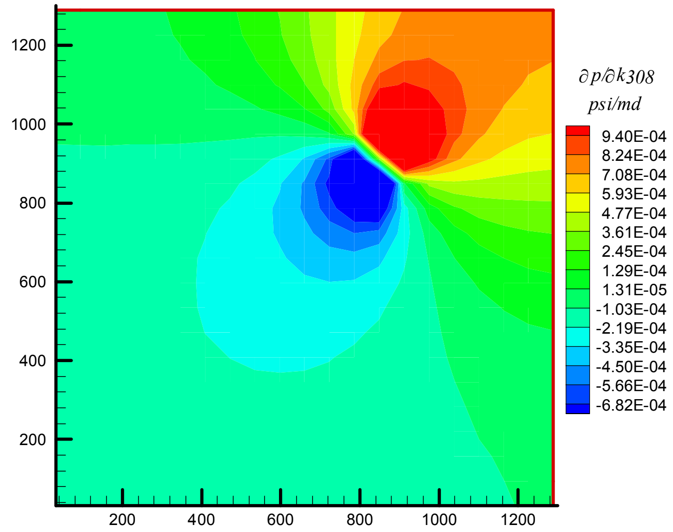

Figure 4.26—Distribution of grid pressure sensitivity (at 5 days) introduced by the permeability perturbation at the marked grid shown in Fig. 4.24.

The concept of a doublet source can be explained with the following example.[69] Let us consider the diffusivity equation in a homogeneous medium

$$\frac{1}{\alpha}\frac{\partial P(x,t)}{\partial t}-\frac{\partial^2 P(x,t)}{\partial x^2}-\frac{\partial^2 P(x,t)}{\partial y^2}-\frac{\partial^2 P(x,t)}{\partial z^2}=0 \tag{4.46}$$

where α is the diffusivity, a constant

$$\alpha=\frac{k}{\phi\mu c_t}$$

We know that

$$P(x,y,z,t)=\frac{Q}{2\sqrt{\pi\alpha t}^{3/2}}e^{-R^2/4\alpha t} \tag{4.47}$$

is a solution of Eq. 4.46, with an instantaneous source of strength $Q/4\pi$ at (x_o, y_o, z_o), and R is the distance between the point (x, y, z) and the source point (x_o, y_o, z_o).

It turns out that

$$-\frac{\partial P}{\partial x}, \qquad or \qquad \frac{Q(x-x_o)}{4(\pi\alpha)^{3/2}t^{5/2}}e^{-R^2/4\alpha t}$$

is also a solution. This solution is a 1D doublet solution of the diffusivity equation, Eq. 4.46, and the source Q is called an instantaneous doublet source along the axis of x.

This solution can be obtained by combining with a source of strength Q' at x_o+dx_o and a sink of strength $-Q'$ at x_o, letting $dx_o \rightarrow 0$ and putting limit $(Q'dx_o) = Q$.

Similarly, we found that a permeability perturbation will introduce a doublet source instead of a conventional source. However, to find an analytical 3D doublet solution is much more difficult, if not impossible. Following the same idea for 1D (combining a conventional source and a conventional sink to come up with a doublet solution), we transform the original source (Eq. 4.43) into multiple sources and sinks. As illustrated in **Fig. 4.27**, we decompose the original source into two sources and two sinks for a 2D problem. For a 3D problem, we will have three sources and three sinks.

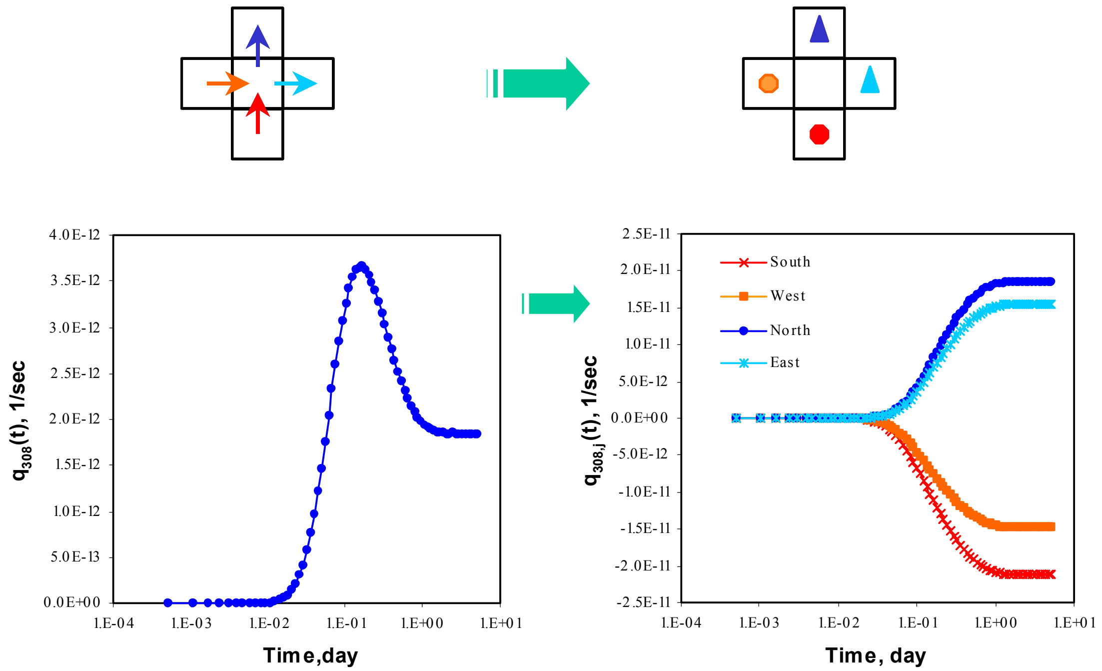

Figure 4.27—Decomposing the source term associated with grid 308 permeability perturbation into multiple source or sink terms.

The diffusivity equation for pressure perturbation now becomes

$$\phi(\mathbf{x})\mu c_t \frac{\partial \delta P(\mathbf{x},t)}{\partial t} - \nabla \cdot \left(k(\mathbf{x})\nabla \delta P(\mathbf{x},t)\right) = \sum_j \frac{A_{i,j}}{V_j} \delta k(\mathbf{x}_i)\nabla P_{i,j}(\mathbf{x}_i,t)\delta(\mathbf{x}-\mathbf{x}_{i,j}) \quad (4.48)$$

where j stands for the surrounding grid blocks of grid i, and the source or sink term for grid j is

$$q_{i,j}(t) = \frac{1}{4\pi}\frac{A_{i,j}}{V_j}\delta k(\mathbf{x}_i)\nabla P_{i,j}(\mathbf{x}_i,t) \quad (4.49)$$

where $A_{i,j}$ is the flow cross-sectional area between grid i and j, Vj is the volume of grid j, and $\nabla P_{i,j}(\mathbf{x}_i,t)$ is the pressure gradient between grid i and j.

We then convolve these sources and sinks with the conventional Green's function solution (Eq. 4.23 or Eq. 4.24) to get the pressure sensitivities (Eq. 4.45).

In the following discussion, we compare our analytical sensitivities with sensitivities produced from the numerical perturbation method. We consider a case of grid size 21×21 with one injection well and one observation well, as shown in **Fig. 4.28**. Our analytical approach requires only a single forward simulation while the numerical perturbation needs (441+1) forward simulations to get the well pressure sensitivities.

We first consider a homogeneous permeability background model with a permeability of 100 md. **Fig. 4.29** shows the pressure responses at the observing well from the background model. **Fig. 4.30** compares the numerical and analytical sensitivities when we perturb the permeability of three grid blocks as indicated in **Fig. 4.28**.

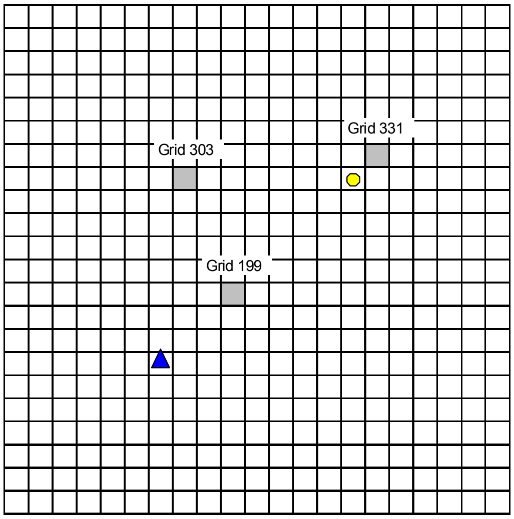

Figure 4.28—Injector and observing well and three perturbing blocks in a 21×21 grid.

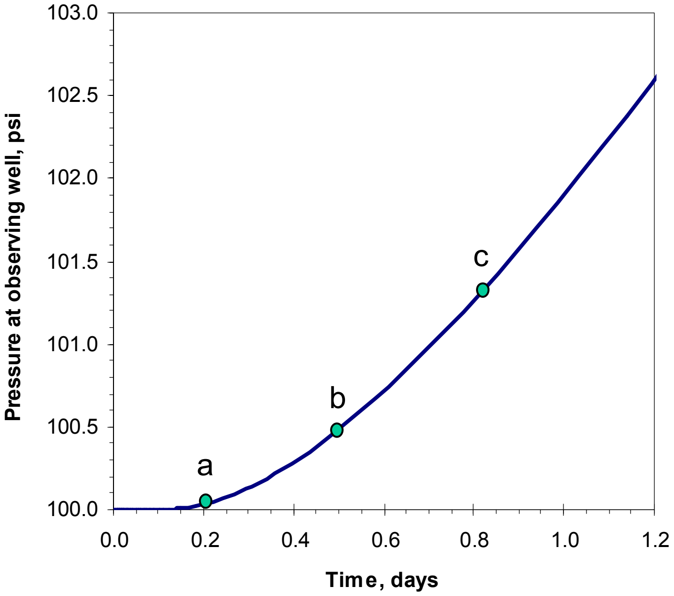

Figure 4.29—Pressure responses at the observing well from the background permeability. Sensitivities at the points a (0.2 day), b (0.5 day), and c (0.82 day) will be calculated.

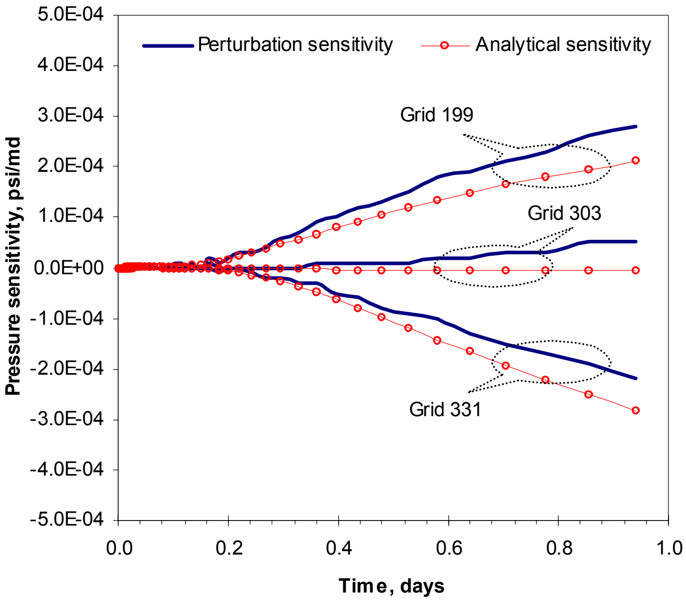

Figure 4.30—Pressure sensitivities to the permeability at the three marked grids.

We can see that there is a good agreement between the numerical and analytical sensitivities. We believe the slight differences are due to the boundary effects since no-flow boundaries are used in the simulation but our analytical formalism neglects the boundary effects. It can be expected that if we move the boundaries far away from the active injection and observation locations, a better agreement would be obtained. In **Fig. 4.31**, the distributions of sensitivities are compared at three different times of 0.2, 0.5 and 0.82 days (**Fig. 4.28**). Again, we can see that the patterns of sensitivities agree quite well although the magnitudes are slightly different.

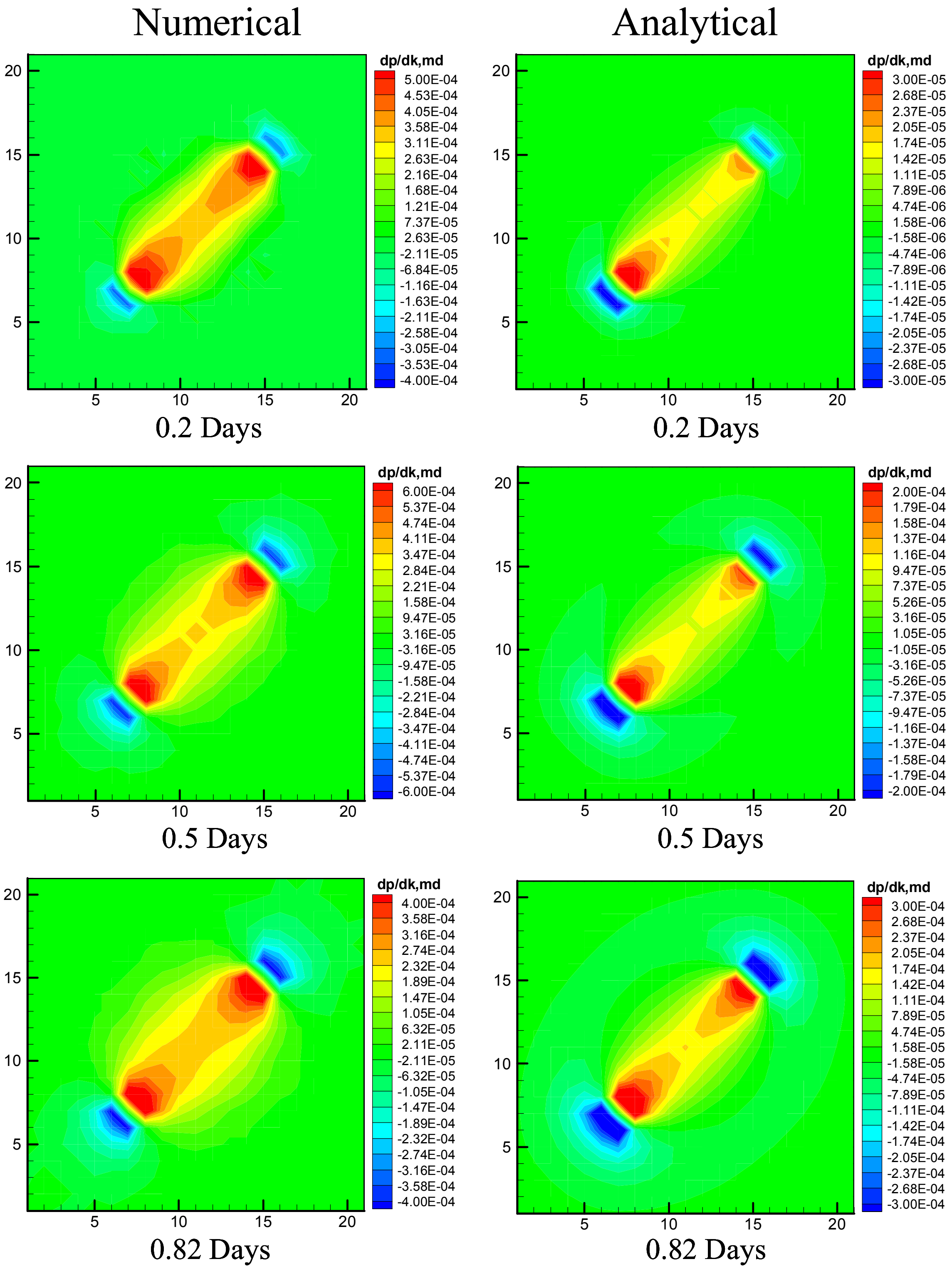

Figure 4.31—Distribution of pressure sensitivity for a homogeneous case.

We also test our approach with a heterogeneous permeability background model (**Fig. 4.32**). **Fig. 4.33** shows a comparison of the sensitivities at 0.2, 0.5 and 0.82 days. We can see that the dominant features of sensitivity distribution have been captured by our analytical sensitivities although the degree of similarity between the numerical and analytical sensitivities is less than that of the homogeneous case. As we discussed previously, our analytical sensitivities are approximate because in our sensitivity computation, we simplify the streamline paths of pressure front propagation in a heterogeneous media as straight lines. Although our analytical sensitivities are not accurate, they are sufficient for their use in the inversion process. Most importantly, our analytical approach for sensitivity computation is extremely computationally efficient since it requires only a single forward simulation; thus it is particularly well suited for integrating transient pressure data into large-scale reservoir models.

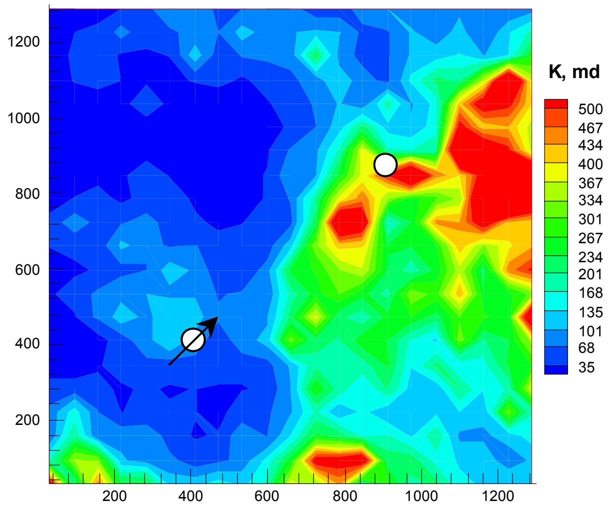

Figure 4.32—The heterogeneous permeability field used for sensitivity comparison.

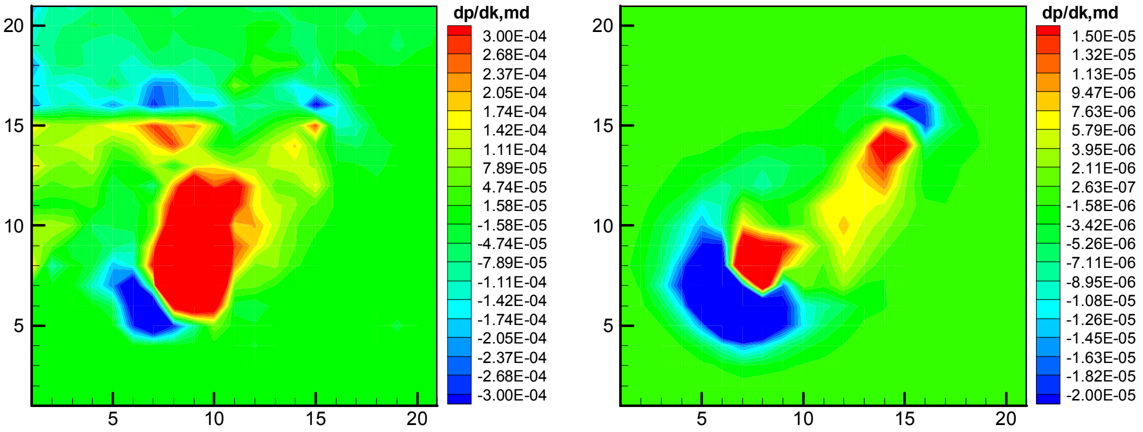
Numerical

Analytical

0.2 Days

0.2 Days

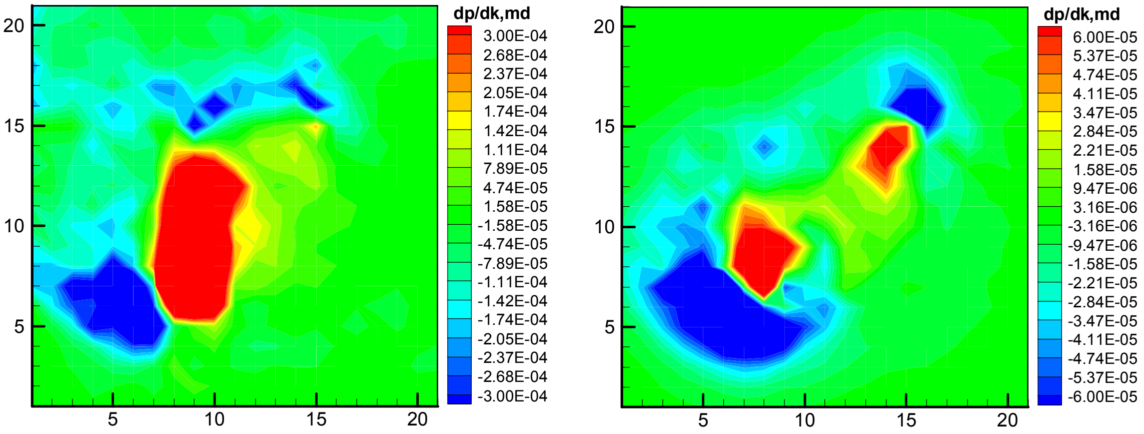

0.5 Days

0.5 Days

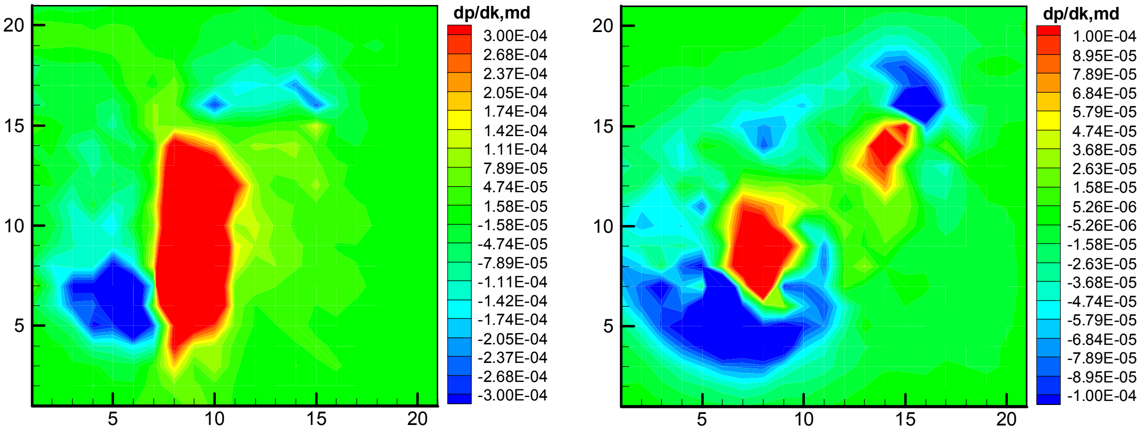

0.82 Days

0.82 Days

Figure 4.33—Distribution of pressure sensitivity for a heterogeneous case.

4.5 Field Application

We now apply our approach to a field example – interference tests at the Conoco Borehole Test Facility in Kay County, Oklahoma. The interference tests were conducted in a skewed 5-spot pattern (consists of the wells GW1 to GW-5 in **Fig. 4.34**). The wells penetrate the Fort Riley formation, which is a naturally fractured limestone, at depths of 10 to 28 meters. The permeability of the limestone itself ranges between 0.11 and 6.06 md with an average value of 1.2 md from laboratory measurements. However, the presence of fractures very likely enhances the formation permeability considerably. The Fort Riley formation contains two orthogonal sets of nearly vertical fractures, with the dominant set striking east-northeast and the less striking fracture in north-northwest[72] (**Fig. 4.35**). To characterize the natural fracture system, a series of field experiments were carried out, including multi-well interference and tracer tests, both cross-well and single-well seismic surveys, and the drilling of a slant well to penetrate the suspected dominant fracture.[71, 72]

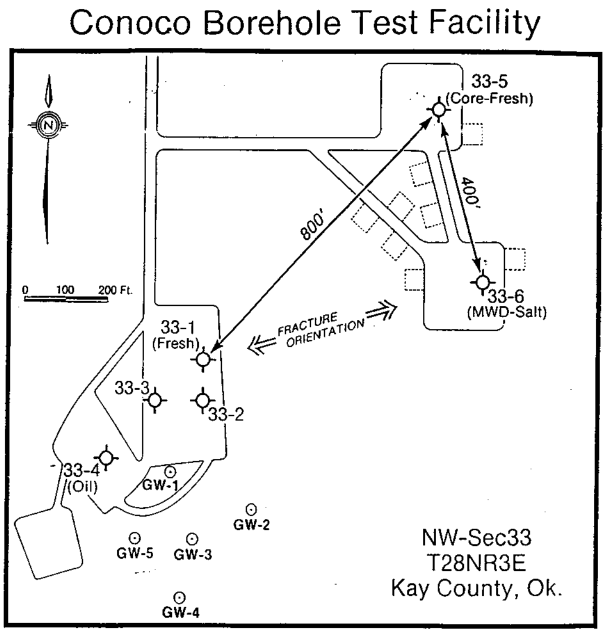

Figure 4.34—Area map, Conoco Borehole Test Facility.

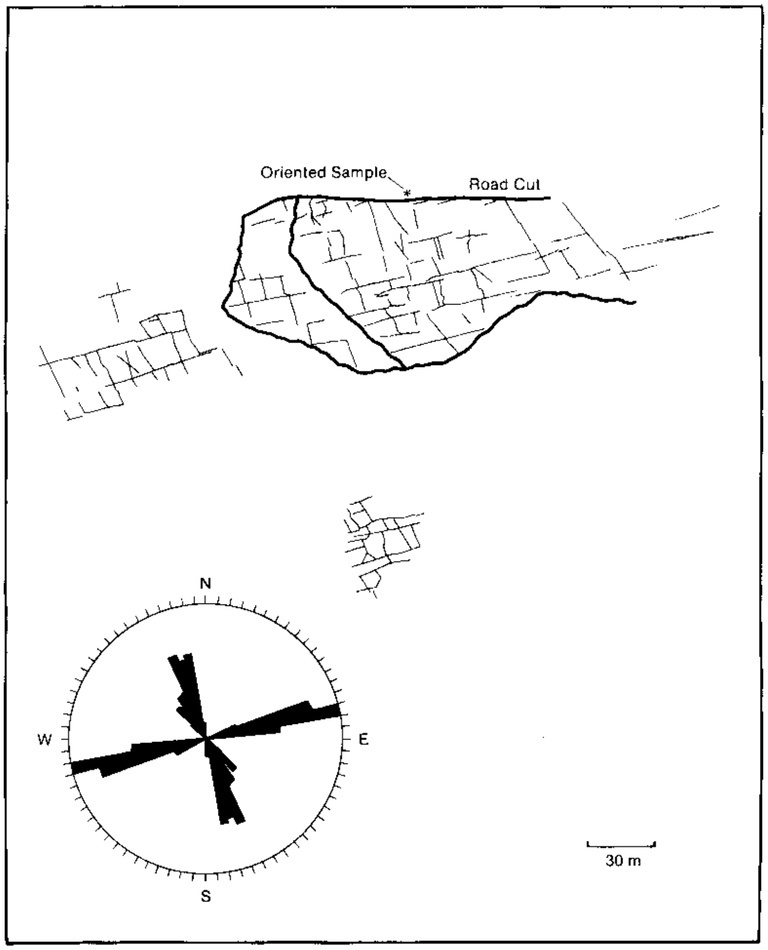

Figure 4.35—Surface fracture pattern mapped at a nearby outcrop.

Two interference tests were performed in the skewed 5-spot pattern consisting of the GW wells. The first test, denoted as Pump 58, involves producing water from well GW-5 and observing pressure responses at wells GW-1 through GW-4. The pumping rate was fairly constant, starting from 0.5 gal/min and dropping `to about 0.46 gal/min by the end of the test.[23] **Fig. 4.36** shows the observed pressure responses at the observing wells during this test. The second test, denoted as Pump 27, involves producing water from well GW-2 and observing pressure responses at wells GW-1, GW-3, GW-4, and GW-5. The pumping rate varied considerably during the test, starting from 0.4 gal/min and gradually decreasing to 0.23 gal/min by the end of test.[23] **Fig. 4.37** shows the observed pressure responses at the observing wells during this test.

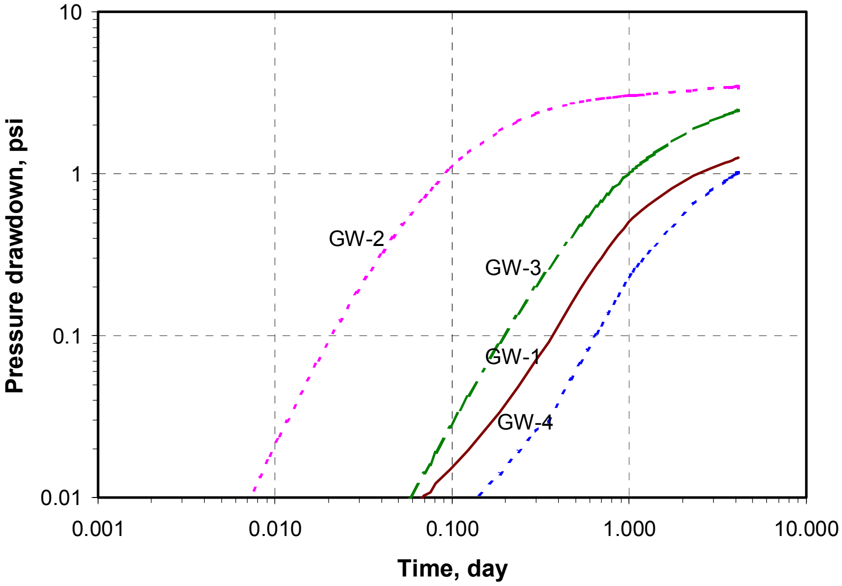

Figure 4.36—Interference pressure responses of test Pump 58.

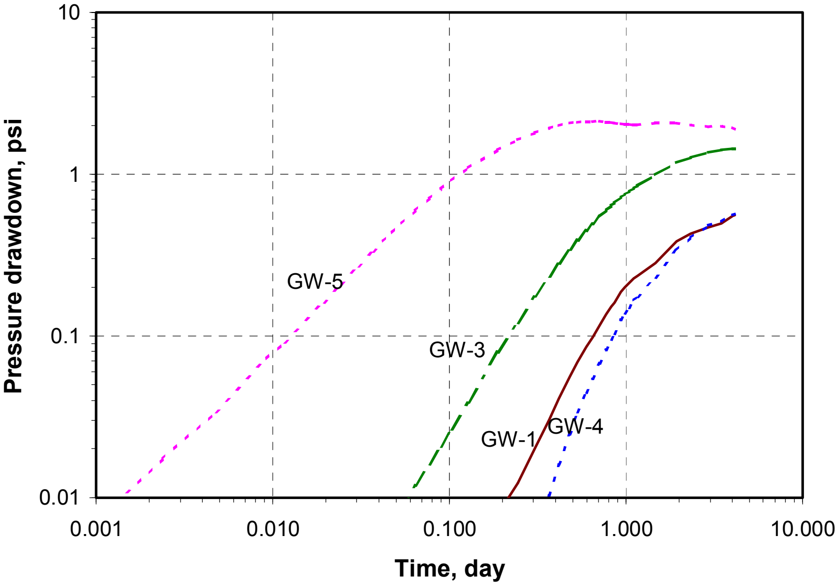

Figure 4.37—Interference pressure responses of test Pump 27.

In our study, we will perform inversion of the pressure response from the first interference test, Pump 58. Then, using the estimated permeability model from the inversion, we will predict the second interference test, Pump 27, and compare the prediction responses with the observed pressure responses for verification. Our inversion result will also be compared with the interpretation of other field tests for characterizing the fracture.

Before proceeding with the inversion, we first discuss the interference transient pressure behavior in a naturally fracture reservoir. This provides us some insights and guidelines on the use of interference transient pressure data during the process of inversion.

4.5.1 Interference Pressure Behavior in a Naturally Fractured Reservoir

A naturally fractured reservoir usually contains both matrix and fracture systems, with storage capacity mainly from the matrix system and flow capacity mainly coming from the fracture system. The interference transient pressure in a naturally fractured reservoir has unique features and is different from that in a homogeneous reservoir. For a homogeneous reservoir, the interference response follows the exponential integral solution at all time and at any observation location.[57-60] Chih-Cheng Chen *et al.*[73] investigated the behavior of interference response in a naturally fractured reservoir. They found that the interference response in a naturally fractured reservoir follows the exponential integral solution at early and late time, with the early one reflecting the storage of the fracture system, and the late one reflecting the storage of the total system (matrix + fracture). They also found that the distance between the source and observing wells has a dominant role for the interference behavior; if the distance is large enough, the interference response may be identical to that of a well in a homogeneous reservoir. They built conventional well test type-curves in terms of two dimensionless group, t_D / r_D^2 and $\lambda'\omega' r_D^2$. The definition of related variables are as follows

$$P_D(r_D, t_D) = \frac{7.2\pi \times 10^{-6} k_f h_f}{qB\mu} \left(P_i - P_{wf}(r,t)\right) \tag{4.50}$$

$$t_D = \frac{3.6 \times 10^{-6} k_f t}{\phi_f c_{tf} \mu r_w^2} \tag{4.51}$$

$$\lambda' = \eta r_w^2 \left(\frac{k_m h_m}{k_f h_f} \right) \tag{4.52}$$

$$\omega' = \frac{\phi_m c_{tm} h_m}{\phi_f c_{tf} h_f} \tag{4.53}$$

$$r_D = \frac{r}{r_w} \tag{4.54}$$

where q is the surface flow rate, B is the formation factor, μ is the viscosity of the fluid, and k, h, ϕ, c_t represent permeability, thickness, porosity, and total compressibility respectively. The subscript, *f*, refers to the fracture, while m refers to the matrix. η is the shape factor that accounts for the shape of the matrix elements. Also, λ' is called the dimensionless transfer coefficient, and ω' is called the dimensionless storage.

We use the observed interference data of Pump 58 to match the type-curves. **Fig. 4.38** through **4.41** shows the type-curve matching for those observing wells GW-1 to GW-4. From these figures, we can see that the interference pressure data of GW-1, GW-3 and GW-4 basically match the late time exponential integral solution, which indicates that the responses of these wells mainly reflect the storage of the total system (matrix + fracture). On the other hand, the interference data of GW-2 match the early time exponential integral solution and some transition to the late time exponential integral solution. This suggests that the response of GW-2 mainly reflect the storage of the fracture system. Based on the type-curve matches, we estimated the storage (ϕc_t) of the total system. The average value of the estimated storages for the total system is 1.12×10^{-5} 1/psi, which will be used in the inversion process.

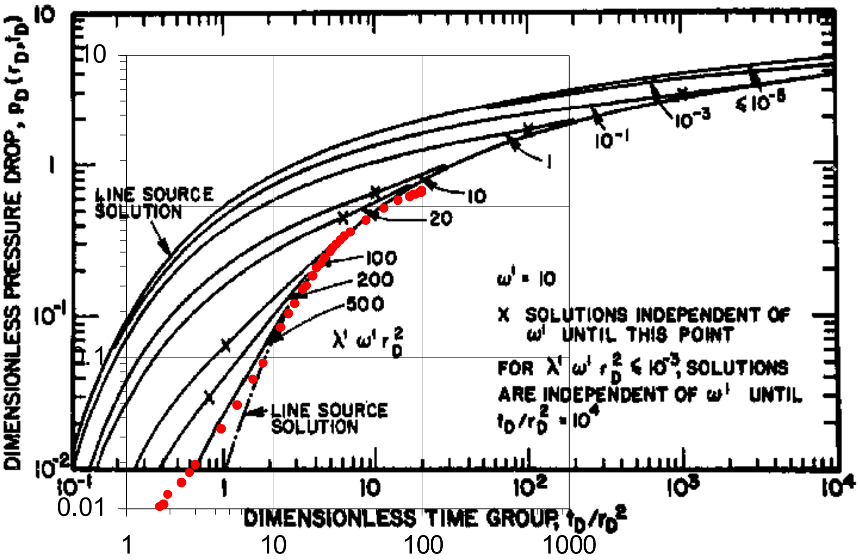

Pressure response at observation well (ω' = 10)

(After Chih-Cheng Chen, SPE 10839)

Figure 4.38—Type-curve match of interference pressure data of GW-1, Pump 58.

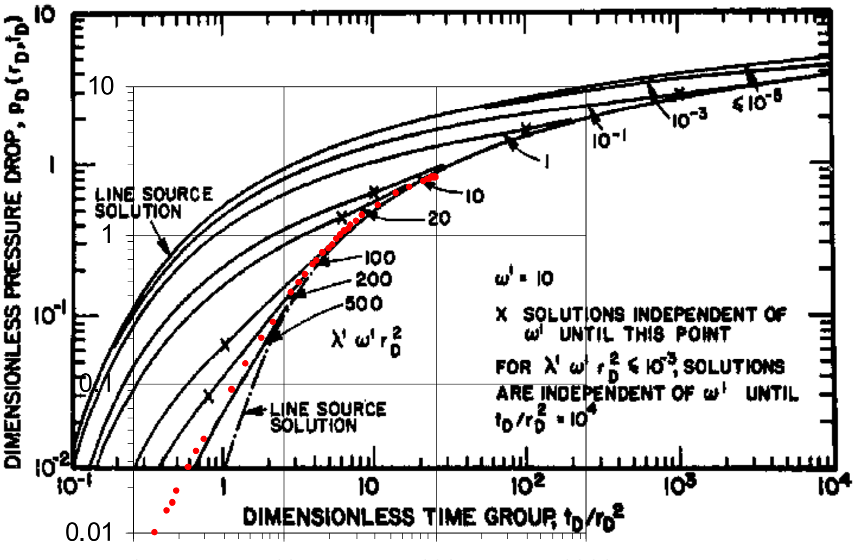

Pressure response at observation well (ω' = 10)

(After Chih-Cheng Chen, SPE 10839)

Figure 4.39—Type-curve match of interference pressure data of GW-3, Pump 58.

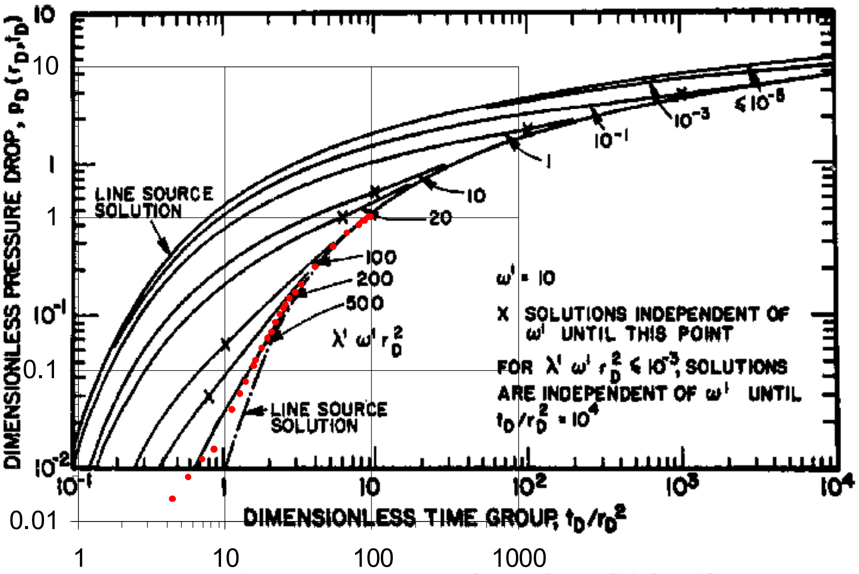

· Pressure response at observation well ($\omega' = 10$)
(After Chih-Cheng Chen, SPE 10839)

Figure 4.40—Type-curve match of interference pressure data of GW-4, Pump 58.

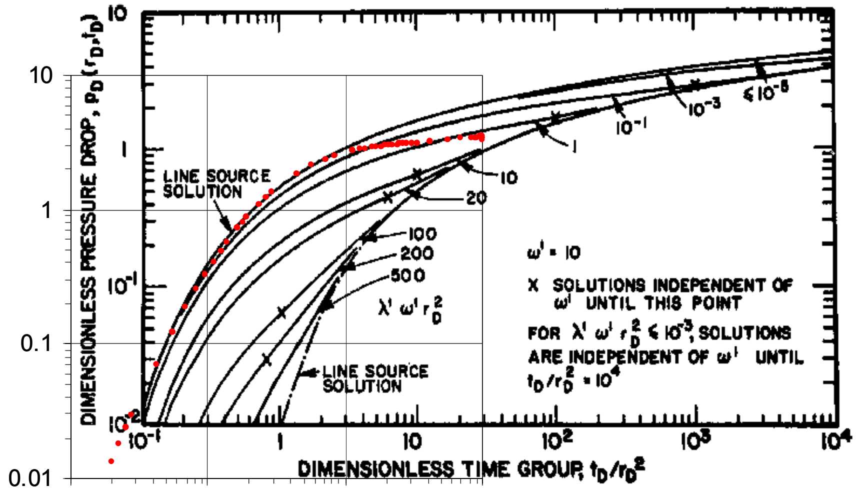

Pressure response at observation well ($\omega' = 10$)
(After Chih-Cheng Chen, SPE 10839)

Figure 4.41—Type-curve match of interference pressure data of GW-2, Pump 58.

A naturally fractured reservoir is usually simulated by a dual-porosity model.[74] In such a model, the permeability of the matrix system is neglected because of its much smaller magnitude compared with that of the fracture system, but dual storages are considered: one is from the matrix system and another from the fracture system. As mentioned before, we use a finite-difference simulator as our forward model. It considers a single porosity and a single permeability system. To model a naturally fractured reservoir, we choose to model the permeability of the fracture system and the storage of the total system (matrix + fracture). Therefore, in the inversion process, we should expect to match the interference responses with the exception of well GW-2 because its interference pressure data mainly reflect the storage of the fracture system.

4.5.2 Inversion of Test Pump 58

As discussed before, we consider the permeability of the fracture system in our simulation. However, we should notice that the grid permeability used in the simulation doesn't represent the actual permeability of the fracture, but is an effective permeability accounting for the high flow capacity of the fracture. That means, for a location which contains no or few fractures, the permeability of the grid basically represents the permeability of the matrix; for a location where high conductive fractures exist, the permeability of the grid represents a equivalent permeability enhanced by the presence of fractures.

We build our starting model using a stochastic approach. Based on the surface fracture pattern mapped at outcrop of Fort Riley formation (**Fig. 4.35**), we determine the azimuth of (112^o, 15^o) for the two sets of orthogonal fractures, and assume a normal distribution for the length of the fractures, with a mean of 15 m and a standard deviation of 5m. By stochastic simulation, we populate the fractures onto our simulation model (**Fig. 4.42a**). For each of the grid block, we calculate the lengths of the fractures within that block to get a flow index associated with that grid block. Then the permeability of the grid blocks are then obtained by rescaling the flow indices. The rescaling is performed based on the expected range of grid effective permeability contributed by the fractures within the grid blocks. **Fig. 4.42b** shows the permeability model generated from the stochastic simulation.

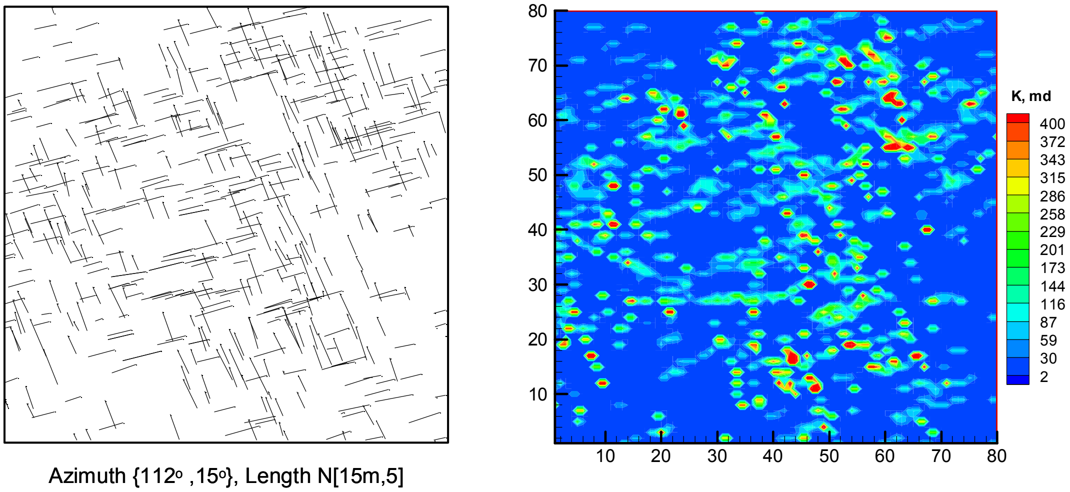

a. Fracture distribution

b. Initial Perm model

Figure 4.42—Initial permeability model generated by stochastic simulation.

Using the interference pressure data of the test Pump 58, we perform travel time + peak amplitude matching. The pressure arrival times are computed for each of the four observing wells, GW-1 to GW-4, by differentiating the pressure drawdown responses with respect to time. After the travel time match (20 iterations), a peak amplitude match (10 iterations) is conducted to further improve the overall match for pressure. **Fig. 4.43** and **Fig. 4.44** show the pressure derivative match and pressure match respectively from the travel time match and peak amplitude match. Also superimposed in these figures are the calculated responses from the initial model. As can be seen, after the inversion, the interference responses of three wells have been well matched except well GW-2, as we expected previously.

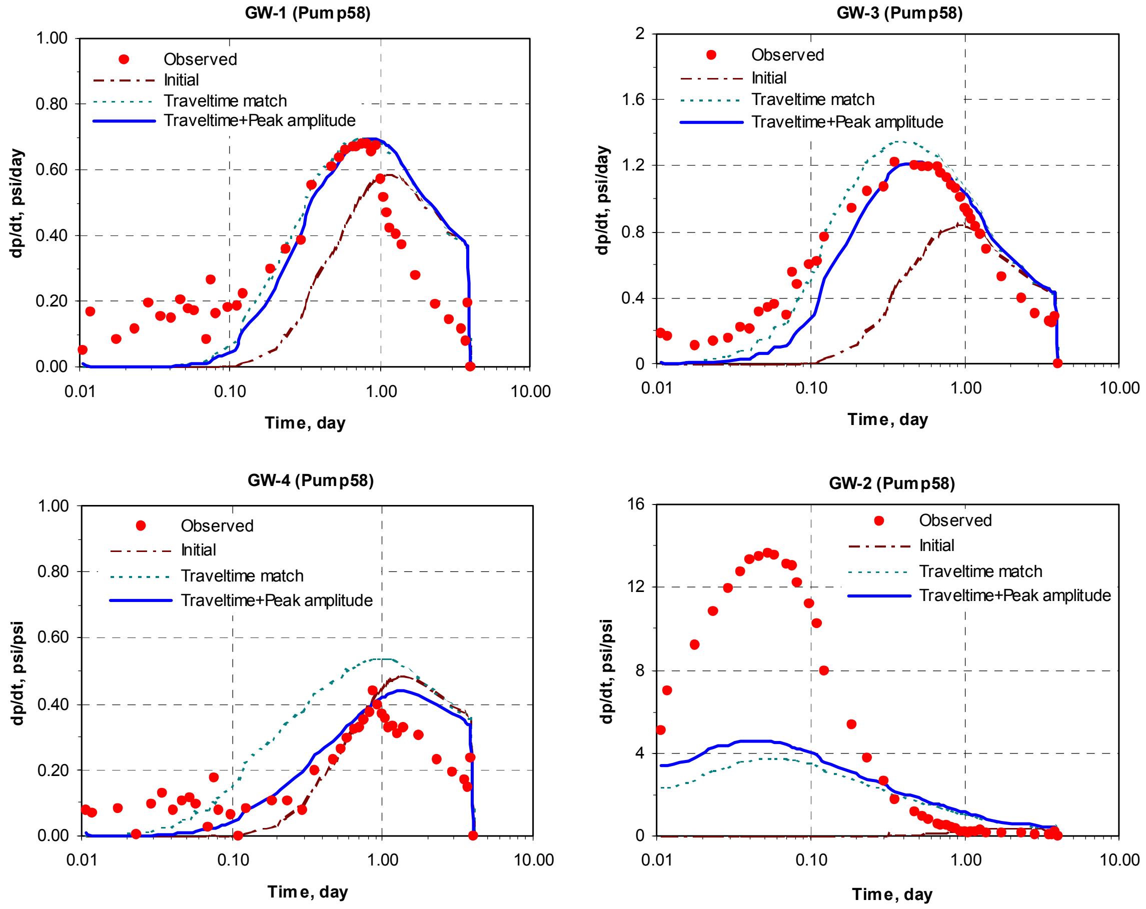

Figure 4.43—Pressure temporal derivative matching by inversion for test Pump 58.

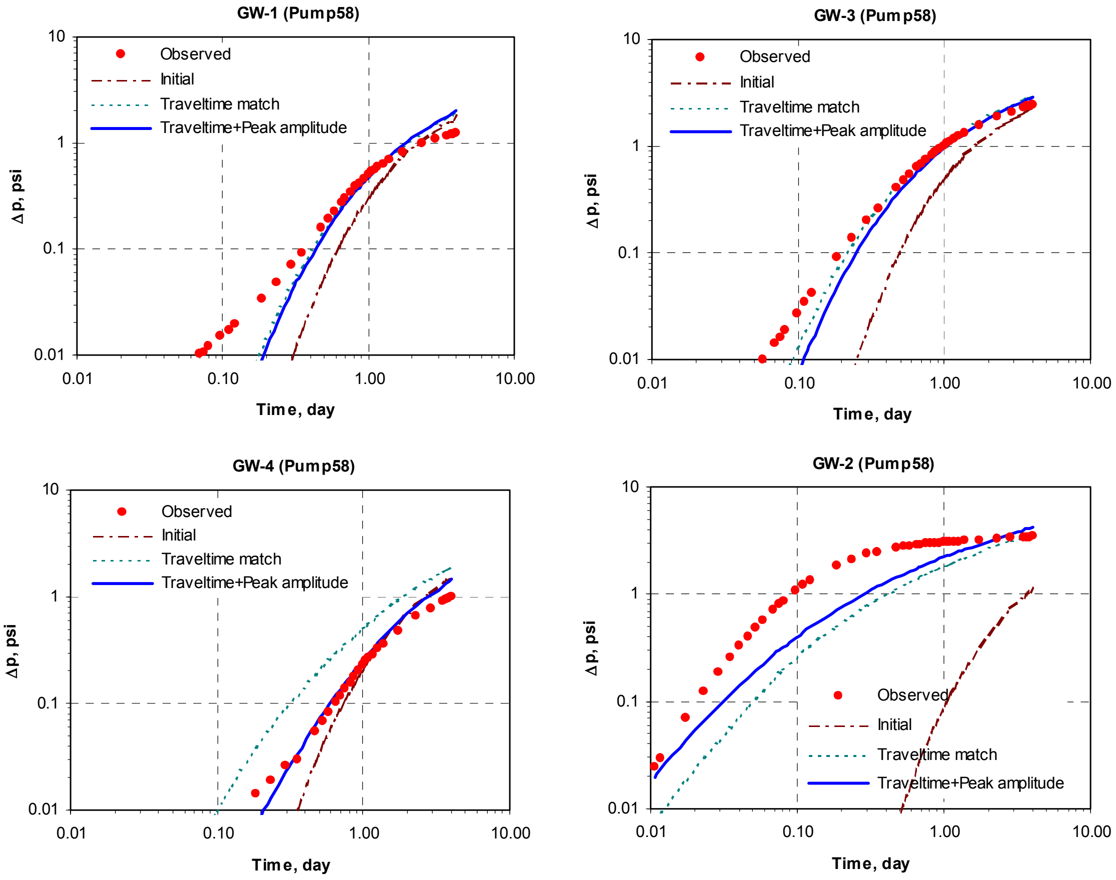

Figure 4.44—Pressure matching by inversion for test Pump 58.

Fig. 4.45 through **4.50** demonstrates the evolution of the estimated permeability models and travel time match during the iterations. We can see that a set of orthogonal high permeable paths is emerging as the inversion proceeds, with a dominant one in the east-northeast direction between GW-5 and GW-2 and to the north of well GW-3, and a less dominant one in the north-northwest direction between Gw-5 and GW-4.

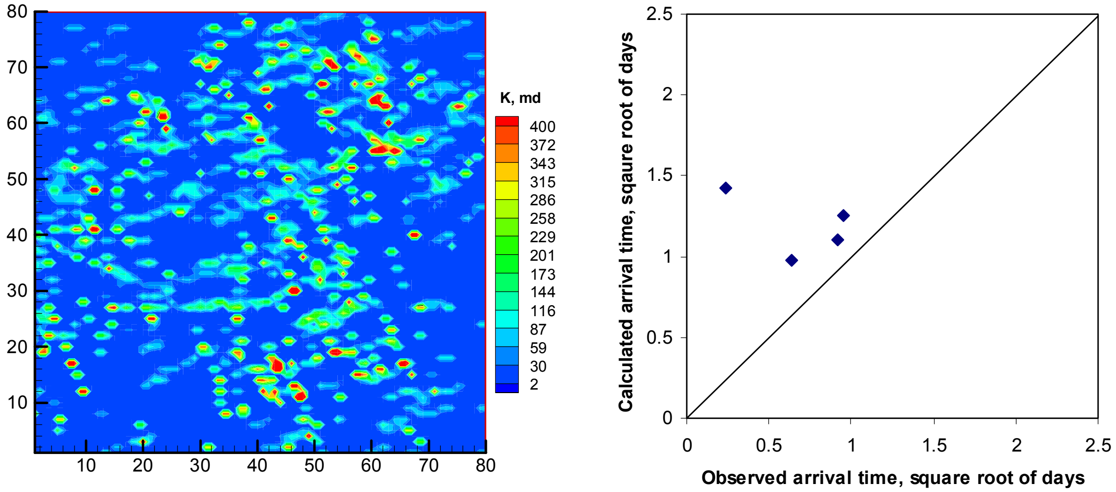

a. Permeability model

b. Travel time match

Figure 4.45—Permeability model and travel time match at iteration = 0.

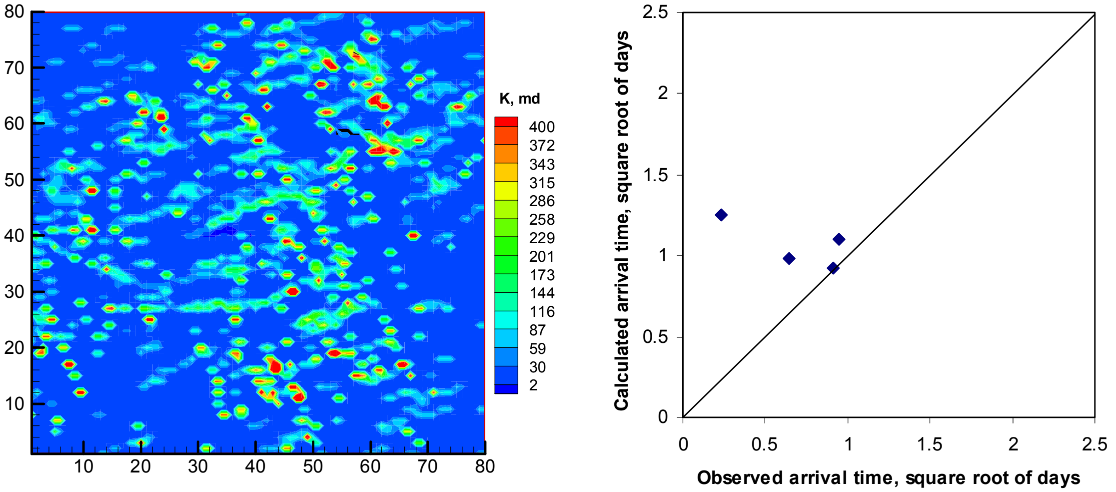

a. Permeability model

b. Travel time match

Figure 4.46—Permeability model and travel time match at iteration = 4.

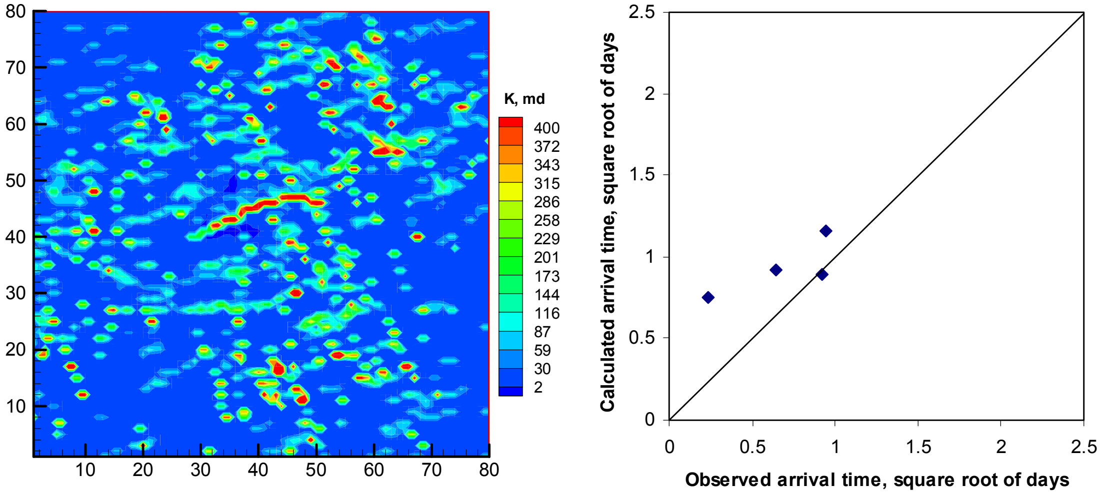

a. Permeability model

b. Travel time match

Figure 4.47—Permeability model and travel time match at iteration = 8.

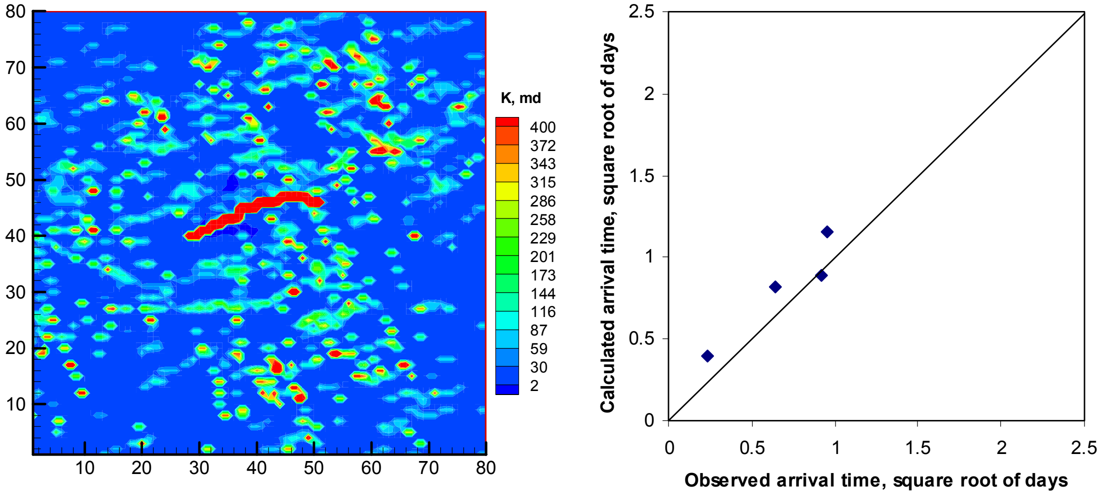

a. Permeability model

b. Travel time match

Figure 4.48—Permeability model and travel time match at iteration = 12.

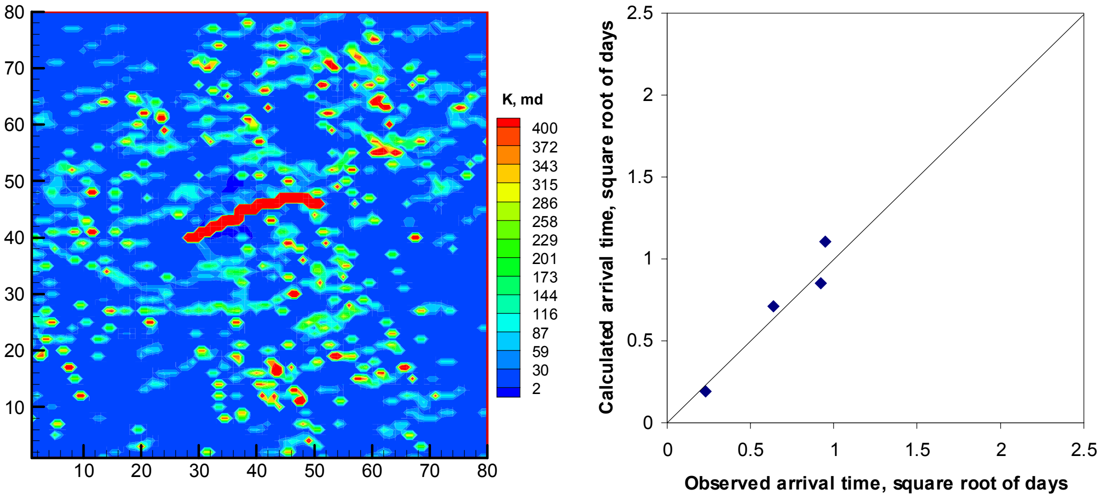

a. Permeability model

b. Travel time match

Figure 4.49—Permeability model and travel time match at iteration = 16.

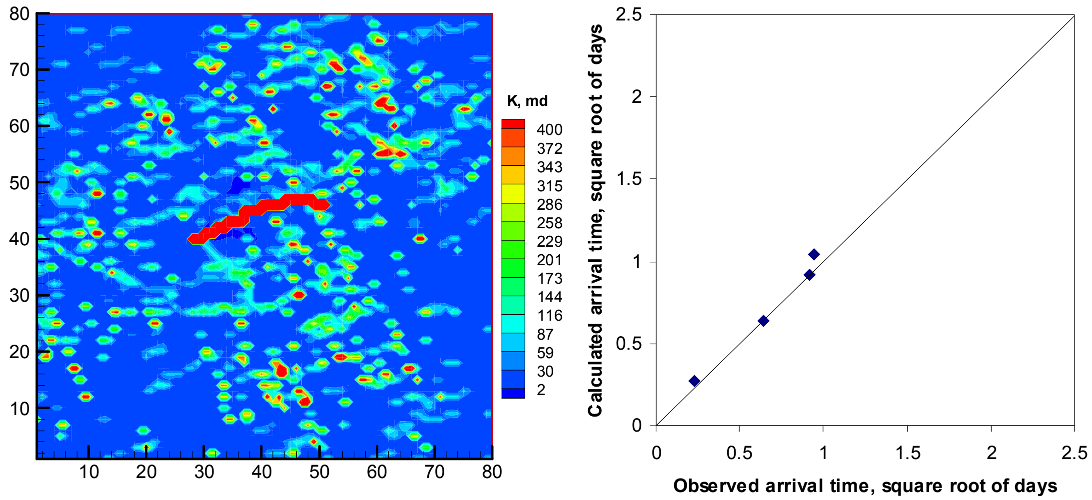

a. Permeability model

b. Travel time match

Figure 4.50—Permeability model and travel time match at iteration = 20.

Fig. 4.51 shows a comparison of the estimated permeability models from travel time match and after peak amplitude match. We can see that although the peak amplitude match improves the pressure match (**Fig. 4.44**), it doesn't change the model much, only with some noticeable reductions in permeability along the path between GW-5 and GW-4. Most of the features in the estimated permeability model are resolved by travel time inversion.

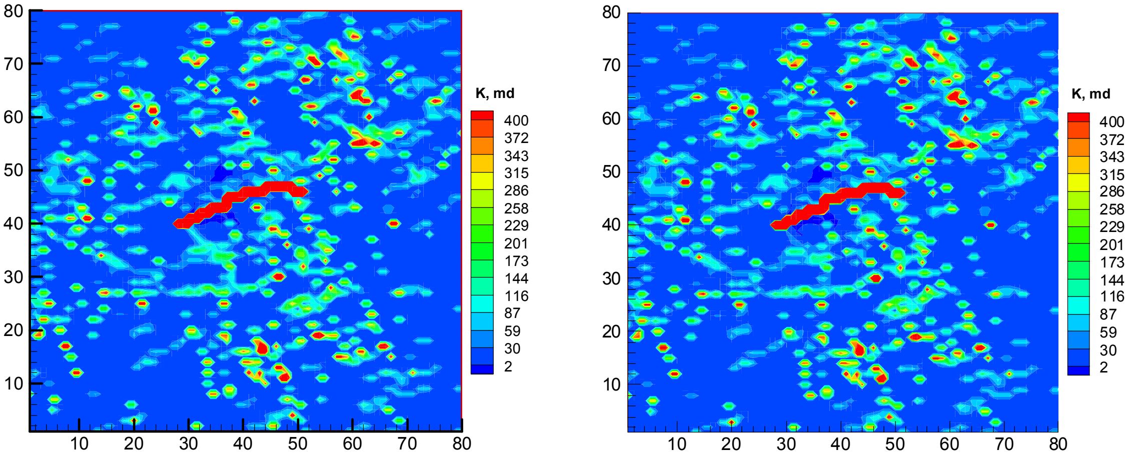

a. Travel time match

b. Peak amplitude match

Figure 4.51—Permeability models after travel time match (iteration = 20) and after peak amplitude match (iteration = 30) .

4.5.3 Verification

As mentioned earlier, various field experiments were performed to characterize the fracture system. In particular, cross-well seismic experiments and additional drilling provide direct evidences of the presence of a high-conductive fracture to the north of GW-3.[71-72] The cross-well seismic experiments were performed before and after air injection between the well pairs of GW-3/GW-1 and GW3/GW4, with a seismic source placed in well GW-3, and the seismic waves recorded in wells GW-1 and GW-4. Air was pushed into the fracture pathway by simultaneously injecting air into well GW-5 and pumping water from well GW-2. As shown in **Fig. 4-52**, after air injection, dramatic reductions in seismic amplitude between the well pair of GW3/GW1 were observed while seismic waves between the well pair of GW-3/GW-4 were relatively unaffected.

The large drop in seismic amplitude between the well pair of GW3/GW1 because of the air injection confirms the presence of a vertical fracture to the north of well GW-3. Furthermore, the drilling of a slant well 14 m north-northwest of GW-3 at the target depth (24m) intersected an open fracture, which is nearly vertical. In addition, a less dominant fracture was also noted by D'Onfro *et al.*[72] We can see that our inversion results are consistent with the results of these experiments.

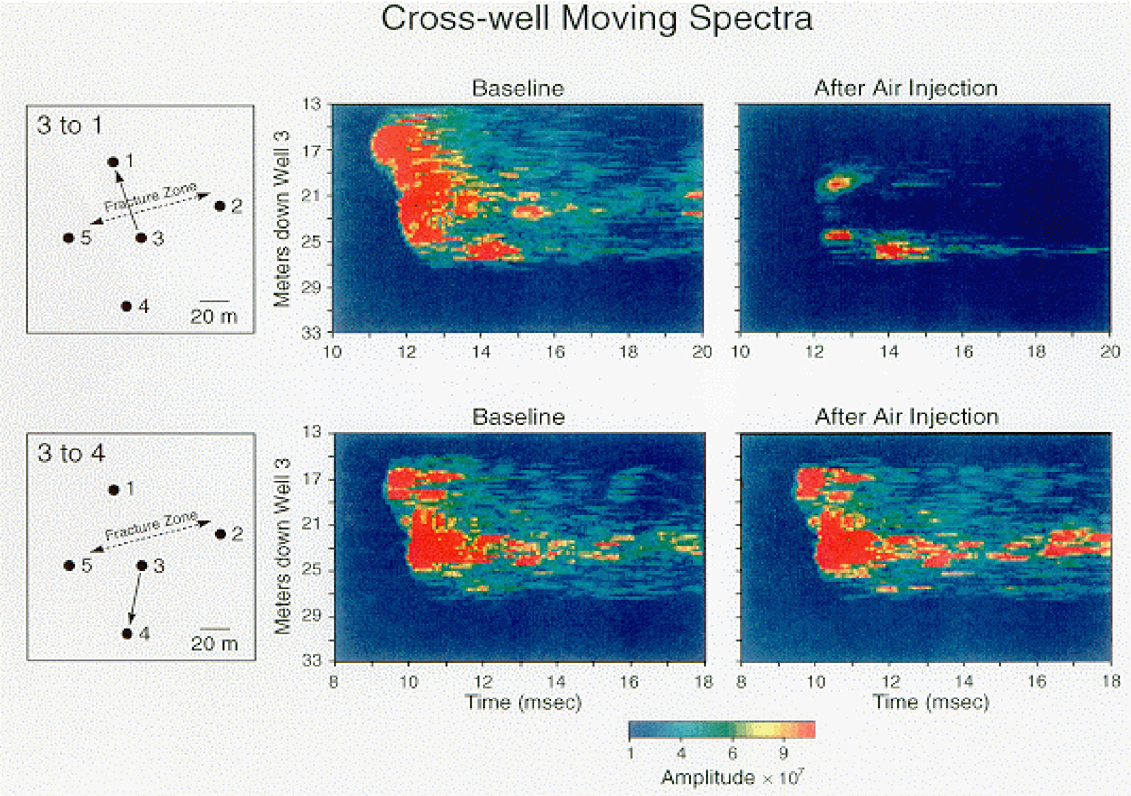

Figure 4.52—Crosswell seismic, Conoco Borehole Test Facility.

Our final exercise is to predict the interference responses of the test Pump 27 based on the estimated permeability model from our inversion. It is thought that if the predicted responses are able to match the actual observed responses, our inversion results will be further verified. In this test, water was produced from well GW-2 while pressure responses are observed at wells GW-1, GW-3, GW-4, and GW-5. In the prediction, we use an average pumping rate of 0.3 gal/min throughout the duration of the test. This rate is different from the actual rate, which varied during the test, as mentioned before. Nevertheless, we get good prediction results, as shown in **Fig. 4.53**. We can see that the interference responses of three wells are remarkably matched, except one well (GW-5), as we expected previously.

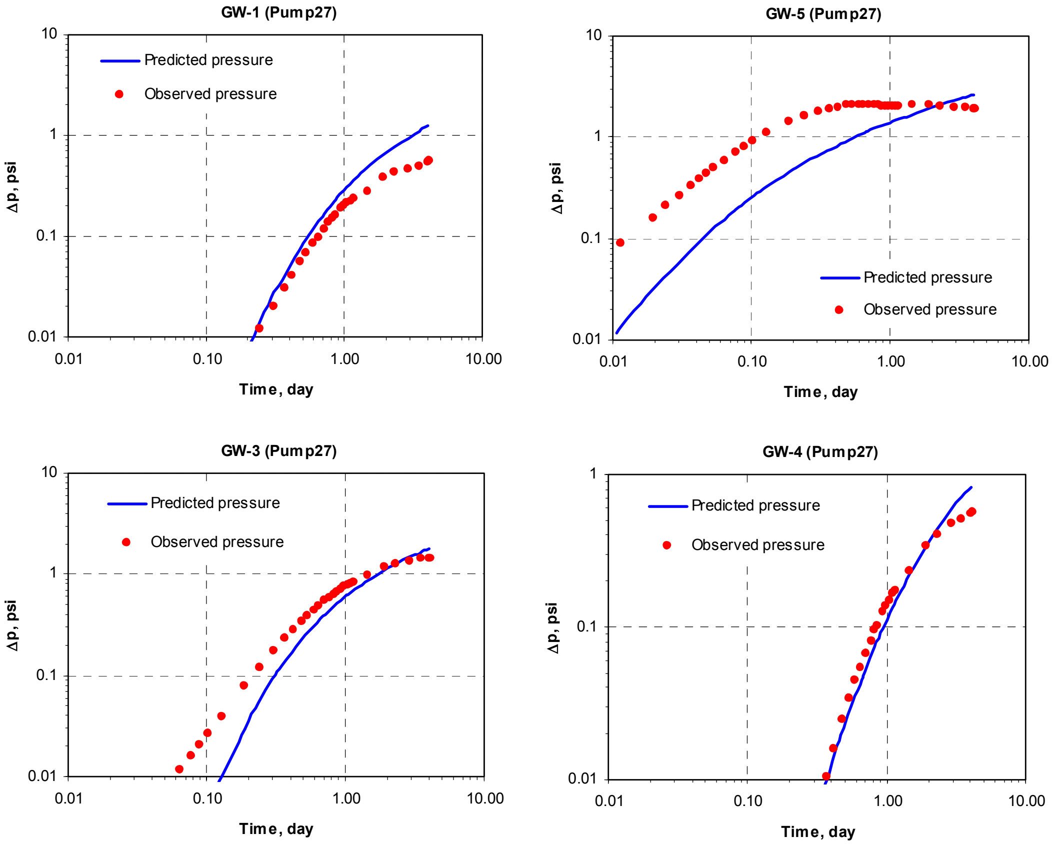

Figure 4.53—Prediction of test Pump 27 based on inversion-derived permeability model.

4.6 Chapter Summary

In this chapter, a robust and computationally efficient approach to integrate the interference transient pressure data into reservoir models is presented. The proposed method extends our previous travel time inversion into an alternating inversion of travel time match followed by peak amplitude match or pressure match. The followed peak amplitude match or pressure match takes the estimates from travel time inversion as the starting model to further improve the matching of pressure. The travel time match and peak amplitude match or pressure match are alternated for multiple cycles until no further improvement on pressure matching can be obtained. The switch of objective function between travel time misfit and peak amplitude misfit or pressure misfit provides a mechanism of bypassing the local minimum. A key development of the proposed approach is the analytic computation of sensitivities required by the inverse modeling. Utilizing the concept of streamline 'diffusive' time of flight developed from the asymptotic solution for compressible flow, the sensitivities of travel time, peak amplitude and pressure are formulated analytically. So the sensitivities required for solving the inverse problems can be obtained using a single forward simulation. Thus, the approach can be orders of magnitude faster than current techniques that require multiple flow simulations.

The proposed inversion approach was validated with a synthetic example. The approach is able to produce satisfactory matching of interference pressure data and to recover the main features of the reference permeability distribution efficiently. The approach was also applied to a field example for characterizing the permeability distribution for a naturally fractured reservoir. An orthogonal fracture pattern was imaged from an interference test, which shows consistency with field experimental observations and interpretations. Using the estimated permeability model, another interference test has been predicted, and shows good matching of the observed pressure responses.

CHAPTER V

IDENTIFICATION OF RESERVOIR COMPARTMENTALIZATION AND FLOW BARRIERS USING PRIMARY PRODUCTION DATA*

In this chapter, we propose a novel approach that utilizes the streamline-based drainage volume computations to infer reservoir compartmentalization during primary production. Reservoir compartmentalization and flow barriers are inferred through a matching of the streamline-based drainage volumes with those from the decline curve analysis. Our approach is completely general and can be applied to reservoirs in the early stages of field development and with very few wells.

We validate our approach via synthetic and field examples. The field example is from a field in the Gulf of Mexico. Starting with a reservoir model based on well log and seismic data, reservoir compartmentalization and flow barriers are identified from three years of primary production response.

5.1 Introduction

Reservoir compartmentalization can have a significant impact on the field development. Pressure discontinuities often observed during field development can be indicative of reservoir compartmentalization.[75,76] Well production histories can also provide important evidence of reservoir compartmentalization in oil and gas reservoirs[2]. A compartmentalized reservoir system consists of two or more distinct reservoirs that may be in hydraulic communication.[75,81] The presence of faults or low-permeable barriers produces poor fluid communication between the compartments.[75,81] The flow barriers can be horizontal, such as shales, micaceous streaks or stylolites, and/or vertical, such as faults, or stratigraphic changes.[75] The presence of flow barriers significantly influence the depletion performance of wells.

---

*Part of this chapter is reprinted with permission from "Identifying Reservoir Compartmentalization and Flow Barriers Using Primary Production: A Streamline Approach," by Zhong He, Harshal Parikh, Akhil Datta-Gupta, Jorge Perez, and Tai Pham, paper SPE 77589 presented at the 2002 SPE Annual Technical Conference and Exhibition, San Antonio, TX, September 29-October 2, Copyright 2002 by the Society of Petroleum Engineers.

Previous efforts on the study of compartmentalized reservoirs focused primarily on the modeling of production performance from compartmentalization systems. Such reservoirs have been commonly modeled using material balance techniques,[77-80] although some models have also taken into account transient flow within compartments.[81,82] The material balance approach models the limited fluid flow across the compartments using reduced barrier transmissibilities, but neglects the internal resistance to fluid flow within the compartments.[82] The transient flow models are more general and can consider the internal resistance to flow within compartments. All these models require prior knowledge of reservoir compartmentalization and flow barriers. However, such information may not be available, particularly in the early stages of field development with limited geologic and well information. Identification of reservoir compartmentalization and flow barriers from well production responses, particularly from primary production, has remained relatively unexplored in the literature.

The objective of this study is to utilize commonly available data such as well production and pressure response to infer the location and transmissibilities of flow barriers in the geologic model. Recent advances in streamline simulation combined with decline type-curve analysis make this possible. Decline type-curve matching technique has been widely used for analysis of well performance and can provide important information on the drainage behavior of the well.[83,94] Recent advances in streamline simulation and the introduction of the concept of a ‘diffusive’ time of flight allows us to define drainage areas or volumes associated with primary production and compressible flow under very general conditions.[18,35]

We propose a novel approach to identify reservoir compartmentalization and flow barriers utilizing streamline-based drainage volume computations during primary production. Our approach consists of two major steps. First, we perform a decline type curve analysis of the primary production data to identify well communications and estimate the drainage volume of individual wells. Second, starting with a geological model the drainage volumes of each well are recomputed using a streamline-based flow simulation. Reservoir compartmentalization and flow barriers are then inferred through a matching of the streamline-based drainage volumes with those from the decline curve analysis. Our approach is general and relies on commonly available data viz. production rate and flowing bottomhole pressure. The approach is particularly suitable for application in the early stages of field development with limited well data.

5.2 Approach

Our proposed approach involves reconciling reservoir drainage volumes derived from decline curve analysis of primary production response with the drainage volumes computed using a streamline model. The major steps in our approach are outlined below.

- **Well Drainage Volume From Decline-Type Curve Analysis.** This step involves a conventional decline type-curve analysis whereby we plot a normalized production rate, $q/\Delta p$, versus a material balance time, N_p/q, on a log-log plot and then match the field data on the decline type-curves.[83,84] This matching yields the drainage volume associated with the producing well. A deviation of the data from the type-curve can be indicative of a drainage volume change resulting from, for example, a new well sharing the drainage volume of the existing well and also indicates pressure communication between the two wells. The deviated data can be rescaled to estimate the new drainage volume associated with each well.

- **Well Drainage Volume From Streamline Simulation.** Streamline models can be utilized to compute drainage volumes during primary depletion or compressible flow by utilizing the concept of a 'diffusive' time of flight.[18,35] This 'diffusive' time of flight is associated with the propagation of a front of maximum pressure drawdown or buildup associated with an impulse source/sink and can be used to determine the drainage volumes in 3D heterogeneous media with multiple wells and under very general conditions.

- **Drainage Volume Matching to Infer the Location of Flow Barriers.** This step reconciles the two drainage volumes for each well: one from decline type-curve analysis and the other from streamline simulation using the geologic model. Discrepancy between them can suggest the presence of flow barriers that are not included in the geologic model. Different locations and transmissibilities of the flow barriers will give different drainage volumes for the wells. The plausible choice of locations and the transmisssiblities are determined by matching the drainage volumes from streamline simulation with those derived using decline type-curve analysis.

- **Quantifying Uncertainties via Statistical Experimental Design.** The locations and transmissibilities of flow barriers cannot be uniquely determined without additional information. Thus, we carry out a statistical experimental design to account for their variability and compute the corresponding changes in the drainage volume from streamline simulation. Finally, an analysis of variance can be performed to determine the relative impact of the locations and transmissibilities of the flow barriers.

5.2.1 An Illustration of the Procedure

The mathematical formulation behind our proposed approach will be discussed later. First, we will illustrate the procedure using a 2D example that involves primary production from two wells in a heterogeneous reservoir. The permeability field and the reference location of the flow barrier for this case are shown in **Fig. 5.1** along with the two producing wells. The barrier is assumed to be sealing, allowing no flow across the barrier. Both the wells are producing at 400 STB/D; however, well 2 begins production 3 months later than well 1. The pertinent data are shown in Table 5.1. **Fig. 5.2** shows the flowing bottomhole pressures of the two wells from the primary depletion. This pressure response was generated using a commercial numerical simulator.

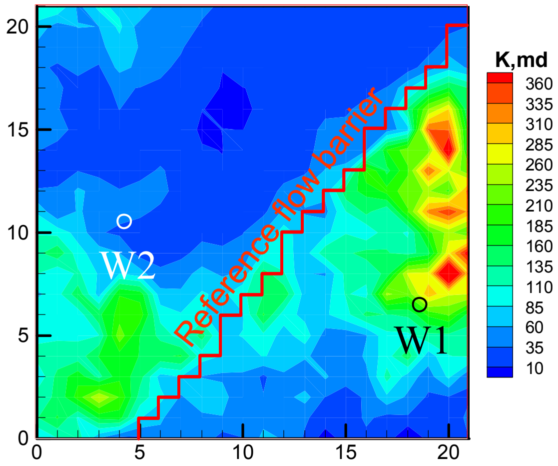

Figure 5.1—Permeability field, well location and reference flow barrier for the 2D, two well example.

TABLE 5.1—RESERVOIR PROPERTIES FOR THE 2D SYNTHETIC EXAMPLE

Boi	1.37	r_w, ft	0.25
c_f, 1/psi	$2.5*10^{-5}$	Φ	0.3
c_o, 1/psi	$9.3*10^{-6}$	μo, cp	0.69
c_w, 1/psi	$2.9*10^{-6}$	S_{wi}	0.25
h, ft	37	p_i, psi	8171

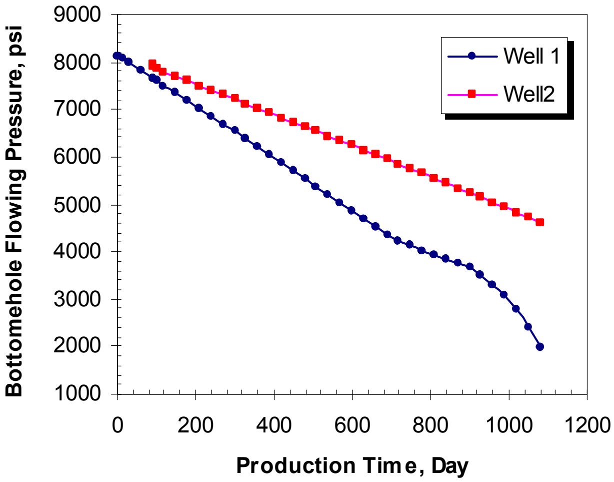

Figure 5.2—Flowing bottomhole pressure for the two producers.

Fig. 5.3 shows the decline type-curve matching for well 1 and yields a drainage volume of 1.7 MMSTB for this well. **Fig. 5.4** shows the decline type-curve matching for well 2. From the match, we determined that the drainage volume for this well is 2.86 MMSTB. Note that the production response from well 1 does not deviate from the type curve after the initiation of production from well 2. This indicates lack of communication between the wells. The total drainage volume for these two wells is 4.56 MMSTB, which is quite close to the OOIP of 4.82 MMSTB in the reference model.

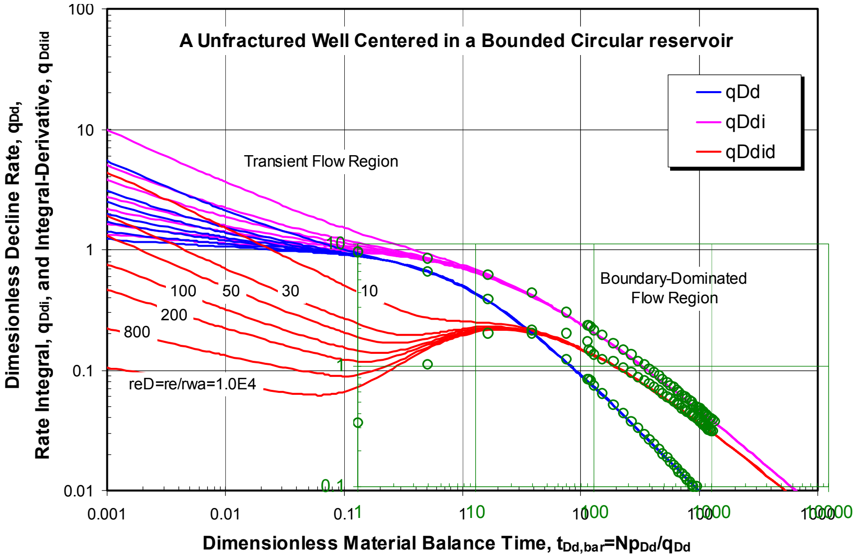

Figure 5.3—Decline type-curve matching of Well 1.

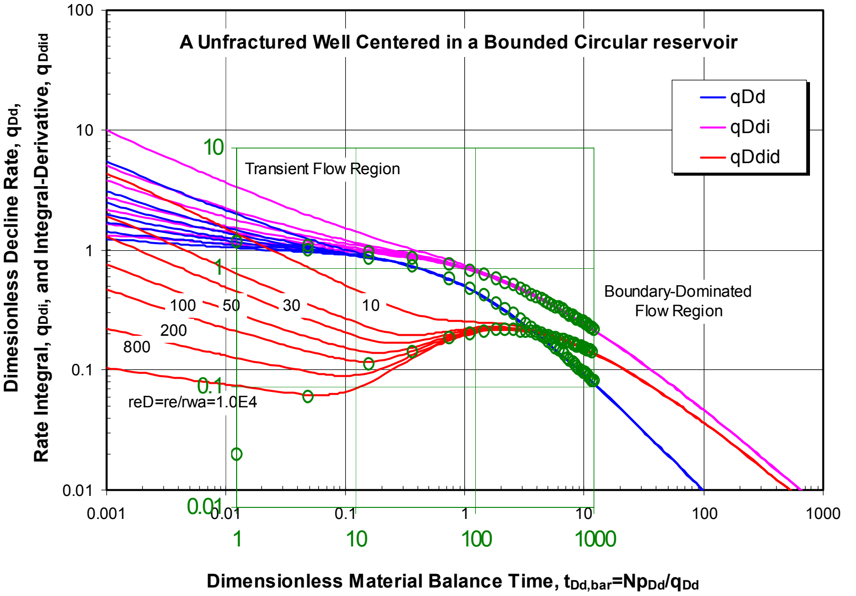

Figure 5.4—Decline type-curve matching of Well 2.

To identify the flow barrier, we considered five possible scenarios as shown in **Fig. 5.5**. In field situations, such scenarios will typically be generated based on some prior information such as expert judgments or seismic data. We compute streamline-based drainage volumes associated with the wells for each of these five cases. **Fig. 5.6a** compares the drainage volumes from streamline simulation and decline type-curve analysis for well 1 for these five cases. **Fig. 5.6b** shows the comparison for well 2. Clearly, Case 3 gives the best match and Cases 1, 2 and 5 can be eliminated as possible barrier locations. Interestingly, Case 4 gives almost as equally good match as Case 3 in terms of drainage volume and thus, underscores the non-uniqueness inherent in such analysis. Additional geological and reservoir information must be used together with the drainage volume matching to further confirm the location of the flow barrier.

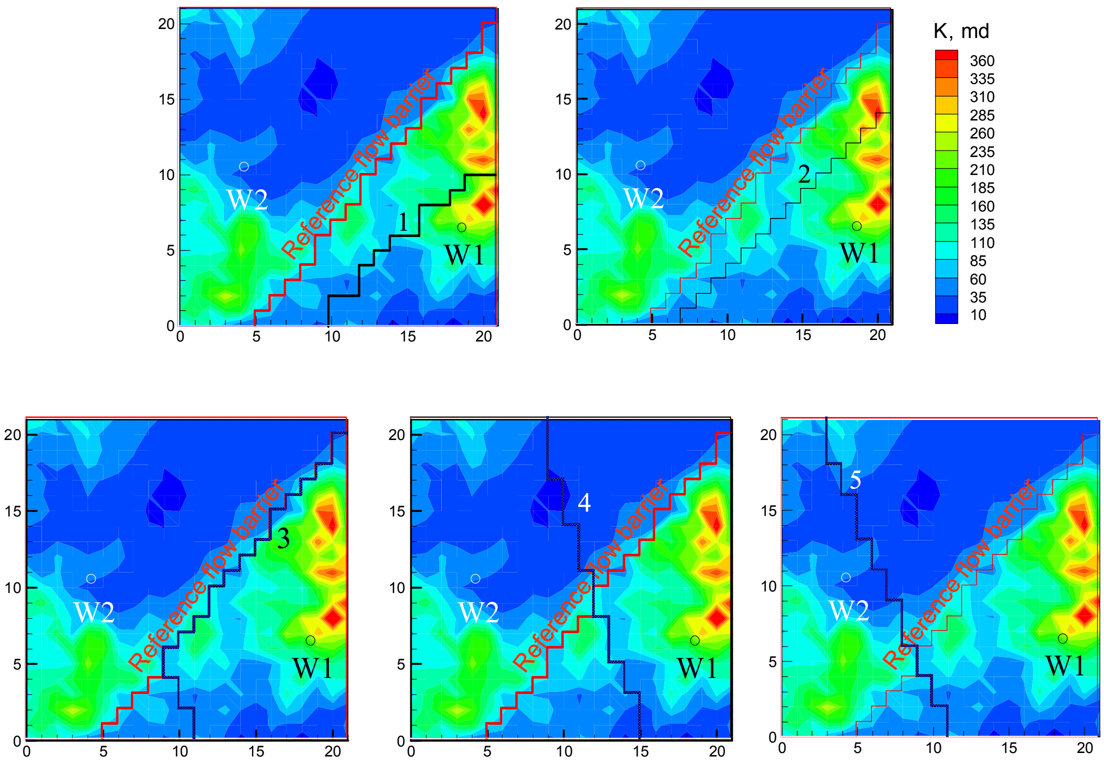

Figure 5.5—Five cases of potential flow barrier location for the 2D, two well example.

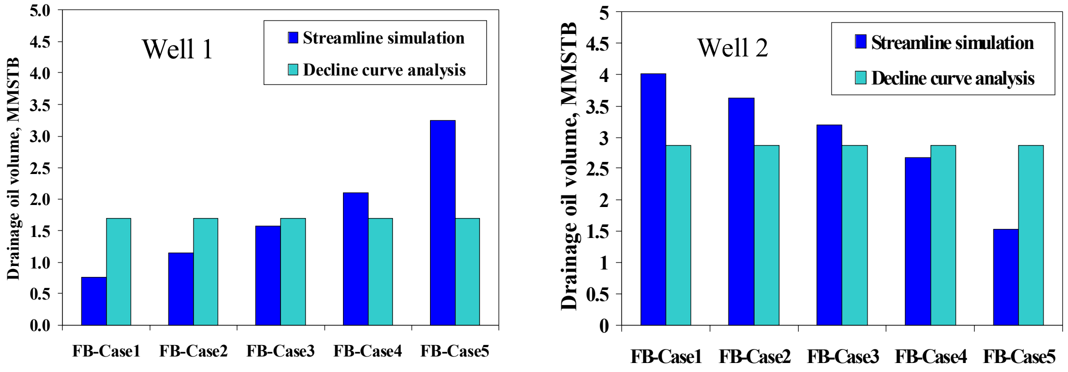

(a) (b)

Figure 5.6—Comparison of drainage volume for (a) well 1 and (b) well 2

5.3 Mathematical Formulation

In this section, we discuss the underlying mathematical formulations behind the proposed method. First, we present a brief background of the decline type-curve analysis for drainage volume calculations from primary production data. We then review the concept of 'diffusive' time of flight for compressible flow and its use in the determination of drainage volume from streamline simulation.

5.3.1 Drainage Volume from Decline Type-Curve Analysis

Consider an unfractured well producing a slightly compressible liquid in a closed system under pseudo-steady state flow conditions (boundary dominated flow). The following relationship can be obtained between a normalized flow rate vs. a 'material balance time': [83,84]

$$\frac{q}{p_i - p_{wf}} b_{pss} = \frac{1}{1 + \dfrac{\bar{B}_o}{NB_{oi} c_e b_{pss}} \bar{t}} \tag{5.1}$$

where,

$$b_{pss} = \frac{141.2 \bar{B}_o \mu_o}{k_o h} \left[\frac{1}{2} \ln \left(\frac{4}{e^{\gamma}} \frac{A}{C_A r_w'^2} \right) \right] \tag{5.2}$$

$$\bar{t} = \frac{N_p}{q} \tag{5.3}$$

In dimensionless form Eq. 5.1 can be expressed as,

$$q_{Dd} = \frac{1}{1+\bar{t}_{Dd}} \tag{5.4}$$

where,

$$q_{Dd} = \frac{141.2\bar{B}_o \mu_o}{k_o h}\left[\frac{1}{2}\ln\left(\frac{4}{e^{\gamma}}\frac{A}{C_A r_w'^2}\right)\right]\frac{q}{p_i - p_{wf}} \tag{5.5}$$

$$\bar{t}_{Dd} = 0.00633\frac{k_o \bar{t}}{\phi \mu_o c_e A}\frac{2\pi}{\frac{1}{2}\ln\left(\frac{4}{e^{\gamma}}\frac{A}{C_A r_w'^2}\right)} \tag{5.6}$$

During decline type curve analysis we simply overlay a log-log plot of $q/\Delta p$ versus $\bar{t}$ on type curves of q_{Dd} versus $\bar{t}_{Dd}$ as shown in **Fig. 5.3** and **5.4**. To facilitate the matching, type curves have also been generated using flow rate integral and flow rate integral derivative as shown in **Fig. 5.3** and **5.4**. A simultaneous match to all the three type curves can reduce the subjectivity and personal bias during the matching process. [9,10] Once the match is obtained, the drainage volume can be calculated as follows:

$$N = \frac{B_o}{B_{oi} c_e}\frac{\left(\bar{t}\right)_{M.P.}}{\left(\bar{t}_{Dd}\right)_{M.P.}}\frac{\left(q_o / \Delta p\right)_{M.P.}}{\left(q_{Dd}\right)_{M.P.}} \tag{5.7}$$

where $M.P.$ refers to the match point value.

If there is aquifer support, the expansion of the aquifer can be incorporated into the drainage volume calculations as follows,

$$N_{psd} = N + N_w \frac{B_w}{B_o}\frac{c_a}{c_e} \tag{5.8}$$

where

$$c_a = c_f + c_w \tag{5.9}$$

$$c_e = (c_f + c_o s_o + c_w s_w) / s_o \tag{5.10}$$

A deviation from the type-curve may occur if a new producing well shares the original drainage volume of an existing well. From Eq. 5.5 and 5.6, we can see that reduction of drainage volume (related to A) has minor influence on dimensionless rate, but significantly changes the dimensionless material balance time and generally causes the data points to concave down from the type curve. Because the deviated data points represent another new pseudo-steady state flow condition, we simply re-scale these data to compute the new drainage volume from the decline type-curve analysis. The material balance time is re-scaled using the cumulative production at the start of the new well, $\bar{t} = (N_p - N_{pi})/q$, while the production rate function is re-scaled using the average reservoir pressure in the drainage volume at the start of the new well, $q/(\bar{p}_i - p_{wf})$. We can expect the re-scaled log-log plot of $q/\Delta p$ versus $\bar{t}$ will again overlay the q_{Dd} versus $\bar{t}_{Dd}$ trend on the type curve and the new drainage volume can then be calculated as before.

It should be pointed out that other factors such as multiphase flow can also result in a deviation from the type curve because water breakthrough and/or gas production may significantly alter the mobility term and/or the total compressibility. But these effects will not be important during the single-phase primary depletion being considered here.

5.3.2 Drainage Volume from Streamline 'Diffusive' Time of Flight

Recently we introduced a 'diffusive' time of flight during streamline simulation for primary depletion and compressible flow.[18,35] The concept is based on a high frequency asymptotic solution to the diffusive pressure equation and leads to an equation for a propagating pressure front that is analogous to the 'Eikonal' equation in wave propagation and seismic tomography, as given below

$$\sqrt{\alpha(\mathbf{x})}\ \left\|\nabla \tau(\mathbf{x})\right\| = 1 \tag{5.11}$$

where α is the diffusivity,

$$\alpha(\mathbf{x}) = \frac{k(\mathbf{x})}{\phi(\mathbf{x})\mu c_t} \tag{5.12}$$

From Eq. 5.11, the pressure front propagates at a velocity given by the square root of diffusivity. The Eikonal equation, being a hyperbolic equation, allows us to invoke characteristic directions and streamlines for propagating fronts. In particular, we can now define a 'diffusive' time of flight for compressible flow as follows,

$$\tau(\mathbf{x}) = \int_{\psi} \frac{ds}{\sqrt{\alpha(\mathbf{x})}} \tag{5.13}$$

where ψ refers to a streamline and s is distance along the streamline. Note that the 'diffusive' time of flight has units of square root of time, which is consistent with the scaling behavior of diffusive flow.

It is important to point out that for compressible flow pathlines can be generated in the same manner as in conventional streamline simulation[19-20,85] using the Pollock algorithm.[86] Fluid compressibility acts as a diffusive source (as opposed to a point source) and the semi-analytic pathline construction applies under such conditions.

An important feature of the 'diffusive' time of flight is that it is related to the propagation of a 'pressure front' of maximum drawdown or build up corresponding to an impulse source or sink. This becomes apparent when we examine the time domain solution to the 0th order asymptotic expansion for an impulse source in a three-dimensional medium,[62]

$$P(t) = A_0(\mathbf{x}) \frac{\tau(\mathbf{x})}{2\sqrt{\pi t^3}} \exp\left(-\frac{\tau^2(\mathbf{x})}{4t} \right) \tag{5.14}$$

At a fixed position, $\boldsymbol{x}$, the pressure response will be maximized when its derivative is set equal to zero, which in turn results in the following relationship between the observed time and the 'diffusive' time of flight

$$t_{\max} = \frac{\tau^2(\mathbf{x})}{6} \tag{5.15}$$

Therefore, the 'diffusive' time of flight is associated with the propagation of a front of maximum drawdown or build up and the time at which the pressure response reaches a maximum at a location can be defined as the transient pressure front arrival time. In fact, this front location is closely related to the concept of drainage volume and drainage radius during conventional well test and decline type curve analysis.[57-60] The analytical radius of drainage for a 3D medium can be expressed[35] as

$$r_D = \sqrt{6t_D} \tag{5.16}$$

In **Fig. 5.7**, we compare analytical radius of drainage (circles) with the diffusive time of flight (contours) at four different times: 6 hours, 21 hours, 36 hours, and 51 hours for a homogeneous case with a center injection well. We can see that the circles and the contour levels are identical.

Note that the streamline-based drainage volume calculations are completely general and apply in the presence of infill drilling and streamline updates. This is illustrated using synthetic and field examples in the next section.

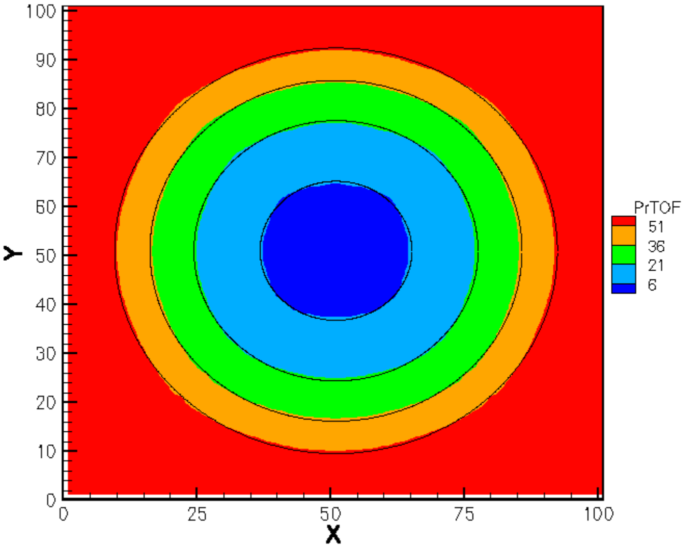

Figure 5.7—Analytical radius of drainage (circles) and diffusive time of flight (contours)

5.4 Applications

In this section, we first demonstrate the correspondence between the drainage volumes from decline type-curve analysis and from streamline simulation using a single well example. Next, we illustrate our proposed approach to identify reservoir compartmentalization using 3D synthetic and field examples. Our synthetic example features a 3D reservoir with a distinct compartment isolated from the main flow channels and involves 3 producing wells starting production at different times. The field example is from a field in the Gulf of Mexico. Starting with a reservoir model based on well log and seismic data, reservoir compartmentalization and flow barriers are identified using three years of primary production response.

5.4.1 Drainage Volume Calculations: A Single Well Example

This example illustrates drainage volume estimation from decline type-curve analysis and its relationship with the drainage volume determined using the concept of 'diffusive' time of flight during streamline simulation. The heterogeneous permeability field is the same as before and the well is located to the right of the center of reservoir, as shown in **Fig. 5.8**. No flow boundary conditions are imposed on all sides. The primary depletion involves a constant production rate of 800 STB/D and the simulated flowing bottomhole pressure is shown in **Fig. 5.9**. **Fig. 5.10** shows the matching with decline type-curves using the flow rate function, the rate integral function and the rate integral derivative function. We select the following match points

$$\left[\bar{t}_{Dd}\right]_{MP} = 1.0 \qquad \left[\bar{t}\,\right]_{MP} = 40 \quad days$$

$$\left[q_{Dd}\right]_{MP} = 1.0 \qquad \left[q/\Delta p\right]_{MP} = 5 \quad STB/D/psi$$

The drainage volume is estimated as 4.64 MMSTB, which is close to the reference OOIP of 4.82 MMSTB.

Next we perform streamline simulation for the heterogeneous reservoir model and compute the 'diffusive' time of flight along the streamlines. The diffusive time of flight can be readily converted to the travel time of the pressure front using Eq. 15. **Fig. 5.11** shows the streamlines and the propagation of the transient pressure front at various times. For a given time, we can now compute the drainage volume by simply calculating the oil volume enclosed by the pressure front at that time. In this example, it appears that the well attains the complete drainage volume in about 15 days of production.

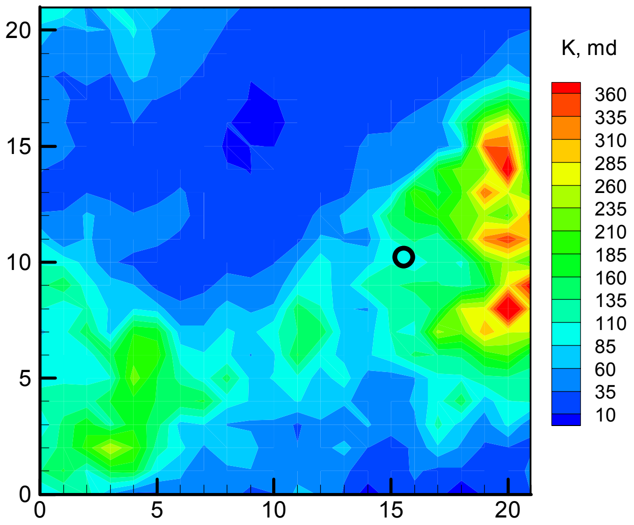

Figure 5.8—Permeability field and well location for the single well example.

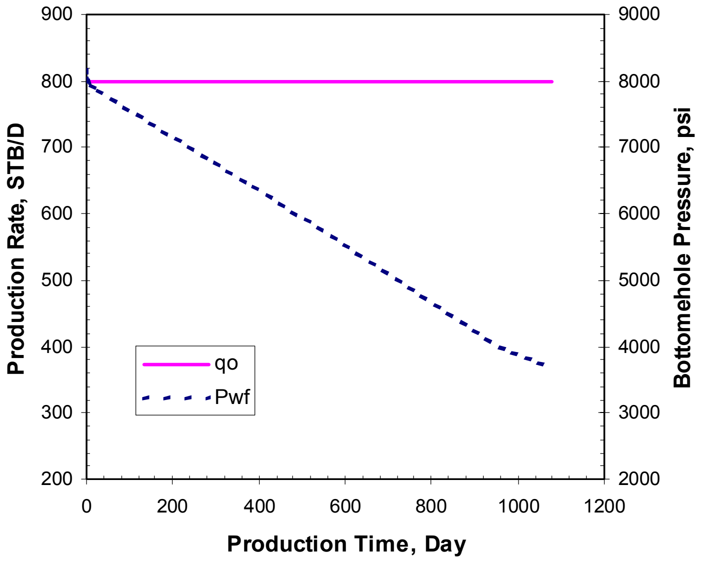

Figure 5.9—Production rate and flowing bottomhole pressures of the producer.

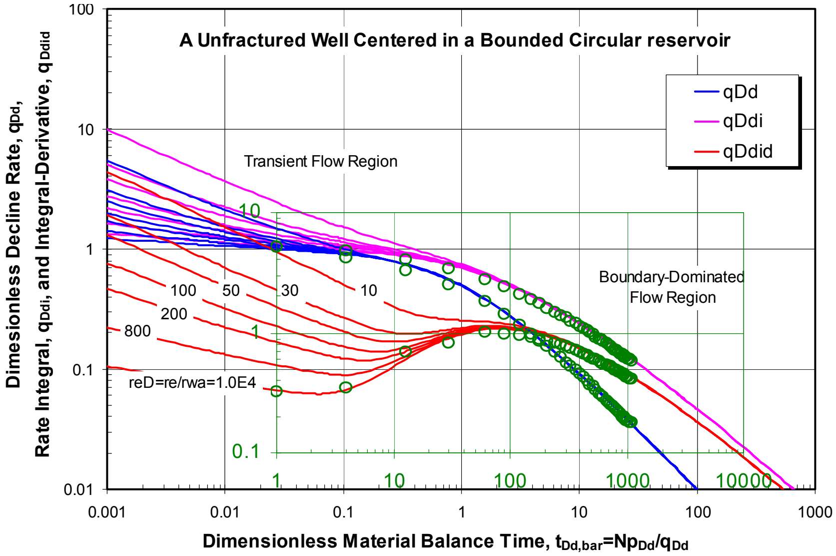

Figure 5.10—Decline type-curve matching for the producer.

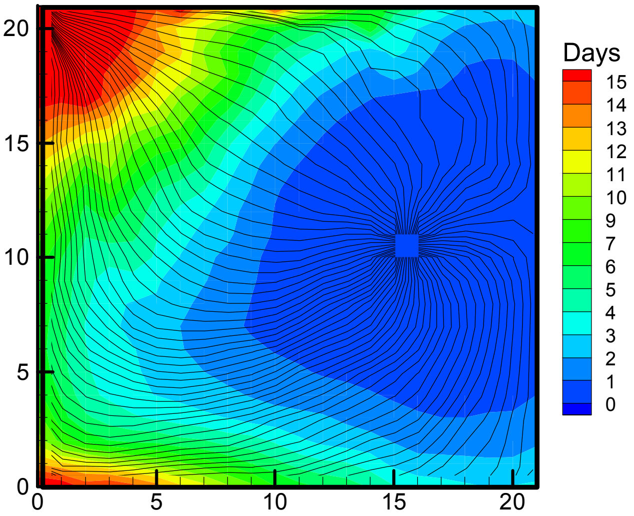

Figure 5.11—Streamlines and the pressure front (drainage volume) for the single well example.

5.4.2 Flow Barrier Identification: A 3D Synthetic Example

This example consists of a reservoir model with 31x28x3 grid cells, with three producing wells under primary depletion. The second and third wells come onto production 3 and 6 months respectively after the first well. In the reference reservoir model, a portion of reservoir is isolated from the main flow channels by the flow barriers indicated in **Fig. 5.12**. The wells are producing at variable rates (**Fig. 5.13**), and the simulated flowing bottomhole pressures for these wells are shown in **Fig. 5.14**.

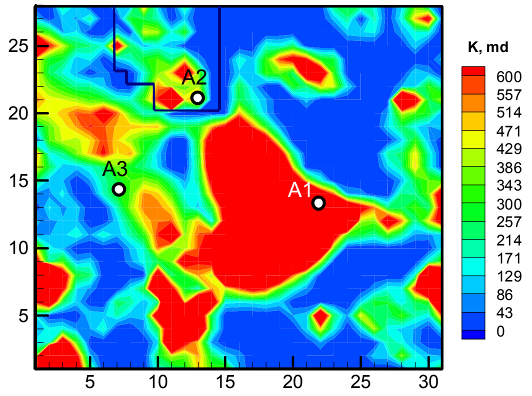

(a). Layer 1

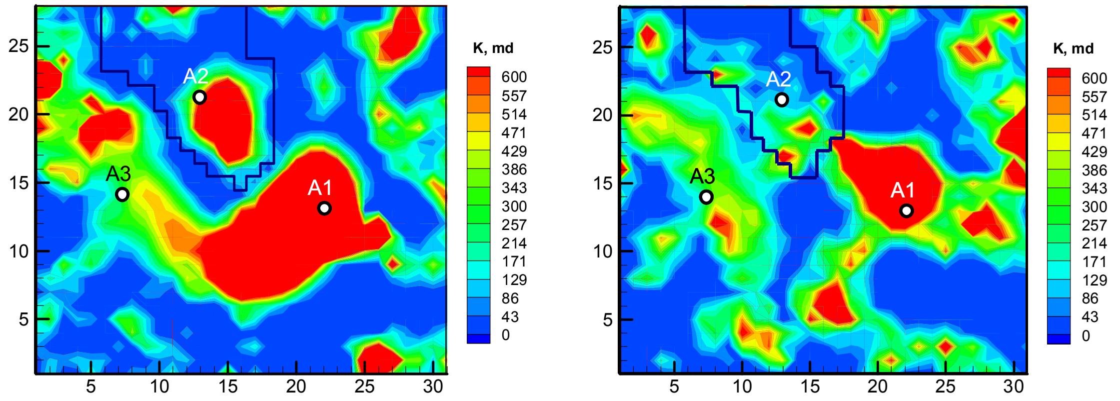

(b). Layer 2

(c). Layer 3

Figure 5.12—Permeability field and reference flow barriers for the 3D synthetic example.

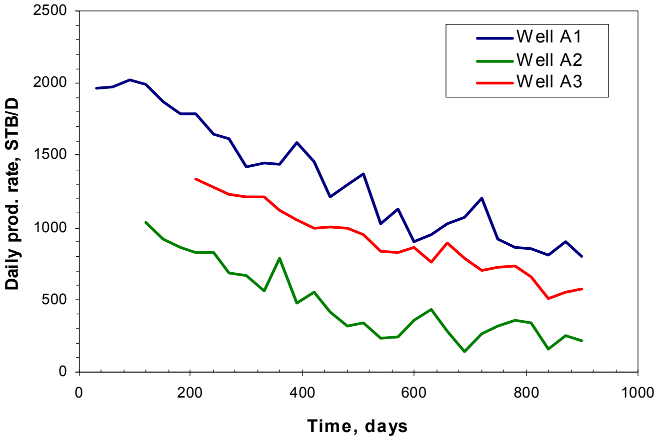

Figure 5.13—Production rates of three producers.

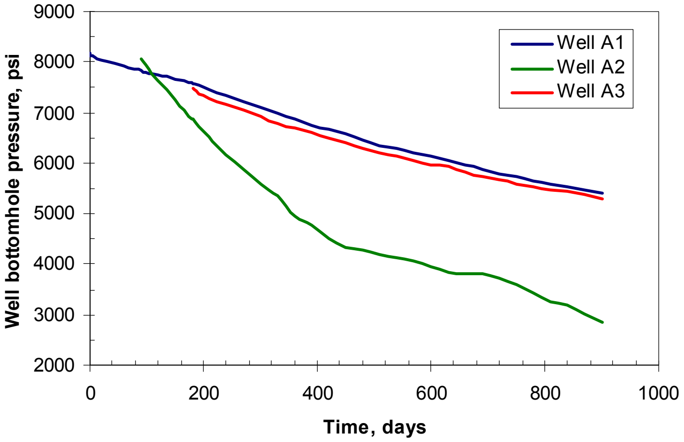

Figure 5.14—Flowing bottomhole pressures of three producers.

The decline type-curve analysis of well A1 is shown in **Fig. 5.15**. It is interesting to note a systematic deviation of data from the type-curve after around 180 days when well A3 comes onto production. Equally important is that the deviation does not start around 90 days when well A2 comes on production. As discussed before, this indicates pressure communication between wells A1 and A3 and lack of communication between wells A1 and A2. By re-scaling the deviated data from well A1, the match is improved significantly as shown in **Fig. 5.16**. The decline type-curve matching for wells A2 and A3 are shown in **Fig. 5.17-18**. Note that unlike well A1the production data for well A2 does not deviate from the type-curves after well A3 comes on production. This indicates no or poor pressure communication between wells A2 and A3. Thus, an important observation follows from the decline type-curve analysis that flow barriers may exist around well A2, which isolate it from the main reservoir. Obviously, this is consistent with our reference model. From the decline type-curve analysis we also estimated the drainage volume for these wells and the results are shown in Table 5.2.

TABLE 5.2—DRAINAGE VOLUMES FROM DECLINE-TYPE-CURVE MATCHING FOR THE 3D SYNTHETIC EXAMPLE

Drainage volume in OOIP, MMSTB		
Well A1	Well A2	Well A3
16.02 (Before A3 on prod.)	1.65	6.48
9.67 (After A3 on prod.)		

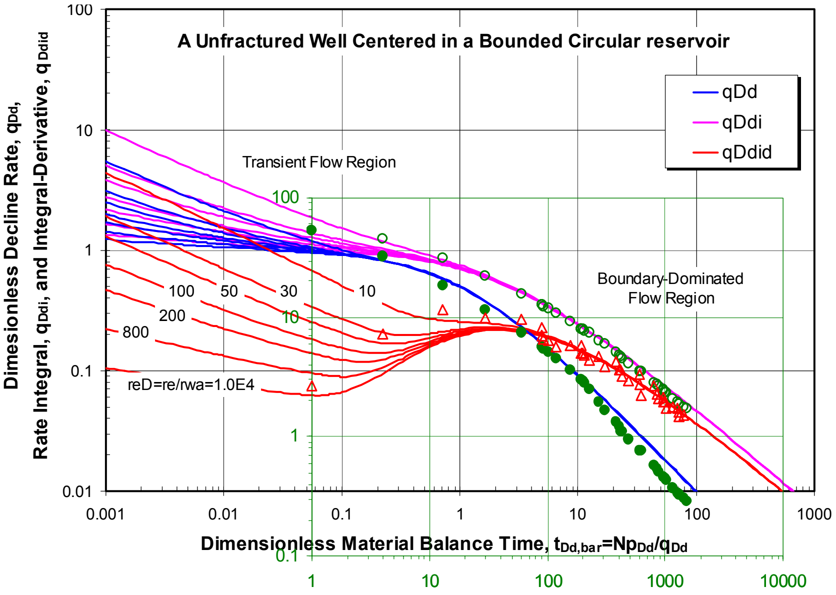

Figure 5.15—Decline type-curve matching of well A1.

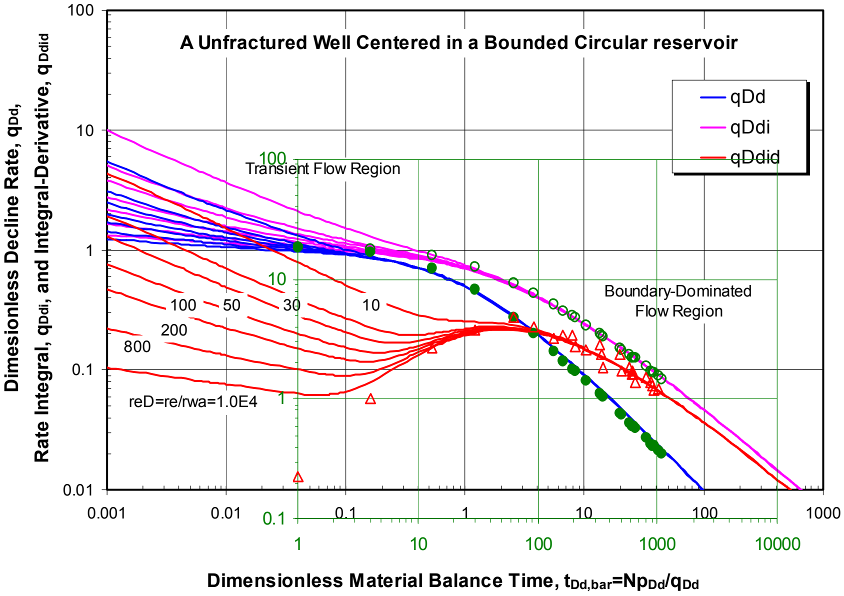

Figure 5.16—Decline type-curve matching of well A1 after accounting well A3 production.

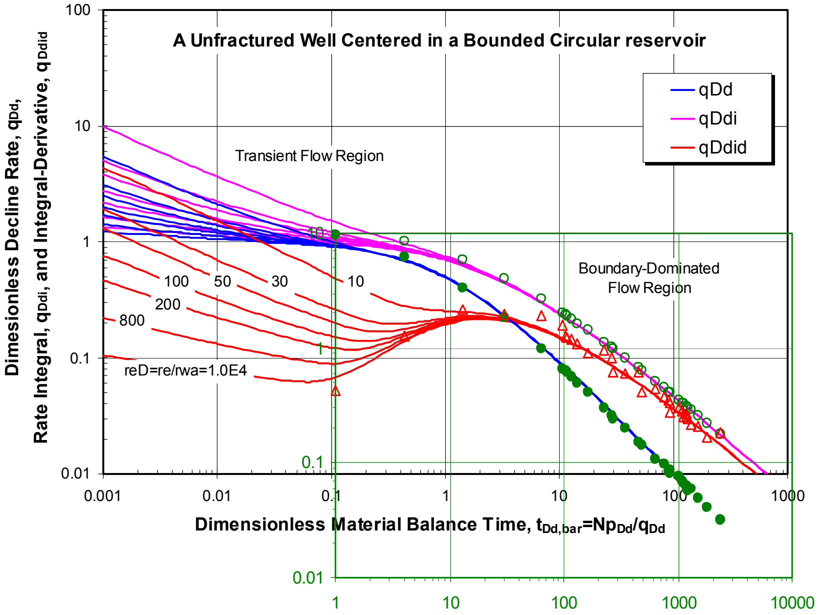

Figure 5.17—Decline type-curve matching of well A2.

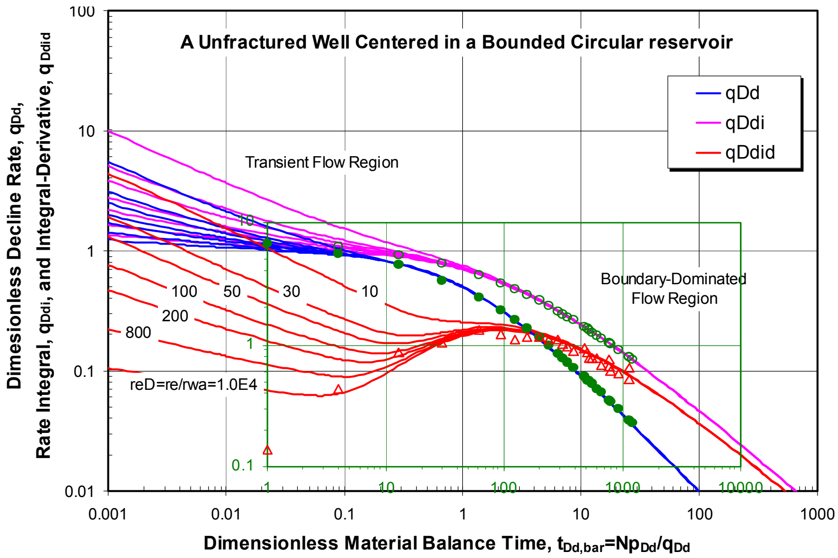

Figure 5.18—Decline type-curve matching of well A3.

Next, we utilize streamline simulation to calculate the drainage volumes of the wells explicitly from the reservoir model. First, drainage volumes are computed without any flow barriers embedded in the reservoir model. **Fig. 5.19 and 5.20** compare the drainage volumes of the wells from streamline simulation and those from decline type-curve matching. There are significant discrepancies in the drainage volumes for well A1 and A2. In particular, the drainage volume from streamline simulation for Well A2 is systematically higher than that from the decline type-curve analysis. The drainage volume from streamline simulation for well A3 seems to match well with that from decline type-curve analysis. This is possible because the flow barriers have little effect on the depletion of well A3. From **Fig. 5.12**, we can see that the sands between well A2 and A3 are not well connected in the reference reservoir model, even without the flow barriers between them.

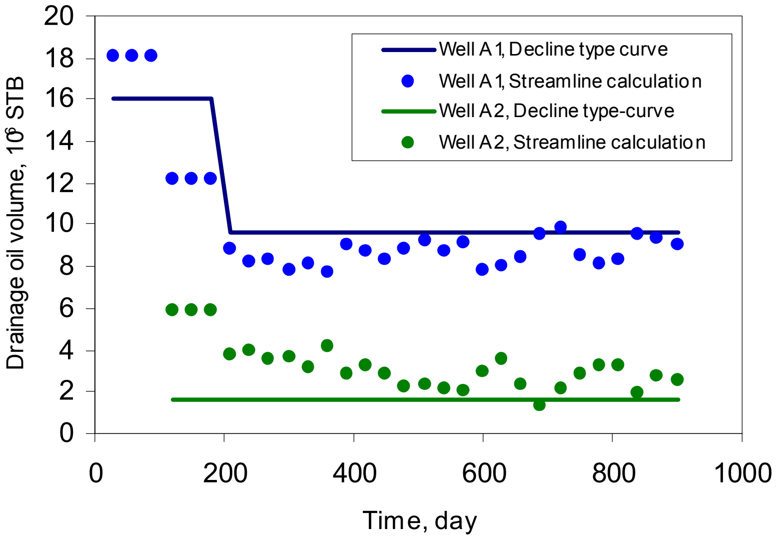

Figure 5.19—Drainage volume matching without flow barriers for wells A1 and A2.

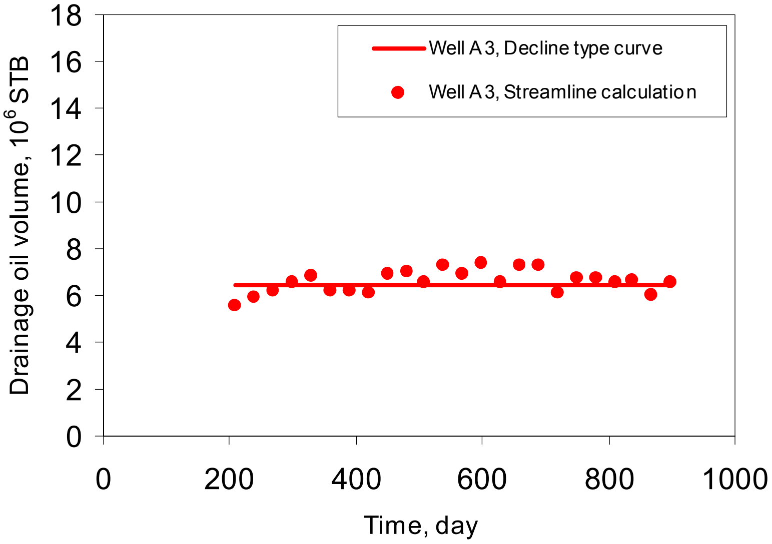

Figure 5.20—Drainage volume matching without flow barriers for well A3.

Finally, we reconcile the drainage volumes of the wells by placing flow barriers into the reservoir model around well A2. For this example, we assume limited or no prior knowledge about the spatial shape of the flow barriers and thus, simply put vertical flow barriers across all three layers. The location of these barriers is same as that shown in **Fig. 5.12b**. After placing these flow barriers in the reservoir model, the drainage volumes from the streamline simulation for all the wells seem to match with those from the decline type-curve analysis (**Fig. 5.21-22**).

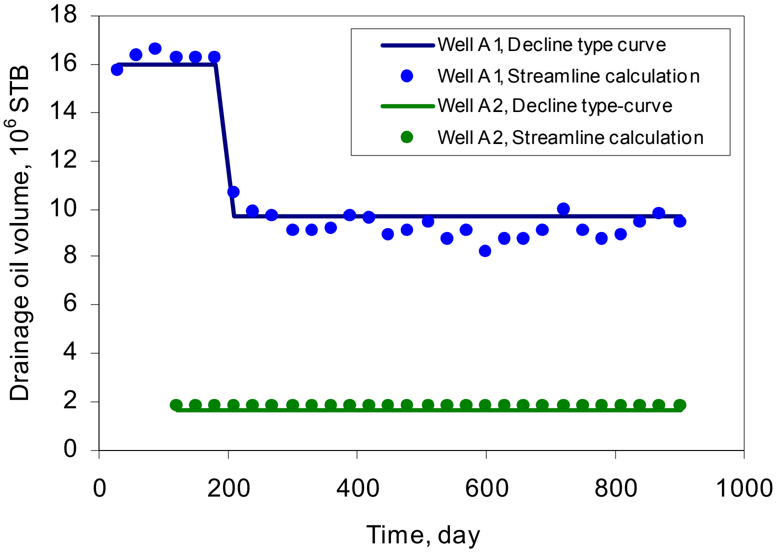

Figure 5.21—Drainage volume matching with flow barriers for wells A1 and A2.

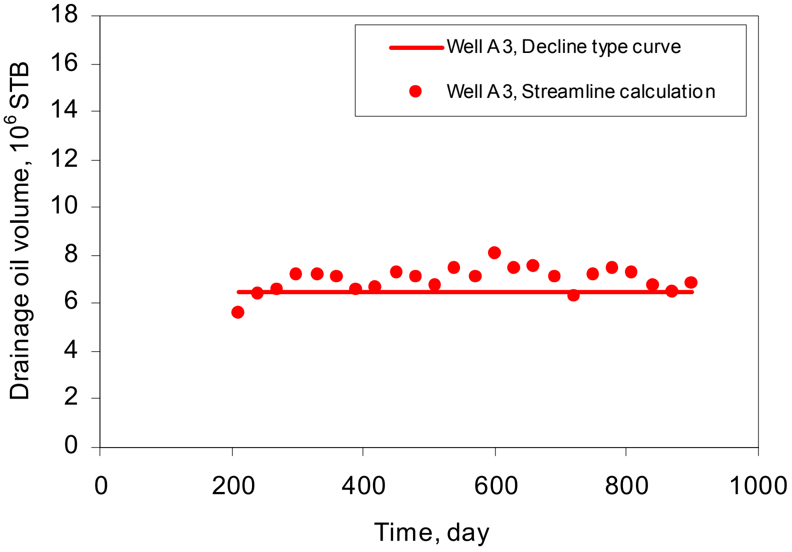

Figure 5.22—Drainage volume matching with flow barriers for well A3.

Fig. 5.23 and **5.24** compare the flowing bottomhole pressures for the wells without and with the flow barriers. Clearly, after the drainage volume matching and placement of flow barriers, we get an excellent match of the pressure response.

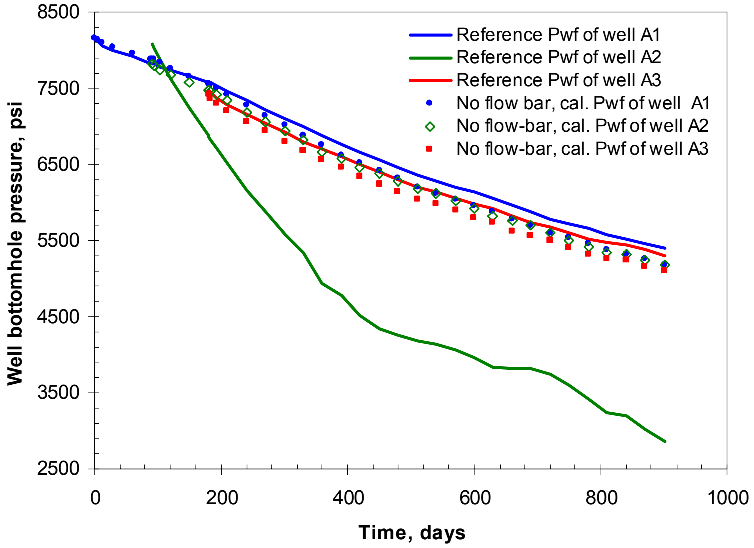

Figure 5.23—Flowing bottomhole pressure matching without flow barriers.

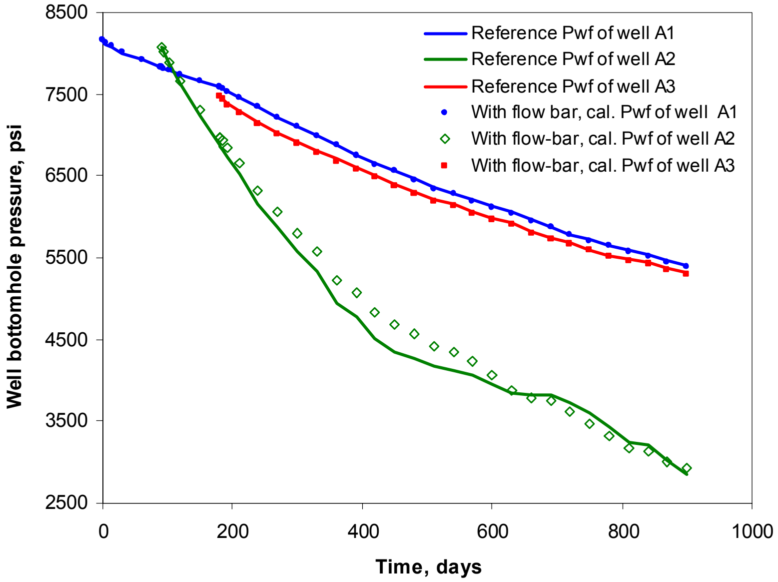

Figure 5.24—Flowing bottomhole pressure matching with flow barriers.

5.4.3 Reservoir Compartmentalization: A Field Example

This field example is from a field in the Gulf of Mexico. It has a single well producing under primary depletion. The production rate and flowing bottomhole pressure (**Fig. 5.25**) are monthly averaged. **Fig. 5.26** shows the decline type-curve matching. The data follows the type-curves pretty well. However, the late-time data appears to systematically fall above the type-curves and runs parallel to the type-curve. This indicates a new pseudo steady-state. In contrast to the concave-down deviation of data noted in our previous examples, such a trend may indicate an extension of the drainage volume. In other words, it may suggest the presence of partially sealing flow barriers that provide production and pressure support at later times via access to additional reservoir volume (compartments). It has been previously observed that a compartmentalized reservoir with a partially sealing flow barrier may result in two pseudo steady-states, the initial one being associated with the producing compartment, and the second one with the whole system.[82] From the decline type-curve matching, we estimated an initial drainage volume is 10.77 MMSTB, and an extended total drainage volume of 12.43 MMSTB based on the type-curve matching of late-time data points **(Fig. 5.27**).

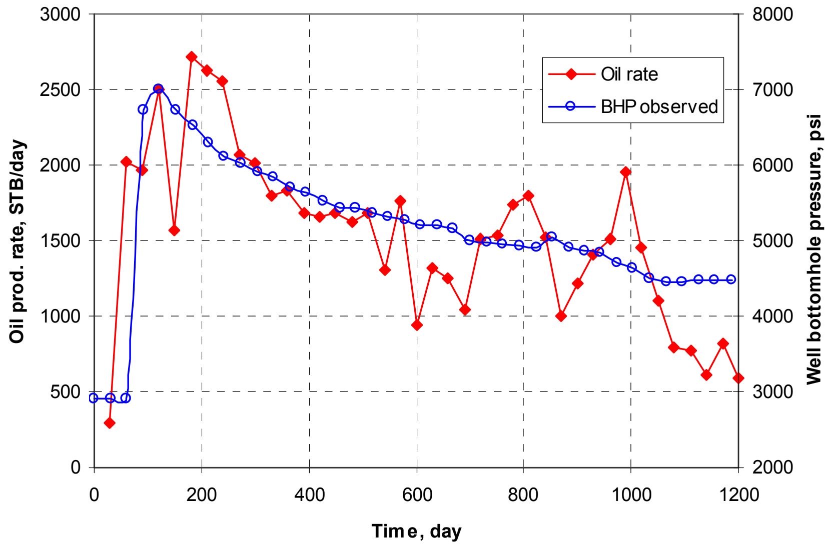

Figure 5.25—Well production rate and flow bottomhole pressure of the production well for the field case.

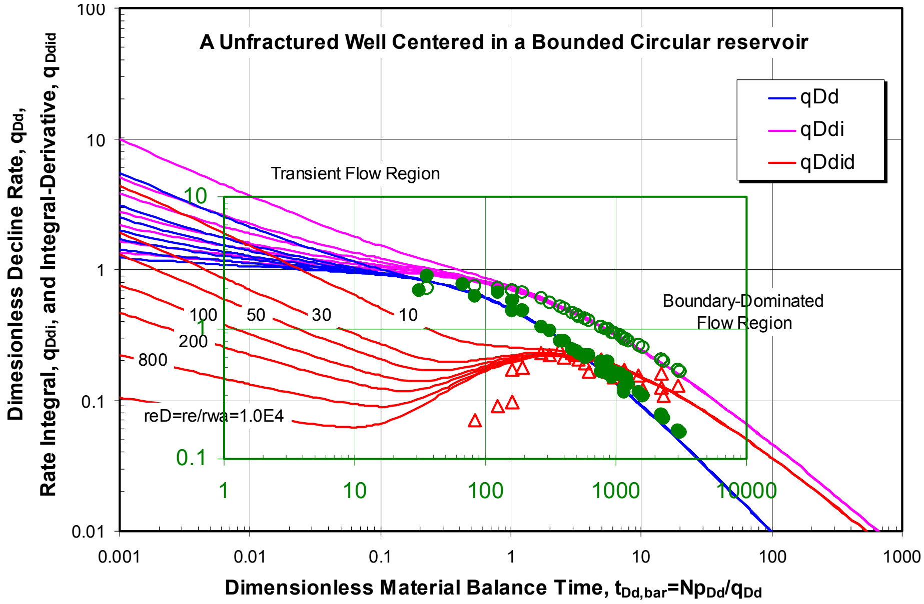

Figure 5.26—Decline type-curve matching of the production well for the field case.

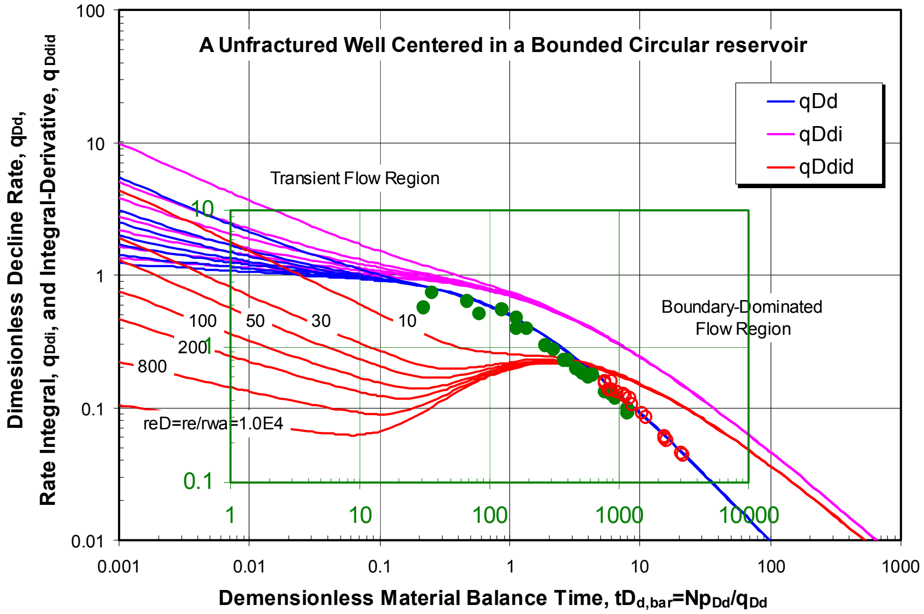

Figure 5.27—Decline type-curve matching of late-time data points.

Next, we compute the drainage volume using streamline simulation. The reservoir model has 77x55x20 grid cells and was constructed using well log and seismic data. **Fig. 5.28** and **5.29** show the permeability and porosity distribution in the reservoir. The OOIP was calculated to be 16.24 MMSTB resulting in a large discrepancy between the drainage volume from the decline type-curve analysis and that from the reservoir model. This appears to indicate that a sealing flow barrier prevents the well draining the whole reservoir. Furthermore, based on the decline curve analysis, there may also be a partially sealing flow barrier isolating a portion of the reservoir from the main reservoir. To locate the potential flow barriers, we examined the distributions of permeability, porosity and oil-footage ($\Phi*h*So$) in the reservoir model for potential trends. Based on low permeability and oil-footage combined with geological input, we placed two flow barriers into the reservoir model (**Fig. 5.30-31**)—a northwest barrier; and a south barrier. We then proceed to investigate the impact of these flow barriers on the drainage volume calculations using streamline simulation.

We investigated several scenarios with respect to the location and transmissibilities of the flow barriers. To start with, we varied the location of south barrier while assuming both the barriers to be almost sealing (a transmissibility multiplier of 0.0001). The results are shown in Table 5.3 and **Fig. 5.32**. This scenario produces the best location of the south barrier at J=26. We then studied the sensitivity of NW barrier transmissibility on the drainage volume. The results are shown in Table 5.4.

Recognizing the non-uniqueness and uncertainty associated with our analysis, we further investigate the barrier location and transmissibility via a statistical experimental design. Table 5.5 shows the various combination of transmissibilities (X1 through X10) of the two barriers selected using a Latin hypercube sampling.[87] The different scenarios for the location of the south barrier range from J=22 to J=28. The simulation results of drainage volume along with the experimental design are summarized in Table 5.6.

TABLE 5.3—COMPARISON OF DRAINAGE VOLUME FOR DIFFERENT LOCATIONS OF THE SOUTH BARRIER

	Location	Trans Multiplier	Streamline simulation	Decline type-curve
			Pseudo Drainage Oil Volume, Npsd, Million STB	Pseudo Drainage Oil Volume, Npsd, Million STB
Case 1	No flow barrier	/	18.2	10.77 ~ 12.43
Case 2	South, J=30	0.0001	10.3 ~ 14.6	
	NW	0.0001		
Case 3	South, J=28	0.0001	10.4 ~ 12.8	
	NW	0.0001		
Case 4	South, J=26	0.0001	10.2 ~ 12.4	
	NW	0.0001		

TABLE 5.4—COMPARISON OF DRAINAGE VOLUME FOR DIFFERENT TRANSMISSIBILITY MULTIPLIERS FOR THE NW BARRIER

	Location	Trans Multiplier	Streamline simulation	Decline type-curve
			Pseudo Drainage Oil Volume, Npsd, Million STB	Pseudo Drainage Oil Volume, Npsd, Million STB
Case 4	South, J=26	0.0001	10.2 ~ 12.4	10.77 ~ 12.43
	NW	0.0001		
Case 5	South, J=26	0.0001	10.0~12.7	
	NW	0.001		
Case 6	South, J=26	0.0001	10.0~13.7	
	NW	0.01		
Case 6	South, J=26	0.0001	10.0~13.7	
	NW	0.1		

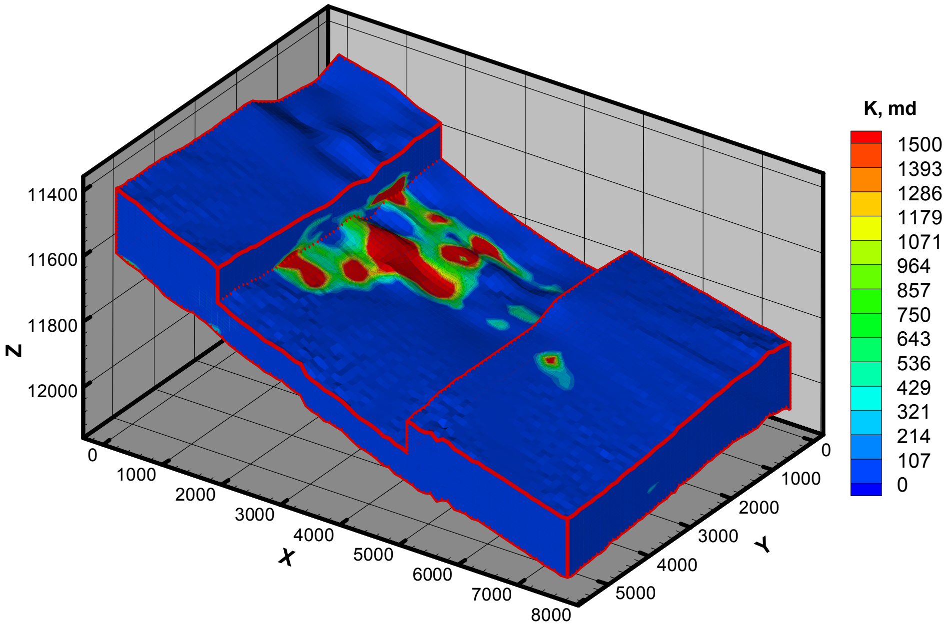

Figure 5.28—Permeability model of the field example.

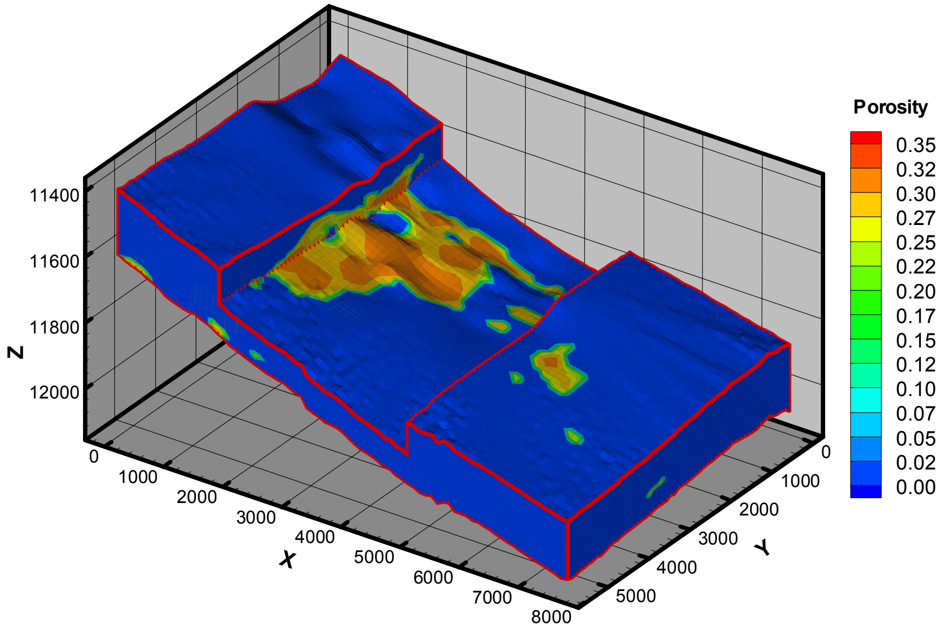

Figure 5.29—Porosity model of the field example.

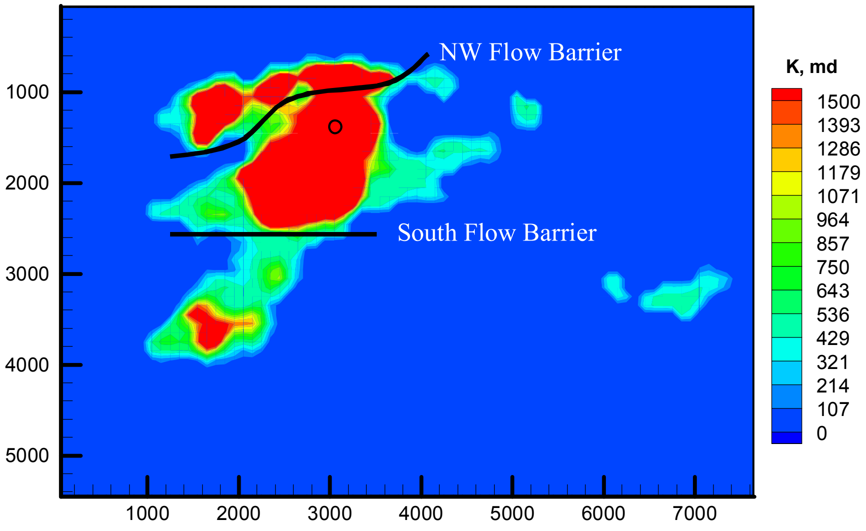

Figure 5.30—Permeability of layer 10 and potential flow barriers.

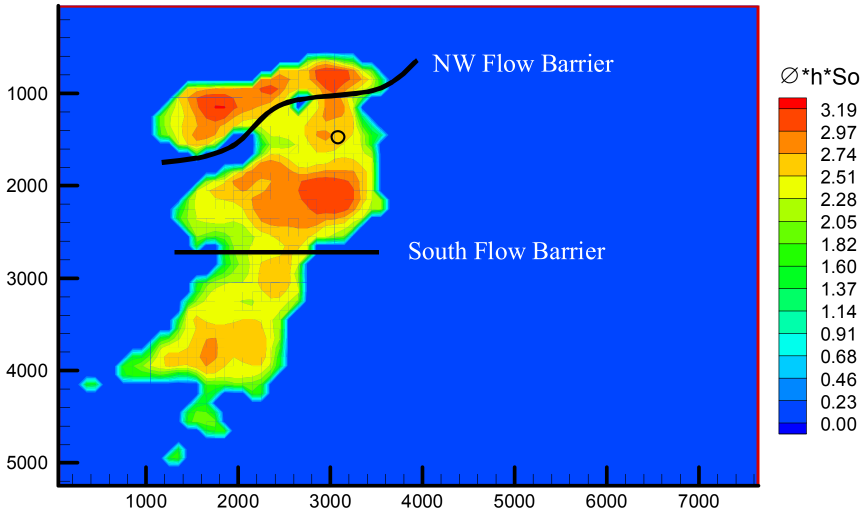

Figure 5.31—Φ*h*So of layer 10 and potential flow barriers.

TABLE 5.5—TRANSMISSIBILITY MULTIPLIERS OF THE SOUTH AND NW BARRIERS OBTAINED USING LATIN HYPERCUBE SAMPLING (LHS)

NV1	NV2	Cases
0.00001	0.58965	X1
0.00031	0.02569	X2
0.07093	0.13699	X3
0.00616	0.00002	X4
0.01924	0.00056	X5
0.00119	0.00006	X6
0.48932	0.0002	X7
0.0006	0.06122	X8
0.00006	0.00897	X9
0.50298	0.00149	X10

Note: NV1 for NW barrier; NV2 for south barrier

TABLE 5.6—EXPERIMENTAL DESIGN SET-UP OF DRAINAGE VOLUME FROM STREAMLINE SIMULATION FOR DIFFERENT SCENERIES

South Barrier Location	X1	X2	X3	X4	X5	X6	X7	X8	X9	X10
	Drainage Volume (Million STB)									
J=22	16.92	16.89	18.19	11.24	12.45	10.57	10.81	17.02	16.51	15.72
J=23	17.05	16.89	18.18	11.18	14.17	11.03	12.07	17.04	16.68	15.74
J = 24	16.94	16.89	18.19	12.89	13.89	11.03	13.03	17.02	16.71	16.84
J = 25	17.10	16.94	18.18	13.31	13.89	12.35	13.37	17.03	16.84	15.33
J = 26	16.93	16.92	18.17	13.54	13.94	12.99	13.54	17.03	16.47	15.18
J = 27	16.98	16.91	18.19	13.71	14.18	13.29	13.88	17.03	16.43	14.74
J = 28	17.05	16.92	18.17	13.93	14.47	13.41	13.98	17.04	16.47	14.99

Based on these results, we performed an analysis of variance (ANOVA) to examine the significance of the location of the south barrier and the transmissibility of both the barriers on the computed drainage volume. The ANOVA included SNK test and Tukey tests[88] and the results indicate that both the location of south flow barrier and the transmissibilities of the barriers have an effect on the drainage volume.

Finally, taking the drainage volume estimated from the decline type-curve analysis as a control value, the mean and standard deviation of the drainage volumes for the various scenarios are summarized in Table 5.7. From this table, we conclude that the most likely scenarios of transmissibility multipliers for the two barriers are X4 and X6. For X4, the transmissibility multiplier of the NW barrier is 0.00616 and that of the south barrier is 0.00002. For X6, transmissibility multiplier of the NW barrier is 0.00119 and that of the south barrier is 0.00006. These results indicate that the NW flow barrier is more leaky compared to the south flow barrier. Under these most likely scenarios of transmissibility multipliers, the south barrier is most likely located at J=24 or J=25, as indicated in the table.

TABLE 5.7—DRAINAGE VOLUME UNCERTAINTIES OVER DIFFERENT TRANSMISSIBILITY MULTIPLIERS AND LOCATION OF BARRIER

TRANS	N	Mean, MMSTB	Mean-12.43, MMSTB	Std Dev, MMSTB
X1	7	16.99	4.56	0.08
X2	7	16.91	4.48	0.02
X3	7	18.18	5.75	0.01
X4	7	12.83	0.4	1.15
X5	7	13.86	1.43	0.65
X6	7	12.09	-0.34	1.2
X7	7	12.95	0.52	1.14
X8	7	17.03	4.6	0.01
X9	7	16.59	4.16	0.16
X10	7	15.51	3.08	0.69

South Barrier Location	X4	X6
	Drainage Volume, MMSTB	
J=22	11.24	10.57
J=23	11.18	11.03
J = 24	12.89	11.03
J = 25	13.31	12.35
J = 26	13.54	12.99
J = 27	13.71	13.29
J = 28	13.93	13.41

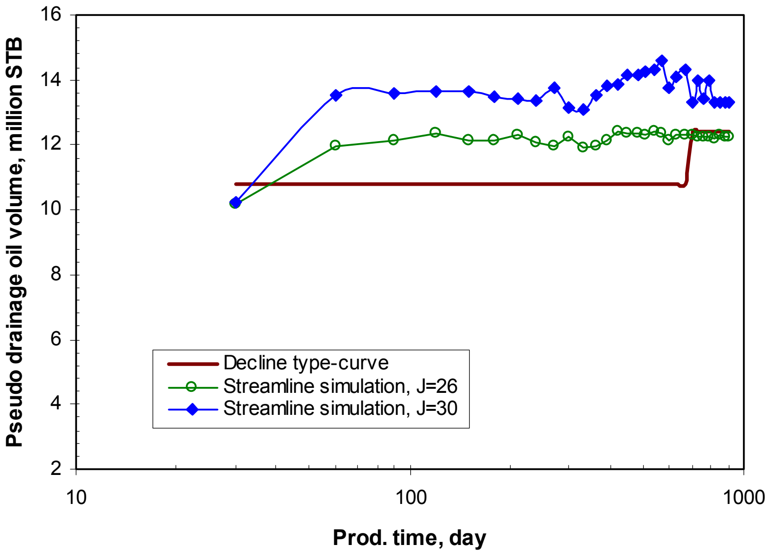

Figure 5.32—Drainage volume matching for different south barrier locations of X6 and J=25.

We then perform simulation using one of the most likely scenario – X6 and J=25 and a permeability multiplier of 0.15 to predict the flowing bottomhole pressure. The result is shown in **Fig. 33**. Overall, the match with the field data is very good, which further validates our approach. We should note that one could also use direct matching of pressure to identify reservoir compartmentalization and flow barriers, however, this is generally not effective and often leads to inadequate identification and poor matching of pressure, since both permeability field and drainage volume control the pressure behavior. Since the permeability model usually contains large uncertainties, one has to play with both permeability and reservoir compartmentalization/flow barriers in order to match the pressure. In contrast, drainage volume matching provides an additional constraint for pressure matching. As the result, pressure matching can be much more easily obtained.

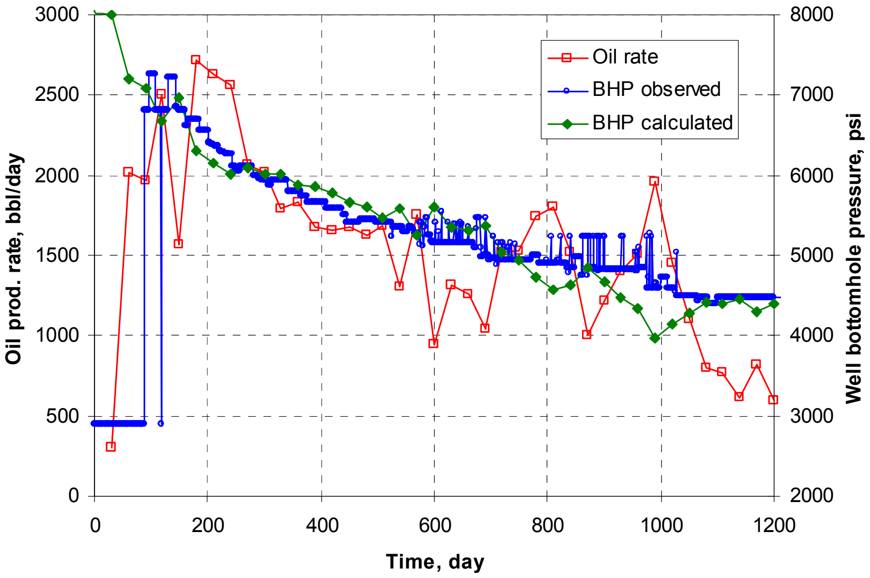

Figure 5.33—Calculated bottomhole pressure vs. observed one for scenario of X6 and J=25.

We also simulated the bottomhole pressure on other two scenarios from the experimental design that give the highest and lowest drainage volume values, respectively. These two scenarios are X2 - J=25 (drainage volume is 16.94 MMSTB from Table 5.6) and X7 - J=22 (drainage volume is 10.81 MMSTB from Table 5.6). The same permeability multiplier of 0.15 was used in the simulation. **Fig. 5.34** and **Fig. 5.35** show the comparison of simulated bottomhole pressure with the observed bottomhole pressure for these two scenarios. It is clear that the pressure matches are much worse compared to the most likely scenario.

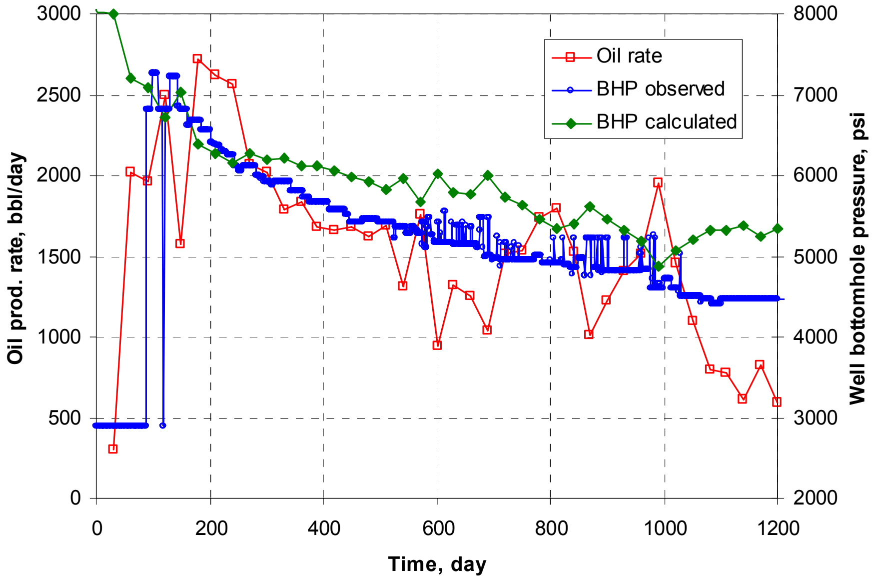

Figure 5.34—Calculated bottomhole pressure vs. observed one for scenario of X2 and J=25.

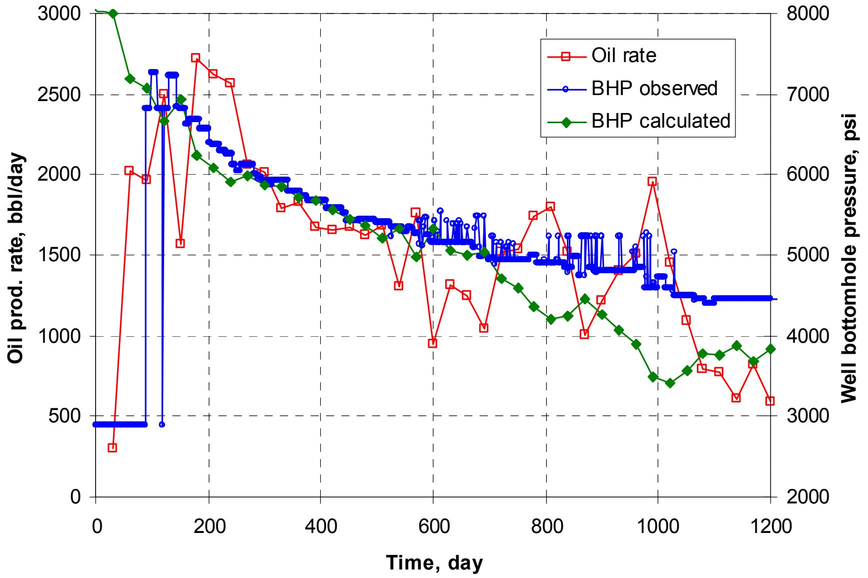

Figure 5.35—Calculated bottomhole pressure vs. observed one for scenario of X7 and J=22.

5.5 Chapter Summary

We have proposed a novel approach to infer reservoir compartmentalization and flow barriers using streamline models and decline type-curve analysis. Our approach is general and relies on commonly available data viz. production rate and flowing bottomhole pressure. An attractive feature of our approach is that it is well-suited for application in the early stages of field development with limited well data and the results are relatively insensitive to small-scale heterogeneities that may be difficult to characterize. Streamline-based drainage volume calculations in conjunction with conventional decline type curve analysis can provide a powerful approach to identification of reservoir compartmentalization and flow barriers during early stages of reservoir development. Our proposed approach relies on inferring flow barriers and reservoir compartmentalization based on a drainage volume matching. Thus, the results will be non-unique in general and will require prior geologic knowledge or additional information to address such non-uniqueness. We have presented a statistical experimental design and an analysis of variance based on a Monte-Carlo analysis to quantify the uncertainty in the location and strength of the barriers. We have validated our approach using 2D and 3D synthetic examples. Finally, a field example from the Gulf of Mexico demonstrates the practical feasibility of our method. In this example, reservoir compartmentalization and flow barriers are identified using three years of primary production response.

CHAPTER VI

CONCLUSIONS AND RECOMMENDATIONS

6.1 Conclusions

Integration of dynamic data has been a critical yet very challenging task in reservoir description. In this work we developed effective and novel production data integration techniques based on streamline approaches to condition static geological models to various kinds of dynamic data, including two-phase production history, interference pressure observations and primary production data. The proposed techniques can integrate the two-phase production history and interference pressure data into high-resolution reservoir models, and utilize primary production data to identify reservoir compartmentalization and flow barriers. We adopted a methodology of parameter estimation that combines fast streamline simulations, analytical sensitivity computations, efficient inversion procedures and regularization of objective function in minimization, and developed highly computationally efficient and robust inversion techniques for dynamic data integration. As a result, these techniques are well-suited to large-scale field applications and provide technical feasibilities for routine integration of dynamic data during reservoir characterization and management.

The specific conclusions of this work are summarized as follows.

- **On integration of two-phase production data into high-resolution reservoir models**

1. **Fast streamline simulation as the forward model.** Streamline simulation serves as an efficient forward model in an inverse modeling. Its high speed of simulation results from the decoupling between pressure and transport calculation. Changing field conditions are accounted via pressure updating. As an extension, compressibility and gravity are included into the streamline model.

2. **Efficient inversion procedures - travel-time inversion and generalized travel-time inversion.** Travel-time inversion and ‘generalized travel–time’ inversion are used for fast and stable inversion. The concept of travel-time is generalized by defining a ‘travel time shift’ derived by maximizing a cross-correlation between the observed and computed production responses for each well. The ‘generalized travel-time’ inversion ensures matching of entire production responses rather than just a single time point while retaining most of the quasi-linear property of travel-time inversion. These inversion procedures appears to be very general, robust and computationally efficient, and particularly well-suited for large-scale field applications.

3. **Analytic sensitivity computation along streamlines.** Streamline-based analytic formulations have been developed to directly compute sensitivities of production data with respect to reservoir properties. Gravity and changing field conditions are accounted for in the computation. The sensitivities for all the reservoir parameters can be obtained using a single forward simulation, resulting in significant savings of computation time.

4. **Successful applications to large-scale field examples.** Our inversion techniques have been successfully applied to large-scale field examples with the ability of accounting for the realistic field conditions, such as rate changes, infill drilling, recompletion, etc. One of these field applications is a giant middle-eastern oil field. Our approach has been able to condition the geological model to over 30 years of water-cut history in about 6 CPU hours with significant improvement in the production history match.

- **On integration of interference pressure data into reservoir models**

5. **Alternating inversion of travel-time and peak amplitude or pressure.** An alternating two-step inversion of travel-time match followed by peak amplitude match or pressure match is proposed in order to improve the overall matching of pressure. The inversion can be in multiple cycles and the switch of objective functions during the inversion helps the minimization to avoid local minimum. However, it should be pointed out that the first-cycle of travel-time inversion plays a vital role in the process of inversion as it produces most of the features in the estimated model.

6. **Analytical computation of sensitivities.** Analytic approaches for computing the sensitivities of travel-time, peak amplitude and pressure are developed using the concept of streamline 'diffusive' time of flight and zero-order asymptotic solution. In particular, like the sensitivities of travel-time and peak amplitude, pressure sensitivity can also be computed analytically in an approximate manner using a single forward simulation. This new approach for pressure sensitivity computations is much more computationally efficient over existing approaches that require multiple forward simulations.

7. **Practical application to field interference tests.** The proposed inversion approach was applied to characterize a naturally fractured reservoir. An orthogonal fracture pattern appears in the inferred permeability model after integrating one interference test. The results are consistent with independent geophysical experiments and the core observations from a slant well drilled later. Moreover, based on the inferred permeability model, we have been able to successfully predict another interference test (the prediction shows good match to the observed pressure responses).

- **On identification of reservoir compartmentalization and flow barriers using primary production data**

8. **Streamline-based drainage volume calculation.** Streamline models can be utilized to compute drainage volume during primary depletion or compressible flow based on the concept of a 'diffusive' time of flight. The 'diffusive' time of flight is closely related to the concept of drainage volume and drainage radius, and can be used to determine the drainage volumes in 3D heterogeneous media with multiple wells and under general conditions.

9. **Drainage volume matching.** We proposed a novel approach to infer reservoir compartmentalization and flow barriers based on a matching of drainage volumes from streamline model and decline type-curve analysis. The approach is well-suited for application in the early stages of field development with limited well data. The practical feasibility of our proposed method was demonstrated with a field example.

6.2 Recommendations

As discussed in the introduction, one of the difficulties in the dynamic data integration is that the data are sparse and have low resolution. So it is very important to incorporate all available data in the integration. Integration of 4D seismic data is becoming more important because it provides the spatial information about the reservoir in contrast to the other data that are localized at the wells. Joint integration of various kinds of dynamic data, such as water-cut history, pressure data, 4D seismic data, can maximize the values of the data. Therefore, development of efficient techniques for joint inversion is an excellent area for research.

Current streamline models and analytical methods of sensitivity calculation are limited to two-phase water/oil flow. This works well in the cases of pressure maintenance with little gas production. In case of significant gas production, current methods need to be extended to three-phase flow.

The forward model used in the inversion of interference pressure data is a single porosity simulator. We have used it to model the interference pressure responses for a naturally fractured reservoir by considering a single storage of fracture + matrix system. Although the late time pressure behavior can be properly modeled, it can't correctly model the early pressure behavior from the storage of fracture system. It is necessary to develop a dual-porosity simulator and the associated sensitivity computation methods to improve the inversion for a naturally fractured reservoir.

Another area for research can be the transformation of reservoir parameters during the inversion. We have observed that use of the logarithm of permeability as the parameter in the minimization is helpful to obtain better convergence. It seems that proper transformation of parameters can reduce the non-linearity of the inverse problem. This area can be further explored.

NOMENCLATURE

A = drainage area
$\mathbf{A}$ = large sparse unsymmetric matrix
$\mathrm{A_o}$ = zero-order amplitude of wave
$\mathrm{A_{i,j}}$ = cross section area between grids *i* and *j*
$\mathrm{B_o}$ = formation volume factor of oil
$\mathbf{B}$ = bidiagonal matrix
$\mathrm{C_A}$ = shape factor of drainage area
c_t = total compressibility
$\mathbf{d}$ = data vector
D = depth
F_w = water fractional flow
g = gravitational constant
G = Green's function
$\mathrm{G_w}$ = water phase velocity resulting from gravity
$\mathbf{I}$ = identity matrix
J = objective function or Jacobian of coordinator transformation
k = permeability
$\mathbf{K}$ = permeability tensor
$\mathbf{L}$ = spatial difference operator
m = reservoir parameter
$\mathbf{m}$ = parameter vector
M = number of reservoir parameters
N = drainage volume
N_p = cumulative production of well
N_{dj} = number of dynamic data observations of *jth* well
N_w = number of wells
P = pressure
P_D = dimensionless pressure
P_i = initial reservoir pressure

P_{wf} = flow bottomhole pressure of well
q = source/sink term
q_{Dd} = dimensionless production rate
$\mathbf{R}$ = vector of parameter change
$\mathrm{r_D}$ = dimensionless distance
$\mathbf{r}$ = residual vector
R^2 = coefficient of determination
s = distance along the streamline
$s(\mathbf{x})$ = slowness
S_w = water saturation
t = time
t_D = dimensionless time
$\bar{t}$ = material balance time
$\bar{t}_{Dd}$ = dimensionless material balance time
$\Delta \mathrm{t}$ = travel time shift
$\Delta\tilde{t}$ = generalized travel time
$\mathbf{v}$ = velocity vector
$\mathrm{V_j}$ = volume of grid j
$\mathbf{x}$ = spatial coordinate vector
y^{cal} = calculated response
y^{obs} = observed response
$\overline{y^{obs}}$ = averaged observed response
α = diffusivity
β = weighting factor
ρ = density of fluid
μ = viscosity of fluid
ϕ = porosity
λ_t = total relative mobility
τ = time of flight or diffusive time of flight
ψ, χ = bi-streamline functions
ω = frequency

ϖ' = dimensionless storage coefficient

λ' = dimensionless transfer coefficient

γ = Euler constant

ξ, η, s = curvilinear coordinates of streamline

REFERENCES

1. Tarantola, A.: *Inverse Problem Theory – Methods for Data Fitting and Model Parameter Estimation*, Elsevier Science Publishers, Amsterdam, The Netherlands, 1987.
2. Tikhonov, A.N. and Arsenin, V.Y.: *Solution of Ill-Posed Problems*, Halsted Press, New York, 1977.
3. Yeh, W. W-G.: "Review of Parameter Identification Procedures in Groundwater Hydrology: The Inverse Problem," *Water Resources Research* (1986), **22**(2), 95-108.
4. McLaughlin, D., and Townley, L.R.: "A Reassessment of the Groundwater Inverse Problem," *Water Resources Research* (1996), **32**(5), 1131-1161.
5. Anterion, F., Eymard, R., and Karcher, B.: "Use of Parameter Gradients for Reservoir History Matching," paper SPE 18433 presented at the 1989 SPE Symposium on Reservoir Simulation, Houston, TX, February 6-8.
6. Tang, Y.N., Chen, Y.M., Chen, W.H., and Wasserman, M.L.: "Generalized Pulse-Spectrum Technique for 2-D and 2-Phase History Matching," *Applied Numerical Mathematics* (1989), **5**(4), 529-539.
7. Chu, L., Reynolds, A.C., and Oliver, D.S.: "Computation of Sensitivity Coefficients for Conditioning the Permeability Field to Well-Test Pressure Data," *In Situ* (1995), **19**(2), 179-223.
8. Jacquard, P. and Jain, C.: "Permeability Distribution From Field Pressure Data," *SPE Journal* (1965), **5**(4), 281-294.
9. Carter, R.D., Kemp, Jr., L.F., Pierce, A.C., and Williams, D.L.: "Performance Matching With Constraints," *SPE Journal* (1974), **14**(2), 187-196.
10. Dogru, A.H. and Seinfeld, J.H.: "Comparison of Sensitivity Coefficient Calculation Methods in Automatic History Matching," *SPE Journal* (1981), **21**(5), 551-557.
11. He, N., Reynolds, A.C., and Oliver, D.S.: "Three-Dimensional Reservoir Description From Multiwell Pressure Data and Prior Information," *SPE Journal* (1997), **2**(3), 312-327.
12. Chen, W.H., Gavalas, G.R., Seinfeld, J.H., and Wasserman, M.L.: "A New Algorithm for Automatic History Matching," *SPE Journal* (1974), **14**(6), 593-608.
13. Chavent, G.M., Dupuy, M., and Lemonnier, P.: "History Matching by Use of Optimal Control Theory," *SPE Journal* (1975), **15**(1), 74-86.

14. Carter, R.D., Kemp, L.F., and Pierce, A.C.: "Discussion of Comparison of Sensitivity Coefficient Calculation Methods in Automatic History Matching," *SPE Journal* (1982), **22**(2), 205-208.
15. Watson, A.T., Seinfeld, J.H., Gavalas, G.R., and Woo, P.T.: "History Matching in Two-Phase Petroleum Reservoirs," *SPE Journal* (1980), **20**(6), 521-532.
16. Wu, Z., Reynolds, A.C., and Oliver, D.S.: "Conditioning Geostatistical Models to Two-Phase Production Data," *SPE Journal* (1999), **4**(2), 142-155.
17. Vasco, D.W., Yoon, S., and Datta-Gupta, A.: "Integrating Dynamic Data Into High-Resolution Reservoir Models Using Streamline-Based Analytic Sensitivity Coefficients," *SPE Journal* (1999), **4**(4), 389-399.
18. Datta-Gupta, A. *et al.:* "Streamlines, Ray Tracing and Production Tomography: Generalization to Compressible Flow," *Petroleum Geoscience* (2001), 7, S75-S86.
19. Yoon, S., Barman, I., Datta-Gupta, A., and Pope, G.A. : "In-Situ Characterization of Residual NAPL Distribution Using Streamline-Based Inversion of Partitioning Tracer Tests," paper SPE 52729 presented at the 1999 SPE/EPA Exploration and Production Environmental Conference, Austin, TX, March 1-3.
20. King, M.J. and Datta-Gupta, A.: "Streamline Simulation: A Current Perspective," *In Situ* (1998), **22**(1), 91-140.
21. Batycky, R. P., Blunt, M. J., and Thiele, M. R.: "A 3-D Field Scale Streamline-Based Reservoir Simulator," *SPE Reservoir Engineering* (1997), **12**(4), 246-254.
22. Sen, M.K., Datta-Gupta, A., Stoffa, P.L., Lake, L.W., and Pope, G.A.: "Stochastic Reservoir Modeling Using Simulated Annealing and Genetic Algorithms," *SPE Formation Evaluation* (1995), **10**(1), 49-50.
23. Datta-Gupta, A., Lake, L.W., and Pope, G.A.: "Characterizing Heterogeneous Permeable Media With Spatial Statistics and Tracer Data Using Sequential Simulated Annealing," *Mathematical Geology* (1995), **27**(6), 763-787.
24. Vasco, D. W. and Datta-Gupta, A., Long, J.C.S.: "Integrating Field Production History in Stochastic Reservoir Characterization," paper SPE 36567 presented at the 1996 SPE Annual Technical Conference and Exhibition, Denver, CO, October 6-9.
25. Datta-Gupta, A., Vasco, D. W., Long, J. C. S., D'Onfro, P. S., and Rizer, W. D.: "Detailed Characterization of a Fractured Limestone Formation by Use of Stochastic Inverse Approach," *SPE Formation Evaluation* (1995), **10**(3), 133-140.

26. Sagar, R. K., Kelkar, M. G., and Thomson, L. G.: "Reservoir Description by Integrating Well-Test Data and Spatial Statistics," *SPE Formation Evaluation* (1995), **10**(4), 267-274.
27. Cobenas, R. H., Aprilian, S. S. and Datta-Gupta, A.: "A Closer Look at Non-Uniqueness During Dynamic Data Integration Into Reservoir Characterization," paper SPE 39669 presented at the 1998 SPE/DOE Improved Oil Recovery Symposium, Tulsa, OK, April 19-22.
28. Gavalas, G.R., Shah, P.C., and Seinfeld, J.H.: "Reservoir History Matching by Bayesian Estimation," *SPE Journal* (1976), **16**(6), 337-350.
29. Oliver, D. S.: "Incorporation of Transient Pressure Data Into Reservoir Characterization," *In Situ* (1994), **18**(3), 243-275.
30. Carrera, J. and Neuman, S.P.: "Estimation of Aquifer Parameters Under Transient and Steady State Conditions: 1. Maximum Likelihood Method Incorporating Prior Information," *Water Resources Research* (1986), **22**(2), 199-210.
31. Phillips, W.S. and Fehler, M.C.: "Traveltime Tomography: A Comparison of Popular Methods," *Geophysics* (1991), **56**(10), 1639-1649.
32. Nemeth, T., Normark, E., and Qin, F.: "Dynamic Smoothing in Crosswell Traveltime Tomography," *Geophysics* (1997), **62**(1), 168-176.
33. Zhou, C., Cai, W., Luo, Y., Schuster, G.T., and Hassanzadeh, S.: "Acoustic Wave-equation Traveltime and Waveform Inversion of Crosshole Seismic Data," *Geophysics* (1995), **60**(3), 765-773.
34. Luo, Y. and Schuster, G.T.: "Wave-equation Traveltime Inversion," *Geophysics* (1991), **56**(5), 645-653
35. Kulkarni, K.N., Datta-Gupta, A. and Vasco, D.W.: "A Streamline Approach for Integrating Transient Pressure Data Into High-Resolution Reservoir Models," *SPE Journal* (September 2001), 273.
36. Vasco, D. W., Karasaki, K., and Keers, H.: "Estimation of Reservoir Properties Using Transient Pressure Data: An Asymptotic Approach," *Water Resour. Res.* (2000), 36, 3447-3465
37. Cheng, H., He, Z., and Datta-Gupta, A.: "A Comparison of Travel-Time and Amplitude Matching for Field-Scale Production Data Integration: Sensitivity, Non-Linearity and Practical Implications," paper SPE 84570 to be presented at the 2003 SPE Annual Technical Meeting, Denver, CO, Oct. 4-8.

38. Idrobo, E.A., Choudhary, M.K., and Datta-Gupta, A.: “Swept Volume Calculations and Ranking of Geostatistical Reservoir Models Using Streamline Simulation,” paper SPE 62557 prepared for presentation at the 2000 SPE/AAPG Western Regional Meeting, Long Beach, CA, June 19-23.
39. Parker, R.L.: *Geophysical Inverse Theory*, Princeton University Press, Princeton, NJ, 1994.
40. Paige, C. C. and Saunders, M. A.: “LSQR: An Algorithm for Sparse Linear Equations and Sparse Least Squares,” *ACM Transactions on Mathematical Software* (1982), **8**(1), 43-71.
41. Nolet, G., Seismic Wave Propagation and Seismic Tomography, *Seismic Tomography* (1987), 1-23.
42. Bissel, R.C.: “Calculating Optimal Parameter for History Matching,” *Proc*. 4th European Conference on the Mathematics of Oil Recovery, Topic E: History Match and Recovery Optimization, 1994.
43. Landa, J.L., Kamal, M.M., Jenkins, C.D., and Horne, R.N.: Reservoir Characterization Constrained to Well Test Data: A Field Example,” paper SPE 36511 presented at the 1996 SPE Annual Technical Conference and Exhibition, Denver, CO, October 6-9.
44. Reynolds, A. C., He, N., and Oliver, D.S.: “Reducing Uncertainty in Geostatistical Description with Well Testing Pressure Data,” in Proc., 1997 International Reservoir Characterization Conference, Houston, TX, March 2-4.
45. Wen, X., Deutsch, C. V., and Cullick, A. S.: “High Resolution Reservoir Models Integrating Multiple-Well Production Data,” SPE 32728, Presented at the 1997 SPE Annual Technical Conference and Exhibition, San Antonio, TX, October 5-8.
46. Landa, J. L., and Horne, R. N.: “A Procedure to Integrate Well Test Data, Reservoir Performance History, and 4-D Seismic Information into a Reservoir Description,” paper SPE 38653 presented at the 1997 SPE Annual Technical Conference and Exhibition, San Antonio, TX, October 5-8.
47. Yoon, S., Malallah, A.H., Datta-Gupta, A. and Vasco, D.W.: “A Multiscale Approach to Production Data Integration Using Streamline Models,” paper SPE 56653 presented at the 1999 SPE Annual Technical Conference and Exhibition, Houston, TX, Oct. 3-6.
48. Milliken, W. J., Emanuel, A. S. and Chakravarty, A., “Application of 3-D Streamline Simulation to Assist History Matching,” SPE 63155 presented at the 2000 SPE Annual Technical Conference and Exhibition, Dallas, TX, October 1-4.

49. Wang, Y. and Kovscek, A. R., "Streamline Approach to History Matching Production Data," *SPEJ* (December 2000), **5**, 353-362.
50. Datta-Gupta, A. and King, M. J.: "A Semianalytic Approach to Tracer Flow Modeling in Heterogeneous Permeable Media," *Advances in Water Resources* (1995), **18**(1), 9-24.
51. Deutsch, C.V. and Journel, A.G.: *GSLIB: Geostatistical Software Library and User's Guide*, Oxford University Press, New York, 1997.
52. Kompanik, G. S., Hell, R. J., Al-Shammary, Z. A. and Al-Shammary, M. J., "Geologic Modeling for Reservoir Simulation: Hanifa Reservoir, Berri Field, Saudi Arabia," SPE 25580 presented at the 1993 SPE Middle-East Technical Conference and Exhibition, Bahrain, April 3-6.
53. Rahman, A., Sunbul, M. S. and McGuire, M. D., "Case Study: Performance of a Complex Carbonate Reservoir Under Peripheral Water Injection," SPE 21370 presented at the 1991 SPE Middle-East Technical Conference and Exhibition, Bahrain, April 3-6.
54. Al Qassab, H., Rahmeh, B. A., Al Khalifa, A., Awami, Bassam and Sarkar, A., "Conditioning Integrated Geological Models to Dynamic Flow Data of Giant Saudi Arabian Reservoir," SPE 71319 presented at the 2001 Annual Technical Conference and Exhibition, New Orleans,LA, Sept. 30-Oct. 2.
55. Behrens, R.A., MacLeod, M.K., Tran, T.T., and Alimi, A.O.: "Incorporating Seismic Attribute Maps in 3D Reservoir Models," *SPE Reservoir Evaluation and Engineering* (April 1998), 122.
56. Lee, S. H., Malallah, A., Datta-Gupta, A. and Higdon, D., "Multiscale Data Integration Using Markov Random Fields," *SPE Reservoir Evaluation and Engineering*, (February 2002).
57. Vela, S., and McKinley, R.M.: "How Areal Heterogeneities Affect Pulse-Test Results," *SPE Journal* (June, 1970), 181-191.
58. Bourdet, D., Ayoub, J.A., and Pirard, Y.M.: "Use of Pressure Derivative in Well-Test Interpretation," *SPE Formation. Evaluation* (1989), **4**(2), 293-302.
59. Lee, J.: *Well Testing*, Society of Petroleum Engineers of AIME, New York, 1982.
60. Horne, R.N.: *Modern Well Test Analysis: A Computer-Aided Approach*, second edition, Petroway, Inc., Palo Alto, CA, 1995.
61. Oliver, D. S. *et al.*: "Integration of Production Data into Reservoir Models," *Petroleum Geoscience* (2001), **7**, S65-S73.

62. Virieux, J., Flores-Luna, C. and Gibert, D.: "Asymptotic Theory for Diffusive Electromagnetic Imaging," *Geophys. J. Int.* (1994) **119**, 857.
63. Fatemi, E., Engquist, B. and Osher, S.: "Numerical Solution of the High Frequency Asymptotic Expansion of the Scalar Wave Equation," *Journal of Computational Physics* (1995) **120**, 145-155.
64. Kline, M. and Kay, I.W.: *Electromagnetic Theory and Geometrical Optics,* John Wiley and Sons, 1965.
65. Cerveny, V., Molotkov, I. A. and Psensik, I.: *The Ray Method in Seismology*, Charles Univ. Press, Prague, 1978.
66. Bear, J.: *Dynamics of Fluid in Porous Media*, American Elsevier, New York, 1972.
67. Bratvedt, F., Bratvedt, K., Buchholz, C. F., Holden, L., Holden, H. and Risebro, N. H.: "A New Front Tracking Method for Reservoir Simulation," *SPE Reservoir Engineering* (1992), **7**(1), 107-116.
68. Kravtsov, Y.A., and Orlov, Y. I.: *Geometrical Optics of Inhomogeneous Media*, Springer-Verlag, New York, 1990.
69. Carslaw, H. S., and Jaeger, J.C.: *Conduction of Heat in Solids*, Oxford University Press, 1959.
70. Ozisik, M. N.: *Heat Conduction*, John Wiley and Sons, New York, 1980.
71. Majer, E.L., Datta-Gupta, A., Peterson, J.E., Vasco, D.W., and Myer, L.R. *et al.*: "Utilizing Crosswell, Single Well and Pressure Transient Tests for Characterizing Fractured Gas Reservoirs," *The Leading Edge* (1996), **15**, 951-56.
72. D'Onfro, P.S., Rizer, W.D., Queen, J.H., Majer, E.L., and Peterson, J.E. *et al.*: "An Integrated Approach for Characterizing Fractured Reservoirs, in Faulting, Fault Sealing, and Fluid Flow in Hydrocarbon Reservoirs," *Geol. Soc. London, Special Publ.* (1998), 193-208.
73. Chen, C. *et al.*: "Pressure Responses at Observation Wells in Fractured Reservoir," paper SPE 10839 presented at the 1982 SPE/DOE Unconventional Gas Recovery Symposium, Pittsburgh, PA, May 16-18.
74. Dean, R. H. and Lo, L. L.: "Simulations of Naturally Fractured Reservoirs," *SPE Reservoir Engineering* (May 1988), **3**(2), 638-648.

75. Junkin, J.E., Sippel, M.A., and Lord, M.E.: "Well Performance Evidence for Compartmented Geometry of Oil and Gas Reservoirs," paper SPE 24365 presented at the 1992 SPE Rocky Mountain Regional Meeting, Casper, WY, May 18-21, 1992.

76. Lord, M.E.: "Detecting Compartmented Gas Reservoir through Production Performance," paper SPE 22941 presented at the 1991 SPE Annual Technical Conference and Exhibition, Dallas, TX, Oct. 6-9.

77. Fox, M.J., Chedburn, A.C.S., and Stewart, G.: "Simple Charaterization of Communication Between Reservoir Regions," paper SPE 18360 presented at the 1998 SPE European Petroleum Conference, London, UK, Oct. 16-19.

78. Ursin, J-R.: "Fault Block Modelling - An Alternative Simulation Tool for Strongly Compartmentalized Gas Reservoirs," *JCPT* (Nov. 2001), **40**, 42-49.

79. Hagort, J. and Hoogstra, R.: "Numerical Solution of the Material Balance Equations of Compartmented Gas Reservoir," *SPE Reservoir Evaluation and Engineering* (Aug. 1999), 385.

80. Ehllg-Economides, C.A.: "Application for Multiphase Compartmentalized Material Balance," paper SPE 27999 presented at the Univ. of Tulsa Centennial Petroleum Engineering Symposium, Tulsa, OK, Aug. 29-31, 1994.

81. Stewart, G. and Whaballa, A.E.: "Pressure Behavior of Compartmentalized Reservoirs," paper SPE 19779 presented at the 1989 SPE Annual Technical Conference and Exhibition, San Antonio, TX, Oct. 8-11.

82. Rahman, N.M.A., and Ambastha, A.K.: "Generalized 3D Analytical Model for Transient Flow in Compartmentalized Reservoir," *SPE Journal* (Sept. 2001), 276.

83. Palacio, J.C. and Blasingame, T.A.: "Decline Curve Analysis Using Type Curves: Analysis of Gas Well Production Data," paper SPE 25909 presented at the 1993 SPE Rocky Mountain Regional/Low Permeability Reservoirs Symposium, Denver, CO, April 12-14.

84. Doublet, L.E. *et al.*: "Decline Curve Analysis Using Type Curve- Analysis of Oil Well production Using Material Balance Time: Application to Field Cases," paper SPE 28688 presented at the 1994 SPE Petroleum Conference and Exhibition of Mexico, Veracruz, Mexico, 10-13 October.

85. Vasco, D.W. and Datta-Gupta, A.: "Asymptotic Solutions for Solute Transport: A Formalism for Tracer Tomography," *Water Resour. Res.* (1999), **35**, 1-16.

86. Pollock, D. W.: "Semianalytical Computation of Pathlines for Finite-Difference Models," *Groundwater* (1988), **26**(6), 743.

87. Iman.R.L., and Conover.W.J.: "Small Sample Sensitivity Analysis Techniques for Computer Models, With an Application to Risk Assessment", *Commun. Statist.-Theor. Math.* (1980), **A9** (17), 1749-1842.

88. Lentner.M., and Bishop.T.: *Experimental Design and Analysis*, Valley Book Company, Blacksburg, VA, 1993.

APPENDIX A

ITERATIVE SPARSE LINEAR SOLVER, LSQR

Solving a linear system can be expressed as a least squares problem as follows.

$$\min_{\mathbf{x}} \parallel \mathbf{A}\mathbf{x} - \mathbf{b} \parallel \tag{A-1}$$

where **A** is a large sparse unsymmetric matrix. To solve the least squares problem, we can equivalently solve the linear system

$$\begin{bmatrix} \mathbf{I} & \mathbf{A} \\ \mathbf{A}^T & \mathbf{0} \end{bmatrix} \begin{bmatrix} \mathbf{r} \\ \mathbf{x} \end{bmatrix} = \begin{bmatrix} \mathbf{b} \\ \mathbf{0} \end{bmatrix} \tag{A-2}$$

where **r** is the residual vector (**b** - **Ax**). This is equivalent to a familiar *normal equation* $\mathbf{A}^T\mathbf{A}\mathbf{x} = \mathbf{A}^T\mathbf{b}$.

Applying Lanczos tridiagonalization scheme to the symmetric linear system (Eq. A-2), we will have the recursion

$$\begin{aligned} \beta_1 \mathbf{u}_1 &= \mathbf{b} \\ \mathbf{A}\mathbf{V}_k &= \mathbf{U}_{k+1}\mathbf{B}_k \\ \mathbf{A}^T\mathbf{U}_{k+1} &= \mathbf{V}_k\mathbf{B}_k^T + \alpha_{k+1}\mathbf{v}_{k+1}\mathbf{e}_{k+1}^T \end{aligned} \tag{A-3}$$

where $\mathbf{B}_k$ is a lower bidiagonal matrix and the columns of $\mathbf{V}_k$ form an orthonormal basis for the Krylov subspace. This can be called a Lanczos bidiagonalization procedure on an unsymmetric matrix **A**. The matrices $\mathbf{V}_k$, $\mathbf{U}_k$, and $\mathbf{B}_k$ are

$$\begin{aligned} \mathbf{V}_k &= (\mathbf{v}_1, \cdots, \mathbf{v}_k), \\ \mathbf{U}_k &= (\mathbf{u}_1, \cdots, \mathbf{u}_k), \\ \mathbf{B}_k &= \begin{bmatrix} \alpha_1 & & & 0 \\ \beta_2 & \alpha_2 & & \\ & \beta_3 & \ddots & \\ & & \ddots & \alpha_k \\ 0 & & & \beta_{k+1} \end{bmatrix} \end{aligned} \tag{A-4}$$

where the nonnegative scalars α_i and β_i's are chosen to normalize $\mathbf{u}_i$ and $\mathbf{v}_i$.

If we assume $\mathbf{x}_k = \mathbf{V}_k\, \mathbf{y}_k$ then Eq. A-1 can be solved when $\mathbf{y}_k$ solves the linear least squares problem

$$\min_{y_k} \parallel \mathbf{B}_k \mathbf{y}_k - \beta_1 \mathbf{e}_1 \parallel \tag{A-5}$$

which can be easily solved by factorizing $\mathbf{B}_k$ through a sequence of orthogonal transformation, the Givens rotation.

APPENDIX B

IMPLEMENTATION OF GRAVITY IN PRESSURE AND SATURATION SOLUTIONS

The pressure equation, Eq. 3.1 can be discretized on a Cartesian grid in 3D as

$$\begin{aligned}
&T_{z,k-1/2}P^{n+1}_{i,j,k-1} + T_{y,j-1/2}P^{n+1}_{i,j-1,k} + T_{x,i-1/2}P^{n+1}_{i-1,j,k} \\
&-(T_{z,k-1/2} + T_{y,j-1/2} + T_{x,i-1/2} + T_{z,k+1/2} + T_{y,j+1/2} + T_{x,i+1/2} + A_{V,i,j,k})P^{n+1}_{i,j,k} \\
&+T_{z,k+1/2}P^{n+1}_{i,j,k+1} + T_{y,j+1/2}P^{n+1}_{i,j+1,k} + T_{x,i+1/2}P^{n+1}_{i+1,j,k} = \\
&-A_{V,i,j,k}P^{n}_{i,j,k} + G_{z,k-1/2}(D_{i,j,k-1} - D_{i,j,k}) + G_{z,k+1/2}(D_{i,j,k+1} - D_{i,j,k}) \\
&\qquad + G_{y,j-1/2}(D_{i,j-1,k} - D_{i,j,k}) + G_{y,j+1/2}(D_{i,j+1,k} - D_{i,j,k}) \\
&\qquad + G_{x,i-1/2}(D_{i-1,j,k} - D_{i,j,k}) + G_{x,i+1/2}(D_{i+1,j,k} - D_{i,j,k}) - q_{i,j,k}
\end{aligned} \tag{B-1}$$

where *P* is the grid pressure and *D* is the depth of the grid. The superscript *n* denotes the previous time step, and *n+1* denotes current time step. The subscript *k* index is in the *z* coordinate direction, the *j* index is in the *y* coordinate direction, and the *i* index is in the *x* coordinate direction. The related coefficients in the equation are defined as follows.

For inter-block transmissibility,

$$T_{z,k+1/2} = \lambda_{t,i,j,k+1/2}\frac{2}{\dfrac{\Delta z_{i,j,k}}{k_{z,i,j,k}\Delta x_{i,j,k}\Delta y_{i,j,k}} + \dfrac{\Delta z_{i,j,k+1}}{k_{z,i,j,k+1}\Delta x_{i,j,k+1}\Delta y_{i,j,k+1}}} \tag{B-2}$$

where $\lambda_{t,i,j,k+1/2}$ is the inter-block total mobility, which is evaluated as

$$\lambda_{t,i,j,k+1/2} = \sum_{l=1}^{n_p}\frac{(k_{r,l})_{upstream}}{\mu_{l,i,j,k+1/2}} \tag{B-3}$$

and the phase viscosity is obtained by arithmetic averaging

$$\mu_{l,i,j,k+1/2} = \frac{\mu_{l,i,j,k+1} + \mu_{l,i,j,k}}{2} \tag{B-4}$$

Other inter-block transmissibility can be expanded similarly.

For inter-block gravity transmissibility,

$$G_{z,k+1/2} = \left(\sum_{l=1}^{n_p} \left(\frac{k_{r,l}\rho_l g}{\mu_l} \right)_{i,j,k+1/2} \right) \frac{2}{\dfrac{\Delta z_{i,j,k}}{k_{z,i,j,k}\Delta x_{i,j,k}\Delta y_{i,j,k}} + \dfrac{\Delta z_{i,j,k+1}}{k_{z,i,j,k-1}\Delta x_{i,j,k+1}\Delta y_{i,j,k+1}}} \qquad \text{(B-5)}$$

where the phase density and viscosity are obtained by arithmetic averaging. Other inter-block gravity transmissibility can be expanded similarly.

For storage coefficient,

$$A_{V,i,j,k} = \frac{\phi_{i,j,k} c_t}{\Delta t} \Delta x_{i,j,k} \Delta y_{i,j,k} \Delta z_{i,j,k} \qquad \text{(B-6)}$$

We discretize Eq.3.17 in space and time to solve for saturation along the gravity lines

$$S_k^{n+1} = S_k^n - \frac{\Delta t_g}{\phi_{ki} \Delta z_k} (\widetilde{G}_{k+1/2} - \widetilde{G}_{k-1/2}) \qquad \text{(B-7)}$$

where k is the node along a gravity line, Δt_g is the local time step size, and $\widetilde{G}$ is defined as

$$\widetilde{G}_{k+1/2} = \frac{\lambda_{o,i,j,k+1} k_{z,i,j,k+1} \lambda_{w,i,j,k} k_{z,i,j,k}}{\lambda_{o,i,j,k+1} k_{z,i,j,k+1} + \lambda_{w,i,j,k} k_{z,i,j,k}} (\rho_w - \rho_o) g \qquad \text{(B-8)}$$

Similar equation can be written for $G_{k-1/2}$.

APPENDIX C

SENSITIVITY COMPUTATIONS USING THE SENSITIVITY EQUATION METHOD

Consider an explicitly discretized version of the Buckley-Leverett equation in the time of flight coordinate for a particular streamline:

$$\frac{1}{\Delta t}\left((S_w)_i^{n+1} - (S_w)_i^{n}\right) + \frac{1}{\tau_i - \tau_{i-1}}\left(f_w(S_w)_i^n - f_w(S_w)_{i-1}^n\right) = 0 \qquad \text{(C-1)}$$

for $i = 1,\cdots,nn$ and nn is the number of nodes used for discretization along the streamline. Differentiating Eq.C-1 with respect to the parameter m_j evaluated at the j^{th} node of the streamline, we obtain

$$\begin{aligned} &\frac{1}{\Delta t}\left[\left(\frac{\partial S_{w_i}}{\partial m_j}\right)^{n+1} - \left(\frac{\partial S_{w_i}}{\partial m_j}\right)^{n}\right] - \frac{\Delta f_w}{(\Delta\tau)^2}\left[\frac{\partial \tau_i}{\partial m_j} - \frac{\partial \tau_{i-1}}{\partial m_j}\right] \\ &+ \frac{1}{\Delta\tau}\left[\left(\frac{\partial f_{w_i}}{\partial S_{w_i}}\frac{\partial S_{w_i}}{\partial m_j}\right)^{n} - \left(\frac{\partial f_{w_{i-1}}}{\partial S_{w_{i-1}}}\frac{\partial S_{w_{i-1}}}{\partial m_j}\right)^{n}\right] = 0 \end{aligned} \qquad \text{(C-2)}$$

where $\Delta f_w = f_w(S_w)_i^n - f_w(S_w)_{i-1}^n$ and $\Delta\tau = \tau_i - \tau_{i-1}$.

Rearranging Eq.C-2, we obtain

$$\left(\frac{\partial S_{w_i}}{\partial m_j}\right)^{n+1} = \left(1 - \frac{\Delta t}{\Delta \tau}\frac{\partial f_{w_i}}{\partial S_{w_i}}\right)\left(\frac{\partial S_{w_i}}{\partial m_j}\right)^{n} + \frac{\Delta t}{\Delta \tau}\frac{\partial f_{w_{i-1}}}{\partial S_{w_{i-1}}}\left(\frac{\partial S_{w_{i-1}}}{\partial m_j}\right)^{n} + \frac{\Delta t \Delta f_w}{(\Delta \tau)^2}\frac{\partial \tau_j}{\partial m_j} \tag{C-3}$$

where we have used the following relationship

$$\frac{\partial \tau_{i+k}}{\partial m_j} = \begin{cases} 0 & \text{if } i+k<j \\ \dfrac{\partial \tau_j}{\partial m_j} & \text{otherwise} \end{cases} \quad \text{for all non - negative integer } k \tag{C-4}$$

Analytic expressions for travel time sensitivities can be used while solving Eq.C-3. The initial conditions in Eq.C-3 during the first pressure solve is set to be zero because the saturation field is assumed to be in equilibrium. Once the time step marching is finished at a particular pressure update, we have the saturation sensitivities at all streamline nodes. These sensitivities can be mapped onto the new set of streamline nodes after updating the pressure field.

VITA

Mr. Zhong He was born in China on March 9, 1965. He received his B.S. from Jianghan Petroleum Institute, China in 1985 and his M.S. from the Graduate School of Research Institute of Petroleum Exploration and Development (RIPED), China in 1988, both in petroleum engineering.

He worked as a research engineer from 1988 to 1993 and as a senior research engineer from 1993 to 1998 in RIPED, specializing in physical modeling, numerical simulation and project design for heavy oil thermal recovery. His U.S. corporate experience includes internships with British Petroleum (BP) and El Paso Production Company during his graduate years.

His permanent address: Xueyuan Road No. 20
Beijing 100083, China